Gravitational waves from compact binary coalescences: Tests of General Relativity and Astrophysics

By

SHILPA KASTHA

PHYS10201404001

The Institute of Mathematical Sciences, Chennai

A thesis submitted to the

Board of Studies in Physical Sciences

In partial fulfillment of requirements

For the Degree of

DOCTOR OF PHILOSOPHY

of

HOMI BHABHA NATIONAL INSTITUTE

August, 2019

STATEMENT BY AUTHOR

This dissertation has been submitted in partial fulfillment of requirements for an advanced degree at Homi Bhabha National Institute (HBNI) and is deposited in the Library to be made available to borrowers under rules of the HBNI.

Brief quotations from this dissertation are allowable without special permission, provided that accurate acknowledgement of source is made. Requests for permission for extended quotation from or reproduction of this manuscript in whole or in part may be granted by the Competent Authority of HBNI when in his or her judgment the proposed use of the material is in the interests of scholarship. In all other instances, however, permission must be obtained from the author.

Shilpa Kastha

DECLARATION

I, hereby declare that the investigation presented in the thesis has been carried out by me. The work is original and has not been submitted earlier as a whole or in part for a degree / diploma at this or any other Institution / University.

Shilpa Kastha

Homi Bhabha National Institute

Recommendations of the Viva Voce Board

As members of the Viva Voce Board, we certify that we have read the dissertation prepared by Shilpa Kastha entitled "Gravitational waves from compact binary coalescences: Tests of General Relativity and Astrophysics" and recommend that it may be accepted as fulfilling the dissertation requirement for the Degree of Doctor of Philosophy.

Balachandran S ______ Date: 06/02/2020

Chairman - Balachandran Sathiapalan

Manjari Bagchi ______ Date: 6/Feb/2020

Guide/Convener - Manjari Bagchi

______ Date: 6/02/2020

Co-guide - K G Arun

______ Date: 06/02/2020

Member 1 - Shrihari Gopalakrishna

Suryanarayana ______ Date: 06/02/2020

Member 2 - Nemani Venkata Suryanarayana

Sibasish Ghosh ______ Date: 06/02/2020

Member 3 - Sibasish Ghosh

BR Iyer ______ Date: 6 Feb 2020

External Examiner - Bala Iyer

Final approval and acceptance of this dissertation is contingent upon the candidate's submission of the final copies of the dissertation to HBNI.

We hereby certify that we have read this dissertation prepared under my direction and recommend that it may be accepted as fulfilling the dissertation requirement.

Date: 6/Feb/2020

Place: Chennai

Co-guide **Guide** Manjari Bagchi

Contents

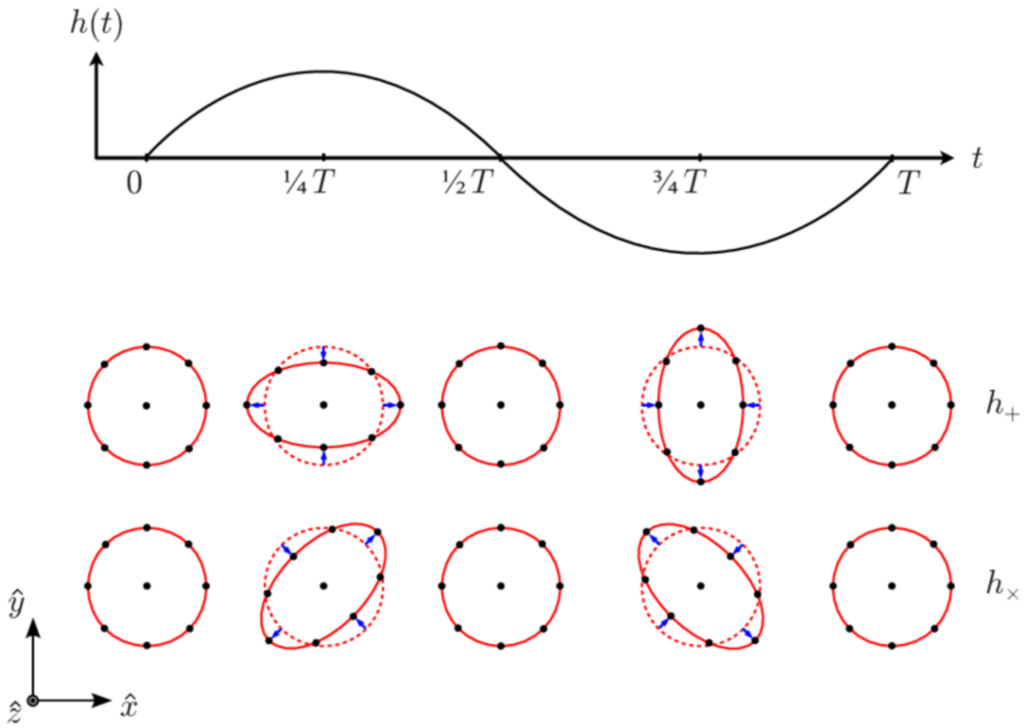

Figure 1.1. Upper panel shows a monochromatic GW, $h(t)$, propagating along the $\hat{z}$ direction. Lower panel shows the effect of the plus and the cross polarization on ring of test particles [218].

for geodesic deviation, which is given by,

$$\frac{D^2\xi^\mu}{D\tau^2} = -R^\mu_{\nu\rho\sigma}\xi^\rho \frac{dx^\nu}{d\tau}\frac{dx^\sigma}{d\tau}, \tag{1.1.11}$$

where D denotes the directional derivative and $R^\mu_{\nu\rho\sigma}$ is the Riemann tensor. After a few algebraic manipulations (see [226] for details), the equation of geodesic deviation, Eq. (1.1.11), at the linearized order, can be written as a function of GW amplitude, which is,

$$\ddot{\xi}^i = \frac{1}{2}\ddot{h}^{TT}_{ij}\xi^j, \tag{1.1.12}$$

where $\ddot{h}^{TT}_{ij}$ denotes the second time derivative of h_{ij}. Using Eq. (1.1.12), one can easily conclude that when a GW passes through a set of test particles, the relative distance between the test masses stretches and squeezes.

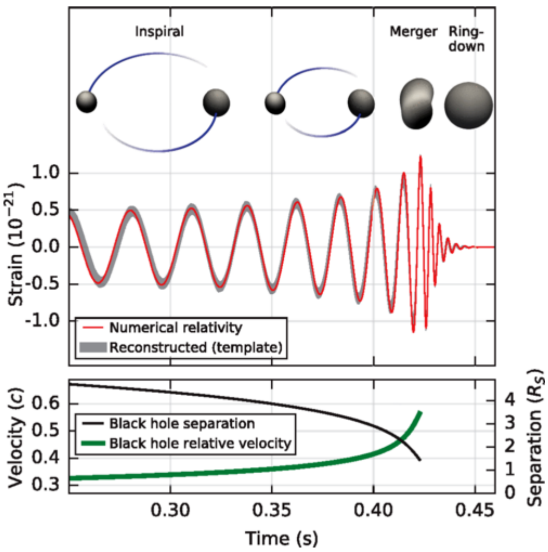

Figure 1.2. The upper panel shows a typical gravitational waveform during the various phases of a binary evolution whereas the lower panel shows the change in the BH velocity and their separation as a function of time (Image credit [18]).

pact binary systems can be produced by a pair of BHs, or a BH and NS, or a pair of NSs. In the case of BH-NS or NS-NS systems, the NS might get tidally disrupted and might produce new features in the waveform, carrying information about the NS's internal structure [12].

In the remainder of this thesis, we focus on GWs from compact binary inspirals to study GWs in the MPM-PN formalism and study the implications of observing these systems for fundamental physics and astrophysics.

1.3 Gravitational waves detectors

Efforts to detect GWs from celestial bodies started in 1960, pioneered by J. Weber. The idea for detection of GWs in this method is to use giant metal cylinders (bar detectors) to measure the vibrations excited in the material due to the passage of gravitational waves. But the bar-detectors did not reach the sensitivity required to detect GWs from astrophysical sources, and a detection claimed by Weber [292] could not be established by other detectors.

In parallel, attempts to construct the interferometric detectors were pursued. Here one uses the

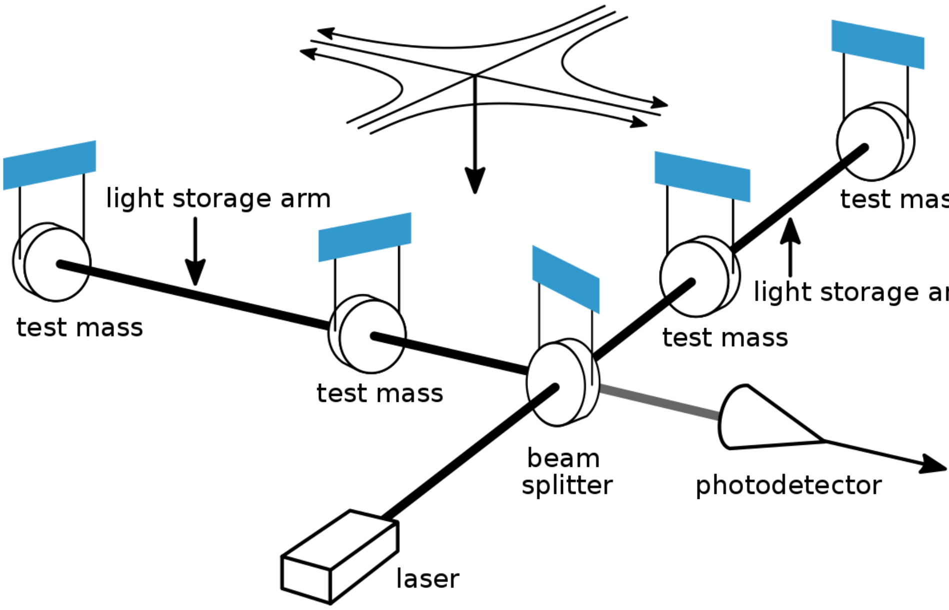

Figure 1.3. Simplified schematic diagram of a LIGO detector (Credit: Caltech/MIT/LIGO Lab).

principle of interferometry to detect GWs where a beam of monochromatic light (laser beam) is first split into two and travels through two different optical cavities at an angle with each other. These two beams get reflected by the freely suspended mirrors at the ends of the cavities and recombine to produce an interference pattern (see fig. 1.3 for a schematic diagram). Due to the passage of GWs, the arm length of the cavities changes, which corresponds to the dimensionless strain with an amplitude of about $h = \frac{\Delta L}{L} \sim 10^{-20}$. This relative change varies over time depending on the intensity of the passing GWs and causes changes in the interference pattern which are monitored through the photo detector and extracts information about the GWs. Unlike the narrow-band bar detectors, interferometric detectors have broad-band responses, which facilitates searches for different types of GW sources.

1.3.1 Currently operational gravitational wave detectors

The two LIGO (Laser Interferometer Gravitational-Wave Observatory) detectors are located in Livingston, Louisiana and Hanford, Washington, two largely separated locations in the USA. These are L-shaped detectors with each arm of length 4 km. Along with these two, Advanced VIRGO is

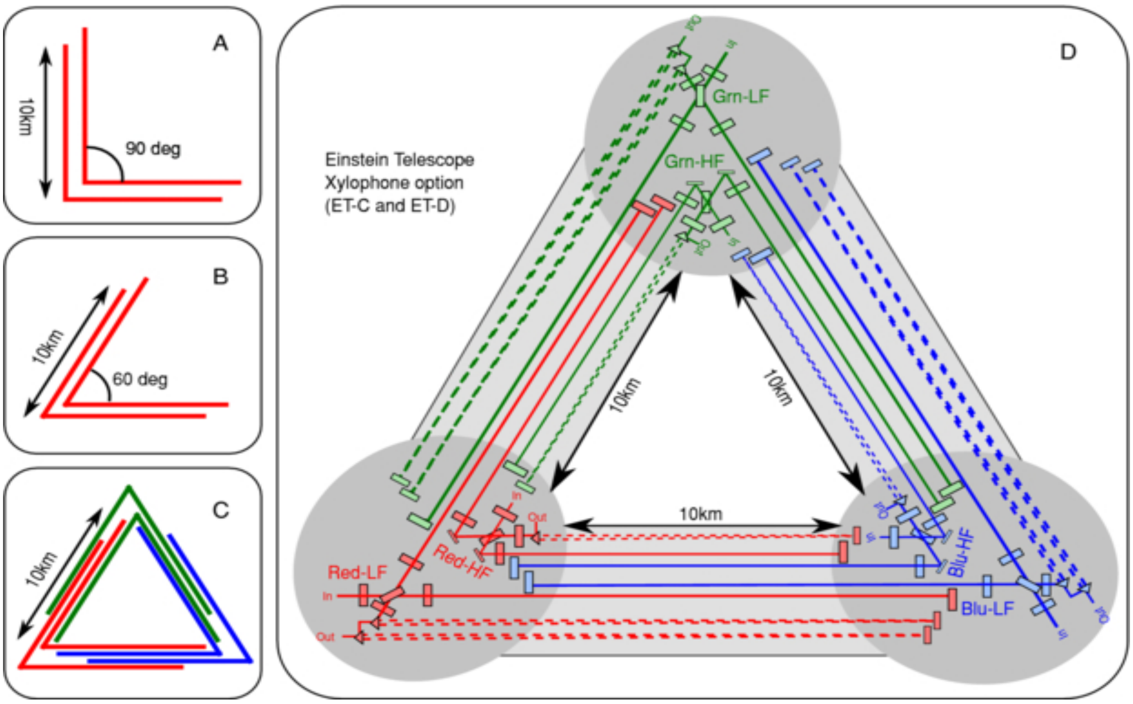

Figure 1.4. simplified schematic diagram of triangular ET [189] .

another detector, located near Pisa in Europe. This is also an L-shaped interferometric detector but with a 3 km arm length, has comparable sensitivity to that of the two LIGO detectors.

1.3.2 Future gravitational wave detectors

1.3.2.1 Future second generation detectors

With improved sensitivities of Advanced LIGO and Virgo in the upcoming observing runs, there are a few more upcoming second generation GW detectors. The Japanese cryogenic detector KAGRA [69] is likely to be operational soon. LIGO-India [201] is also expected to join the world-wide network of GW detectors by mid-2020s. A worldwide network of five GW detectors will increase the expected event rates as well as boost the detection confidence. The source localizations of the GW sources will also improve tremendously [164, 209].

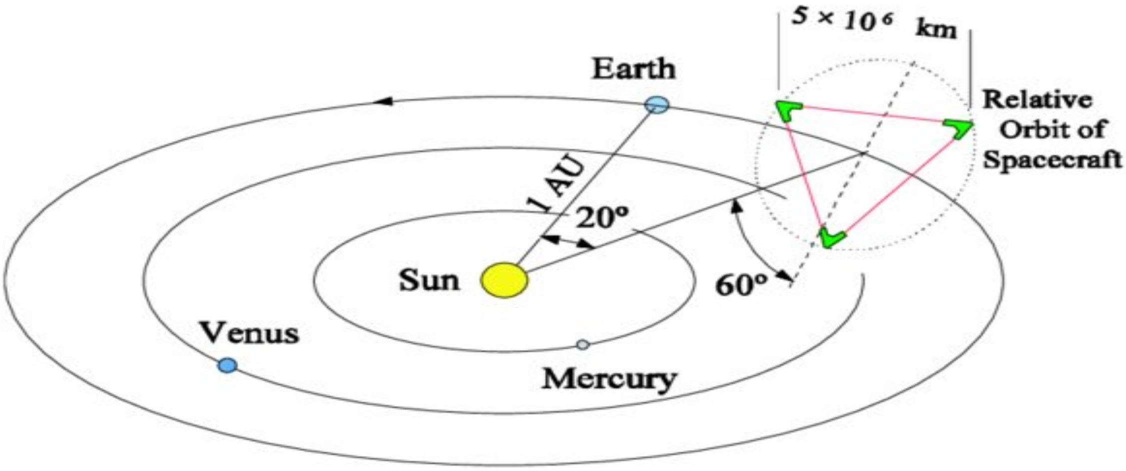

Figure 1.5. The orbital configuration of the LISA mission concept [198]

1.3.2.2 Future third generation detectors

There are ongoing research and developments, including science case studies for third-generation detectors such as the Einstein Telescope (ET) [11] and Cosmic Explorer (CE) [24]. Among the third generation detectors, CE is an L-shaped interferometric detector but with much larger arm length(~40 km) compared to the second generations ones, whereas ET is a triangular shaped detector with each arm of length 10 km (a simplified diagram of ET is given in fig. 1.4). Due to their improved sensitivity in the low frequency regime (till ~1Hz) and the leap in the sensitivity compared to the second generation detectors, they are unique probes of the high redshift universe. Roughly around 10^6 of BNS mergers [39] are expected to be detected by the 3G detector network, which will help to test astrophysical models of the formation and evolution of double neutron stars. In addition to stellar-mass compact binaries, ET and CE can detect intermediate-mass BHs with a total mass of several hundreds of solar masses, which will last longer (compared to the equal-mass binaries) in the detector sensitivity band and hence are accurate probes of the compact binary dynamics and the BH nature of the compact objects [118, 265].

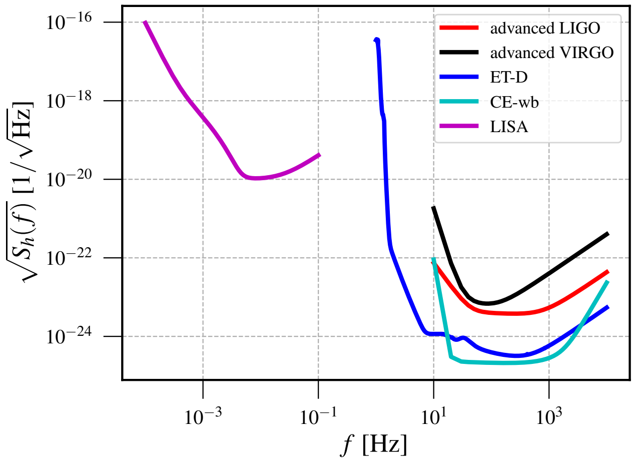

Figure 1.6. Various noise PSDs of the ground based and space-based GW detectors used in this thesis for various studies.

$$+ 0.7431 \times \left(\frac{50}{f}\right)^2 + 0.9404 \times \left(\frac{70}{f}\right) + 0.2107 \times \left(\frac{100}{f}\right)^{0.5} + 26.02\left(\frac{f}{500}\right)^2\Bigg] \text{Hz}^{-1}\,, \quad (1.4.6)$$

where f is in units of Hz. For the Japanese detector KAGRA we use the noise PSD given in Ref. [3].

Third generation ground based detectors : In case of third generation ground based detectors, we use the noise PSD given in Ref. [11] for ET-D. For CE we use the following fit,

$$\begin{aligned} S_h(f) &= 5.62 \times 10^{-51} + 6.69 \times 10^{-50} f^{-0.125} + \frac{7.80 \times 10^{-31}}{f^{20}} \\ &+ \frac{4.35 \times 10^{-43}}{f^6} + 1.63 \times 10^{-53} f + 2.44 \times 10^{-56} f^2 \\ &+ 5.45 \times 10^{-66} f^5 \ \text{Hz}^{-1}\,, \end{aligned} \quad (1.4.7)$$

where f is in units of Hz .

Space based detector LISA : We quote the noise PSD for LISA here which we have used in further computations following Ref. [70]. The analytical form of the sky-averaged detector sensitivity

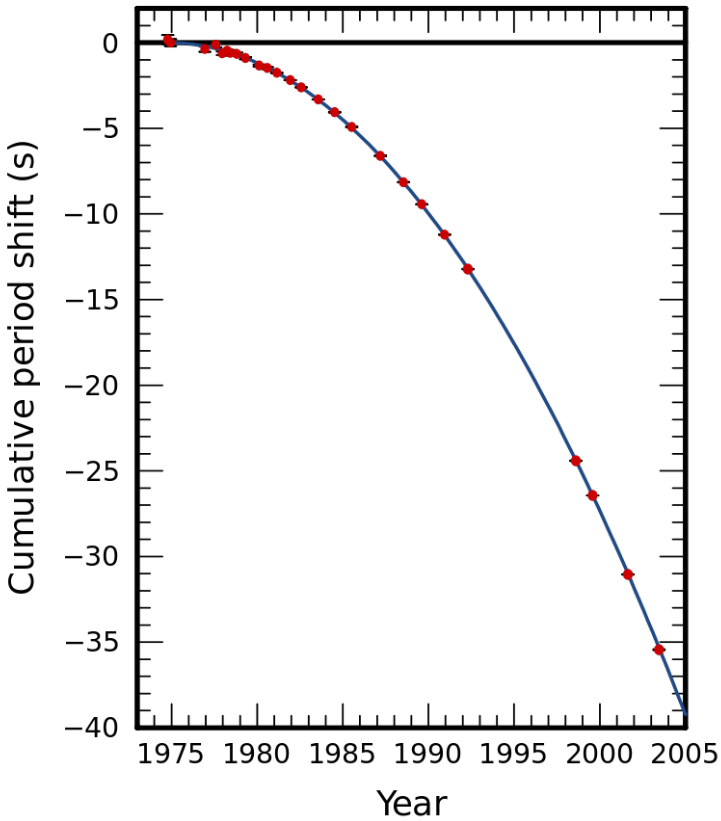

Figure 1.7. Orbital decay caused by the loss of energy by gravitational radiation [293].

tion [40, 174, 197, 241].

After two decades of development, a combination of the initial interferometric detectors including TAMA 300 in Japan, GEO 600 in Germany, LIGO in the United States, and Virgo in Italy operated between 2002 and 2010. These observations did not lead to the detection of GWs, which was consistent with the expected event rates of the GW sources. However, these observations put the first observational upper limits on the rate of mergers of BBH, BNS and NS-BH systems [5,6,8,38].

Between 2010-2015 initial LIGO was upgraded, and in 2015 it started the first observation run with a sensitivity much better than the initial LIGO. With this sensitivity, on 14 September 2015, the two LIGO detectors, Livingstone and Hanford, jointly detected the GWs from a BBH merger with a statistical confidence $> 5\sigma$ [13, 18] . The duration of the signal detected was ~ 0.2 sec. The individual BHs of masses $36^{+5}_{-4}M_{\odot}$and $29^{+4}_{-4}M_{\odot}$ at a distance of 410^{+160}_{-180} Mpc, merged to form a final

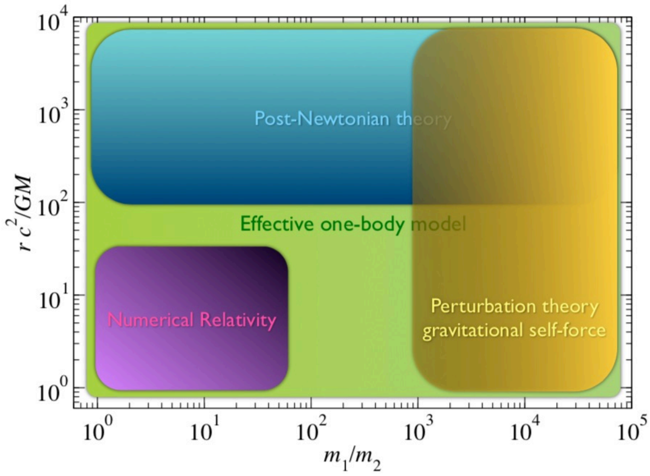

Figure 2.1. Regime of validity of various approximation schemes and numerical methods in the plane defined by the two perturbation parameters rc^2/Gm and m_1/m_2. Figure courtesy [123].

effects of back-reaction are consistently taken into account within the gravitational self-force formalism [75,76,151–153,254]. In contrast, numerical relativity provides a description of the merger of two compact objects at high velocity [256] and is valid for any mass ratio in principle. However, this method is computationally very expensive.

Apart from the above described methods, a semi-analytical description, namely the *Effective One Body* (EOB) approach of compact binary dynamics and emission of GW radiation is proposed in refs. [119,120,139,144] to include the post-inspiral effects. Assuming a comparable mass compact binary system is a smooth deformation of that of the test particle limit, the EOB approach uses three ingredients; the conserved Hamiltonian of the two body system in GR, the radiation-reaction force, and the gravitational waveform. Each of these ingredients is estimated using the higher order PN-expanded results in a *resummed form* to incorporate non-perturbative and strong-field effects.

After the remarkable progress in developing analytical as well as numerical techniques to solve the two body dynamics in GR over more than a hundred years, we now can predict highly accurate gravitational waveforms from compact binary mergers. The dynamics of a compact binary system is conventionally divided into the *adiabatic inspiral, merger*, and *ringdown* phases. During the inspiral phase the orbital time scale is much smaller than the radiation backreaction time

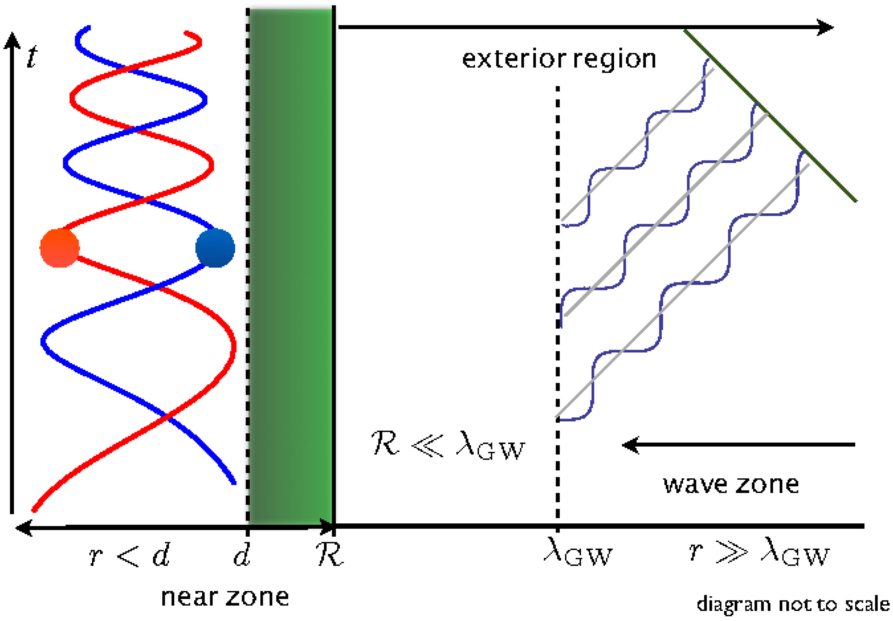

Figure 2.2. Various scales used in PN approximation. Figure courtesy Ref. [123].

near zone where $r << \lambda_{\rm GW}$. Though slow motion is one of the main criteria of this scheme, the characteristic speed for a compact binary inspiral could be as high as 50% of the speed of light in their last orbit, which demands the computation of higher PN order corrections. On the other hand, in the weak field limit, post-Minkowskian (PM) formalism is valid outside the source in the region where $r >> \lambda_{\rm GW}$ spanned till $r \to \infty$ denoted as wave zone. In addition to the PM expansion, multipolar expansion of the complete non-linear theory [84, 94] provides the full MPM scheme which is valid over all the regions outside the compact source. In principle, this scheme is valid for all kinds of sources but for PN sources there exists a buffer/matching zone where both the approximation schemes are valid, which gives rise to the complete wave generation formalism.

PN order	frequency dependences	Multipole coefficients
0 PN	$f^{-5/3}$	μ_2
1 PN	f^{-1}	μ_2, μ_3, ϵ_2
1.5 PN	$f^{-2/3}$	μ_2
2 PN	$f^{-1/3}$	μ_2, μ_3, μ_4, ϵ_2, ϵ_3
2.5 PN log	$\log f$	μ_2, μ_3, ϵ_2
3 PN	$f^{1/3}$	μ_2, μ_3, μ_4, μ_5, ϵ_2, ϵ_3, ϵ_4
3 PN log	$f^{1/3}\log f$	μ_2
3.5 PN	$f^{2/3}$	μ_2, μ_3, μ_4, ϵ_2, ϵ_3

Table 3.1. Summary of the multipolar structure of the PN phasing formula. The contributions of various multipoles to different phasing coefficients and their frequency dependences are tabulated. Following the definitions introduced in this thesis, μ_l are associated to the deformations of mass-type multipole moments and ϵ_l refer to the deformations of current-type multipole moments.

simultaneously certain PN coefficients[1].

3.3 Parameter estimation of the multipole coefficients

In this section, we set up the parameter estimation problem to measure the multipolar coefficients and present our forecasts for Advanced LIGO, the Einstein Telescope, Cosmic Explorer and LISA. Using the frequency-domain gravitational waveform, we study how well the current and future generations of GW detectors can probe the multipolar structure of GR. We derive the projected accuracies with which various multipole moments may be measured, in case of various detector configurations by using standard parameter estimation techniques. Following the philosophy of Refs. [44, 66, 237], while computing the errors, we consider the deviation of only one multipole at a time. An ideal test would have been where all the coefficients are varied at the same time, but this would lead to almost no meaningful constraints due to the strong degeneracies among different coefficients. However, this would not affect our ability to detect a potential deviation because in the multipole structure, a deviation of more than one multipole coefficient would invariably show up in the set of tests performed by varying one coefficient at a time [44, 221, 231, 237].

[1] We thank Archisman Ghosh for pointing out this possibility to us.

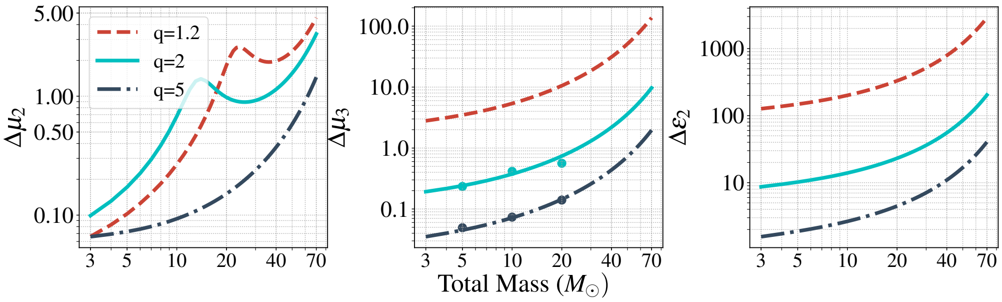

Figure 3.1. Projected 1σ errors on μ_2, μ_3 and ϵ_2 as functions of the total mass for the aLIGO noise PSD. Results from Bayesian analysis using MCMC sampling are given as dots showing good agreement. All the sources are considered to be at a fixed luminosity distance of 100 Mpc.

estimated.

3.4 Results and Discussion

In this section, we report the 1σ measurement errors on the multipole coefficients introduced in the previous section, obtained using the Fisher matrix as well as Bayesian analysis and discuss their implications.

Our results for the four different detector configurations are presented in figs. 3.1, 3.3 and 3.5, which show the errors on the various multipole coefficients μ_l, ϵ_l for aLIGO, ET-D, CE-wb and LISA, respectively. For all the estimates we consider the sources to be at fixed distances. In addition to the intrinsic parameters there are four more (angular) parameters that are needed to completely specify the gravitational waveform. More precisely, one needs two angles to define the location of the source on the sky and another two angles to specify the orientation of the orbital plane with respect to the detector plane and the polarization of the wave [268]. Since we are using a pattern-averaged waveform [143] (i.e., a waveform averaged over all four angles), the luminosity distance can be thought of as an *effective* distance which we assume to be 100 Mpc for aLIGO, ET-D and CE-wb and 3 Gpc for LISA. For aLIGO, ET-D and CE-wb, we explore the bounds for the binaries with total masses in the range [1,70] $M_\odot$ and for LISA detections, in the range $[10^5, 10^7]$ $M_\odot$.

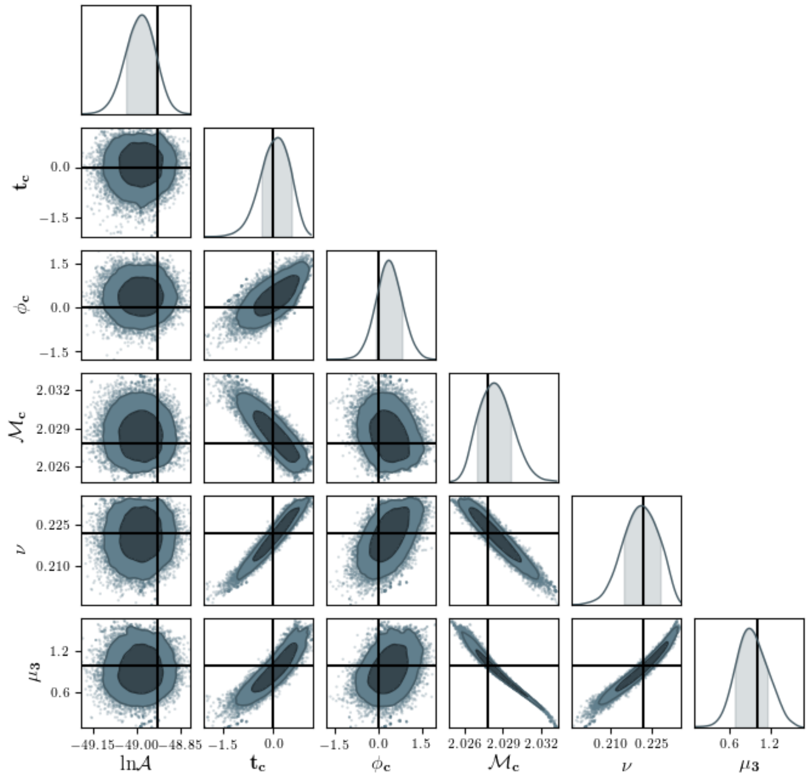

Figure 3.2. The posterior distributions of all six parameters $\{\ln\mathcal{A}, t_c, \phi_c, \mathcal{M}_c, \eta, \mu_3\}$ and their corresponding contour plots obtained from the MCMC experiments (see section 1.4.2 for details) for a compact binary system at a distance of 100 Mpc with $q = 2$, $m = 5\ M_\odot$ using the noise PSD of aLIGO. The darker shaded regions in the posterior distributions as well as in the contour plots show the 1σ bounds on the respective parameters.

3.4.1 Advanced LIGO

In fig. 3.1, we demonstrate the projected 1-σ errors on the three leading multipole coefficients, μ_2, μ_3 and ϵ_2, as a function of the total mass of the binary for the aLIGO noise PSD using the Fisher matrix. Different curves are for different mass ratios, $q = m_1/m_2 = 1.2$ (red), 2 (cyan) and 5 (blue). For the multipole coefficients considered, low-mass systems obtain the smallest errors and hence the tightest constraints. This is expected as low-mass systems live longer in the detector band and have larger number of cycles, thereby allowing us to measure the parameters very well. The bounds on μ_3 and ϵ_2, associated with the mass octupole and current quadrupole,

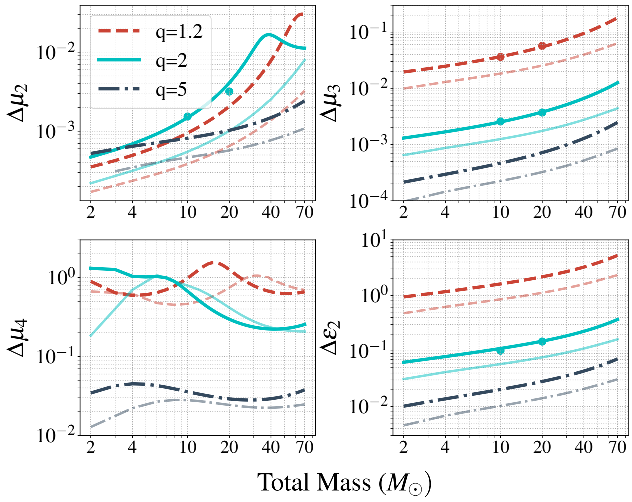

Figure 3.3. Dark shaded curves correspond to the projected 1σ error bars on μ_2, μ_3, μ_4 and ϵ_2 using the proposed CE-wb noise PSD as a function of the total mass, where as lighter shades denote the bounds obtained using the ET-D noise PSD. All the sources are considered to be at a fixed luminosity distance of 100 Mpc. The higher-order multipole moments such as μ_4 and ϵ_2 cannot be measured well using aLIGO and hence it may be a unique science goal of the third-generation detectors.

in the corner plots in fig. 3.2. In fig. 3.1 we see that the 1σ errors in μ_3 from the Fisher analysis agree very well with the MCMC results for $q = 2$ and 5. We did not find such an agreement for $q = 1.2$. We suspect that this is because for comparable-mass systems the likelihood function, defined in chapter 1, Eq. (1.4.16), becomes shallow and it is computationally very difficult to find its maximum given a finite number of iterations. As a result, the MCMC chains did not converge and 1σ bounds cannot be trusted for such cases. We find the nonconvergence of MCMC chains for all of the cases for μ_2 and ϵ_2. Hence we do not show those results in fig. 3.1. In a nutshell, our findings indicate only μ_2 and μ_3 can be measured with a good enough accuracy using aLIGO detectors.

3.4.2 Third-generation detectors

Third-generation detectors such as CE-wb (and ET-D) can put much better bounds on μ_2, μ_3 and ϵ_2 compared to aLIGO. Additionally, they can also measure μ_4 with reasonable accuracy, as shown by

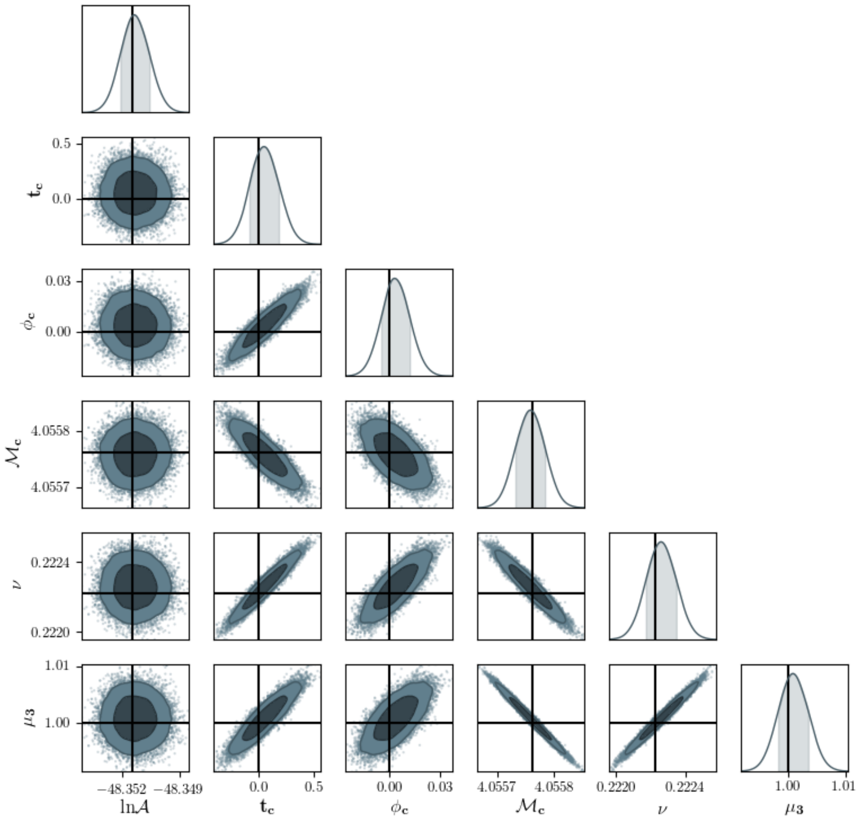

Figure 3.4. The posterior distributions of all six parameters $\{\ln\mathcal{A}, t_c, \phi_c, \mathcal{M}_c, \eta, \mu_3\}$ and their corresponding contour plots obtained from the MCMC experiments (see Sec. 1.4.2 for details) for a compact binary system at a distance of 100 Mpc with $q = 2$, $m = 10\ M_\odot$ using the noise PSD of CE-wb. The darker shaded region in the posterior distributions as well as in the contour plots show the 1σ bounds on the respective parameters.

the darker (and lighter) shaded curves in fig. 3.3. The bounds on μ_2, μ_3 and ϵ_2 show similar trends as in the case of aLIGO except the overall accuracy of the parameter estimation is much better. For a few cases in low-mass regime, μ_2 and μ_4 are better estimated for comparable-mass binaries (i.e., $q = 1.2$). We also find that the bounds (denoted by the lighter shaded curves in fig. 3.3) obtained by using the ET-D noise PSD are even better than the bounds from CE-wb, though the other features are more or less similar for both of the detectors. This improvement in the precision of measurements is due to two reasons. The triangular shape of ET-D enhances the sensitivity roughly by a factor of 1.5 and its sensitivity is much better than CE-wb in the low-frequency

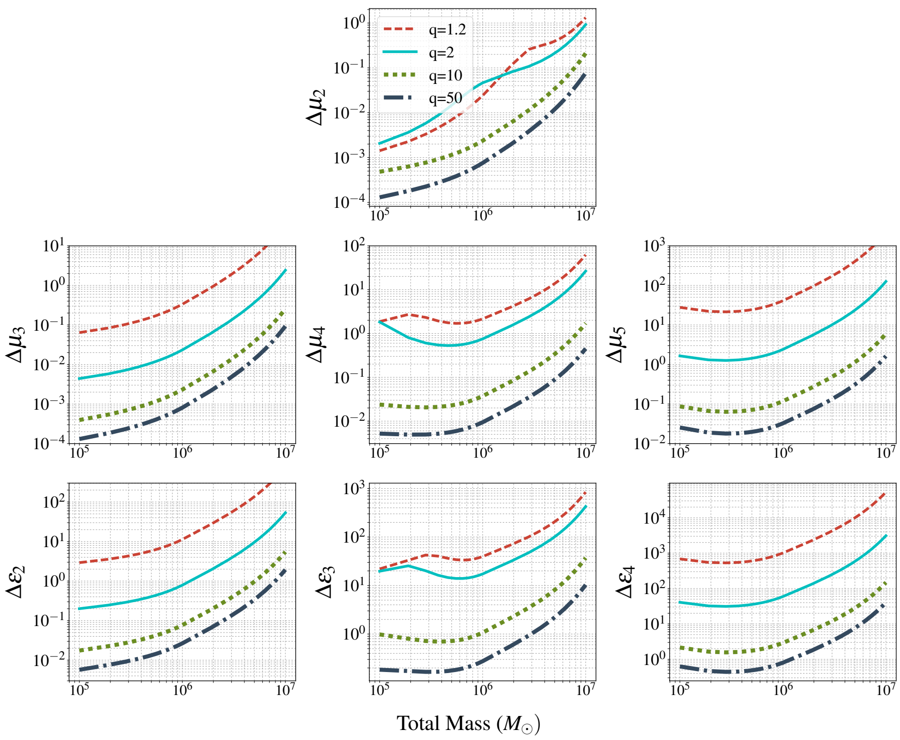

Figure 3.5. Projected constraints on various multipole coefficients using LISA sensitivity, as a function of the total mass of the binary. All the sources are considered to be at a fixed luminosity distance of 3 Gpc. LISA can measure all seven multipoles which contribute to the phasing and hence will be able to place extremely stringent bounds on the multipoles of the compact binary gravitational field.

regime.

For a few representative cases, we compute the errors in μ_2, ϵ_2 and μ_3 using Bayesian analysis and the results are shown as dots with the same color in fig. 3.3. The MCMC results are in good agreement with the Fisher matrix results. Unlike the aLIGO PSD, for CE-wb the MCMC chains converge quickly in the case of μ_2 and ϵ_2 because of the high signal-to-noise-ratios, which naturally lead to high likelihood values. As a result, it becomes relatively easier for the sampler to find the global maximum of the likelihood function in relatively fewer iterations. Moreover, we show an example of corner plot for the CE-wb PSD with $q = 2$, $m = 10$ M$_\odot$ in fig. 3.4.

PN order	frequency dependences	Multipole coefficients
0 PN	$f^{-5/3}$	μ_2
1 PN	f^{-1}	μ_2, μ_3, ϵ_2
1.5 PN	$f^{-2/3}$	μ_2, $\underline{\epsilon_2}$
2 PN	$f^{-1/3}$	μ_2, μ_3, μ_4, ϵ_2, ϵ_3
2.5 PN log	$\log f$	μ_2, μ_3, ϵ_2, $\underline{\epsilon_3}$
3 PN	$f^{1/3}$	μ_2, μ_3, μ_4, μ_5, ϵ_2, ϵ_3, ϵ_4
3 PN log	$f^{1/3}\log f$	μ_2
3.5 PN	$f^{2/3}$	μ_2, μ_3, μ_4, ϵ_2, ϵ_3, $\underline{\epsilon_4}$

Table 4.1. Update of the summary given in table 3.1 of chapter 3 for the multipolar structure of the PN phasing formula. Contribution of various multipoles to different phasing coefficients and their frequency dependences are tabulated. The additional multipole coefficients appearing due to spin are underlined. Following the definitions introduced in chapter 3 [204], μ_l refer to mass-type multipole moments and ϵ_l refer to current-type multipole moments.

The cross-terms of the multipole coefficients with $\kappa_\pm$ showcase the degeneracy between BBHs in alternative theories and non-BHs in GR. As one can see from Eq. (4.3.10), μ_2, μ_3 and ϵ_2 are the multipole coefficients which are sensitive to the non-BH nature (vis-a-vis the above mentioned parametrization). As can be seen from the phasing formula, these imprints will be higher order corrections to the multipole coefficients and may not influence their estimates unless the values of $\kappa_\pm$ are sufficiently high.

4.4 Methodology for numerical analysis

We have discussed the the semi-analytical Fisher information matrix based parameter estimation scheme [67, 133, 136, 258] in section 1.4. We follow the same prescription to discuss the projected bounds on the multipolar deviation coefficients for the spinning binaries. We also discuss the leading order bounds on the systematics of the estimated parameters due to the difference between the spinning and non-spinning waveforms in the Appendix A for LISA.

For $\vec{\theta}$ being the set of parameters defining the GW signal $\tilde{h}(f;\vec{\theta})$, the Fisher information matrix is defined in Eq. (1.4.18). In the large signal-to-noise ratio (SNR) limit, the distribution of the

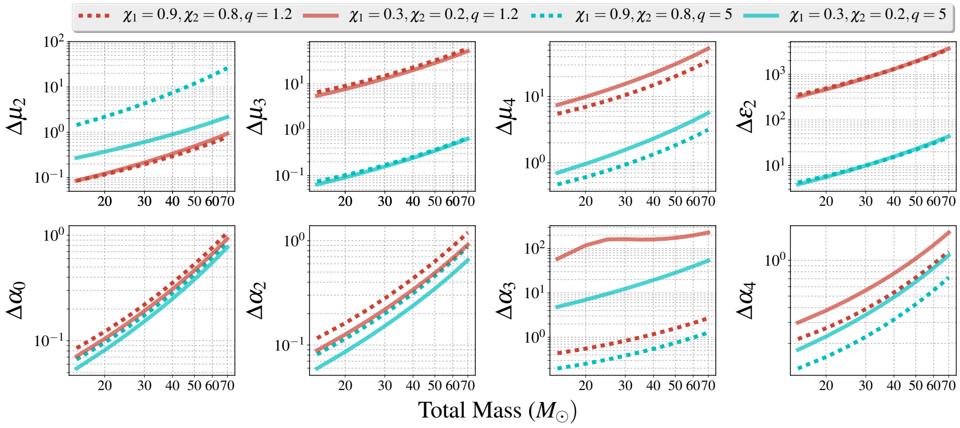

Figure 4.1. Projected 1σ errors on the multipole and the energy coefficients as a function of total mass for two different mass ratios $q = m_1/m_2 = 1.2, 5$ and two spin configurations, $\chi_1 = 0.9, \chi_2 = 0.8$ and $\chi_1 = 0.3, \chi_2 = 0.2$ for the second generation detector network. All the sources are at a fixed luminosity distance of 100 Mpc with the angular position and orientations to be $\theta = \pi/6, \phi = \pi/3, \psi = \pi/6, \iota = \pi/5$. To obtain the numerical estimates showed in this plot, we also consider a prior distribution on ϕ_c. To be precise, we assume the prior on ϕ_c for each detector in the network to follow a Gaussian distribution with a zero mean and a variance of $1/\pi^2$.

4.5.1 Ground-based second generation detector network

As a representative case, we consider a world-wide network of five second-generation ground based detectors: LIGO-Hanford, LIGO-Livingston, Virgo, KAGRA [69], and LIGO-India [201]. We assume the noise PSD for LIGO-Hanford, LIGO-Livingstone and LIGO-India to be the analytical fit given in Ref. [46] whereas the fit given in Eq. (1.4.6) is used for Virgo PSD. We consider the lower cut off frequency, $\mathrm{f_{low}} = 10$ Hz for these detectors. For the Japanese detector, KAGRA, we use the noise PSD given in Ref. [3] with $\mathrm{f_{low}} = 1$ Hz. For all the detectors, f_{high} is taken to be the frequency at the last stable orbit, $f_{\mathrm{LSO}} = 1/(\pi\, m\, 6^{3/2})$. As opposed to the single detector Fisher matrix analysis, for a network of detectors, Fisher matrix is evaluated for each detector and then added to obtain the network-Fisher-matrix. To estimate the individual Fisher matrices we use a waveform that is weighted with the correct antenna pattern functions $F_{+/\times}(\theta, \phi, \psi)$ of the detectors, where θ, ϕ and ψ are the declination, the right ascension and the polarization angle of the source in

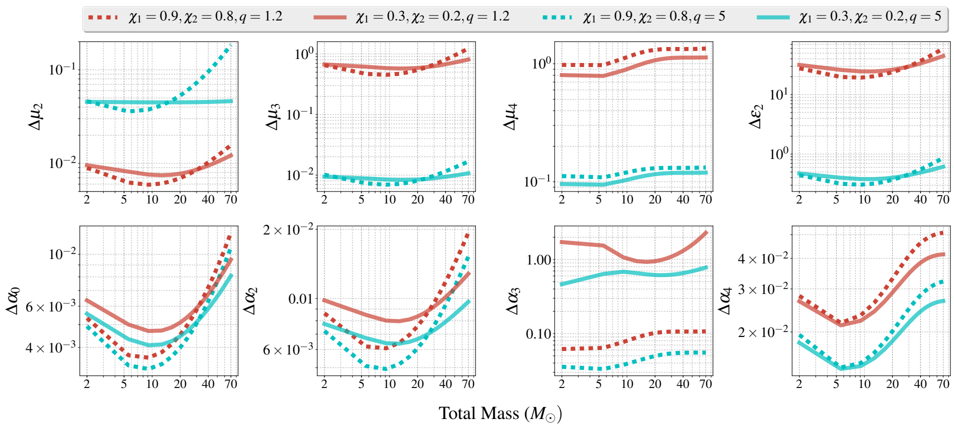

Figure 4.2. Projected 1σ errors on the multipole and the energy coefficients as a function of total mass for two different mass ratios $q = m_1/m_2 = 1.2, 5$ and two spin configurations, $\chi_1 = 0.9, \chi_2 = 0.8$ and $\chi_1 = 0.3, \chi_2 = 0.2$ for the third generation detector network. All the sources are at a fixed luminosity distance of 100 Mpc with the angular position and orientations to be $\theta = \pi/5, \phi = \pi/6, \psi = \pi/4, \iota = \pi/4$. To obtain the numerical estimates showed in this plot, we also consider a prior distribution on ϕ_c. To be precise, we assume the prior on ϕ_c for each detector in the network to follow a Gaussian distribution with a zero mean and a variance of $1/\pi^2$.

the sky. More precisely we use the following waveform

$$\tilde{h}(f) = \frac{1+\cos^2\iota}{2} F_+(\theta,\phi,\psi)\,\tilde{h}_+(f) + \cos\iota\, F_\times(\theta,\phi,\psi)\,\tilde{h}_\times(f) \tag{4.5.1}$$

with

$$\tilde{h}_+(f) = \mathcal{A}\mu_2\, f^{-7/6} e^{-i\Psi_s}\,, \tag{4.5.2}$$

$$\tilde{h}_\times(f) = -i\,\tilde{h}_+(f)\,. \tag{4.5.3}$$

The individual $F_{+/\times}(\theta,\phi,\psi)$ for each detector are estimated incorporating the location of the detectors on Earth as well as Earth's rotation as given in Ref. [4]. We calculate the Fisher matrix for each detector considering an eight dimensional parameter space, $\{t_c, \phi_c, \log\mathcal{A}, \log\mathcal{M}_c, \log\eta, \chi_s, \chi_a, \mu_\ell$ or ϵ_ℓ or $\alpha_m\}$, which specifies the true GW signal. Here we fix the four angles, $\theta, \phi, \psi, \iota$ to be $\pi/6, \pi/3, \pi/6, \pi/5$ respectively and do not treat them as parameters in the Fisher matrix estimation. These four angles, being the extrinsic parameters, have negligible correlations with the intrinsic

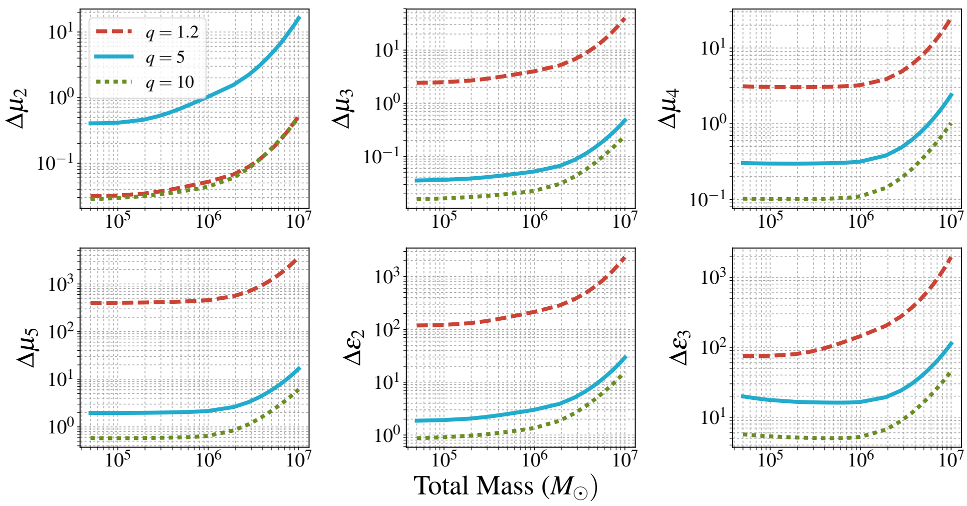

Figure 4.3. Projected 1σ errors on the multipole coefficients as a function of total mass for three different mass ratios $q = m_1/m_2 = 1.2, 5$ and 10 in case of LISA noise PSD. We assume $\chi_1 = 0.9, \chi_2 = 0.8$. All the sources are considered to be at a fixed luminosity distance of 3 Gpc. To obtain the numerical estimates showed in this plot, we also consider a prior distribution on ϕ_c. To be precise, we assume ϕ_c to follow a Gaussian distribution with a zero mean and a variance of $1/\pi^2$.

above.

4.6 Results

Our results for the ground-based detectors are depicted in Figs. 4.1 for second generation and 4.2 for third generation and those for the space-based LISA detector are presented in Figs. 4.3, 4.4, 4.5, 4.6 and 4.7. For the second and third generation ground-based detectors configurations, we choose the binary systems with two different mass ratios $q = 1.2, 5$ for two sets of spin configurations: high spin case with $\chi_1 = 0.9, \chi_2 = 0.8$ and low spin case with $\chi_1 = 0.3, \chi_2 = 0.2$. We also assume the luminosity distance to all these prototypical sources to be 100 Mpc. We consider these sources are detected with a network of second or third generation detectors as detailed in the last section. For LISA, we consider our prototypical supermassive BHs to be at the luminosity distance of 3 Gpc with three different mass ratios of $q = 1.2, 5, 10$. For these mass ratios, we investigate both high spin ($\chi_1 = 0.9, \chi_2 = 0.8$) and low spin ($\chi_1 = 0.3, \chi_2 = 0.2$) scenarios.

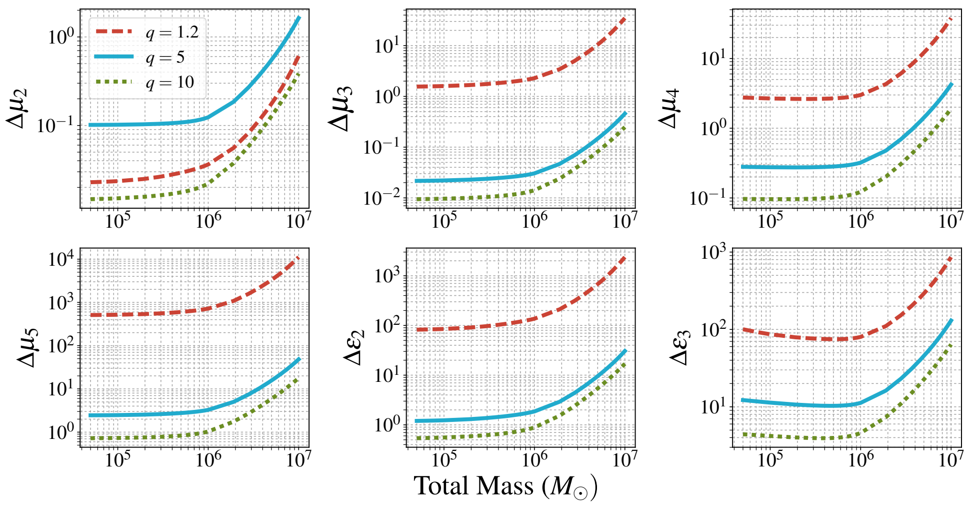

Figure 4.4. Projected 1σ errors on the multipole coefficients as a function of total mass for three different mass ratios $q = m_1/m_2 = 1.2, 5$ and 10 in case of LISA noise PSD. We assume $\chi_1 = 0.3, \chi_2 = 0.2$. All the sources are considered to be at a fixed luminosity distance of 3 Gpc. To obtain the numerical estimates showed in this plot, we also consider a prior distribution on ϕ_c. To be precise, we assume ϕ_c to follow a Gaussian distribution with a zero mean and a variance of $1/\pi^2$.

First we discuss the qualitative features in the plots. As expected, the third generation detector network which has better bandwidth and sensitivity does better than the second generation detectors. On the other hand LISA and third generation detectors perform comparably, though for totally different source configurations. The bounds on the multipole coefficients describing the dissipative dynamics broadly follow the trends seen in the non-spinning study carried out in chapter 3 [204]. The mass-type multipole moments are measured with better accuracies than the current-type ones appearing at the same PN order. Among all the coefficients, μ_2 (corresponding to the mass quadrupole) yields the best constraint as it is the dominant multipole contributing to the flux and the phasing. Due to the interplay between the sensitivity and mass dependent upper cut-off frequency, the errors increase as a function of mass in the regions of the parameter space we explore. The errors improve as the mass ratio increases for all cases except μ_2. As argued in chapter 3 [204], μ_2 is the only multipole parameter which appears both in the amplitude and the phase of the waveform and hence shows trends different from the other multipole coefficients. Inclusion of spins, on the whole, worsens the estimation of the multipole coefficients compared to the non-

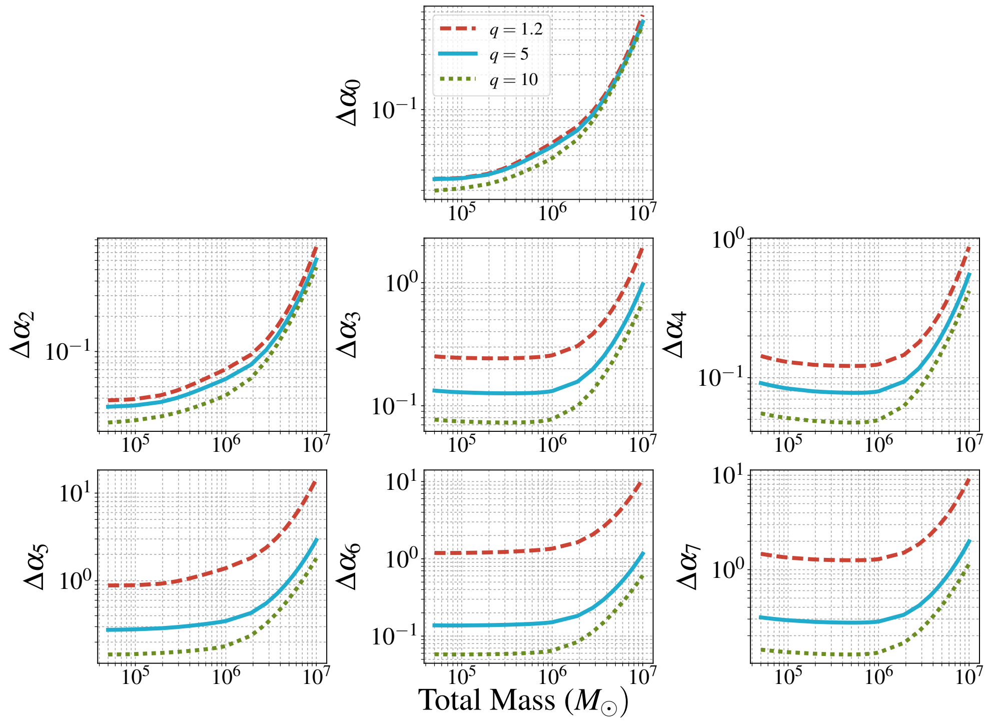

Figure 4.5. Projected 1σ errors on the energy coefficients as a function of total mass for three different mass ratios $q = m_1/m_2 = 1.2, 5$ and 10 in case of LISA noise PSD. We assume $\chi_1 = 0.9, \chi_2 = 0.8$. All the sources are considered to be at a fixed luminosity distance of 3 Gpc. To obtain the numerical estimates showed in this plot, we also consider a prior distribution on ϕ_c. To be precise, we assume the prior on ϕ_c to follow a Gaussian distribution with a zero mean and a variance of $1/\pi^2$.

spinning case. This is expected as the spins increase the dimensionality of the parameter space but do not give rise to any new features which may help the estimation. Effects such as spin-induced precession, which brings in a new time scale and associated modulations, may help counter this degradation in the parameter estimation. But this will be a topic for a future investigation. We also explore the bounds on the multipole coefficients as a function of the spin magnitudes in case of LISA (see fig. 4.7). Here we consider two mass ratio cases $q = 10, 20$ but fix the total mass of the system to be 2×10^5M$_\odot$and plot the bounds as a function of primary spin χ_1. Since we vary the secondary spin, χ_2 as well, we get a spread on the bounds at each χ_1 along the y-axis due to different values of χ_2 in the limit $[-1, 1]$. We find that the parameter estimation improves with the spin mag-

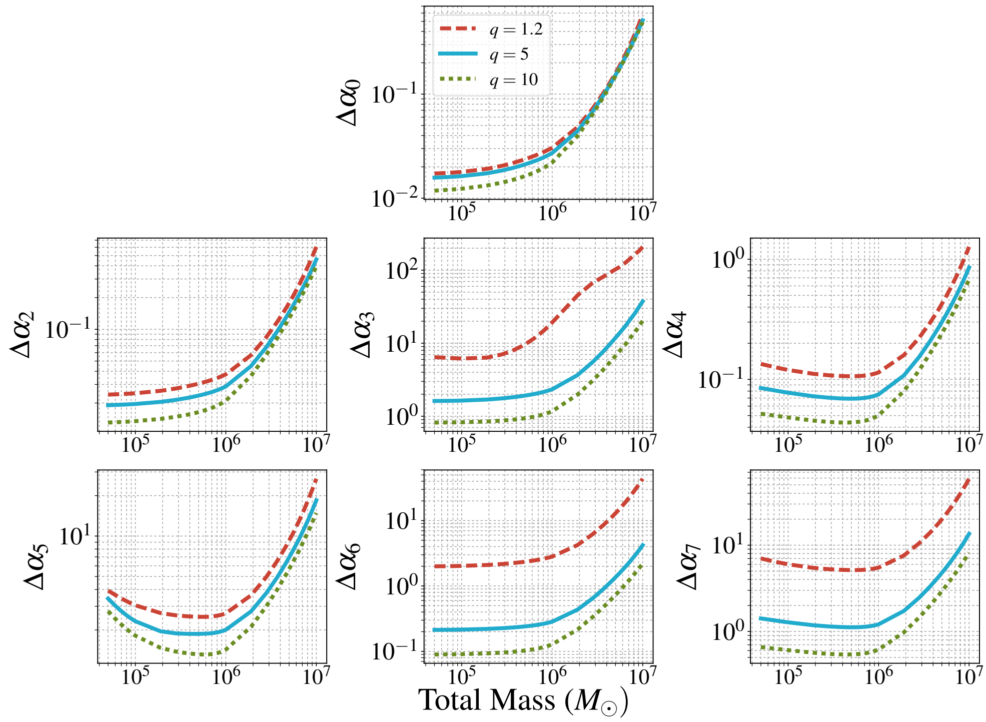

Figure 4.6. Projected 1σ errors on the energy coefficients as a function of total mass for three different mass ratios $q = m_1/m_2 = 1.2, 5$ and 10 in case of LISA noise PSD. We have considered $\chi_1 = 0.3, \chi_2 = 0.2$. All the sources are considered to be at a fixed luminosity distance of 3 Gpc. To obtain the numerical estimates showed in this plot, we also consider a prior distribution on ϕ_c. To be precise, we assume the prior on ϕ_c to follow a Gaussian distribution with a zero mean and a variance of $1/\pi^2$.

nitudes and hence highly spinning systems would yield stronger constraints on these coefficients. The estimations of various α_k, parametrizing the conservative dynamics, also broadly follow these trends. However, there is an important exception. The bounds on α_3 is consistently worse than those of α_4. This may be attributed to the important difference between them. α_3 parametrizes the 1.5PN term in the conserved energy which has only spin-dependent terms whereas the 2PN term contains both non-spinning and spinning contributions. Hence though α_4 is sub-leading in the PN counting, the bounds on it are better.

We now discuss the quantitative results from these plots. One of the most interesting results is the projected constraints on coefficients that parametrize conservative dynamics. For third generation

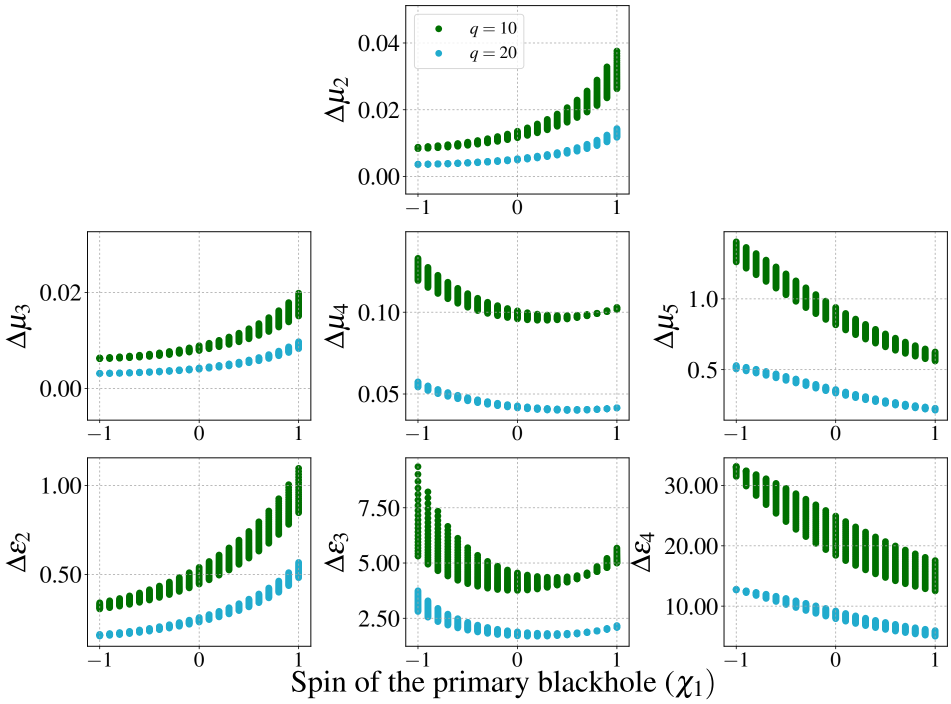

Figure 4.7. Projected 1σ errors on multipole coefficients as a function of the spin of the heavier black hole, χ_1, for LISA noise PSD. All the sources are considered to be at a fixed luminosity distance of 3 Gpc with a total mass of 2×10^5 $M_\odot$. The green dots are for mass ratio 10 and the cyan dots denotes mass ratio 20. The vertical spread in the bounds at each χ_1 value is due to different χ_2 in the range $[-1, 1]$.To obtain the numerical estimates showed in this plot, we also consider a prior distribution on ϕ_c. To be precise, we assume the prior on ϕ_c to follow a Gaussian distribution with a zero mean and a variance of $1/\pi^2$.

ground-based detectors and the prototypical source configurations, the bounds on 2PN conservative dynamics can be$\sim 10^{-2}$ which is comparable to or even better than the corresponding bounds expected from LISA. On the multipole coefficients side, the quadrupole coefficient μ_2 may be constrained to $\leq 10^{-1}(10^{-2})$ for second (third) generation detector network while the bounds from LISA are $\sim 10^{-2}$. The best bounds on μ_3 are $\sim 10^{-1}, 10^{-2}, 10^{-2}$ for second generation, third generation and LISA, respectively, corresponding to highly spinning binaries. The projected bounds on the higher multipole coefficients from third generation detector network and LISA are comparable in all these cases, though one should keep in mind the specifications of the sources we consider for

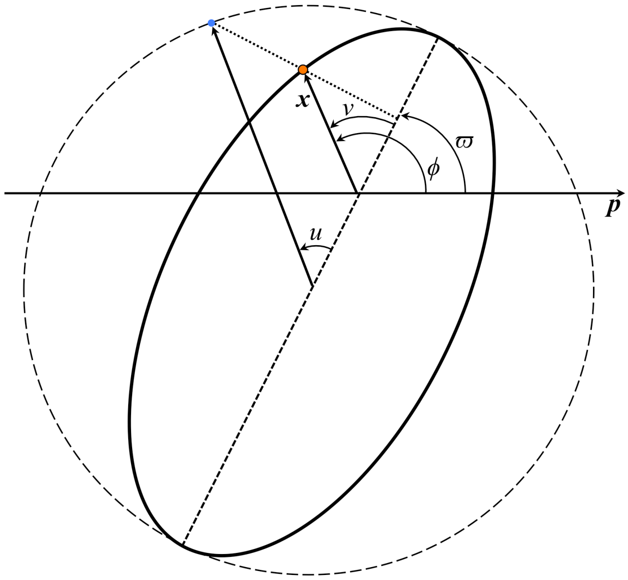

Figure 5.1. **p** is a unit vector along a reference axis. **x** is the relative separation vector joining the focus of the ellipse to the position of the reduced mass making an angle ϕ with **p** and an angle v with the semi-major axis of the ellipse. Eccentric anomaly u is the angle between the semi-major axis and the line drawn from the center to a point on the auxiliary circle, i.e. the point on the circle made by extended perpendicular line drawn from the semi-major axis to the reduced mass. Figure courtesy ref. [239]

The above expression for linear momentum flux is given in terms of generic dynamical variables $r, \dot{r}, \phi$ and $\dot{\phi}$. While specializing to the case of quasi-elliptical orbits, it is usually convenient to express these dynamical variables in terms of the parameters associated with quasi-elliptical orbits, namely the generalized quasi-Keplerian representation (QKR) of the orbital dynamics. One needs 2PN QKR to compute the 2PN LMF in terms of the orbital parameters. In the next section we briefly start with the description of the parametrization of Keplerian orbits followed by its PN generalization, the quasi-Keplerian (QK) representation.

5.5 Keplerian and Quasi-Keplerian parametrization

The Keplerian parametrization for the Newtonian motion of a compact binary system is widely used in describing celestial mechanics. In polar coordinates and in the center of mass frame, the

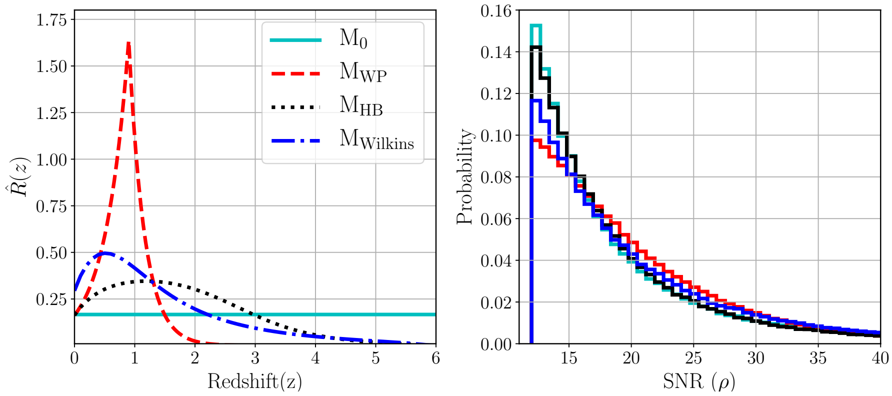

Figure 6.1. Figure on the left panel shows the evolution of co-moving merger rate density with redshift for four different models, M_0 stands for the constant comoving merger rate, $M_{\rm WP}$ represents the model for rate density evolution obtained by Wandermann & Piran [291], $M_{\rm HB}$ and $M_{\rm Wilkins}$ denote the merger rate models obtained in Ref. [259, 284] following the star formation rates given in ref. [195] and [295] respectively. The figure on the right most panel contains the corresponding normalized SNR distributions.

Given that z is a function of co-moving distance, D (Eq. 6.2.5), it is clear from Eq. 6.2.4 that the simple scaling relation for SNR ($\rho \propto 1/D$) would no longer hold. Hence it is obvious that the universal SNR distribution, given in Eq. 6.1.1, does not apply any more. In the next section we discuss the effect of redshift evolution of the DNS merger rate on the SNR distribution.

6.3 Imprints of co-moving merger rate density evolution of DNS systems on the SNR distribution

Usually it is assumed that the DNS formation rate follows the star formation rate, whereas their merger rate will depend also on the delay time distribution, i.e. the distribution of the time delay between the formation and the merger. Hence, following Ref. [259], the binary merger rate density can be written as

$$R(z) \propto \int_{t_d^{\rm min}}^{\infty} \frac{\dot{\rho}_*(z_f(z,t_d))}{1+z_f(z,t_d)} P(t_d)\, dt_d, \tag{6.3.1}$$

where $\dot{\rho}_*$ is the star formation rate, t_d is the delay time and $t_d^{\rm min}$ is the minimum delay time for a binary to merge since its formation. The redshift z describes the epoch at which the compact binary merges and z_f is

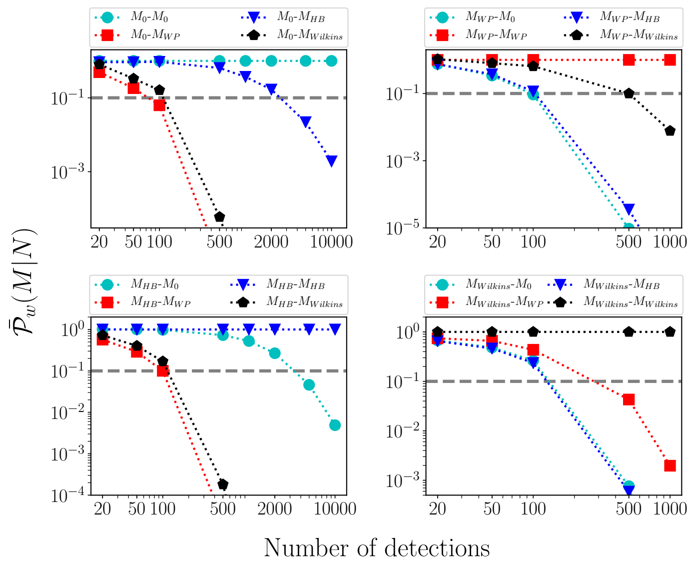

Figure 6.2. Weighted p-values ($\bar{\mathcal{P}}_w(M|N)$) from Anderson-Darling test performed on the data obtained from the four models as functions of the number of detections. The first argument in each legend represents the data generated by following a particular model M (denoted as data$_M$ in the main text), whereas the second argument is the theoretical model with which the data is compared to. We put a gray horizontal line in every panel corresponding to the threshold on $\bar{\mathcal{P}}_w(M|N)$ (see main text for details).

6.4.3 Weighted p-values

As mentioned earlier (in section 6.4.1), we have used Rice distribution to model the errors in SNR. The presence of these errors in the data will affect the p values which in turn can lead to false detection or false rejection. For example, the median of the p value distribution resulting from AD test of data$_M$ with the model M, in principle, should be 0.5. But due to the errors, the test may return a lower median which may even lead to the rejection of the null hypothesis when it is actually true. In our case, we have multiple models $\{N\}$ to be tested against the data$_M$ and p value for each model ($\bar{\mathcal{P}}(M|N)$) will decrease due to the errors thereby reducing the ability to distinguish between various models.

In order to quantify the distinguishability between the data and a model along the lines described earlier, we introduce the notion of *weighted* p values. For a given data$_M$, we define a weighting function $\mathcal{W}$ as

$$\mathcal{W} = \frac{1}{\bar{\mathcal{P}}(M|M)}. \tag{6.4.1}$$

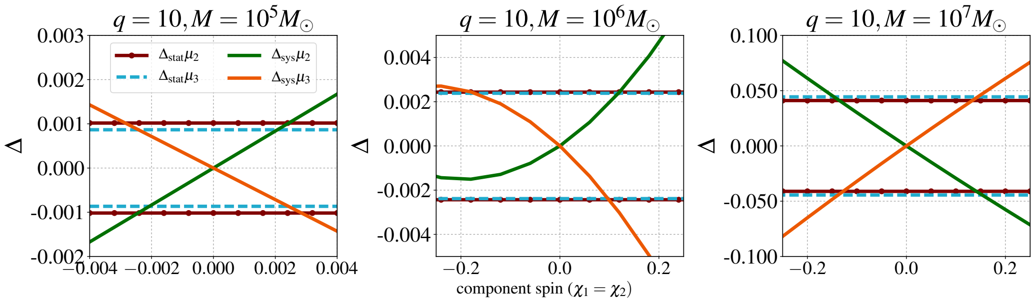

Figure A.1. Numerical estimates of systematic biases on the two leading multipole coefficients μ_2 and μ_3 as a function of $\chi_1 = \chi_2 = \chi$ for LISA noise PSD. We consider systems with three different total masses, $m = 10^5, 10^6, 10^7 M_\odot$ having mass ratio $q = 10$. All the sources are considered to be at a fixed luminosity distance of 3 Gpc.

$M_\odot$, 10^6 $M_\odot$, 10^7 $M_\odot$ and mass ratio $q = 10$ as a function of individual spin parameter $\chi_1 = \chi_2 = \chi$ for LISA. Due to a smaller total mass ($M = 10^5 M_\odot$) a large number of inspiral cycles reside in the LISA band. Hence even with very small spin values $\chi \sim O(10^{-3})$, the systematic errors become larger than the statistical errors, which demands a parametrized spinning waveform model. In contrast, for larger total masses of about 10^6 $M_\odot$ or 10^7 $M_\odot$, the systematics affect the parameter estimation when the spin magnitude is slightly larger $\sim O(10^{-1})$, as expected. Hence it is very crucial to incorporate the spin corrections in the waveform to reduce the effects of systematics when extracting the information about the multipole coefficients. We also find that as the total mass of binary increases the slope of the systematic bias curves changes from positive to negative for μ_2 and vice-versa for μ_3. This could be due to the nature of the correlation (positive or negative) between these multipole coefficients and the binary parameters (such as masses and spins) with increasing total mass. We quote the leading order estimates for the systematic biases in case of LISA only. Since the Fisher matrix-based leading order estimation of systematic biases for network configuration demands reformulation of the prescription, we postpone these for future study in a more rigorous and accurate Bayesian framework.

SUMMARY

The first two observation runs of advanced Laser Interferometer Gravitational-Wave Observatory (LIGO) and Virgo interferometers have led to the detections of gravitational waves (GWs) from ten binary black hole (BBH) mergers and a binary neutron star (BNS) merger. Among other things, GWs from these compact binary mergers can be used to probe the behavior of gravity in highly non-linear and dynamical regime and gain insights about the astrophysics associated with the formation of these binaries. In this thesis, we explore the dynamics of the compact binary system within the post-Newtonian (PN) framework in the context of GW astronomy and develop tests of general relativity (GR) in the strong field regime.

We propose a new model-independent test of GR by parametrizing the gravitational waveform in terms of the multipole moments of the compact binary using the PN framework. We derive the parametrized multipolar GW phase evolution for compact binaries (CBs) in quasi-circular orbit including spin effects in the inspiral dynamics at 3.5PN order and deviations to the PN coefficients in the 3.5PN conserved energy. We assume that the companion spins are either aligned or anti-aligned with respect to the orbital angular momentum and compute spin-orbit corrections that are accurate up to the next-to-next-to-leading order (3.5PN order) and the quadratic-in-spin effects up to 3PN order in the GW flux and the PN phase. We find that third generation detector such as Cosmic Explorer (CE) and space based Laser Interferometer Space Antenna (LISA) mission have the similar ability and can measure the first 4 leading order multipole coefficients with reasonable accuracies.

Asymmetric emission of GWs from a compact binary can lead to a flux of linear momentum from the system. As a result, depending on the system configuration, the center of mass (CM) of a binary system recoils. In this thesis we compute 2PN accurate LMF from various mass and current type multipole moments for an inspiralling, non-spinning compact binary system in quasi-elliptical orbit. 2PN Quasi-Keplarian representation (QKR) of the parametric solution to the PN equation of motion is employed to obtain the LMF at 2PN.

We also propose a new method to track the redshift evolution of the double neutron star mergers. Proposed third generation detectors such as CE will have the sensitivity to observe double neutron star (DNS) mergers up to a redshift of ~ 5 with good signal to noise ratios (SNRs). We argue that the co-moving spatial distribution of DNS mergers leaves a unique imprint on the statistical distribution of SNRs of the detected DNS mergers. Hence the SNR distribution of DNS mergers can be used as a novel probe of their redshift evolution. We consider detections of DNS mergers by CE and study the SNR distributions for different possible redshift evolution models of DNSs and employ Anderson Darling *p-value* statistic to demonstrate the distinguishability between these different models. We find that a few hundreds of DNS mergers in the CE era will allow us to distinguish between different models of redshift evolution.

SUMMARY

The first two observation runs of advanced Laser Interferometer Gravitational-Wave Observatory (LIGO) and Virgo interferometers have led to the detections of gravitational waves (GWs) from ten binary black hole (BBH) mergers and a binary neutron star (BNS) merger. Among other things, GWs from these compact binary mergers can be used to probe the behavior of gravity in highly non-linear and dynamical regime and gain insights about the astrophysics associated with the formation of these binaries. In this thesis, we explore the dynamics of the compact binary system within the post-Newtonian (PN) framework in the context of GW astronomy and develop tests of general relativity (GR) in the strong field regime.

We propose a new model-independent test of GR by parametrizing the gravitational waveform in terms of the multipole moments of the compact binary using the PN framework. We derive the parametrized multipolar GW phase evolution for compact binaries (CBs) in quasi-circular orbit including spin effects in the inspiral dynamics at 3.5PN order and deviations to the PN coefficients in the 3.5PN conserved energy. We assume that the companion spins are either aligned or anti-aligned with respect to the orbital angular momentum and compute spin-orbit corrections that are accurate up to the next-to-next-to-leading order (3.5PN order) and the quadratic-in-spin effects up to 3PN order in the GW flux and the PN phase. We find that third generation detector such as Cosmic Explorer (CE) and space based Laser Interferometer Space Antenna (LISA) mission have the similar ability and can measure the first 4 leading order multipole coefficients with reasonable accuracies.

Asymmetric emission of GWs from a compact binary can lead to a flux of linear momentum from the system. As a result, depending on the system configuration, the center of mass (CM) of a binary system recoils. In this thesis we compute 2PN accurate LMF from various mass and current type multipole moments for an inspiralling, non-spinning compact binary system in quasi-elliptical orbit. 2PN Quasi-Keplarian representation (QKR) of the parametric solution to the PN equation of motion is employed to obtain the LMF at 2PN.

We also propose a new method to track the redshift evolution of the double neutron star mergers. Proposed third generation detectors such as CE will have the sensitivity to observe double neutron star (DNS) mergers up to a redshift of ~ 5 with good signal to noise ratios (SNRs). We argue that the co-moving spatial distribution of DNS mergers leaves a unique imprint on the statistical distribution of SNRs of the detected DNS mergers. Hence the SNR distribution of DNS mergers can be used as a novel probe of their redshift evolution. We consider detections of DNS mergers by CE and study the SNR distributions for different possible redshift evolution models of DNSs and employ Anderson Darling *p-value* statistic to demonstrate the distinguishability between these different models. We find that a few hundreds of DNS mergers in the CE era will allow us to distinguish between different models of redshift evolution.

1 Introduction

Einstein's general relativity (GR) is a relativistic description of gravity based on fundamental principles such as the Equivalence principle, local Lorenz invariance, and minimal coupling [159]. GR has passed all the observational tests so far with flying colors [299]. One of the most important predictions of GR is the existence of gravitational waves (GWs). From a geometrical perspective, GWs may be thought of as ripples in the curvature of space time, that travel at the speed of light, produced due to accelerating objects.

According to GR, gravity is a property of space-time itself. The Einstein field equations, which relate the curvature of the space-time to the stress-energy tensor of the mass-energy that produces it, can be written as [161],

$$G_{\mu\nu} = \frac{8\pi G}{c^4} T_{\mu\nu}, \tag{1.0.1}$$

where on the left hand side $G_{\mu\nu}$ is the Einstein tensor, constructed out of the metric tensor $g_{\mu\nu}$ which carries all the properties of the space-time including its curvature. On the right hand side $T_{\mu\nu}$ is the total energy momentum tensor of all mass-energy field. The above equations are ten coupled partial differential equations for the metric tensor, $g_{\mu\nu}$. Due to diffeomorphism invariance, only six of them are independent.

1.1 Linearized gravity

In order to understand GWs, we first study the expansion of the Einstein's field equations, Eq. (1.0.1), around the flat space-time metric $\eta_{\mu\nu}$, where we write the space-time metric, $g_{\mu\nu} = \eta_{\mu\nu} + h_{\mu\nu}$ with $|h_{\mu\nu}| << 1$ and signature for $\eta_{\mu\nu}$ is $(-,+,+,+)$. Retaining terms only at linear order in $h_{\mu\nu}$, Einstein's equations can be re-cast as,

$$\Box\bar{h}_{\mu\nu} + \eta_{\mu\nu}\partial^{\rho}\partial^{\sigma}\bar{h}_{\rho\sigma} - \partial^{\rho}\partial_{\nu}\bar{h}_{\mu\rho} - \partial^{\rho}\partial_{\mu}\bar{h}_{\nu\rho} = -\frac{16\pi G}{c^4}T_{\mu\nu}, \tag{1.1.1}$$

with $\bar{h}_{\mu\nu} = h_{\mu\nu} - \frac{1}{2}\eta_{\mu\nu}h$ and the flat space-time d'Alembertian, $\Box = \eta_{\mu\nu}\partial^{\mu}\partial^{\nu}$. In the harmonic gauge (Lorenz gauge), $\partial^{\mu}\bar{h}_{\mu\nu} = 0$, we can write the linearized Einstein's equations (1.1.1) as,

$$\Box\bar{h}_{\mu\nu} = -\frac{16\pi G}{c^4}T_{\mu\nu}, \tag{1.1.2}$$

which precisely denotes the (GW) equation at the linearized order where the background metric is assumed to be the flat Minkowski metric, $\eta_{\mu\nu}$. Physically what it means is that the source of GWs is modeled within Newtonian gravity but the effect of GWs on the test masses is computed using the linear perturbation, $h_{\mu\nu}$, to $\eta_{\mu\nu}$. These equations can be solved by using the method of Green's function and the resulting solution may be written as,

$$\bar{h}_{\mu\nu} = \frac{4G}{c^4}\int d^3x' \frac{1}{|\mathbf{x}-\mathbf{x}'|}T_{\mu\nu}(t - \frac{|\mathbf{x}-\mathbf{x}'|}{c}, \mathbf{x}'). \tag{1.1.3}$$

In case of compact sources of size $\sim R$, moving with a speed $v \sim \omega R << c$, the solution given in Eq. (1.1.3) in the far zone (the distance from the source $|\mathbf{x}| = r >> c/\omega$) can be written in terms of the time varying quadrupole moment as,

$$\bar{h}_{ij} = \frac{2G}{c^4 r}\ddot{I}_{ij}(t - r/c), \tag{1.1.4}$$

where $I_{ij} = \int d^3x \frac{T_{00}}{c^2}(x^i x^j - \frac{1}{3}r^2\delta_{ij})$ is the quadrupole moment and $\ddot{I}_{ij}$ denotes the second time derivative of the quadrupole moment. One can conclude from the above equation that the GWs are generated from the sources having a time-varying quadrupole moment. We also quote the corresponding total radiated power or the flux of GWs at the quadrupolar order, which is,

$$\begin{aligned} \mathcal{F}_{\text{quad}} &= \frac{c^3 r^2}{32\pi G}\int d\Omega \langle \dot{h}_{ij}\dot{h}_{ij}\rangle \\ &= \frac{G}{5c^5}\langle \dddot{I}_{ij}\dddot{I}_{ij}\rangle, \end{aligned} \tag{1.1.5}$$

where $d\Omega = dA/r^2$ is the solid angle subtended by a surface element dA, $\dddot{I}_{ij}$ denotes the triple time derivative of the quadrupole moment and "$\langle \cdots \rangle$" denotes averaging over several gravitational wavelengths.

1.1.1 Propagation of gravitational waves

Having discussed the generation of GWs at the leading order, we now focus on the solution of the linearized field equations in the vacuum. In vacuum, $T_{\mu\nu} = 0$ which further reduces Eq. (1.1.2) to

$$\Box \bar{h}_{\mu\nu} = 0. \tag{1.1.6}$$

To understand the Lorenz gauge and to obtain the independent physical degrees of freedom of the GWs, we consider the infinitesimal coordinate transformation, $x^\mu \rightarrow x^{\mu\prime} = x^\mu + \xi^\mu$. Under this transformation the metric perturbation transforms as,

$$\bar{h}_{\mu\nu} \rightarrow h'_{\mu\nu} = \bar{h}_{\mu\nu} - (\partial_\mu \xi_\nu + \partial_\nu \xi_\mu - \eta_{\mu\nu}\partial_\rho \xi^\rho). \tag{1.1.7}$$

with $\partial^\nu h'_{\mu\nu} = \partial^\nu \bar{h}_{\mu\nu} - \Box \xi_\mu$. To preserve the Lorenz gauge, the coordinate transform has to be such that $\partial^\nu \bar{h}_{\mu\nu} = \Box \xi_\mu$. To be noted here, the harmonic gauge condition assumed earlier, can further be preserved by assuming $\Box \xi^\mu = 0$. Yet, it does not completely specify the gauge. Hence to reduce the residual degrees of freedom, we first choose ξ_0 so that $\bar{h}' = 0$. In this traceless gauge we have

$\bar{h}_{\mu\nu} = h_{\mu\nu}$. Secondly, we choose ξ_i such that $h_{0i} = 0$; Having fixed h_{0i}, using the Lorenz gauge condition, we choose $h_{00} = 0$. To summarize, in the *transverse traceless gauge* (TT) we set,

$$h^{0\mu} = 0, \quad h^i_i = 0, \quad \partial^j h_{ij} = 0. \tag{1.1.8}$$

In this gauge, the wavelike solution to Einstein's equation can be written as (we have chosen the propagation direction to be $+\hat{z}$ and the $\hat{x}, \hat{y}$ are the two transverse directions),

$$h^{TT}_{\mu\nu} = \begin{pmatrix} 0 & 0 & 0 & 0 \\ 0 & h_+ & h_\times & 0 \\ 0 & h_\times & -h_+ & 0 \\ 0 & 0 & 0 & 0 \end{pmatrix}_{\mu\nu} \sin[\omega(t - z/c)], \tag{1.1.9}$$

where h_+ and $h_\times$ are the amplitudes of the two independent polarizations of GWs. This means a general GW is any real combination of these two polarization states.

1.1.2 Properties of gravitational waves

GWs interact very weakly with intervening matter. In order to understand the effects of these on the matter, we use the geodesic equation governing the trajectory of a test mass, m, in the curved background described by the metric $g_{\mu\nu}$, which is,

$$\frac{d^2 x^\mu}{d\tau^2} + \Gamma^\mu_{\nu\rho} \frac{dx^\nu}{d\tau} \frac{dx^\rho}{d\tau} = 0, \tag{1.1.10}$$

where τ denotes the particle's proper time. In order to obtain the equation of geodesic deviation, we consider two trajectories $x^\mu(\tau)$ and $x^\mu(\tau) + \xi^\mu(\tau)$, which satisfy the geodesic equation (1.1.10). Re-writing the geodesic equation in terms of their relative separation, $\xi^\mu(\tau)$, we find the equation

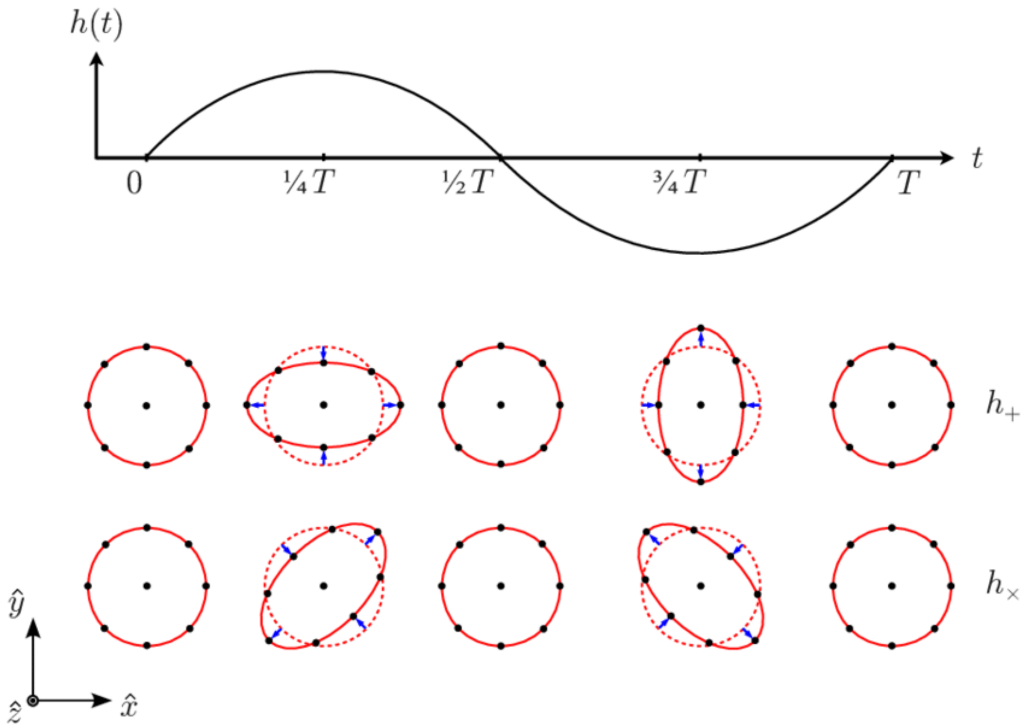

Figure 1.1. Upper panel shows a monochromatic GW, $h(t)$, propagating along the $\hat{z}$ direction. Lower panel shows the effect of the plus and the cross polarization on ring of test particles [218].

for geodesic deviation, which is given by,

$$\frac{D^2\xi^\mu}{D\tau^2} = -R^\mu_{\nu\rho\sigma}\xi^\rho \frac{dx^\nu}{d\tau}\frac{dx^\sigma}{d\tau}, \tag{1.1.11}$$

where D denotes the directional derivative and $R^\mu_{\nu\rho\sigma}$ is the Riemann tensor. After a few algebraic manipulations (see [226] for details), the equation of geodesic deviation, Eq. (1.1.11), at the linearized order, can be written as a function of GW amplitude, which is,

$$\ddot{\xi}^i = \frac{1}{2}\ddot{h}^{TT}_{ij}\xi^j, \tag{1.1.12}$$

where $\ddot{h}^{TT}_{ij}$ denotes the second time derivative of h_{ij}. Using Eq. (1.1.12), one can easily conclude that when a GW passes through a set of test particles, the relative distance between the test masses stretches and squeezes.

Now we use the geodesic deviation equation (1.1.12), to obtain the observational effects of a passing GWs on a ring of test particles in the (x, y)-plane. We treat the plus and cross polarizations of GWs separately. We also assume that the GW is moving in $+\hat{z}$ direction. Hence at t=0, z=0, the two polarizations in Eq. (1.1.9) reduce to,

$$h_{ij}^{TT} = \begin{pmatrix} 1 & 0 \\ 0 & -1 \end{pmatrix} h_+ \sin \omega t, \qquad h_{ij}^{TT} = \begin{pmatrix} 0 & 1 \\ 1 & 0 \end{pmatrix} h_\times \sin \omega t \tag{1.1.13}$$

We consider the center of the ring (see fig. 1.1) to be the origin of our coordinate system with (x_0, y_0) being the unperturbed position of a single particle in the ring. If the displacement of each particle from its unperturbed position is $(\delta x, \delta y)$, using the geodesic equations (1.1.12), we obtain,

$$\delta x(t) = \frac{h_+}{2} x_0 \sin \omega t, \tag{1.1.14}$$

$$\delta y(t) = -\frac{h_+}{2} y_0 \sin \omega t, \tag{1.1.15}$$

and similarly for the cross polarization,

$$\delta x(t) = \frac{h_\times}{2} y_0 \sin \omega t, \tag{1.1.16}$$

$$\delta y(t) = \frac{h_\times}{2} x_0 \sin \omega t. \tag{1.1.17}$$

As evident from the above equations, the distance of each particle from the center changes over time depending on the GW strain giving rise to the deformation of the whole ring. The pictorial description of the displacements given in the above equations as the GW passes by are also sketched in fig. 1.1 at different phases of the wave, where $T = 2\pi/\omega$. As is evident from the above equation, the relative changes in the position of the particles are proportional to the GW amplitude.

1.2 Sources of gravitational waves

From the quadrupole formula, quoted in Eq. (1.1.4), it is clear that any object with time varying quadrupole moment is a source of GWs. Suppose a mass M moves in a circular trajectory of radius R with an angular speed of ω. Its quadrupole moment can be written as $\sim MR^2$. Since the GW energy flux is proportional to the square of the triple time derivative of quadrupole moment, that brings in a factor of ω^6. Furthermore, using Kepler's law we replace ω with $\sqrt{M/R^3}$. Finally one can approximately write the GW luminosity as,

$$\mathcal{F} \sim \frac{L_0}{r}\left(\frac{M}{R}\right)^5, \tag{1.2.1}$$

where $L_0 = \frac{c^5}{G} \sim 3.6 \times 10^{52}$ W and r is distance to the source. Though L_0 is a huge number and the factor M/R is extremely small for any terrestrial object. Hence, in order to generate detectable GWs, we need compact objects like black holes (BHs) or neutron stars (NS) etc., for which $M/R \sim O(1)$.

From the viewpoint of observation, based on the duration of the signals, GW sources can broadly be classified into four categories.

Gravitational Wave Burst: Signals of short duration in the detector band are characterized as GW bursts. Searches for these signals rely on identifying the excess power in the detector data. The typical sources for this type of GWs can be core-collapse supernovae [243], the late stages of merging compact binaries [9], cosmic strings [225] etc. In a typical supernova, simulations suggest that the gravitational wave frequency might lie in the range of ~200 -1000 Hz. Since very little is known about the sources of this type of GWs, search algorithms are built with little assumptions on the source models. One of the widely used search methods is the coincident methods, which first identify events in individual detectors by using an excess power statistic [52, 170] and then require coincidence between detectors. Other than coincident method there are coherent search algorithms [208] that search for these types of GWs in the detector data stream.

Continuous GWs: Continuous gravitational waves (CWs) are the nearly monochromatic signals whose frequencies can be assumed to be constant for a long period of time. Hence the signal builds up in a narrow frequency bin. CWs may be produced by various non-axisymmetric processes, such as single spinning of neutron stars [196, 210] and are expected to be comparatively weak. There are various methods to search for this type of GWs. For example, the targeted searches, where the various source parameters like sky location, frequency and frequency derivatives are assumed to be known as with known sources like the Crab pulsar [10]. There are also all sky searches [158, 163] for unknown sources.

Stochastic Gravitational Waves: A stochastic Gravitational Wave background (SGWB) is produced by the superimposition of GWs from various astrophysical phenomena. The sources for this type of GW signals could be primordial cosmological processes or the incoherent addition of individually unresolvable astrophysical sources, such as compact binary coalescences or exotic topological defects. These types of GW signals are parametrized in terms of their effective energy-density spectrum (Ω_{GW}). The latest constraint on this parameter is $\Omega_{GW} < 1.7 \times 10^{-7}$ [33].

Compact binary mergers: These types of GWs are produced by two orbiting compact objects such as BHs or NSs. These systems have time varying quadrupole moments, leading to emission of GWs. As the system loses energy through GWs, their orbit shrinks. The frequency of the emitted GWs changes over time and can be modeled in GR, either analytically in the initial times or numerically in the later stages of its evolution. The waveform from these objects can be obtained in terms of the various source parameters such as masses, spins, etc. When the two inspiralling objects in the binary are far apart, GWs from these systems can accurately be modeled by the perturbative solution of Einstein's equation within the post-Newtonian (PN) formalism. But close to the merger, the waveform is modeled by numerical relativity simulations where Einstein's equations are "exactly" solved in a computer. Finally in the ring down, the merger remnant settles into a Kerr BH by radiating a spectrum of quasi-normal modes. These three stages are stitched together to construct the complete hybrid phenomenological gravitational waveforms. A typical gravitational waveform in the various stages of the system's evolution is shown in fig. 1.2. Com-

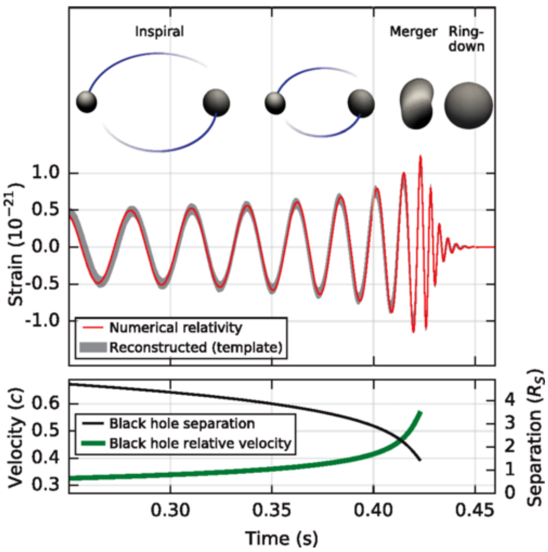

Figure 1.2. The upper panel shows a typical gravitational waveform during the various phases of a binary evolution whereas the lower panel shows the change in the BH velocity and their separation as a function of time (Image credit [18]).

pact binary systems can be produced by a pair of BHs, or a BH and NS, or a pair of NSs. In the case of BH-NS or NS-NS systems, the NS might get tidally disrupted and might produce new features in the waveform, carrying information about the NS's internal structure [12].

In the remainder of this thesis, we focus on GWs from compact binary inspirals to study GWs in the MPM-PN formalism and study the implications of observing these systems for fundamental physics and astrophysics.

1.3 Gravitational waves detectors

Efforts to detect GWs from celestial bodies started in 1960, pioneered by J. Weber. The idea for detection of GWs in this method is to use giant metal cylinders (bar detectors) to measure the vibrations excited in the material due to the passage of gravitational waves. But the bar-detectors did not reach the sensitivity required to detect GWs from astrophysical sources, and a detection claimed by Weber [292] could not be established by other detectors.

In parallel, attempts to construct the interferometric detectors were pursued. Here one uses the

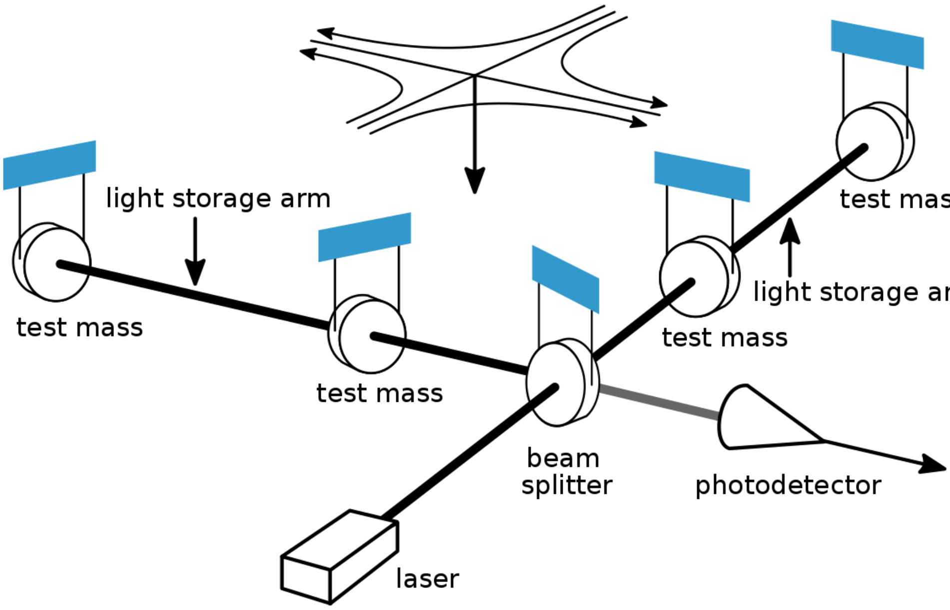

Figure 1.3. Simplified schematic diagram of a LIGO detector (Credit: Caltech/MIT/LIGO Lab).

principle of interferometry to detect GWs where a beam of monochromatic light (laser beam) is first split into two and travels through two different optical cavities at an angle with each other. These two beams get reflected by the freely suspended mirrors at the ends of the cavities and recombine to produce an interference pattern (see fig. 1.3 for a schematic diagram). Due to the passage of GWs, the arm length of the cavities changes, which corresponds to the dimensionless strain with an amplitude of about $h = \frac{\Delta L}{L} \sim 10^{-20}$. This relative change varies over time depending on the intensity of the passing GWs and causes changes in the interference pattern which are monitored through the photo detector and extracts information about the GWs. Unlike the narrow-band bar detectors, interferometric detectors have broad-band responses, which facilitates searches for different types of GW sources.

1.3.1 Currently operational gravitational wave detectors

The two LIGO (Laser Interferometer Gravitational-Wave Observatory) detectors are located in Livingston, Louisiana and Hanford, Washington, two largely separated locations in the USA. These are L-shaped detectors with each arm of length 4 km. Along with these two, Advanced VIRGO is

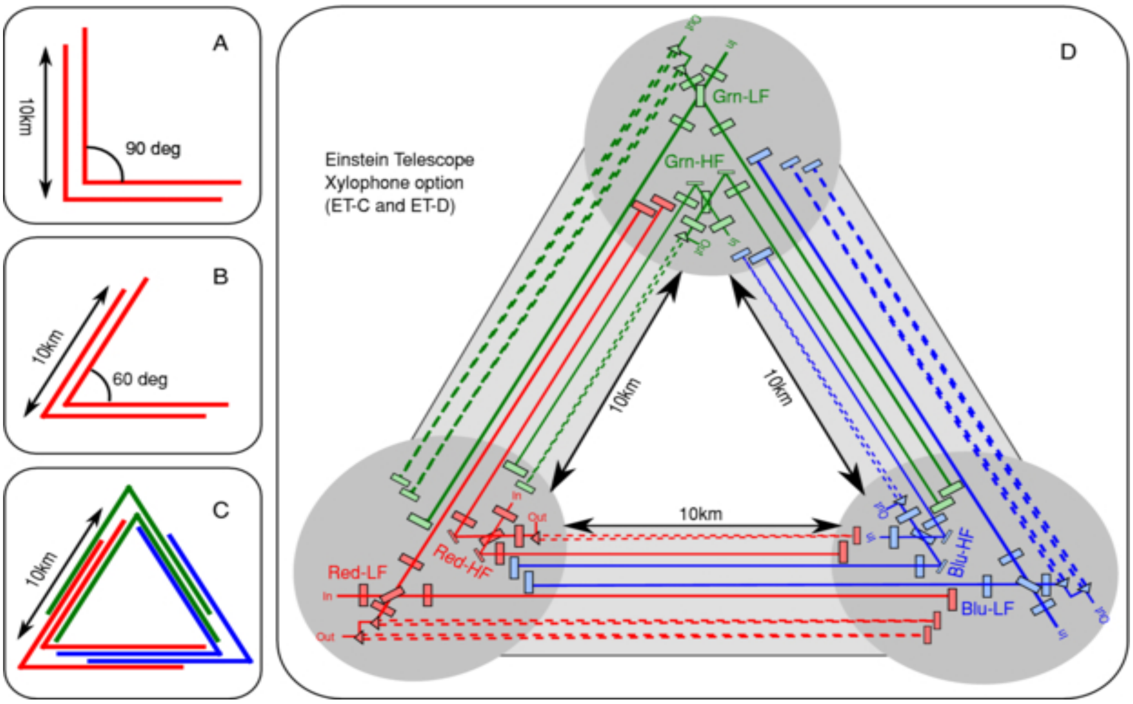

Figure 1.4. simplified schematic diagram of triangular ET [189] .

another detector, located near Pisa in Europe. This is also an L-shaped interferometric detector but with a 3 km arm length, has comparable sensitivity to that of the two LIGO detectors.

1.3.2 Future gravitational wave detectors

1.3.2.1 Future second generation detectors

With improved sensitivities of Advanced LIGO and Virgo in the upcoming observing runs, there are a few more upcoming second generation GW detectors. The Japanese cryogenic detector KAGRA [69] is likely to be operational soon. LIGO-India [201] is also expected to join the world-wide network of GW detectors by mid-2020s. A worldwide network of five GW detectors will increase the expected event rates as well as boost the detection confidence. The source localizations of the GW sources will also improve tremendously [164, 209].

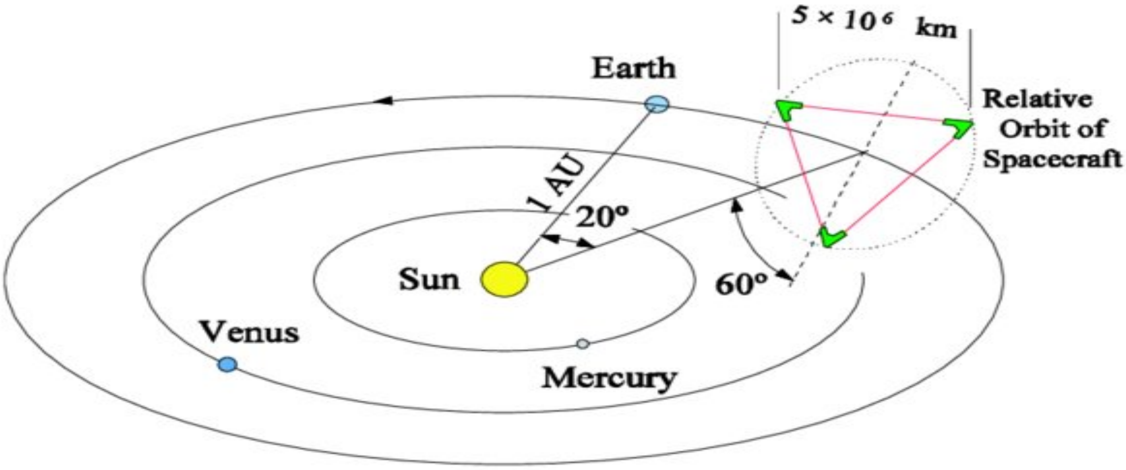

Figure 1.5. The orbital configuration of the LISA mission concept [198]

1.3.2.2 Future third generation detectors

There are ongoing research and developments, including science case studies for third-generation detectors such as the Einstein Telescope (ET) [11] and Cosmic Explorer (CE) [24]. Among the third generation detectors, CE is an L-shaped interferometric detector but with much larger arm length($\sim$40 km) compared to the second generations ones, whereas ET is a triangular shaped detector with each arm of length 10 km (a simplified diagram of ET is given in fig. 1.4). Due to their improved sensitivity in the low frequency regime (till $\sim$1Hz) and the leap in the sensitivity compared to the second generation detectors, they are unique probes of the high redshift universe. Roughly around 10^6 of BNS mergers [39] are expected to be detected by the 3G detector network, which will help to test astrophysical models of the formation and evolution of double neutron stars. In addition to stellar-mass compact binaries, ET and CE can detect intermediate-mass BHs with a total mass of several hundreds of solar masses, which will last longer (compared to the equal-mass binaries) in the detector sensitivity band and hence are accurate probes of the compact binary dynamics and the BH nature of the compact objects [118, 265].

1.3.2.3 Space-based Laser Interferometer Space Antenna mission

The space-based Laser Interferometer Space Antenna (LISA) mission consists of three spacecraft that are separated by 2.5 million miles. These three satellites comprising the interferometer are in a heliocentric orbit which trails the Earth by 22°. The schematic structure of the orbital motion of LISA is shown in fig. 1.5. The funding for the space-based mission LISA [2] has already been approved. LISA will be sensitive to millihertz GWs produced by the inspirals and merger of supermassive BH binaries in the mass range $\sim 10^4 - 10^7 M_\odot$. These sources may also have a large diversity in their mass ratios, ranging from comparable mass (mass ratio $\leq$10) and intermediate mass ratios (mass ratio $\geq$100), to extreme mass ratios (mass ratio $\geq 10^6$) where a stellar mass BH spirals into the central supermassive BH. This diversity, together with the sensitivity in the low-frequency window, makes LISA a very efficient probe of possible deviations from general relativity (GR) in different regimes of dynamics [68, 82, 173, 268].

1.3.2.4 Pulsar timing array

Millisecond pulsars are expected to send pulses in equal time intervals. But the gravitational waves cause the time of arrival of the pulses to vary slightly. By measuring the time-of-arrival of the electromagnetic pulses from an array of pulsars one can model the GWs affecting the arrival time of those pulses. Nearly 100 millisecond pulsars can be monitored for the timing calculations. The distances to these pulsars are thousands of light years from the Earth, which can be thought off as the effective "arm length" of this type of detector. Since the GW frequency is proportional to the arm length of the detector, the accurate measurement of the arrival time of the pulses from these are sensitive to the GWs in the frequency band of $10^{-9} - 10^{-8}$ Hertz [192]. Pulsar Timing Array (PTA) can probe a completely different spectrum of GWs and are hence sensitive to a different category of GW sources such as supermassive BH binaries or stochastic backgrounds.

1.4 Gravitational waves data analysis for compact binary coalescence

Since various implications of GWs from compact binary coalescence (CBC) are the theme of this thesis, we now focus on GWs emitted by CBCs only and discuss the techniques employed in the data analysis of CBCs. The data analysis of a CBC addresses two basic aspects, the detection problem and the parameter estimation (PE) problem.

1.4.1 Detection problem

The GW data or the detector output is a time series describing the phase shift of the light due to the total travel inside the detector arms, which consists of the detector noise, $n(t)$ and a GW signal, $h(t)$,

$$s(t) = n(t) + h(t). \tag{1.4.1}$$

The first challenge one faces is to identify the weak signal buried in the detector noise. This problem requires accurate noise characterizations and a prior knowledge of the expected gravitational waveform. In case of stationary noise, the different Fourier components are uncorrelated, hence,

$$\langle \tilde{n}^*(f)\tilde{n}(f')\rangle = \delta(f - f')\frac{1}{2}S_n(f), \tag{1.4.2}$$

where $\tilde{n}(f)$ is the Fourier transform of $n(t)$ and $S_n(f)$ is the detector's power spectral density (PSD) (see fig. 1.6 for the various noise PSDs used in this thesis) and $\langle \cdots \rangle$ denotes the ensemble average over noise realizations. The detection and the subsequent parameter estimation process in case of GWs from compact binaries, rely on the data analysis technique of matched filtering [186, 290]. For detecting a GW signal, the precomputed theoretical waveforms (also known as templates) are cross correlated with the data and the signal to noise ratio (S/N) (SNR) is maximized over the set of templates. SNR for a true signal $h(t)$ with a filter function $K(t)$ is denoted as the matched filtered

SNR and is given by

$$\frac{S}{N} = \frac{\int_{-\infty}^{\infty} df \tilde{h}(f) \tilde{K}^*(f)}{\left[\int_{-\infty}^{\infty} df (1/2) S_n(f) |\tilde{K}(f)|^2\right]^{1/2}}, \tag{1.4.3}$$

where $\tilde{h}(f)$ and $\tilde{K}(f)$ are the Fourier components of $h(t)$ and $K(t)$ respectively. When this SNR is maximized over all the templates, and if the resulting SNR crosses a certain pre-determined threshold, it is called a detection. This particular template is referred to as the optimal template and the corresponding signal to noise ratio is called the optimal SNR (See, for instance, Sec. (5.1) of [268] for details), which is defined as

$$\rho = \sqrt{4 \int_0^{\infty} \frac{|\tilde{h}(f)|^2}{S_n(f)} df}, \tag{1.4.4}$$

where we have replaced the limits $[-\infty, \infty]$, as used in Eq. (1.4.3), by $[0, \infty]$ and $S_n(f)$ is the one sided noise PSD. In practice, we replace the lower and the upper limits of the integration by the lower cut off frequency $f_{\rm low}$ imposed by the seismic cut off of the detector and an upper cutoff $f_{\rm high}$.

The matched filtered SNR for various templates follow the Rice distribution of the following form:

$$f(x, \rho) = x \exp\left(-\frac{x^2 + \rho^2}{2}\right) I_0(\rho x), \tag{1.4.5}$$

where x is the matched filtered SNR and I_0 is the zeroth-order modified Bessel function of the first kind (see [240] for a discussion about the Rice distribution in the context of GW data analysis).

In this thesis we use various noise PSDs to asses the PE problem in various contexts. They are given below.

Second generation ground based detectors: As representatives of second generation ground based detectors, we use three different noise PSDs for advanced LIGO, advanced VIRGO and the Japanese detector KAGRA. For advanced LIGO we use the analytical fits to the PSD given in Refs. [46] where as the following fit is used for VIRGO PSD,

$$S_h^{\rm virgo}(f) = 1.5344 \times 10^{-47} \left[1 + 1871 \times \left(\frac{16}{f}\right)^{10} + 11.72 \times \left(\frac{30}{f}\right)^{6}\right.$$

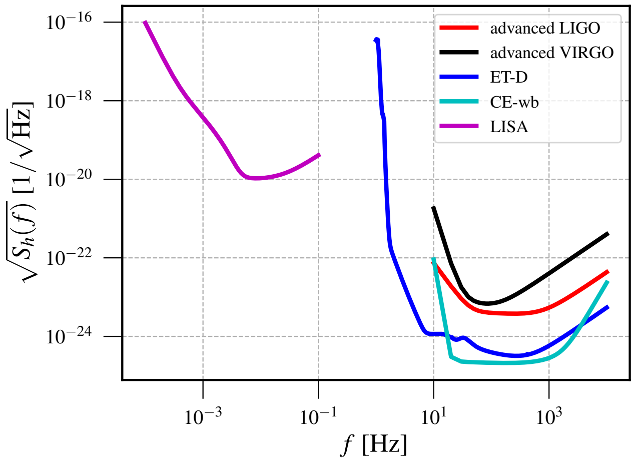

Figure 1.6. Various noise PSDs of the ground based and space-based GW detectors used in this thesis for various studies.

$$+ 0.7431 \times \left(\frac{50}{f}\right)^2 + 0.9404 \times \left(\frac{70}{f}\right) + 0.2107 \times \left(\frac{100}{f}\right)^{0.5} + 26.02\left(\frac{f}{500}\right)^2\Bigg]\,\mathrm{Hz}^{-1}\,, \quad (1.4.6)$$

where f is in units of Hz. For the Japanese detector KAGRA we use the noise PSD given in Ref. [3].

Third generation ground based detectors : In case of third generation ground based detectors, we use the noise PSD given in Ref. [11] for ET-D. For CE we use the following fit,

$$\begin{aligned} S_h(f) &= 5.62 \times 10^{-51} + 6.69 \times 10^{-50} f^{-0.125} + \frac{7.80 \times 10^{-31}}{f^{20}} \\ &+ \frac{4.35 \times 10^{-43}}{f^6} + 1.63 \times 10^{-53} f + 2.44 \times 10^{-56} f^2 \\ &+ 5.45 \times 10^{-66} f^5\ \mathrm{Hz}^{-1}\,, \end{aligned} \quad (1.4.7)$$

where f is in units of Hz .

Space based detector LISA : We quote the noise PSD for LISA here which we have used in further computations following Ref. [70]. The analytical form of the sky-averaged detector sensitivity can be written as

$$S_n(f) = \frac{20}{3}\frac{4S_n^{\rm acc}(f) + 2S_n^{\rm loc} + S_n^{\rm sn} + S_n^{\rm omn}}{L^2} \times\left[1+\left(\frac{2Lf}{0.41c}\right)^2\right], \tag{1.4.8}$$

where L is the arm length and the noise contributions $S_n^{\rm acc}(f)$, $S_n^{\rm loc}$, $S_n^{\rm sn}$ and $S_n^{\rm omn}$ are due to low-frequency acceleration, local interferometer noise, shot noise and other measurement noise respectively. The acceleration noise, $S_n^{\rm acc}(f)$, has been fitted to the level successfully demonstrated by the LISA Pathfinder [57], which is given as,

$$S_n^{\rm acc}(f) = \left\{9\times10^{-30} + 3.24\times10^{-28}\left[\left(\frac{3\times10^{-5}\ {\rm Hz}}{f}\right)^{10} + \left(\frac{10^{-4}\ {\rm Hz}}{f}\right)^2\right]\right\}\frac{1}{(2\pi f)^4}\ {\rm m^2\,Hz^{-1}}, \tag{1.4.9}$$

whereas, the other contributions are the following,

$$\begin{aligned} S_n^{\rm loc} &= 2.89\times10^{-24}\ {\rm m^2\,Hz^{-1}}, \\ S_n^{\rm sn} &= 7.92\times10^{-23}\ {\rm m^2\,Hz^{-1}}, \\ S_n^{\rm omn} &= 4.00\times10^{-24}\ {\rm m^2\,Hz^{-1}}. \end{aligned} \tag{1.4.10}$$

Besides the above described instrumental noise in Eq. (1.4.8), a galactic confusion noise component is also added, which is modeled by the fit given below,

$$S_{\rm gal} = A_{\rm gal}\left(\frac{f}{1\ {\rm Hz}}\right)^{-7/3}\exp\left[-\left(\frac{f}{s_1}\right)^{\alpha}\right] \times\frac{1}{2}\left[1+\tanh\left(-\frac{f-f_0}{s_2}\right)\right]. \tag{1.4.11}$$

The overall amplitude of the background $A_{\rm gal} = 3.266\times10^{-44}\ {\rm Hz^{-1}}$ depends on the astrophysical model for the population of white dwarf binaries in the Galaxy, which is modeled following ref. [50]. The power law $f^{-7/3}$ is what is expected from a population of almost monochromatic binaries. Assuming two-year observation period, the fitting parameters appearing in the above expression for $S_{\rm gal}$ have the values: $\alpha = 1.183$, $s_1 = 1.426$ mHz, $f_0 = 2.412$ mHz, $s_2 = 4.835$ mHz. The various noise PSDs, discussed above, are shown as a function of the frequency in fig. 1.6.

1.4.2 Parameter estimation

Parameter estimation (PE) is the process of extracting the source parameters of the compact binary that is detected. Recovering of the most probable values for the source parameters also requires the prior knowledge of the accurate functional dependence of $h(t)$ on these parameters $(\theta_1, \theta_2 ... \theta_n)$ such as masses, spins etc., for CBC. This question is addressed by constructing the likelihood function followed by posterior probability. For simplicity the detector noise is assumed to be stationary and Gaussian. Hence the probability distribution for noise can be written as,

$$\begin{aligned} p(n) &\propto \exp\left[-\langle n, n\rangle/2\right] \qquad (1.4.12) \\ &\propto \exp\Big[-\frac{1}{2}\Big\langle s - h(\theta_i), s - h(\theta_i)\Big\rangle\Big], \qquad (1.4.13) \end{aligned}$$

where the angular bracket, $\langle ..., ...\rangle$, denotes the noise-weighted inner product given by,

$$\langle a, b\rangle = 2\int_{f_{\rm low}}^{f_{\rm high}} \frac{a(f)\, b^*(f) + a^*(f)\, b(f)}{S_h(f)}\, df\,, \qquad (1.4.14)$$

where $S_h(f)$ is the one sided noise PSD discussed in the previous section. The posterior probability of the parameters can be obtained using Bayes' theorem. Bayes' rule states that the probability distribution for a set of parameters $\vec{\theta}$ given data s is,

$$p(\vec{\theta}|s) = \frac{p(s|\vec{\theta})\, p(\vec{\theta})}{p(s)}\,, \qquad (1.4.15)$$

where $p(s|\vec{\theta})$ is called the *likelihood* function, which gives the probability of observing data s given the model parameter $\vec{\theta}$ and is defined as

$$p(s|\vec{\theta}) = \exp\left[-\frac{1}{2} \int_{f_{\rm low}}^{f_{\rm high}} \frac{|\tilde{s}(f) - \tilde{h}(f;\vec{\theta})|^2}{S_n(f)} \, df \right], \tag{1.4.16}$$

where $\tilde{s}(f)$ and $\tilde{h}(f;\vec{\theta})$ are the Fourier transforms of $s(t)$ and $h(t)$, respectively. In Eq. (1.4.15), $p(\vec{\theta})$ is the *prior probability distribution* of parameters $\vec{\theta}$ and $p(s)$ is known as the *evidence* and defined as,

$$p(s) = \int p(s|\vec{\theta})\, p(\vec{\theta})\, d\vec{\theta}\,. \tag{1.4.17}$$

Hence by estimating the likelihood as stated in Eq. (1.4.16), the posterior probability is obtained using Eq. (1.4.15) assuming a prior distribution if available or one may use a flat distribution on the parameters as the prior.

Fisher information matrix technique: The Fisher matrix is a useful semi-analytic method which uses a quadratic fit to the log-likelihood (logarithm of Eq. (1.4.16)) function to derive the 1σ error bars on the parameters of the signal [67, 133, 136, 258]. To be precise, the inverse of the Fisher matrix provides the lower bound for the error covariance of the true source parameters, which is known as Cramér-Rao bound [258]. This method provides a reasonably good bounds on the source parameters ($\vec{\theta}$) in a high SNR limit where the quadratic approximation to the log-likelihood holds [136, 253, 283]. Given a GW signal $\tilde{h}(f;\vec{\theta})$ the Fisher information matrix is defined as

$$\Gamma_{mn} = \langle \tilde{h}_m, \tilde{h}_n \rangle, \tag{1.4.18}$$

where $\tilde{h}_m = \partial \tilde{h}(f;\vec{\theta})/\partial\theta_m$ evaluated at the true value of the parameters, $\vec{\theta}_0$. The variance-covariance matrix is defined by the inverse of the Fisher matrix,

$$C^{mn} = (\Gamma^{-1})^{mn} \tag{1.4.19}$$

where the diagonal components, C^{mm}, are the variances of θ^m. The 1σ errors on θ^m are, therefore, given by,

$$\sigma^m = \sqrt{C^{mm}}\,. \tag{1.4.20}$$

Markov chain Monte Carlo (MCMC): As discussed in ref. [283], the above discussed Fisher information matrix (FIM) technique is valid in the large SNR limit. Also FIM assumes that the likelihood is peaked at the true values of the parameters, which might not happen due to the presence of noise except in the large SNR limit. Since in practice, the realistic waveform templates are generated from a high dimensional parameter space, FIM becomes ill-conditioned in those cases. The solution to address this problem is to sample the likelihood surface numerically using algorithms such as Markov-Chain Monte Carlo (MCMC) [285, 286] or Nested sampling [273, 287]. When the parameter space is of higher dimensions, these are computationally challenging. However, MCMC allows for multimodal, non-Gaussian posterior probability distributions of the estimated parameters. This method also allows inclusion of non-Gaussian prior probability on the parameters. In this thesis, apart from using FIM techniques, we also did some spot checks by MCMC sampling of the likelihood function using the `emcee` [171] algorithm.

1.5 Towards the direct detections of gravitational waves

As discussed in section 1.3, in the mid-seventies several attempts by Weber, as well as by some improved versions of Weber's original designs, were unable to claim a firm detection of gravitational waves. However, in 1974, Hulse and Taylor detected pulsed radio emissions from a pulsar. By measuring the variation in the arrival time of the pulses they concluded the source to be a binary pulsar [199]. After the detection, continuous monitoring of the system was used to model the orbital decay over time, accurately fitting the GR predictions if the orbital decay was due to gravitational radiation [276]. Though not a direct detection of GWs, this provides a solid proof for the existence of GWs. This sped up further development of interferometric detection techniques. The discussion about the interferometric detectors for GW got the much needed atten-

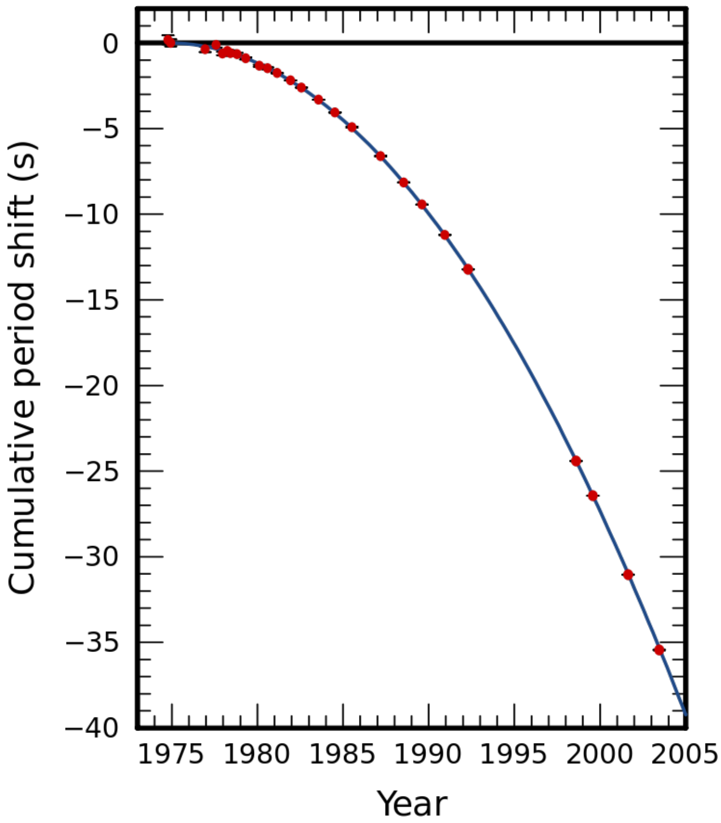

Figure 1.7. Orbital decay caused by the loss of energy by gravitational radiation [293].

tion [40, 174, 197, 241].

After two decades of development, a combination of the initial interferometric detectors including TAMA 300 in Japan, GEO 600 in Germany, LIGO in the United States, and Virgo in Italy operated between 2002 and 2010. These observations did not lead to the detection of GWs, which was consistent with the expected event rates of the GW sources. However, these observations put the first observational upper limits on the rate of mergers of BBH, BNS and NS-BH systems [5,6,8,38].

Between 2010-2015 initial LIGO was upgraded, and in 2015 it started the first observation run with a sensitivity much better than the initial LIGO. With this sensitivity, on 14 September 2015, the two LIGO detectors, Livingstone and Hanford, jointly detected the GWs from a BBH merger with a statistical confidence $> 5\sigma$ [13, 18] . The duration of the signal detected was ~ 0.2 sec. The individual BHs of masses $36^{+5}_{-4}\mathrm{M}_{\odot}$and $29^{+4}_{-4}\mathrm{M}_{\odot}$ at a distance of 410^{+160}_{-180} Mpc, merged to form a final

BH of mass $62^{+4}_{-4}\mathrm{M}_{\odot}$. The second detection, GW151226 ($14.2^{+8.3}_{-3.7}$+$7.5^{+2.3}_{-2.3}\mathrm{M}_{\odot}$) [17] also happened in the same year. Apart from these two, the first two observation runs of advanced LIGO and Virgo interferometers have led to the detections of eight more binary black hole mergers [15, 26–28, 34, 36].

Another breakthrough in the context of GW detections, happened in 2017. During the second observation run a binary neutron star merger [12] was detected. The short Gamma ray bursts followed by the binary neutron star merger was also observed in various bands of the electromagnetic spectrum from gamma rays to the radio [29, 148, 177, 217, 224, 227, 260, 264, 280, 282]. The joint detection of GWs as well as the EM counter part opens the new era of multi-messenger astronomy.

1.6 Topics addressed in this thesis

The detections of the compact binaries by advanced LIGO and Virgo have given us unique insights about fundamental physics [17, 20, 23, 25, 26, 30–32, 35, 37, 49], astrophysics [14, 19, 21, 23, 25, 30, 31, 37, 49], and cosmology [22]. Among the most important aspects of these discoveries, is the unprecedented opportunity they have provided to study the behavior of gravity in the highly nonlinear and dynamical regime associated with the merger of two BHs or two NSs (see Refs. [268, 303] for reviews). GW observations have put stringent constraints on the allowed parameter space of alternative theories of gravity by different methods [16, 20, 26]. At present, there are no theories of gravity other than GR which can predict a complete waveform model which can be used as an alternative to the GR templates. Hence we proceed with the various *null tests* of GR. This is achieved by parametrizing the gravitational waveforms about GR and introduce deformation parameters in the waveform. These deformation parameters are 0 in GR. Given the gravitational detections, we ask the question if the data is consistent with the GR predictions and set bounds on any possible deformations. These tests are called parameterized tests. There are proposals for the parametrized tests of post-Newtonian theory [44, 65, 66, 221, 231, 237, 302], where parametric deviations are introduced at different post-Newtonian orders of the GW phasing, and the GW data is compared against this modified phasing to put bounds on the deviation parameters. Furthermore, the bounds obtained from these generic tests have also been translated into bounds on the free parameters of certain specific theories of gravity [304]. All the bounds we obtain using GW detections are consistent with the predictions of GR within the statistical uncertainties. Several more of such events are expected to be detected in future observing runs. Hence, developing efficient methods to carry out such tests will play a central role in extracting the best science from these observations.

Though the parametrized tests of PN theory are very effective, they have an important drawback. The bounds we set are on the phasing coefficients, which can not be mapped uniquely to any fundamental quantities of the compact binary. In this thesis, in order to overcome this problem, we propose a novel test to measure the multipolar structure of the gravitational field produced by CBC. We pose this as a null test of GR and ask the question if the multipolar structure of a compact binary space-time predicted by GR is consistent with the data. Detailed discussion along this line is given in chapters 3 and 4.

Gravitational recoil, associated to the anisotropic GW radiation, has potential astrophysical consequences. The anisotropic GW radiation from compact binary merger leads to a flux of linear momentum. As a result of this, the system recoils. Massive black hole formation, following successive mergers, may lead to large enough recoils to eject coalescing BHs from dwarf galaxies or globular clusters, resulting in termination of the merger process. This is the key motivation to estimate the recoil velocity of coalescing black hole binaries. Various analytic or semi-analytic studies [108, 141, 167] of recoil for non-spinning BBH mergers in quasi-circular orbits reveal a typical estimate of the kick to be a few hundreds km/s. More accurate estimates for the kick are provided by the numerical relativity calculations in Refs. [179, 180]. In contrast, compact binaries with spinning component masses may receive a very high kick (see refs. [188, 212]) $\sim \mathcal{O}(500)$ km/s. These recoil estimates rely on the accurate estimation of the linear momentum flux (LMF). However, LMF and associated recoil in case of the CB moving in quasi-elliptical orbits are much less studied. The first leading order (Newtonian order) estimates are quoted in ref. [168]. In this thesis we explore the computation of LMF at higher PN order, to be specific the second PN order.

Another astrophysical implication of the recent GW detections is to track the redshift evolution of the compact binary mergers. On very general grounds, Schutz argued [272] that the SNRs of detected GW events would follow a universal distribution which is inversely proportional to the forth power of the SNRs. This universal distribution is also used in ref [21] as an ingredient to derive a bound on the rate of the binary black hole mergers from the first observation run of LIGO [17]. Following ref. [129] we show that the universal SNR distribution breaks down for sources at arbitrary redshifts due to cosmological evolution of the universe and the change in the properties of the sources as a function of redshift. Motivated by this, we show how the observed distribution of SNRs for the detected GWs from BNS mergers are affected by the redshift evolution of their rate density in the context of third generation GW detector, CE [24]. This provides a novel method to track the BNS merger rate distribution as a function of redshift. The novelty of this method lies in the fact that it does not directly depend on parameter estimation of these systems and uses only the SNR estimates obtained from the detection problem.

The various chapters of this thesis are organized as follows. In chapter 2 we briefly discuss the multipola post Minkowskian post Newtonian (MPM-PN) formalism used in various contexts of CBC. In chapters 3 and 4 we develop the prameterized tests of multipolar structure of the CB space-time in the case of non-spinning as well as spinning component masses. In chapter 5, using the MPM-PN framework, we compute the LMF from CB moving in quasi-elliptical orbits. Finally we discuss the implications of SNR distributions of the binary NS systems detected at arbitrary redshifts in the context of a third generation detector, Cosmic Explorer (CE), in chapter 6. We also explore how these distributions can be used to probe the evolution of the BNS merger rate as a function of redshift.

2 Post-Newtonian Theory

2.1 Various analytical approximations of general relativity

As discussed in the last chapter, the detection and parameter estimation of compact binaries require a reliable waveform model accounting for all the physical effects. For a generic source, solving Einstein's equations leads to different levels of difficulties. Hence, various approximation methods have been developed to tackle the two-body problem in GR. These include the multipolar post-Minkowskian (MPM) formalism and post-Newtonian (PN) approximation scheme, perturbation theory [54, 135, 137, 251, 275], gravitational self-force formalism [75, 76, 151–153, 254] and the Effective One Body (EOB) approach [119, 120, 139, 144] etc. As opposed to these approximation methods, in numerical relativity (NR) [72, 125, 255], numerical algorithms are used to solve Einstein's equations to obtain the full gravitational waveforms which include the highly nonlinear merger phase of the binary evolution.

In fig. 2.1 different regions of validity for different methods are shown in a two parameter-space spanned by the inverse of PN expansion parameter ($(c/v)^2 \sim rc^2/Gm$) and the mass ratio (m_1/m_2), where r is the typical separation of the two bodies, m_1, m_2 are the component masses, $m = m_1 + m_2$ is the total mass and v is the characteristic velocity of the system. As is evident from the figure, the PN formalism is valid for any mass ratio, in principle, but for slowly moving systems. In BH perturbation theory, Einstein's Equation is solved in a perturbative manner with the perturbation parameter being the mass ratio of the component masses. At the leading order the smaller mass moves along its geodesic governed solely by the bigger mass, whereas, at higher order, the

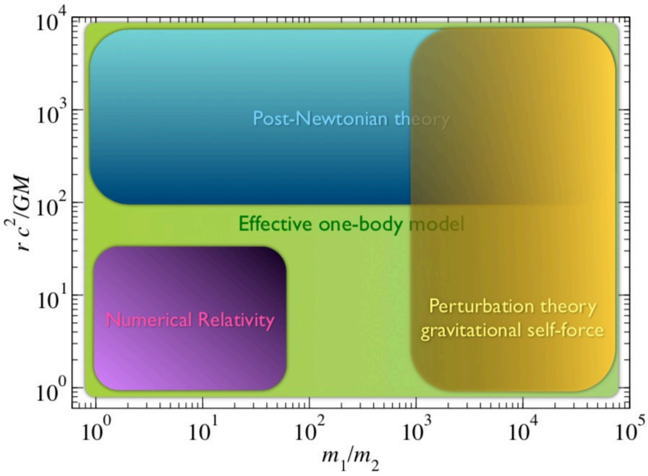

Figure 2.1. Regime of validity of various approximation schemes and numerical methods in the plane defined by the two perturbation parameters rc^2/Gm and m_1/m_2. Figure courtesy [123].

effects of back-reaction are consistently taken into account within the gravitational self-force formalism [75,76,151–153,254]. In contrast, numerical relativity provides a description of the merger of two compact objects at high velocity [256] and is valid for any mass ratio in principle. However, this method is computationally very expensive.

Apart from the above described methods, a semi-analytical description, namely the *Effective One Body* (EOB) approach of compact binary dynamics and emission of GW radiation is proposed in refs. [119,120,139,144] to include the post-inspiral effects. Assuming a comparable mass compact binary system is a smooth deformation of that of the test particle limit, the EOB approach uses three ingredients; the conserved Hamiltonian of the two body system in GR, the radiation-reaction force, and the gravitational waveform. Each of these ingredients is estimated using the higher order PN-expanded results in a *resummed form* to incorporate non-perturbative and strong-field effects.

After the remarkable progress in developing analytical as well as numerical techniques to solve the two body dynamics in GR over more than a hundred years, we now can predict highly accurate gravitational waveforms from compact binary mergers. The dynamics of a compact binary system is conventionally divided into the *adiabatic inspiral, merger*, and *ringdown* phases. During the inspiral phase the orbital time scale is much smaller than the radiation backreaction time scale. The post-Newtonian (PN) approximation to GR has proved to be a very effective method to describe the inspiral phase of a compact binary of comparable masses [89]. A description of the highly nonlinear phase of the merger of two compact objects is modeled by NR. The ringdown radiation of GWs from the merger remnant, can be modeled within the framework of BH perturbation theory [256, 267]. More recently, there are developments of various phenomenological models where analytically modeled inspirals are stitched smoothly with the numerically generated merger and ring down; this allows us to generate the complete GW signals from compact binary mergers [47, 48].

In this chapter, we briefly describe the general MPM-PN scheme for a generic PN source, followed by the specific formulation of the same in case of inspiralling compact binary (ICB).

2.2 Multipolar post-Minkowskian and post-Newtonian formalism

This formalism has given us several useful insights about various facets of the two-body dynamics and the resulting gravitational radiation [90]. The complete wave generation formalism within the MPM-PN framework is based on consistently matching the various approximation methods: post-Newtonian method (or non-linear $1/c$-expansion), the post-Minkowskian (PM) method or non-linear iteration in orders of G, and the multipole decomposition of the gravitational fields [84, 85, 93–95, 97, 98, 100, 101, 106, 145, 277]. The PM formalism is valid in the zone far from a weakly gravitating source whereas the PN approximation is applicable for a slowly moving and weakly gravitating source in the near zone. On the other hand, the multipole expansion of the gravitational field is valid over the entire region exterior to the source. A cocktail of these approximations plays a central role in the analytical treatment of the two-body problem in GR.

We follow the prescription developed by Blanchet, Damour, Iyer, and co-workers, also known as the BDI formalism to study the PN approach to solve Einstein's equations. In the next section we briefly summarize the scheme.

2.2.1 Einstein's field equations

Variation of the space-time metric $g_{\alpha\beta}$ in the Einstein-Hilbert action,

$$I_{\rm EH} = \frac{c^3}{16\pi G}\int d^4x\,\sqrt{-g}R + I_{\rm mat}[\Psi, g_{\alpha\beta}], \tag{2.2.1}$$

leads to the set of ten second-order partial differential equations, namely Einstein's equations,

$$R^{\alpha\beta} - \frac{1}{2}Rg^{\alpha\beta} = \frac{8\pi G}{c^4}T^{\alpha\beta}[\Psi, g],$$

where $g^{\alpha\beta}$ is the covariant metric with a determinant g and Ψ denotes matter fields. In *harmonic coordinates* (or *de Donder* coordinates) (where $\partial_\mu h^{\alpha\mu} = 0$), with a redefinition of the gravitational field amplitude of the form $h^{\alpha\beta} = \sqrt{-g}g^{\alpha\beta} - \eta^{\alpha\beta}$, Einstein's equations can be recast as follows:

$$\Box h^{\alpha\beta} = \frac{16\pi G}{c^4}\tau^{\alpha\beta}. \tag{2.2.2}$$

In Eq. 2.2.2, $\Box$ is the flat d'Alembertian $\Box_\eta = \eta^{\mu\nu}\partial_\mu\partial_\nu$ and $\tau^{\alpha\beta}$ is the stress-energy pseudo tensor composed of matter field $T^{\alpha\beta}$ and the gravitational source term $\Lambda^{\alpha\beta}$,

$$\tau^{\alpha\beta} = |g|T^{\alpha\beta} + \frac{c^4}{16\pi G}\Lambda^{\alpha\beta}. \tag{2.2.3}$$

In harmonic coordinates, $\Lambda^{\alpha\beta}$ is given by

$$\begin{aligned}\Lambda^{\alpha\beta} &= -h^{\mu\nu}\partial^2_{\mu\nu}h^{\alpha\beta} + \partial_\mu h^{\alpha\nu}\partial_\nu h^{\beta\mu} + \frac{1}{2}g^{\alpha\beta}g_{\mu\nu}\partial_\lambda h^{\mu\tau}\partial_\tau h^{\nu\lambda} \\ &- g^{\alpha\mu}g_{\nu\tau}\partial_\lambda h^{\beta\tau}\partial_\mu h^{\nu\lambda} - g^{\beta\mu}g_{\nu\tau}\partial_\lambda h^{\alpha\tau}\partial_\mu h^{\nu\lambda} + g_{\mu\nu}g^{\lambda\tau}\partial_\lambda h^{\alpha\mu}\partial_\tau h^{\beta\nu} \\ &+ \frac{1}{8}(2g^{\alpha\mu}g^{\beta\nu} - g^{\alpha\beta}g^{\mu\nu})(2g_{\lambda\tau}g_{\epsilon\pi} - g_{\tau\epsilon}g_{\lambda\pi})\partial_\mu h^{\lambda\pi}\partial_\nu h^{\tau\epsilon}\,. \end{aligned} \tag{2.2.4}$$

Considering the matter stress energy tensor to be of spatially compact support with a smooth distribution of matter inside the source and imposing the "*no incoming radiation*" condition, Eq. (2.2.2) can be solved using the retarded Green function

$$h^{\alpha\beta}(\mathbf{r},t) \equiv -\frac{4G}{c^4}\int \frac{d^3\mathbf{r}'}{|\mathbf{r}-\mathbf{r}'|}\tau^{\alpha\beta}(\mathbf{r}',t-|\mathbf{r}-\mathbf{r}'|/c)\,. \tag{2.2.5}$$

At the linear order in $h^{\alpha\beta}$, the solution given in Eq. (2.2.5) is straight forward and is obtained in Eq. (1.1.4) of chapter 1. However, in higher orders, the RHS of Eq. (2.2.5) is a functional with respect to $h^{\alpha\beta}$. Hence, in order to solve this, a consistent approximation scheme is required.

2.2.2 Validity regions of various approximation schemes

Due to different characteristics of gravitational field in different regions from the source, a mixture of different approximation schemes, valid in these different regions, has been adopted to obtain a successful wave generation formalism. The wave generation formalism at the lowest order (the quadrupolar formalism) is first prescribed by Einstein [160] and then by Landau and Lifshitz. Later the corrections to this leading order estimation was obtained by Damour and Blanchet [84, 94, 97] in a more mathematically consistent way. This is known as the multipolar post-Minkowskian - post-Newtonian (MPM-PN) formalism.

In fig. 2.2 the different regions applicable for different approximation schemes (discussed below) are schematically shown for a compact binary merger. The region at a distance $r >> d$, (d is the typical size of the source) extended till $\mathcal{R} << \lambda_{\rm GW}$ from the source, is denoted as the near zone, where the post-Newtonian approximation is valid. Within this approximation the source is assumed to be slowly moving and weakly stressed. For post-Newtonian sources, the perturbation parameter, defined by the components of the matter stress-energy tensor $T^{\alpha\beta}$ and the source's Newtonian potential U is $\epsilon \sim |T^{0i}/T^{00}| \sim \sqrt{|T^{ij}/T^{00}|} \sim \sqrt{U/c^2} << 1$ which is essentially v/c. In other words, the gravitational wavelength can approximately be written as $\lambda_{\rm GW} \sim (c/v)d$ and expanding different quantities in terms of v/c restricts the validity of this approximation to the

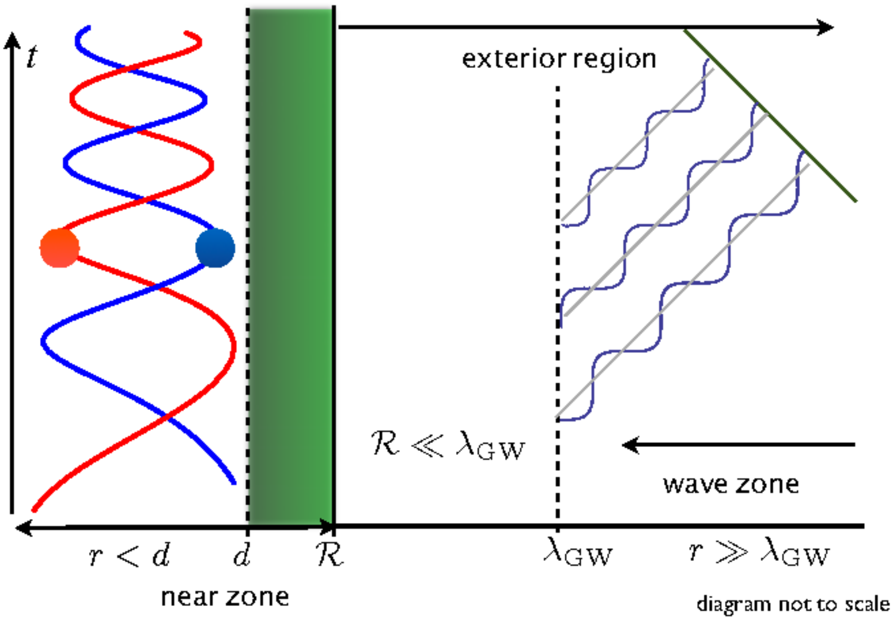

Figure 2.2. Various scales used in PN approximation. Figure courtesy Ref. [123].

.

near zone where $r << \lambda_{\rm GW}$. Though slow motion is one of the main criteria of this scheme, the characteristic speed for a compact binary inspiral could be as high as 50% of the speed of light in their last orbit, which demands the computation of higher PN order corrections. On the other hand, in the weak field limit, post-Minkowskian (PM) formalism is valid outside the source in the region where $r >> \lambda_{\rm GW}$ spanned till $r \to \infty$ denoted as wave zone. In addition to the PM expansion, multipolar expansion of the complete non-linear theory [84, 94] provides the full MPM scheme which is valid over all the regions outside the compact source. In principle, this scheme is valid for all kinds of sources but for PN sources there exists a buffer/matching zone where both the approximation schemes are valid, which gives rise to the complete wave generation formalism.

2.2.3 MPM approximation in the wave zone

In the MPM formalism the vacuum Einstein's equation (where $\tau^{\alpha\beta}$ is simply the source term $\Lambda^{\alpha\beta}$ in Eq. (2.2.2)) is solved iteratively in powers of Newton's constant G considering the field variable $h^{\alpha\beta}$ as a non-linear metric perturbation of Minkowski space-time. With the post-Minkowskian ansatz as

$$h^{\alpha\beta} = \sum_{n=1} G^n h_n^{\alpha\beta}, \tag{2.2.6}$$

the vacuum Einstein's equation (Eq. (2.2.2) reads,

$$\Box h^{\alpha\beta} = \Lambda^{\alpha\beta} = \Lambda_2^{\alpha\beta}(h,h) + \Lambda_3^{\alpha\beta}(h,h,h) + O(h^4)\,. \tag{2.2.7}$$

Above equation is solved at each successive order in G knowing the previous order solution. At the leading order, the solution can be written in terms of the symmetric trace free tensors (STF) i.e. $h_1^{\alpha\beta} = \sum_{\ell=0} \partial_L \left(\frac{K_L^{\alpha\beta}(t-r/c)}{r} \right)$, where $L = i_1, i_2...i_\ell$ and $K_L^{\alpha\beta} \equiv K_{i_1,i_2...i_\ell}^{\alpha\beta}$ are the multi-index tensors which are symmetric and trace free with respect to all its indices. Furthermore, using the harmonic gauge condition ($\partial_\alpha h_1^{\alpha\beta} = 0$), the general solution is $h_1^{\alpha\beta} = k_1^{\alpha\beta} + \partial^\alpha \varphi_1^\beta + \partial^\beta \varphi_1^\alpha - \eta^{\alpha\beta}\partial_\rho \varphi_1^\rho$, where $k_1^{\alpha\beta}$ and φ_1^α can be expressed in terms of two source moments $\{I_L, J_L\}$ and four gauge moments $\{W_L, X_L, Y_L, Z_L\}$, or equivalently two canonical moments $\{M_L, S_L\}$. At the n^{th} order in G, we need to solve $\Box h_n^{\alpha\beta} = \Lambda_n^{\alpha\beta}(h_1, h_2, ..., h_{n-1})$ and so on. Since the wave equation is valid only outside the source and the source term, $\Lambda_n^{\alpha\beta}(h_1, h_2, ..., h_{n-1})$, is composed of the product of many multipole expansions, which are singular at $r = 0$, a retarded Green's function method is not directly applicable. Thus one regularizes the multipolar expansion to the source term $\Lambda_n^{\alpha\beta}(h_1, h_2, ..., h_{n-1})$ by multiplying by r^B and use as the retarded Green's Function to solve [84, 90, 94, 97]. Eventually extracting the coefficient of the zeroth power of r, the final solution is obtained, which schematically reads,

$$u_n^{\alpha\beta} = \mathrm{FP}_{B=0} \left\{ \Box_{\text{ret}}^{-1} [r^B \Lambda_n^{\alpha\beta}] \right\}, \tag{2.2.8}$$

where FP stands for finite part. Moreover, to satisfy the harmonic gauge condition, this solution is added to a homogeneous solution, say, $v_n^{\alpha\beta}$ to obtain the complete general solution. It can be shown that this most general solution to Einstein's vacuum equation at any order depends on only two types of canonical moments $\{M_L, S_L\}$.

In the above mentioned scheme, there appear logarithmic terms in the wave zone expansion of the metric in harmonic-coordinate. The study of the "asymptotic" structure of space-time at future null infinity by Bondi et al. [117], Sachs [266], and Penrose [245,246] has shown the existence of other coordinate systems– namely radiative coordinates– in which the far-zone expansion of the metric can be written in simple powers of the inverse radial distance. Hence using the coordinate transformation between the harmonic coordinate to the radiative ones provides the relation between the canonical moments $\{M_L, S_L\}$ and the radiative moments $\{U_L, V_L\}$ and removes all the logarithmic divergences due to the usage of harmonic coordinates.

2.2.4 Near-zone post-Newtonian approximation

As opposed to the far zone, the near zone solution is obtained by using a multipolar post-Newtonian (PN) approach where $h^{\alpha\beta}$ and $\tau^{\alpha\beta}$ are expanded in powers of $1/c$, that is $h^{\alpha\beta} = \sum_{n=2} {}^{(n)}h^{\alpha\beta}/c^n$ and $\tau^{\alpha\beta} = \sum_{n=-2} {}^{(n)}\tau^{\alpha\beta}/c^n$. Due to non-compact-support terms at higher PN order, the solution faces the convergence issue at large r instead of $r = 0$. Hence one uses the similar regularization procedure applied in case of the wave-zone treatment except the fact that the exponent of r, B, is negative here. Following the same prescription afterwards, the near zone solution can be written in terms of STF tensors. These tensors can be fixed by matching with the far zone multipolar-post-Minkowskian results in the buffer region $d < r < \mathcal{R}$ where both the multipolar PN and post-Minkowskian series are valid. This matching provides the complete solution to the metric perturbation in the range $0 < r < +\infty$ and provides the relation between the far zone radiative moments U_L and V_L and the canonical multipole moments M_L and S_L or equivalently the source multipole moments $\{I_L, J_L, W_L, X_L, Y_L, Z_L\}$, and finally in terms of various source integrals (composed of the stress energy tensor of matter and the gravitational field). At the lowest order, the radiative moments are same as the canonical moments, whereas, starting from 1.5PN order, there appear the nonlinear interactions between the various moments denoted as tails [96, 101, 111], tails-of tails [87], tail-square [88], memory [59, 131, 165, 278] etc. The dominant tail effects on the radiative multipole moments first appear at 1.5PN and are caused by the multipolar waves getting scattered off the Schwarzschild curvature generated by the total mass of the source. The complete expressions of these relations between the radiative and source moments are quoted in ref. [90] at 3.5PN, which has been used in further calculations provided in this thesis.

2.3 Compact binary sources

In the previous sections we have briefly discussed the general scheme of perturbative (MPM-PN) solution to Einstein's equation. In this section we will briefly review how to employ this prescription in case of compact binary dynamics in GR within the PN-framework. The effects due to the finite size of the compact objects being a higher order one, the inspiralling compact binary is modeled by two structureless point-like masses (and spins) orbiting each other in the first order approximation. To date, the time evolution of the GW phase and the amplitude corrections for ICB have been computed at 3.5PN and 3.5PN order respectively. There are ongoing efforts to obtain higher order corrections from different groups also. While the component masses are spinning, the complete linear in spin effects (spin-orbit coupling [SO]) are known at 3.5PN order and the spin-spin couplings (SS) at 3PN order.

The GW phase evolution for compact binary mergers, can be obtained from the energy flux of the emitted GW radiation and the conserved orbital energy of the binary orbits by using the energy balance argument, which equates the GW energy flux $\mathcal{F}$ to the decrease in the binding energy $E_{\rm orb}$ of the binary [101],

$$\mathcal{F} = -\frac{d}{dt}E_{\rm orb}. \tag{2.3.1}$$

Due to the clean separation between conservative ($E_{\rm orb}$) and dissipative terms ($\mathcal{F}$), the phase evolution is obtained simply in two steps – (a) calculating the conserved energy or the equation of motion (b) Computation of the flux. At higher order, such as 4PN, 4.5PN, 5PN etc., there will be a mixture of conservative and dissipative effects and one needs a more careful treatment in order to obtain the conserved energy and GW flux. In order to compute the conserved energy or the equation of motion at 3.5PN, we first need to obtain the metric at the desired accuracy. The 3.5PN metric can be written in terms of some particular retarded type potentials V, V^i, W^{ij} , ... , which are constructed out of the pseudo-stress-energy tensor (τ^{ij}) of an extended regular PN source. For the compact binary sources, since the stress tensor is composed of delta functions (because of the point-mass approximation), these terms can be computed by means of the Hadamard regularization and dimensional regularization techniques to avoid the self-field divergences. After computing the metric, using the following equations we obtain the equation of motion,

$$\frac{d\mathcal{P}^i}{dt} = F^i, \tag{2.3.2}$$

where the linear momentum density $\mathcal{P}^i$ and the force density F^i is given by

$$\begin{aligned} \mathcal{P}^i &= c\frac{g_{i\mu}v^\mu}{\sqrt{-g_{\rho\sigma}v^\rho v^\sigma}}, & (2.3.3)\\ F^i &= \frac{c}{2}\frac{\partial_i g_{\mu\nu}v^\mu v^\nu}{\sqrt{-g_{\rho\sigma}v^\rho v^\sigma}}. & (2.3.4) \end{aligned}$$

Finally retaining the corrections at the 1PN, 2PN and 3PN orders of the equation of motion and neglecting the radiation reaction terms at 2.5PN and 3.5PN, the conserved orbital energy is computed.

On the other hand, computation of energy flux $\mathcal{F}$ needs the the radiative multipole moments U_L and V_L in terms of the canonical multipole moments M_L and S_L of the compact binary system and the non-linear interactions between them. Computation of the source moments involves the similar techniques used to obtain the equation of motion. First the multipole moments are expressed as a function of some general source densities (function of stress tensor of a general PN fluid system) by means of PN expansion and eventually using the various regularization schemes they are reduced to the case of point particles. All the multipole moments for nonspinning compact binaries in quasi circular orbits at 3.5PN order, used in further calculations, are quoted in Eqs. (300)-(305b) of ref [90]. We do not provide the explicit expressions here.

2.3.1 Compact binary sources with spins

Astrophysical evidence indicates that stellar-mass BHs and supermassive BHs (see Ref. [262] for a review) can be very close to maximally spinning. Having discussed the complete formalism of modeling the GW phase for the non-spinning compact binaries, we now focus on its extension to the spinning case. The spins of the component masses affect the gravitational waveform through a modulation of their amplitude, phase, and frequency. If the spins are not aligned or anti-aligned with respect to the orbital angular momentum, the orbital plane of the binary precesses. The leading order terms consist of spins of the component masses and start appearing at 1.5PN order. These contributions are linear in spin magnitude and hence termed as spin-orbit (SO) effects. At 2PN, quadratic in spin terms appear; these are known as spin-spin (SS) contributions. In this thesis we consider SO contributions at 3.5PN and SS contributions to 3PN. The very same prescription of computing orbital energy, flux etc. in the case of non-spinning binaries has been adopted in order to estimate various GW observables for compact binary systems with spinning component masses. The only modification is the computation of the spin effects on the pseudo-tensor $\tau^{\alpha\beta}$ (or simply the matter tensor $T^{\alpha\beta}$ at the leading order) which is obtained in the framework of the pole-dipole approximation and is suitable for both SO and SS couplings. The details about the computation of GW flux accounting for these effects are revisited in chapter 4 of this thesis.

2.3.2 Compact binary sources in eccentric orbit

Though astrophysical binaries may have large eccentricity during birth, gravitational radiation reaction circularizes the orbit towards the late stages of inspiral. Especially when the compact binary merger enters the Adv. LIGO detector band, they are likely to have zero eccentricity. Hence modeling of compact binaries in quasi-circular orbits is quite well motivated. But there are various astrophysical scenarios where binaries may have non-zero eccentricity in the gravitational-wave detector bandwidth, especially for the space-based detector LISA. In case of a major fraction of hierarchical triplets, inner binaries undergoing Kozai oscillations could have non-negligible eccentricities when they enter the sensitivity band of advanced ground based interferometers. Moreover, the population of stellar mass binaries in globular clusters may have a thermal distribution of eccentricities. Hence, this necessitates the exploration of compact binaries in quasi-eccentric orbit.

In case of compact binaries in elliptical orbits, the orbital revolution as well as the periastron advance per orbital revolution leads to the so-called "doubly periodic" motion of the binary. The GW flux and angular momentum for these binaries are first computed by Peters and Mathews at Newtonian order [250]. Later it is extended till 3PN in ref. [59–63,181]. Here, the various quantities (such as the rate of change of orbital separation, $\dot{r}$, orbital velocity $v = \dot{r}^2 + r^2\dot{\phi}^2$) are first written in terms of orbital separation r, conserved energy (E) and angular momentum (J). Eventually parametrizing the binary dynamics by using the quasi-Keplerian representation (QKR) [140,142,147,270,294], various observables such as GW flux or the waveforms are expressed in terms of quasi-Keplerian parameters such as three types of eccentricities (e_t, e_r, e_ϕ), mean anomaly (u), mean motion (n), etc. The detailed discussion along this line is given in Chapter 5 while discussing the linear momentum flux (LMF) emission in this context.

3 Testing the multipole structure of compact binaries : Non-spinning case [204]

3.1 Introduction

Setting stringent limits on possible departures from GR as well as constraining the parameter space of exotic compact objects that can mimic the properties of BHs [127, 128, 130, 154, 176, 202, 214, 215], are among the principal science goals of the next-generation detectors. They should also be able to detect any new physics, or modifications to GR, if present. Formulating new methods to carry out such tests is crucial in order to efficiently extract the physics from GW observations. In alternative theories of gravity, the dynamics of the compact binary during its inspiral merger and ringdown phases of evolution could be different from that predicted by GR. Hence GWs can be used to probe the presence of non-GR physics.

One of the most generic tests of the binary dynamics has been the measurement of the PN coefficients of the GW phasing formula [44, 65, 66, 109, 110, 237, 302]. This test captures a possible departure from GR by measuring the PN coefficients in the GW signal. In addition to the source physics, the different PN terms in the phase evolution contain information about different nonlinear interactions the wave undergoes as it propagates from the source to the detector. Hence the predictions for these effects in an alternative theory of gravity could be very different from that of

GR, which is what is being tested using the parametrized tests of PN theory.

In this chapter, we go one step further by proposing a novel way to test the multipolar structure of the gravitational field of a compact binary as it evolves through the adiabatic inspiral phase. The multipole moments of the compact binary and their interactions among themselves, are responsible for the various physical effects we see at different PN orders. By measuring these effects we can constrain the multipolar structure of the system. As discussed in chapter 2, the GW phase and frequency evolution is obtained from the energy flux of GWs and the conserved orbital energy by using the energy balance argument, which equates the GW energy flux $\mathcal{F}$ to the decrease in the binding energy $E_{\rm orb}$ of the binary [101]

$$\mathcal{F} = -\frac{d}{dt}E_{\rm orb}. \tag{3.1.1}$$

In an alternative theory of gravity, one or more multipole moments of a binary system may be different from those as described in GR. For instance, in Ref. [162], the authors discuss how effective field theory-based approach can be used to go beyond Einstein's gravity by introducing additional terms to the GR Lagrangian which are higher-order operators constructed out of the Riemann tensor, but suppressed by appropriate scales comparable to the curvature of the compact binaries. They find that such generic modifications will lead to multipole moments of compact binaries that are different from GR. Our proposed method aims to constrain such generic extensions of GR by directly measuring the multipole moments of the compact binaries through GW observations.

Here we consider that the conserved orbital energy of the binary is the same as in GR and modify the gravitational wave flux by deforming the multipole moments which contribute to it by employing the multipolar post-Minkowskian formalism [89, 101] discussed in chapter 2. We then rederive the GW phase and its frequency evolution (sometimes referred to as the *phasing formula*) explicitly in terms of the various deformed multipole moments (In chapter 4 we provide a more general expression for the phasing where the conserved energy is also deformed at different PN orders, in addition to the multipole moments of the source.). We use this parametrized multipolar phasing formula to measure possible deviations from GR and discuss the level of bounds we can expect from the current and next-generation ground-based GW detectors, as well as the space-based LISA detector. We obtain the measurement accuracy of the system's physical parameters and the deformation of the multipole moments using the semianalytical Fisher information matrix [133, 258]. These results are validated for several configurations of the binary system by Markov chain Monte Carlo (MCMC) sampling of the likelihood function using the `emcee` [171] algorithm.

We find that Advanced LIGO-like detectors can constrain at most two of the leading multipoles, while a third-generation detector, such as ET or CE, can set constraints on as many as four of the leading multipoles. The space-based LISA detector will have the ability to set bounds on all seven multipole moments that contribute to the 3.5PN phasing formula.

The organization of this chapter is as follows. In Sec. 3.2 we describe the basic formalism to obtain the parametrized multipolar GW phasing formula. In Sec. 3.3 we briefly explain the two parameter estimation schemes (Fisher information matrix and Bayesian inference) used in our analysis, followed by Sec. 3.4 where we discuss the results we obtain for various ground-based and space-based detectors. Section 3.5 summarizes the various estimates and lists some of the follow-ups we are pursuing.

3.2 Parametrized multipolar gravitational wave phasing

For quasi-circular inspirals, the PN terms in the phasing formula explicitly encode the information about the multipolar structure of the gravitational field of the two-body dynamics. In this chapter, we separately keep track of the contributions from various radiative multipole moments to the GW flux allowing us to derive a parametrized multipolar gravitational wave flux and phasing formula, thereby permitting tests of the multipolar structure of the PN approximation to GR.

We first rederive the phasing formula for nonspinning compact binaries moving in quasi-circular orbits up to 3.5 PN order. The computation is described in the next section. Before we proceed, we clarify that in our notation the first post-Newtonian (1PN) correction would refer to the relative corrections to the leading of order v^2/c^2, where $v = (\pi m f)^{1/3}$ is the characteristic orbital velocity of the binary, m is the total mass of the binary and f is the orbital frequency.

3.2.1 The multipolar structure of the energy flux

The multipole expansion of the energy flux within the MPM formalism, schematically reads as [101, 277]

$$\mathcal{F} = \sum_l \left[\frac{\alpha_l}{c^{l-2}} U_L^{(1)} U_L^{(1)} + \frac{\beta_l}{c^l} V_L^{(1)} V_L^{(1)} \right], \tag{3.2.1}$$

where α_l, β_l are known real numbers and U_L, V_L, introduced in chapter 2, are the mass- and current-type radiative multipole moments with l indices respectively; the superscript (1) denotes the first time derivative of the multipoles. Following the basic MPM-PN scheme discussed in chapter 2, the U_L and V_L can be rewritten in terms of the canonical multipole moments as

$$U_L = M_L^{(l)} + \text{Nonlinear interaction terms}, \tag{3.2.2}$$

$$V_L = S_L^{(l)} + \text{Nonlinear interaction terms}, \tag{3.2.3}$$

where the right-hand side involves l^{th} time derivative of the mass- and current-type source multipole moments and nonlinear interactions between the various multipoles due to the propagation of the wave in the curved spacetime of the source. (see Refs. [87, 88, 98, 106] for details). The various types of interactions can be decomposed as follows [101, 106]

$$\mathcal{F} = \mathcal{F}_{\text{inst}} + \mathcal{F}_{\text{tail}} + \mathcal{F}_{\text{tail}^2} + \mathcal{F}_{\text{tail(tail)}}. \tag{3.2.4}$$

As opposed to $\mathcal{F}_{\text{inst}}$ (a contribution that depends on the dynamics of the binary solely at the retarded instant of time, referred to as instantaneous terms), the last three contributions $\mathcal{F}_{\text{tail}}$, $\mathcal{F}_{\text{tail}^2}$ and $\mathcal{F}_{\text{tail(tail)}}$ contain nonlinear multipolar interactions in the flux [87] that depend on the dynamical history of the system and referred to as *hereditary* contributions.

In an alternative theory of gravity, the multipole moments may not be the same as in GR; if the mass- and current-type radiative multipole moments deviate from their GR values by a fractional amount δU_L and δV_L, i.e., $U_L \to U_L^{\rm GR} + \delta U_L$ and $V_L \to V_L^{\rm GR} + \delta V_L$, then we can parametrize such deviations in the multipoles by considering the scalings

$$\begin{aligned} U_L &\to \mu_l\, U_L, \\ V_L &\to \epsilon_l\, V_L, \end{aligned} \tag{3.2.5}$$

where the parameters $\mu_l = 1 + \delta U_L/U_L^{\rm GR}$ and $\epsilon_l = 1 + \delta V_L/V_L^{\rm GR}$ are equal to unity in GR.

We first recompute the GW flux from nonspinning binaries moving in quasi-circular orbit at 3.5PN order with the above scaling using the prescription outlined in chapter 2 [85, 100, 101, 106]. With the parametrizations introduced above, the computation of the energy flux would proceed similarly to that in GR [106] but contributions from every radiative multipole are now separately kept track of.

In order to calculate the fluxes up to the required PN order, we need to compute the time derivatives of the multipole moments as can be seen from Eqs. (3.2.1)-(3.2.3). These are computed by using the equations of motion of the compact binary for quasi-circular orbits given by [104, 106],

$$\frac{d\mathbf{v}}{dt} = -\omega^2\, \mathbf{x}, \tag{3.2.6}$$

where the expression for ω, the angular frequency of the binary, up to 3PN order is given by [99, 102, 104, 145, 146, 149, 200]

$$\begin{aligned} \omega^2 &= \frac{Gm}{r^3}\Bigg\{1 + [-3+\eta]\,\gamma + \left[6 + \frac{41}{4}\eta + \eta^2\right]\gamma^2 \\ &+ \left[-10 + \left(22\ln\left(\frac{r}{r'_0}\right) + \frac{41\pi^2}{64} - \frac{75707}{840}\right)\eta \right. \\ &+ \left.\frac{19}{2}\eta^2 + \eta^3\right]\gamma^3 + O(\gamma^4)\Bigg\}, \end{aligned} \tag{3.2.7}$$

where $\gamma = Gm/rc^2$ is the PN expansion parameter, r'_0 is a gauge-dependent length scale which does not appear when observables, such as the energy flux, are expressed in terms of gauge-independent variables.

The hereditary terms are calculated using the prescriptions given in Refs. [86, 101, 106, 111] for tails, Ref. [87] for tails of tails and Ref. [88] for tail square. The complete expression for the energy flux $\mathcal{F}$ in terms of the scaled multipoles is given as

$$\begin{aligned}
\mathcal{F} \;=\; & \frac{32}{5}\frac{c^5v^{10}}{G}\eta^2\mu_2^2\Bigg\{1+v^2\bigg(-\frac{107}{21}+\frac{55}{21}\eta+\hat{\mu}_3^2\bigg[\frac{1367}{1008}-\frac{1367}{252}\eta\bigg]+\hat{\epsilon}_2{}^2\bigg[\frac{1}{36}-\frac{\eta}{9}\bigg]\bigg)+4\pi v^3 \\
& +v^4\bigg(\frac{4784}{1323}-\frac{87691}{5292}\eta+\frac{5851}{1323}\eta^2+\hat{\mu}_3^2\bigg[-\frac{32807}{3024}+\frac{3515}{72}\eta-\frac{8201}{378}\eta^2\bigg]+\hat{\mu}_4^2\bigg[\frac{8965}{3969} \\
& -\frac{17930}{1323}\eta+\frac{8965}{441}\eta^2\bigg]+\hat{\epsilon}_2{}^2\bigg[-\frac{17}{504}+\frac{11}{63}\eta-\frac{10}{63}\eta^2\bigg]+\hat{\epsilon}_3{}^2\bigg[\frac{5}{63}-\frac{10}{21}\eta+\frac{5}{7}\eta^2\bigg]\bigg) \\
& +\pi v^5\bigg(-\frac{428}{21}+\frac{178}{21}\eta+\hat{\mu}_3^2\bigg[\frac{16403}{2016}-\frac{16403}{504}\eta\bigg]+\hat{\epsilon}_2{}^2\bigg[\frac{1}{18}-\frac{2}{9}\eta\bigg]\bigg)+v^6\bigg(\frac{99210071}{1091475}+\frac{16\pi^2}{3} \\
& -\frac{1712}{105}\gamma_E-\frac{856}{105}\log[16v^2]+\bigg[\frac{1650941}{349272}+\frac{41\pi^2}{48}\bigg]\eta-\frac{669017}{19404}\eta^2+\frac{255110}{43659}\eta^3+\hat{\mu}_3^2\bigg[\frac{7345}{297} \\
& -\frac{30103159}{199584}\eta+\frac{10994153}{49896}\eta^2-\frac{45311}{891}\eta^3\bigg]+\hat{\mu}_4^2\bigg[-\frac{1063093}{43659}+\frac{20977942}{130977}\eta-\frac{12978200}{43659}\eta^2 \\
& +\frac{1568095}{14553}\eta^3\bigg]+\hat{\mu}_5^2\bigg[\frac{1002569}{249480}-\frac{1002569}{31185}\eta+\frac{1002569}{12474}\eta^2-\frac{2005138}{31185}\eta^3\bigg]+\hat{\epsilon}_2^2\bigg[-\frac{2215}{254016} \\
& -\frac{13567}{63504}\eta+\frac{65687}{63504}\eta^2-\frac{853\eta^3}{5292}\bigg]+\hat{\epsilon}_3{}^2\bigg[-\frac{193}{567}+\frac{1304}{567}\eta-\frac{2540}{567}\eta^2+\frac{365}{189}\eta^3\bigg]+\hat{\epsilon}_4{}^2\bigg[\frac{5741}{35280} \\
& -\frac{5741}{4410}\eta+\frac{5741}{1764}\eta^2-\frac{5741}{2205}\eta^3\bigg]\bigg)+\pi v^7\bigg(\frac{19136}{1323}-\frac{144449}{2646}\eta+\frac{33389}{2646}\eta^2+\hat{\mu}_3^2\bigg[-\frac{98417}{1512} \\
& +\frac{55457}{192}\eta-\frac{344447}{3024}\eta^2\bigg]+\hat{\mu}_4^2\bigg[\frac{23900}{1323}-\frac{47800}{441}\eta+\frac{23900}{147}\eta^2\bigg]+\hat{\epsilon}_2{}^2\bigg[-\frac{17}{252}+\frac{9}{28}\eta-\frac{13}{63}\eta^2\bigg] \\
& +\hat{\epsilon}_3{}^2\bigg[\frac{20}{63}-\frac{40}{21}\eta+\frac{20}{7}\eta^2\bigg]\bigg)\Bigg\},
\end{aligned} \tag{3.2.8}$$

where $\hat{\mu}_\ell = \mu_\ell/\mu_2$, $\hat{\epsilon}_\ell = \epsilon_\ell/\mu_2$, Euler constant, $\gamma_E = 0.577216$ and η is the symmetric mass ratio defined as the ratio of reduced mass μ to the total mass m. As an algebraic check of the result, we recover the GR results of Ref. [106] in the limit $\mu_l \to 1, \epsilon_l \to 1$.

3.2.2 Conservative dynamics of the binary

A model for the conservative dynamics of the binary is also required to compute the phase evolution of the system. This affects the phasing formula in two ways. First, the equation of motion of the binary [104] in the center-of-mass frame is required to compute the derivatives of the multipole moments while calculating the energy flux. Second, the expression for the 3PN orbital energy [102, 104] is necessary to obtain the phase evolution [see Eqs. (3.2.13)–(3.2.14) below]. As the computation of the radiative multipole moments requires two or more derivative operations w.r.t. time, they are implicitly sensitive to the equation of motion. Hence, formally, a constraint on the deformation of the radiative multipole moment does take into account a potential deviation in the equation of motion from the predictions of GR.

The assumption about the conserved energy being the same as in GR , is motivated by practical considerations. We could have taken a more generic approach by deforming the PN coefficients in the equation of motion and conserved energy as well. As the former is degenerate with the definition of radiative multipole moments, one would need to consider a parametrized expression for the conserved energy which will give us a phasing formula with four additional parameters corresponding to the different PN orders in the expression for conserved energy. A simultaneous estimation of these parameters with the multipole coefficients would significantly degrade the resulting bounds and may not yield meaningful constraints. However, in chapter 4, we present a parametrized phasing formula where in addition to the multipole coefficients, various PN-order terms in the conserved 3PN energy expression are also deformed [see Eq. (4.3.4)]. Interestingly, as can be seen from Eq. (4.3.4), if there is a modification to the conservative dynamics, they will be fully degenerate with at least one of the multipole coefficients appearing at the same order. Due to this degeneracy, such modifications will be detected by this test as modifications to “effective" multipole moments. We are, therefore, confident that the power of the proposed test is not diminished by this assumption. The conserved energy (per unit mass) up to 3PN order is given by [99, 102, 104, 145, 146, 149, 200]

$$
\begin{aligned}
E(v) &= -\frac{1}{2}\eta v^2\left[1-\left(\frac{3}{4}+\frac{1}{12}\eta\right)v^2-\left(\frac{27}{8}-\frac{19}{8}\eta+\frac{1}{24}\eta^2\right)v^4\right.\\
&\left.-\left\{\frac{675}{64}-\left(\frac{34445}{576}-\frac{205}{96}\pi^2\right)\eta+\frac{155}{96}\eta^2+\frac{35}{5184}\eta^3\right\}v^6\right]. \qquad (3.2.9)
\end{aligned}
$$

Using the expressions for the modified flux and the orbital energy we next proceed to compute the phase evolution of the compact binary.

3.2.3 Computation of the parametrized multipolar phasing formula

With the parametrized multipolar flux and the energy expressions, we compute the 3.5PN, frequency-domain phasing formula following the standard prescription [122, 143] by employing the stationary phase approximation (SPA) [269]. Consider a GW signal of the form

$$h(t) = \mathcal{A}(t)\cos\phi(t). \qquad (3.2.10)$$

The Fourier transform of the signal will involve an integrand whose amplitude is slowly varying and whose phase is rapidly oscillating. In the SPA, the dominant contributions to this integral come from the vicinity of the stationary points of its phase [143]. As a result the frequency-domain gravitational waveform may be expressed as

$$
\begin{aligned}
\tilde{h}^{\rm SPA}(f) &= \frac{\mathcal{A}(t_f)}{\sqrt{\dot{F}(t_f)}}e^{i[\psi_f(t_f)-\pi/4]}, \qquad (3.2.11)\\
\psi_f(t) &= 2\pi f t-\phi(t), \qquad (3.2.12)
\end{aligned}
$$

where t_f can be obtained by solving $d\psi_f(t)/dt\big|_{t_f}=0$, $F(t)$ is the gravitational wave frequency and at $t=t_f$ the GW frequency coincides with the Fourier variable f. More explicitly,

$$t_f = t_{\rm ref}+m\int_{v_f}^{v_{ref}}\frac{E'(v)}{\mathcal{F}(v)}dv, \qquad (3.2.13)$$

$$\psi_f(t_f) = 2\pi f t_{\rm ref} - \phi_{\rm ref} + 2\int_{v_f}^{v_{ref}} (v_f^3 - v^3)\frac{E'(v)}{\mathcal{F}(v)}dv, \tag{3.2.14}$$

where $E'(v)$ is the derivative of the binding energy of the system expressed in terms of the PN expansion parameter v. Expanding the factor in the integrand in Eq. (3.2.14) as a PN series and truncating up to 3.5PN order, we obtain the 3.5PN accurate TaylorF2 phasing formula.

Following the very same procedure, but using Eq. (3.2.8) to be the parametrized flux, $\mathcal{F}$, together with the leading quadrupolar order amplitude (related to the Newtonian GW polarizations), we derive the standard *restricted* PN waveform in the frequency domain, which reads as

$$\tilde{h}(f) = \mathcal{A}\mu_2 f^{-7/6} e^{i\psi(f)}, \tag{3.2.15}$$

where $\psi(f)$ is the parametrized multipolar phasing, amplitude, $\mathcal{A} = \mathcal{M}_c^{5/6}/\sqrt{30}\pi^{2/3}D_L$; $\mathcal{M}_c = (m_1 m_2)^{3/5}/(m_1+m_2)^{1/5}$ and D_L are the chirp mass and luminosity distance, respectively, and m_1, m_2 denote the component masses of the binary. To be noted here, that μ_2 is also present in the GW amplitude. This is due to the mass quadrupole that contributes to the amplitude at the leading PN order. If we incorporate the higher-order PN terms in the GW polarizations [59, 103, 107], higher-order multipoles will enter the GW amplitude also.

Finally the expression for the 3.5PN frequency-domain phasing formula, $\psi(f)$ is given by,

$$\begin{aligned}
\psi(f) = {} & 2\pi f t_c - \frac{\pi}{4} - \phi_c + \frac{3}{128 v^5 \mu_2^2 \eta}\Bigg\{1 + v^2\bigg(\frac{1510}{189} - \frac{130}{21}\eta + \hat{\mu}_3^2\bigg[-\frac{6835}{2268} + \frac{6835}{567}\eta\bigg] \\
& + \hat{\epsilon}_2^{\,2}\bigg[-\frac{5}{81} + \frac{20}{81}\eta\bigg]\bigg) - 16\pi v^3 + v^4\bigg(\frac{242245}{5292} + \frac{4525}{5292}\eta + \frac{145445}{5292}\eta^2 + \hat{\mu}_3^2\bigg[-\frac{66095}{7056} \\
& + \frac{170935}{3024}\eta - \frac{403405}{5292}\eta^2\bigg] + \hat{\mu}_3^2\hat{\epsilon}_2^{\,2}\bigg[\frac{6835}{9072} - \frac{6835}{1134}\eta + \frac{6835\eta^2}{567}\bigg] + \hat{\mu}_3^4\bigg[\frac{9343445}{508032} - \frac{9343445}{63504}\eta \\
& + \frac{9343445}{31752}\eta^2\bigg] + \hat{\mu}_4^2\bigg[-\frac{89650}{3969} + \frac{179300}{1323}\eta - \frac{89650}{441}\eta^2\bigg] + \hat{\epsilon}_2^{\,2}\bigg[-\frac{785}{378} + \frac{7115}{756}\eta - \frac{835}{189}\eta^2\bigg] \\
& + \hat{\epsilon}_2^{\,4}\bigg[\frac{5}{648} - \frac{5}{81}\eta + \frac{10}{81}\eta^2\bigg] + \hat{\epsilon}_3^{\,2}\bigg[-\frac{50}{63} + \frac{100}{21}\eta - \frac{50}{7}\eta^2\bigg]\bigg) + \pi v^5\bigg(3\log\bigg[\frac{v}{v_{\rm LSO}}\bigg] + 1\bigg)\bigg(\frac{80}{189}\bigg[151 \\
& - 138\eta\bigg] - \frac{9115}{756}\hat{\mu}_3^2\big[1 - 4\eta\big] - \frac{20}{27}\hat{\epsilon}_2^{\,2}\big[1 - 4\eta\big]\bigg) + v^6\bigg(\frac{5334452639}{2037420} - \frac{640}{3}\pi^2 - \frac{6848}{21}\gamma_E
\end{aligned}$$

$$
\begin{aligned}
&-\frac{6848}{21}\log[4v]-\left[\frac{7153041685}{1222452}-\frac{2255}{12}\pi^2\right]\eta+\frac{123839990}{305613}\eta^2+\frac{18300845}{1222452}\eta^3\\
&+\hat{\mu}_3^2\left[-\frac{4809714655}{29338848}+\frac{8024601785}{9779616}\eta-\frac{19149203695}{29338848}\eta^2-\frac{190583245}{7334712}\eta^3\right]\\
&+\hat{\mu}_3^2\hat{\epsilon}_2{}^2\left[-\frac{656195}{95256}+\frac{229475\eta}{3888}-\frac{3369935\eta^2}{23814}+\frac{82795\eta^3}{1323}\right]+\hat{\mu}_3^2\hat{\epsilon}_2{}^4\left[\frac{6835}{108864}-\frac{6835}{9072}\eta\right.\\
&\left.+\frac{6835}{2268}\eta^2-\frac{6835}{1701}\eta^3\right]+\hat{\mu}_3^2\hat{\epsilon}_3{}^2\left[-\frac{34175}{7938}+\frac{170875}{3969}\eta-\frac{375925}{2646}\eta^2+\frac{68350}{441}\eta^3\right]\\
&+\hat{\mu}_3^2\hat{\mu}_4^2\left[-\frac{61275775}{500094}+\frac{306378875}{250047}\eta-\frac{674033525}{166698}\eta^2+\frac{122551550}{27783}\eta^3\right]\\
&+\hat{\mu}_3^4\left[\frac{868749005}{10668672}-\frac{2313421945}{3556224}\eta+\frac{191974645}{148176}\eta^2+\frac{9726205}{666792}\eta^3\right]+\hat{\mu}_3^4\hat{\epsilon}_2{}^2\left[\frac{9343445}{3048192}\right.\\
&\left.-\frac{9343445}{254016}\eta+\frac{9343445}{63504}\eta^2-\frac{9343445}{47628}\eta^3\right]+\hat{\mu}_3^6\left[\frac{12772489315}{256048128}-\frac{12772489315}{21337344}\eta\right.\\
&\left.+\frac{12772489315}{5334336}\eta^2-\frac{12772489315}{4000752}\eta^3\right]+\hat{\mu}_4^2\left[-\frac{86554310}{916839}+\frac{553387330}{916839}\eta-\frac{289401650}{305613}\eta^2\right.\\
&\left.-\frac{4322750}{101871}\eta^3\right]+\hat{\mu}_4^2\hat{\epsilon}_2{}^2\left[-\frac{89650}{35721}+\frac{896500}{35721}\eta-\frac{986150}{11907}\eta^2+\frac{358600\eta^3}{3969}\right]+\hat{\mu}_5^2\left[\frac{1002569}{12474}\right.\\
&\left.-\frac{4010276}{6237}\eta+\frac{10025690}{6237}\eta^2-\frac{8020552}{6237}\eta^3\right]+\hat{\epsilon}_2{}^2\left[\frac{3638245}{190512}-\frac{2842015}{31752}\eta+\frac{760985}{13608}\eta^2\right.\\
&\left.-\frac{328675}{23814}\eta^3\right]+\hat{\epsilon}_2{}^2\hat{\epsilon}_3{}^2\left[-\frac{50}{567}+\frac{500}{567}\eta-\frac{550}{189}\eta^2+\frac{200}{63}\eta^3\right]+\hat{\epsilon}_2{}^4\left[-\frac{265}{1512}+\frac{20165}{13608}\eta-\frac{5855}{1701}\eta^2\right.\\
&\left.+\frac{310}{243}\eta^3\right]+\hat{\epsilon}_2{}^6\left[\frac{5}{11664}-\frac{5}{972}\eta+\frac{5}{243}\eta^2-\frac{20}{729}\eta^3\right]+\hat{\epsilon}_3{}^2\left[\frac{27730}{3969}-\frac{179990}{3969}\eta+\frac{341450}{3969}\eta^2\right.\\
&\left.\left.-\frac{51050}{1323}\eta^3\right]+\hat{\epsilon}_4{}^2\left[\frac{5741}{1764}-\frac{11482}{441}\eta+\frac{28705}{441}\eta^2-\frac{22964}{441}\eta^3\right]\right)+\pi v^7\left(\frac{484490}{1323}-\frac{141520}{1323}\eta\right.\\
&+\frac{442720}{1323}\eta^2+\hat{\mu}_3^2\left[-\frac{88205}{2352}+\frac{63865}{252}\eta-\frac{182440}{441}\eta^2\right]+\hat{\mu}_3^2\hat{\epsilon}_2{}^2\left[\frac{54685}{9072}-\frac{54685}{1134}\eta+\frac{54685}{567}\eta^2\right]\\
&+\hat{\mu}_3^4\left[\frac{6835}{254016}-\frac{6835}{31752}\eta+\frac{6835}{15876}\eta^2\right]+\hat{\mu}_4^2\left[-\frac{400}{3969}+\frac{800}{1323}\eta-\frac{400}{441}\eta^2\right]+\hat{\epsilon}_2{}^2\left[-\frac{1570}{63}\right.\\
&\left.\left.\left.+\frac{7220}{63}\eta-\frac{3760}{63}\eta^2\right]+\hat{\epsilon}_3{}^2\left[-\frac{400}{63}+\frac{800}{21}\eta-\frac{400}{7}\eta^2\right]+\hat{\epsilon}_2{}^4\left[\frac{10}{81}-\frac{80}{81}\eta+\frac{160}{81}\eta^2\right]\right)\right\}. \quad (3.2.16)
\end{aligned}
$$

This parametrized multipolar phasing formula is one of the most important results of this chapter and is the basis for the analysis which follows.

3.2.4 Multipole structure of the post-Newtonian phasing formula

We summarize the multipole structure of the PN phasing formula, based on Eq. (3.2.16), in table 3.1. The main features are as follows. As we go to higher PN orders, in addition to the higher-order multipoles making their appearances, higher-order PN corrections to the lower-order multipoles also contribute. For example, the mass quadrupole and its corrections (terms proportional to μ_2) appear at every PN order starting from 0PN. The 1.5PN and 3PN log terms are due to the leading-order tail effect [111] and tails-of-tails effect [87], respectively, hence contain only μ_2. The 3PN nonlogarithmic term contains all seven multipole coefficients.

Due to the aforementioned structure, it is evident that if one of the multipole moments is different from GR, it is likely to affect the phasing coefficients at more than one PN order. For instance, a deviation in μ_2 could result in a dephasing of each of the PN phasing coefficients. There are total seven independent multipole coefficients which determine eight PN coefficients. The eight equations which relate the phasing terms to the multipoles are inadequate to extract all seven multipoles. This is because three of the eight equations relate the PN coefficients only to μ_2, and another two relate the 1PN and 2.5PN logarithmic terms to a set of three multipole coefficients $\{\mu_2, \mu_3, \epsilon_2\}$. It turns out that, in principle, by independently measuring the eight PN coefficients, we can measure all the multipoles except two, μ_5 and ϵ_4. It is well known that measuring all eight phasing coefficients together provides very bad bounds [65, 66]. The version of the parametrized tests of post-Newtonian theory, where we vary only one parameter at a time [44, 65], cannot be mapped to the multipole coefficients, as varying multipole moments will cause more than one PN order to change, which conflicts with the original assumption.

Though mapping the space of PN coefficients to that of the multipole coefficients is not possible, it is possible to relate the multipole deformations to that of the parametrized test. If, for instance, μ_2 is different from GR, it can lead to dephasing in one or more of the PN phasing terms depending on what the correction is to the mass quadrupole at different PN orders. Based on the multipolar structure, this provides a motivation to perform parametrized tests of PN theory while varying

PN order	frequency dependences	Multipole coefficients
0 PN	$f^{-5/3}$	μ_2
1 PN	f^{-1}	μ_2, μ_3, ϵ_2
1.5 PN	$f^{-2/3}$	μ_2
2 PN	$f^{-1/3}$	μ_2, μ_3, μ_4, ϵ_2, ϵ_3
2.5 PN log	$\log f$	μ_2, μ_3, ϵ_2
3 PN	$f^{1/3}$	μ_2, μ_3, μ_4, μ_5, ϵ_2, ϵ_3, ϵ_4
3 PN log	$f^{1/3}\log f$	μ_2
3.5 PN	$f^{2/3}$	μ_2, μ_3, μ_4, ϵ_2, ϵ_3

Table 3.1. Summary of the multipolar structure of the PN phasing formula. The contributions of various multipoles to different phasing coefficients and their frequency dependences are tabulated. Following the definitions introduced in this thesis, μ_l are associated to the deformations of mass-type multipole moments and ϵ_l refer to the deformations of current-type multipole moments.

simultaneously certain PN coefficients[1].

3.3 Parameter estimation of the multipole coefficients

In this section, we set up the parameter estimation problem to measure the multipolar coefficients and present our forecasts for Advanced LIGO, the Einstein Telescope, Cosmic Explorer and LISA. Using the frequency-domain gravitational waveform, we study how well the current and future generations of GW detectors can probe the multipolar structure of GR. We derive the projected accuracies with which various multipole moments may be measured, in case of various detector configurations by using standard parameter estimation techniques. Following the philosophy of Refs. [44, 66, 237], while computing the errors, we consider the deviation of only one multipole at a time. An ideal test would have been where all the coefficients are varied at the same time, but this would lead to almost no meaningful constraints due to the strong degeneracies among different coefficients. However, this would not affect our ability to detect a potential deviation because in the multipole structure, a deviation of more than one multipole coefficient would invariably show up in the set of tests performed by varying one coefficient at a time [44, 221, 231, 237].

[1] We thank Archisman Ghosh for pointing out this possibility to us.

We first use the Fisher information matrix approach discussed in chapter 1 to derive the $1-\sigma$ error bars (see Eq. (1.4.20)) on the multipole coefficients. Since Fisher-matrix-based estimates are only reliable in the high signal-to-noise ratio limit [74, 136, 283], we spot check representative cases for consistency, with the estimates based on a Bayesian inference algorithm that uses an MCMC method to sample the likelihood function, which is also discussed in chapter 1. This method is not limited by the quadratic approximation to the log-likelihood and hence is considered to be a more reliable estimate of measurement accuracies one might have in a real experiment (see section 1.4 of chapter 1 for detailed discussion). In this thesis, we use uniform prior on all the parameters we are interested in and used `python`-based MCMC sampler, `emcee` [171] to sample the likelihood surface and get the posterior distribution for all the parameters.

We compute the Fisher matrix assuming the noise PSDs of various detectors given in section 1.3.2 of chapter 1. Furthermore, we consider that the signal can be described by the set of parameters $\{\ln\mathcal{A}, \ln M_c, \ln\eta, t_c, \phi_c\}$ and any one of the seven additional parameters μ_l or ϵ_l. In order to compute the inner product using Eq. (1.4.14), we assume $f_{\rm low}$ to be 20, 1, 5 and 10^{-4} Hz for the aLIGO, ET-D, CE-wb and LISA noise PSDs respectively. We choose $f_{\rm high}$ to be the frequency at the last stable circular orbit (LSO) of a Schwarzschild BH with a total mass m equal to the sum of the binary's component masses, given by $f_{\rm LSO} = 1/(\pi\, m\, 6^{3/2})$ for the aLIGO, ET-D and CE-wb noise PSDs. For LISA, we choose the upper cut off frequency to be the minimum of $[0.1, f_{\rm LSO}]$. Additionally, LISA being a triangular shaped detector, we multiply our gravitational waveform by a factor of $\sqrt{3}/2$ while calculating the Fisher matrix for LISA.

All of the parameter estimations for aLIGO, CE-wb and LISA carried out here, assume detections of the signals with a single detector, whereas for ET-D, due to its triangular shape, we consider the noise PSD to be enhanced roughly by a factor of 1.5. As our aim is to estimate the intrinsic parameters of the injected GW waveform, which directly affect the binary dynamics, the single detector estimates are good enough for our purposes and a network of detectors may improve it by the square root of the number of detectors. Hence the reported errors are likely to give rough, but conservative bounds on the expected accuracies with which the multipole coefficients may be

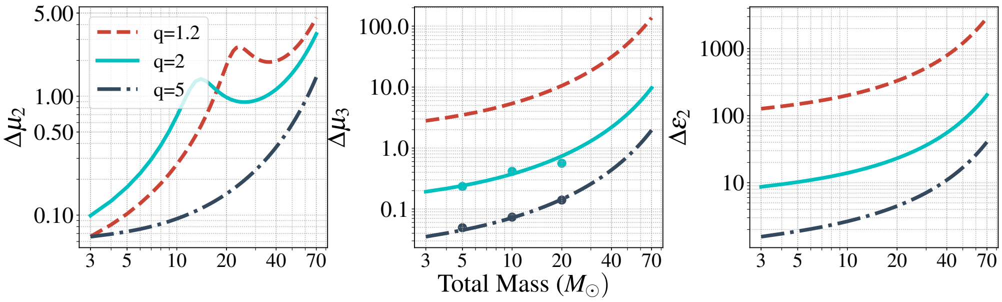

Figure 3.1. Projected 1σ errors on μ_2, μ_3 and ϵ_2 as functions of the total mass for the aLIGO noise PSD. Results from Bayesian analysis using MCMC sampling are given as dots showing good agreement. All the sources are considered to be at a fixed luminosity distance of 100 Mpc.

estimated.

3.4 Results and Discussion

In this section, we report the 1σ measurement errors on the multipole coefficients introduced in the previous section, obtained using the Fisher matrix as well as Bayesian analysis and discuss their implications.

Our results for the four different detector configurations are presented in figs. 3.1, 3.3 and 3.5, which show the errors on the various multipole coefficients μ_l, ϵ_l for aLIGO, ET-D, CE-wb and LISA, respectively. For all the estimates we consider the sources to be at fixed distances. In addition to the intrinsic parameters there are four more (angular) parameters that are needed to completely specify the gravitational waveform. More precisely, one needs two angles to define the location of the source on the sky and another two angles to specify the orientation of the orbital plane with respect to the detector plane and the polarization of the wave [268]. Since we are using a pattern-averaged waveform [143] (i.e., a waveform averaged over all four angles), the luminosity distance can be thought of as an *effective* distance which we assume to be 100 Mpc for aLIGO, ET-D and CE-wb and 3 Gpc for LISA. For aLIGO, ET-D and CE-wb, we explore the bounds for the binaries with total masses in the range [1,70] $M_\odot$ and for LISA detections, in the range $[10^5, 10^7]$ $M_\odot$.

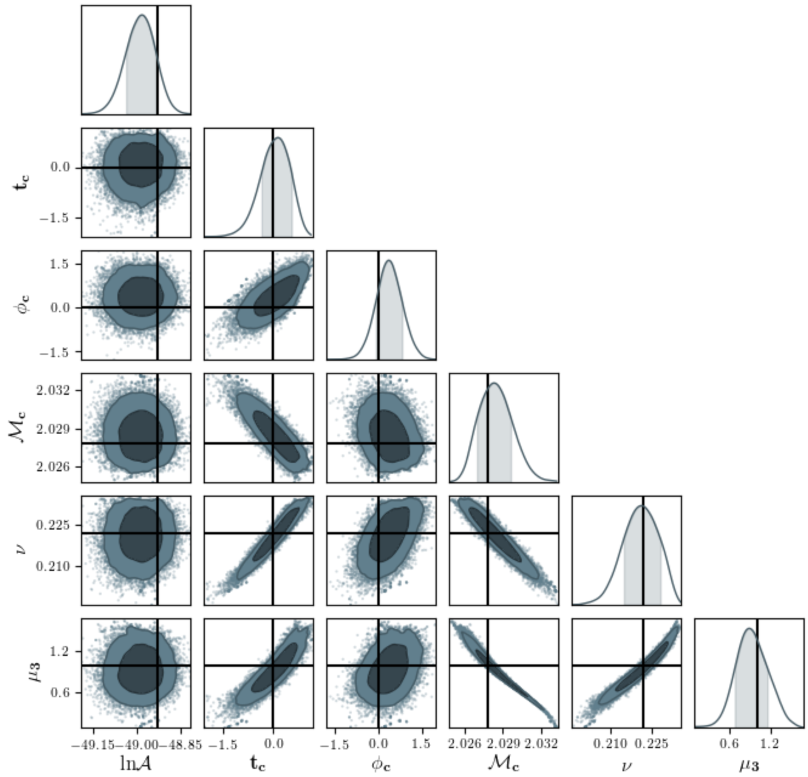

Figure 3.2. The posterior distributions of all six parameters $\{\ln\mathcal{A}, t_c, \phi_c, \mathcal{M}_c, \eta, \mu_3\}$ and their corresponding contour plots obtained from the MCMC experiments (see section 1.4.2 for details) for a compact binary system at a distance of 100 Mpc with $q = 2$, $m = 5\,\mathrm{M}_\odot$ using the noise PSD of aLIGO. The darker shaded regions in the posterior distributions as well as in the contour plots show the 1σ bounds on the respective parameters.

3.4.1 Advanced LIGO

In fig. 3.1, we demonstrate the projected 1-σ errors on the three leading multipole coefficients, μ_2, μ_3 and ϵ_2, as a function of the total mass of the binary for the aLIGO noise PSD using the Fisher matrix. Different curves are for different mass ratios, $q = m_1/m_2 = 1.2$ (red), 2 (cyan) and 5 (blue). For the multipole coefficients considered, low-mass systems obtain the smallest errors and hence the tightest constraints. This is expected as low-mass systems live longer in the detector band and have larger number of cycles, thereby allowing us to measure the parameters very well. The bounds on μ_3 and ϵ_2, associated with the mass octupole and current quadrupole, increase monotonically with the total mass of the system for a given mass ratio. However, the bounds on μ_2 show a local minimum in the intermediate-mass regime for smaller mass ratios. This is because, unlike other multipole parameters, μ_2 appears both in the amplitude and the phase of the signal.Schematically, the Fisher matrix element is given by

$$\Gamma_{\mu_2\mu_2} \sim \int_{f_{\rm low}}^{f_{\rm high}} \frac{\mathcal{A}^2 f^{-7/3}}{S_h(f)} \left(1 + \mu_2^2 \psi'^2\right) df, \tag{3.4.1}$$

where $\psi' = \partial\psi/\partial\mu_2$. As the inverse of this term dominantly determines the error on μ_2, the local minimum is a result of the trade-off between the contributions from the amplitude and the phase of the waveform. Interestingly, as we go to higher mass ratios, this feature disappears resulting in a monotonically increasing curve (such as for $q = 5$).

We find that the mass multipole moments μ_2 and μ_3 are much better estimated as compared to the current multipole moment ϵ_2. Another important feature is that the bounds μ_3 and ϵ_2 are worse for equal mass binaries. The mass-octupole and current-quadrupole are odd-parity multipole moments (unlike, say, the mass quadrupole which is even)[2]. Every odd-parity multipole moment comes with a mass asymmetry factor $\sqrt{1-4\eta}$ that vanishes in the equal-mass limit and as a consequence the errors diverge. Consequently, the Fisher matrix becomes badly conditioned and the precision with which we recover these parameters appears to become very poor, but this is an artifact of the Fisher matrix.

In order to cross-check the validity of the Fisher-matrix-based estimates, we perform a Bayesian analysis to find the posterior distribution of the three multipole parameters, for the same systems as in the Fisher matrix analysis. Moreover we considered a flat prior probability distribution for all six parameters $\{\ln\mathcal{A}, M_c, \eta, t_c, \phi_c, \mu_\ell \text{ or } \epsilon_\ell\}$ in a large enough range around their respective injection values. Given the large number of iterations, once the MCMC chains are stabilized, we find good agreements with the Fisher estimates as in the case of μ_3 for $q = 2$ and 5, shown in Fig. 3.1. As an example, we present our results from the MCMC analysis for μ_3 with $m = 5\,\mathrm{M}_\odot$ and $q = 2$,

[2]Mass-type multipoles with even l and current-type moments with odd l are considered 'even' and odd l mass multipoles and even l current moments are 'odd'.

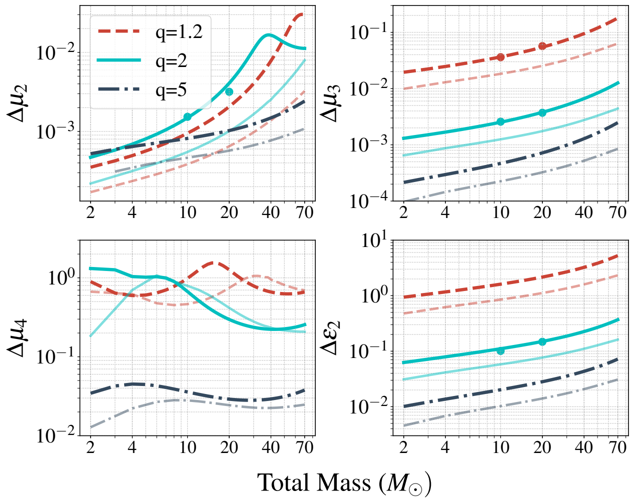

Figure 3.3. Dark shaded curves correspond to the projected 1σ error bars on μ_2, μ_3, μ_4 and ϵ_2 using the proposed CE-wb noise PSD as a function of the total mass, where as lighter shades denote the bounds obtained using the ET-D noise PSD. All the sources are considered to be at a fixed luminosity distance of 100 Mpc. The higher-order multipole moments such as μ_4 and ϵ_2 cannot be measured well using aLIGO and hence it may be a unique science goal of the third-generation detectors.

in the corner plots in fig. 3.2. In fig. 3.1 we see that the 1σ errors in μ_3 from the Fisher analysis agree very well with the MCMC results for $q = 2$ and 5. We did not find such an agreement for $q = 1.2$. We suspect that this is because for comparable-mass systems the likelihood function, defined in chapter 1, Eq. (1.4.16), becomes shallow and it is computationally very difficult to find its maximum given a finite number of iterations. As a result, the MCMC chains did not converge and 1σ bounds cannot be trusted for such cases. We find the nonconvergence of MCMC chains for all of the cases for μ_2 and ϵ_2. Hence we do not show those results in fig. 3.1. In a nutshell, our findings indicate only μ_2 and μ_3 can be measured with a good enough accuracy using aLIGO detectors.

3.4.2 Third-generation detectors

Third-generation detectors such as CE-wb (and ET-D) can put much better bounds on μ_2, μ_3 and ϵ_2 compared to aLIGO. Additionally, they can also measure μ_4 with reasonable accuracy, as shown by

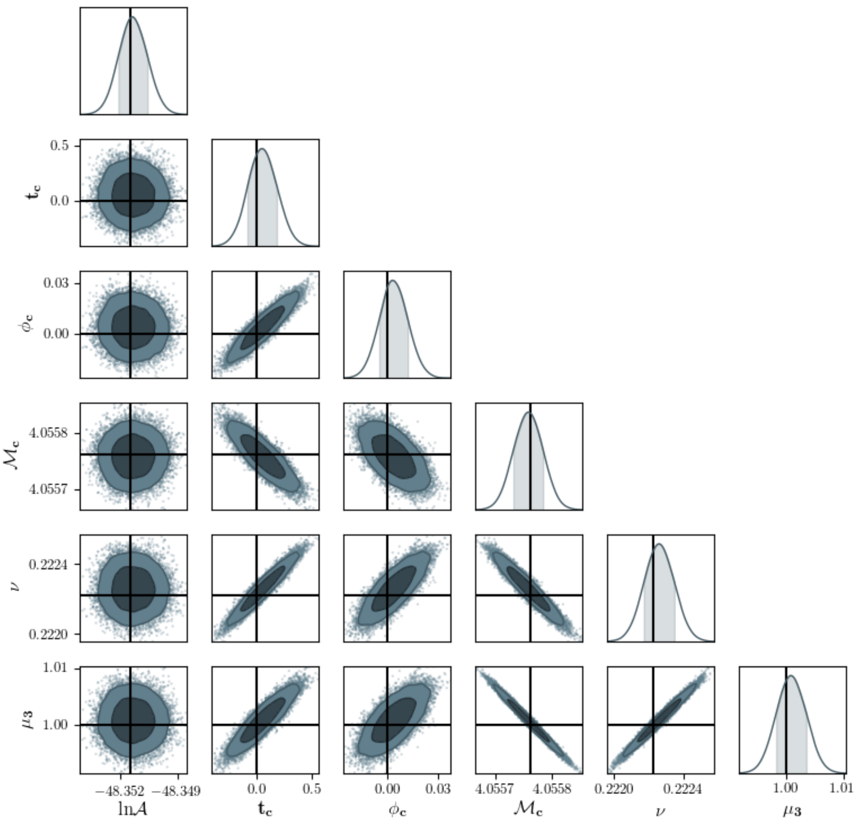

Figure 3.4. The posterior distributions of all six parameters $\{\ln\mathcal{A}, t_c, \phi_c, \mathcal{M}_c, \eta, \mu_3\}$ and their corresponding contour plots obtained from the MCMC experiments (see Sec. 1.4.2 for details) for a compact binary system at a distance of 100 Mpc with $q = 2$, $m = 10\ \mathrm{M}_\odot$ using the noise PSD of CE-wb. The darker shaded region in the posterior distributions as well as in the contour plots show the 1σ bounds on the respective parameters.

the darker (and lighter) shaded curves in fig. 3.3. The bounds on μ_2, μ_3 and ϵ_2 show similar trends as in the case of aLIGO except the overall accuracy of the parameter estimation is much better. For a few cases in low-mass regime, μ_2 and μ_4 are better estimated for comparable-mass binaries (i.e., $q = 1.2$). We also find that the bounds (denoted by the lighter shaded curves in fig. 3.3) obtained by using the ET-D noise PSD are even better than the bounds from CE-wb, though the other features are more or less similar for both of the detectors. This improvement in the precision of measurements is due to two reasons. The triangular shape of ET-D enhances the sensitivity roughly by a factor of 1.5 and its sensitivity is much better than CE-wb in the low-frequency

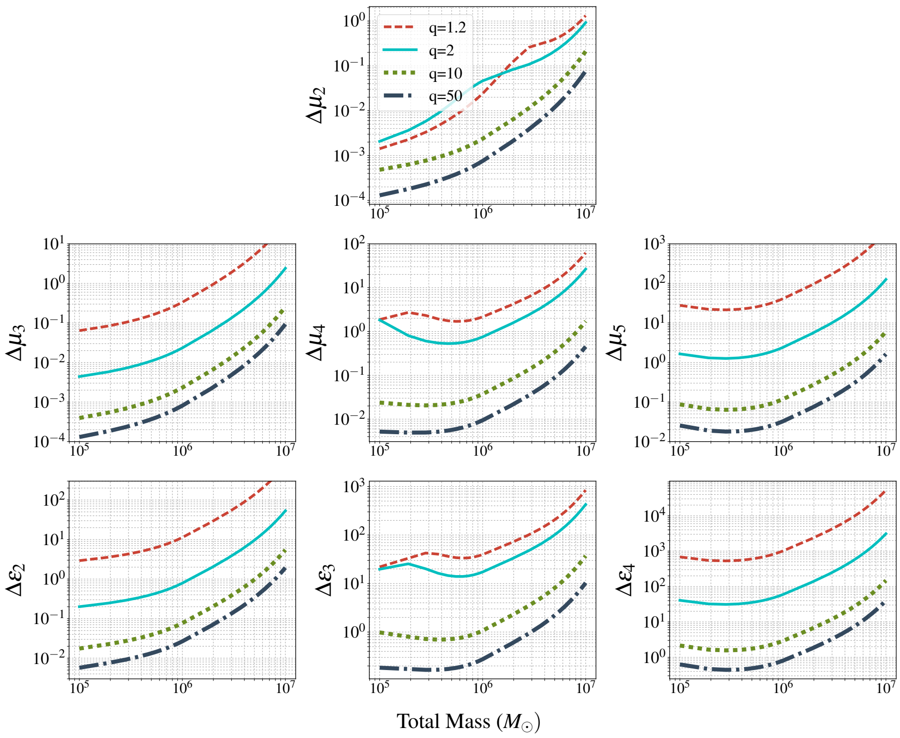

Figure 3.5. Projected constraints on various multipole coefficients using LISA sensitivity, as a function of the total mass of the binary. All the sources are considered to be at a fixed luminosity distance of 3 Gpc. LISA can measure all seven multipoles which contribute to the phasing and hence will be able to place extremely stringent bounds on the multipoles of the compact binary gravitational field.

regime.

For a few representative cases, we compute the errors in μ_2, ϵ_2 and μ_3 using Bayesian analysis and the results are shown as dots with the same color in fig. 3.3. The MCMC results are in good agreement with the Fisher matrix results. Unlike the aLIGO PSD, for CE-wb the MCMC chains converge quickly in the case of μ_2 and ϵ_2 because of the high signal-to-noise-ratios, which naturally lead to high likelihood values. As a result, it becomes relatively easier for the sampler to find the global maximum of the likelihood function in relatively fewer iterations. Moreover, we show an example of corner plot for the CE-wb PSD with $q = 2$, $m = 10\ \mathrm{M}_\odot$ in fig. 3.4.

3.4.3 Laser Interferometer Space Antenna

In this section, we discuss the projected bounds on various multipole coefficients for the LISA detector. Here we consider four mass ratios, $q = 1.2$ (red), 2 (cyan), 10 (blue) and 50 (green). The first three are representatives of comparable-mass systems, while $q = 50$ refers to the intermediate-mass ratio systems. Here we do not consider the extreme-mass-ratio-systems. The analysis of these systems needs phasing information at much higher PN orders such as in Ref. [172] which is beyond the scope of the present work. Moreover, in such systems, the motion of the smaller BH around the central compact object is expected to help us understand the multipolar structure of the central object and test its BH nature [265]. This is quite different from our objective here which is to use GW observations to understand the multipole structure of the gravitational field of the two-body problem in GR. The $q = 50$ case, in fact, falls in between these two classes and hence has a cleaner interpretation in our framework.

In fig. 3.5 we show the projected errors from the observations of supermassive BH mergers, detectable by the space-based LISA observatory. The error estimates for multipole moments with LISA are similar to that of CE-wb for mass ratios $q = 1.2, 2$. For $q = 10$ all the parameters except ϵ_4 are estimated very well. For $q = 50$, we find that LISA will be able to measure all seven multipole coefficients with good precession. It is not completely clear if PN model is accurate enough for the detections and parameter estimations of supermassive binary BHs with $q = 50$, for which the number of GW cycles could be an order of magnitude higher than that of equal-mass configurations. However, our findings carry important information, as they point to the huge potential such systems have for fundamental physics.

To summarize, we find, in general, that even-parity multipoles (i.e., μ_2 and μ_4) are better measured when the binary constituents are of equal or comparable masses, whereas the odd multipoles (i.e., μ_3, μ_5, ϵ_2 and ϵ_3) are better measured when the binary has mass asymmetry. This happens because the even multipoles are proportional to the symmetric mass ratio η, whereas the odd ones are proportional to the mass asymmetry factor, $\sqrt{1-4\eta}$, which vanishes in the equal-mass limit of the systems (see, e.g., Eq. (4.4) of Ref. [101]).

3.5 Summary and Future directions

We propose a novel way to search for possible deviations from GR using GW observations from compact binaries, by probing the multipolar structure of the GW phasing in any alternative theories of gravity. We compute a parametrized multipolar GW phasing formula which can be used to probe potential deviations from the multipolar structure of compact binary space-time in GR. Using the Fisher information matrix and Bayesian parameter estimation, we predict the accuracies with which the multipole coefficients could be measured from GW observations with present and future detectors. We find that the space mission LISA, currently under development, can measure all the multipoles of the compact binary system. Hence this will be among the unique fundamental science goals LISA can achieve.

In deriving the parametrized multipolar phasing formula, we assume that the conservative dynamics of the binary follow the predictions of GR. In the next chapter, we provide a phasing formula where we also deform the PN terms in the orbital energy of the binary. This might be seen as a first step towards a more generic parametrization of the phasing, where we separate the conservative and dissipative contributions to it. A systematic revisit of the problem, starting from the foundations of PN theory while applying to the compact binary, is needed to obtain a complete phasing formula parametrizing uniquely the conservative and dissipative sectors.

The present results using nonspinning waveforms should be considered to be a proof-of-principle demonstration, which will be followed up with a more realistic waveform that accounts for spin effects (the extension to the spinning case, we discuss in next chapter 4), effects of orbital eccentricity and higher modes. The incorporation of the proposed test in the framework of the effective one-body formalism [119] is also among the future directions we plan to pursue.

4 Testing the multipole structure and conservative dynamics : The spinning case [205]

4.1 Introduction

The parametrized multipolar waveform developed in the previous chapter facilitates tests of GR in a model independent way with GW observations [204]. However, there are strong astrophysical evidences that stellar mass BH binaries [41, 182] as well as super-massive BH binaries [261] may have highly spinning component masses. The spins of the compact binary components affect the binary dynamics and give rise to different radiation profile as compared to their non-spinning counterparts. Hence a physically realistic waveform model should account for the spin dynamics of compact binaries. Within the PN formalism, the gravitational waveform has been calculated considering the point masses with arbitrary spins up to a very high accuracy [55, 64, 90–92, 114–116, 121, 184, 185, 206, 207, 219, 220, 228–230, 234, 252, 296]. In this chapter, we extend our parametrized multipolar GW energy flux as well as PN waveform model considering spin-orbit (SO) and spin-spin (SS) contributions from binary constituents. We assume that the component spins are either aligned or anti-aligned with respect to the orbital angular momentum of the binary, inspiraling in quasi-circular orbits. Here, in addition to the multipolar structure, we present the phasing formula which also parametrizes the conservative dynamics of the binary.

As done in chapter 3, in this chapter also we use Fisher information matrix based parameter estimation scheme, discussed in chapter 1, to compute projected bounds on the various multipolar coefficients. Along with the study on the bounds of the multipolar parameters, we also provide the bounds on the parameters associated to the conservative sector in this chapter. We consider GW observation through networks of the various second and third generation ground-based detectors as well the proposed space-based LISA mission [50]. Inclusion of spin effects not only increases the dimension of the parameter space but also degrades the measurement accuracy of parameters. We find that a network of third-generation ground-based detectors and the space-based LISA mission would have comparable sensitivity to detect potential deviations in the multipolar structure of compact binaries.

This chapter is organized as follows. In section 4.2 we discuss our computational scheme for the multipolar parametrized gravitational wave energy flux. In section 4.3 we explore the modifications in the parametrized frequency domain (TaylorF2) waveform due to the various contributions from spins. Thereafter, in section 4.4 we briefly describe the parameter estimation techniques we use here. Section 4.5 provides a detailed description about the various GW detector configurations used for our analysis. In section 4.6 we discuss the bounds on the multipole coefficients for various GW detectors with our concluding remarks in section 4.7.

4.2 Parametrized gravitational wave energy flux

During the inspiral phase of the compact binary dynamics, the radiation reaction time scale is much longer than the time scale for orbital motion. Due to this separation of time scales, as discussed in chapters 2 and 3 also, two vital ingredients for computing the phase evolution are the *conserved orbital energy* of the binary and the *gravitational wave energy flux* from the system. While the former characterizes the conservative dynamics of the binary, the latter describes the dissipative dynamics.

The computation of the multipolar parametrized flux formula makes use of the entire machinery of the MPM-PN formalism discussed in chapter 2 [85, 91, 94, 96, 100, 101, 106, 112, 146] (see [89] for a review). We follow the same scheme developed in chapter 3 [204], i.e. GW energy flux parametrized in terms of the various radiative multipole moments of the compact binary while including contributions from the spins of the binary components in quasi-circular orbits. More explicitly, we use the same parametrizations introduced in Eq. (3.2.5) of chapter 3 at the level of mass-type (U_L) and current-type (V_L) radiative multipole moments. In this chapter we focus on the contributions to the flux from spin angular momentum of the binary components and hence quote only the spin-dependent part of the parametrized GW energy flux which may be added to the non-spinning results of chapter 3 [204] to get the complete phasing. Among the different approaches of considering spin corrections to the conservative dynamics as well as gravitational radiation from a compact binary system, we adopt the PN iteration scheme in harmonic coordinates [90] to obtain spin contributions to the radiative moments in GR which we further rescale as depicted in Eqs. (3.2.5).

We closely follow the prescription given in Refs. [90–92, 115, 116] to account for the contributions to the conservative and dissipative sectors of the compact binary dynamics from the individual spins of the component masses. In our notation, the individual spins of the component masses, m_1 and m_2 are $\mathbf{S_1}$ and $\mathbf{S_2}$ with quadrupolar polarisabilities κ_1 and κ_2, respectively, which are unity for Kerr black holes. We denote the total mass for the system to be $m = m_1 + m_2$, relative mass difference to be $\delta = (m_1 - m_2)/m$ and the symmetric mass ratio being $\eta = m_1 m_2/m^2$. Furthermore, following the usual notation used in the literature, we present our results in terms of the symmetric combination of the quadrupolar polarisabilities, $\kappa_+ = \kappa_1 + \kappa_2$ and the anti-symmetric combination, $\kappa_- = \kappa_1 - \kappa_2$. Our results are expressed in the center of mass (CM) frame where the spin variables $\mathbf{S}$ and $\mathbf{\Sigma}$ have the following relations with the spins of each of the constituent masses of the binary,

$$\mathbf{S} = \mathbf{S_1} + \mathbf{S_2}\,, \tag{4.2.1}$$

$$\mathbf{\Sigma} = m\left(\frac{\mathbf{\Sigma_2}}{m_2} - \frac{\mathbf{\Sigma_1}}{m_1}\right), \tag{4.2.2}$$

and $S_L = \mathbf{S}\cdot\mathbf{L}$ and $\Sigma_L = \mathbf{\Sigma}\cdot\mathbf{L}$ are the projections along the direction of orbital angular momentum.

Depending on the order of spin corrections, the GW flux schematically has the following structure,

$$\mathcal{F} = \mathcal{F}_{\rm NS} + \mathcal{F}_{\rm SO} + \mathcal{F}_{\rm SS} + \mathcal{F}_{\rm SSS} + ..., \tag{4.2.3}$$

where $\mathcal{F}_{\rm NS}$ is the non-spinning contribution quoted in Eq. (3.2.8) of chapter chapter 3 and does not depend on the spin parameters, $\mathcal{F}_{\rm SO}$ is the SO contribution which depends linearly on the spins and $\mathcal{F}_{\rm SS}$ is quadratic in spins arising due to the SS interactions. Similarly $\mathcal{F}_{\rm SSS}$ denotes the cubic-in-spin effects on the GW energy flux. Here we report the parametrized multipolar flux accounting for SO effects up to 3.5PN order and SS contributions up to 3PN order. We do not provide the cubic spin and the partial quadratic-in-spin contribution at 3.5PN order. The non-spinning flux and the parameterized phasing formula computed in chapter 3 should be added to the corresponding ones computed in this chapter to obtain the total flux and the phasing. We provide explicit expressions for the spin-orbit and quadratic-in-spin contributions to multipolar parametrized GW fluxes in the following subsections.

4.2.1 Spin-orbit contributions

Considering the leading order spin corrections to the multipole moments as well as in the equation of motion (EOM) and following the same technique as prescribed in Refs. [91, 92, 115], we re-compute the parametrized SO part of the energy flux, which is given as,

$$\begin{aligned}
\mathcal{F}_{\rm SO} \;=\;& \frac{32}{5}\frac{c^5}{G}\eta^2\hat{\mu}_2^2 x^5\Bigg\{\frac{x^{3/2}}{Gm^2}\Bigg(-4S_L+\delta\Sigma_L\Big[-\frac{4}{3}+\frac{\hat{\epsilon}_2^2}{12}\Big]\Bigg)+\frac{x^{5/2}}{Gm^2}\Bigg(S_L\Big[\frac{316}{63}-\frac{514}{63}\eta-\hat{\mu}_3^2\Big(\frac{598}{63}-\frac{2392}{63}\eta\Big)\\
&-\hat{\epsilon}_2^2\Big(\frac{43}{126}-\frac{86}{63}\eta\Big)+\hat{\epsilon}_3^2\Big(\frac{20}{63}-\frac{20}{21}\eta\Big)\Big]+\delta\Sigma_L\Big[\frac{208}{63}-\frac{10}{9}\eta-\hat{\mu}_3^2\Big(\frac{1025}{252}-\frac{1025}{84}\eta\Big)-\hat{\epsilon}_2^2\Big(\frac{367}{1008}-\frac{11}{18}\eta\Big)\\
&+\hat{\epsilon}_3^2\Big(\frac{20}{63}-\frac{20}{21}\eta\Big)\Big]\Bigg)-\frac{\pi x^3}{Gm^2}\Bigg(16S_L+\delta\Sigma_L\Big[\frac{16}{3}-\frac{\hat{\epsilon}_2^2}{6}\Big]\Bigg)+\frac{x^{7/2}}{Gm^2}\Bigg(S_L\Big[\frac{58468}{1323}+\frac{154424}{1323}\eta+\frac{3494}{1323}\eta^2\\
&+\hat{\mu}_3^2\Big(\frac{120121\eta^2}{1134}-\frac{345665\eta}{1512}+\frac{65491}{1296}\Big)+\hat{\mu}_4^2\Big(-\frac{272392\eta^2}{1323}+\frac{544784\eta}{3969}-\frac{272392}{11907}\Big)-\hat{\epsilon}_2^2\Big(\frac{1534\eta^2}{3969}\\
&+\frac{1165\eta}{2646}-\frac{2131}{15876}\Big)+\hat{\epsilon}_3^2\Big(-\frac{7300\eta^2}{567}+\frac{7150\eta}{567}-\frac{1556}{567}\Big)+\hat{\epsilon}_4^2\Big(\frac{5741\eta^2}{882}-\frac{5741\eta}{1176}+\frac{5741}{7056}\Big)\Big]\\
&+\delta\Sigma_L\Big[\frac{28423\eta^2}{3969}+\frac{366697\eta}{7938}+\frac{49844}{3969}+\hat{\mu}_3^2\Big(\frac{319661\eta^2}{18144}-\frac{811795\eta}{9072}+\frac{253385}{9072}\Big)
\end{aligned}$$

$$
+\hat{\mu}_4^2\Big(-\frac{3184\eta^2}{49}+\frac{7960\eta}{147}-\frac{1592}{147}\Big)+\hat{\epsilon}_2^2\Big(-\frac{41471\eta^2}{127008}-\frac{37585\eta}{31752}+\frac{14383}{63504}\Big)
+\hat{\epsilon}_3^2\Big(-\frac{490\eta^2}{81}+\frac{5140\eta}{567}-\frac{188}{81}\Big)+\hat{\epsilon}_4^2\Big(\frac{5741}{7056}-\frac{28705}{7056}\eta+\frac{5741}{1176}\eta^2\Big)\Big]\Big)\Big\}. \quad (4.2.4)
$$

SO corrections start appearing in the flux for compact objects from 1.5PN order due to spin-dependent terms in mass quadrupole moments at 1.5PN order and current quadrupole moment at 0.5PN order. Hence the leading order SO corrections make μ_2 and ϵ_2 to appear in the parametrized GW flux at 1.5PN. As clearly stated in Ref. [91], at 2.5PN order the SO contributions come from mass- and current-type quadrupole and octupole moments, which is evident from Eq. (4.2.4) since only μ_2, μ_3, ϵ_2 and ϵ_3 are present up to 2.5PN order. At 3PN order, the spin dependences come from the 1.5PN tail integral performed on mass quadrupole moment and the 2.5PN tail integral performed on current quadrupole moment [92]. Hence at 3PN only μ_2 and ϵ_2 are present. As we go to higher order we find that at 3.5PN, μ_4 and ϵ_4 are also present along with the lower order coefficients. As a check on the calculation, in the limit where all the coefficients, $\{\mu_2, \mu_3, \mu_4, \mu_5, \epsilon_2, \epsilon_3, \epsilon_4\} \to 1$, Eq. (4.2.4) reduces to Eq. (4) of Ref. [91].

4.2.2 Spin-spin contribution

Quadratic-in-spin corrections first appear at 2PN of the GW flux and the waveform (see Refs. [206, 207, 234, 257, 296] for details). Next to leading order contributions from SS terms appear at 3PN and are first calculated in Ref. [116].

Along with the terms quadratic-in-spin in the EOM, the complete SS contributions to the flux are generated from the four leading multipole moments, I_{ij}, I_{ijk}, J_{ij} and J_{ijk}. Hence $\mathcal{F}_{\rm SS}$ is completely parametrized by μ_2, μ_3, ϵ_2 and ϵ_3 (see Eq. (4.2.5)). We have also written the SS contribution at 3.5PN order arising from the two leading order tail integrals performed on mass and current quadrupole moments. However, at 3.5PN SS contributions are partial. Hence these contributions are neglected for the waveform computations. The closed form expression for SS contributions to the GW flux is given by,

$$
\begin{aligned}
\mathcal{F}_{\rm SS} = \; & \frac{32}{5}\frac{c^5}{G}\eta^2\mu_2^2x^5\frac{1}{G^2m^4}\Bigg\{x^2\Big(S_L^2\big[4+2\kappa_+\big]+S_L\Sigma_L\big[2\kappa_+\delta+4\delta-2\kappa_-\big]+\Sigma_L^2\Big[\frac{\hat{\epsilon}_2^2}{16}+\kappa_+-\delta\kappa_- \\
& -(4+2\kappa_+)\eta\Big]\Big)+x^3\Big(S_L^2\Big[-\frac{1198}{63}-\frac{46\kappa_+}{7}+\frac{55\delta\kappa_-}{21}+\hat{\mu}_3^2\Big(\frac{1367}{168}+\frac{1367\kappa_+}{336}-\frac{\delta\kappa_-}{1008}\Big) \\
& +\hat{\epsilon}_2^2\Big(\frac{1}{6}+\frac{\kappa_+}{12}-\frac{\delta\kappa_-}{18}\Big)+\frac{20}{63}\hat{\epsilon}_3^2+\eta\Big(\frac{82}{7}+\frac{41\kappa_+}{7}-\hat{\mu}_3^2\Big[\frac{1367}{42}+\frac{1367\kappa_+}{84}\Big]-\hat{\epsilon}_2^2\Big[\frac{2}{3}+\frac{\kappa_+}{3}\Big]\Big)\Big] \\
& +S_L\Sigma_L\Big[-\frac{193\delta\kappa_+}{21}-\frac{1436\delta}{63}+\frac{193\kappa_-}{21}+\hat{\mu}_3^2\Big(\frac{293\delta\kappa_+}{72}+\frac{1367\delta}{168}-\frac{293\kappa_-}{72}\Big)+\hat{\epsilon}_2^2\Big(\frac{5\delta\kappa_+}{36}-\frac{143\delta}{252} \\
& -\frac{5\kappa_-}{36}\Big)+\frac{40}{63}\delta\hat{\epsilon}_3^2+\eta\Big(\frac{41\delta\kappa_+}{7}+\frac{82\delta}{7}-\frac{49\kappa_-}{3}+\hat{\mu}_3^2\Big[\frac{293\kappa_-}{18}-\frac{1367\delta}{42}-\frac{1367\kappa_+\delta}{84}\Big] \\
& -\hat{\epsilon}_2^2\Big[\frac{\delta\kappa_+}{3}+\frac{2\delta}{3}-\frac{5\kappa_-}{9}\Big]\Big)\Big]+\Sigma_L^2\Big[-\frac{26}{9}-\frac{193\kappa_+}{42}+\frac{193\delta\kappa_-}{42}+\hat{\mu}_3^2\Big(\frac{293\kappa_+}{144}-\frac{293\delta\kappa_-}{144}\Big) \\
& -\hat{\epsilon}_2^2\Big[\frac{31}{56}-\frac{5\kappa_+}{72}+\frac{5\delta\kappa_-}{72}\Big]+\frac{20}{63}\hat{\epsilon}_3^2+\eta\Big(\frac{1562}{63}+\frac{619\kappa_+}{42}-\frac{233\delta\kappa_-}{42}-\hat{\mu}_3^2\Big[\frac{1367}{168}+\frac{12305\kappa_+}{1008} \\
& -\frac{8203\delta\kappa_-}{1008}\Big]+\hat{\epsilon}_2^2\Big(\frac{167}{168}-\frac{13\kappa_+}{36}+\frac{2\delta\kappa_-}{9}\Big)-\frac{80}{63}\hat{\epsilon}_3^2\Big)+\eta^2\Big(-\frac{41\kappa_+}{7}-\frac{82}{7}+\hat{\mu}_3^2\Big[\frac{1367}{42}+\frac{1367\kappa_+}{84}\Big] \\
& +\hat{\epsilon}_2^2\Big[\frac{2}{3}+\frac{\kappa_+}{3}\Big]\Big)\Big]\Big)+\pi x^{7/2}\Big(S_L^2\big[16+8\kappa_+\big]+S_L\Sigma_L\big[8\kappa_+\delta+16\delta-8\kappa_-\big]+\Sigma_L^2\Big[\frac{\hat{\epsilon}_2^2}{8}+4\kappa_+-4\delta\kappa_- \\
& -(16+8\kappa_+)\eta\Big]\Big)\Bigg\}. \qquad (4.2.5)
\end{aligned}
$$

As an algebraic check, in the limit, $\mu_2 = \mu_3 = \mu_4 = \mu_5 = \epsilon_2 = \epsilon_3 = \epsilon_4 = 1$ in Eq. (4.2.5), we confirm the correct expression for SS contribution to GW flux in GR reported in Eq. (4.14) of Ref. [116].

4.3 Parametrized multipolar gravitational wave phasing

The GW phase and its frequency evolution are obtained by using the energy conservation law, Eq. (2.3.1), which essentially balances the rate of change of conserved orbital energy E and the emitted GW flux. Hence an accurate model for conserved orbital energy is needed to obtain the GW phasing formula.

In GR, for a non-spinning compact binary inspiraling in quasi-circular orbits, the expression for the conserved energy per unit mass is given in Refs. [99, 102, 104, 145, 146, 149, 200], whereas the SO corrections up to 3.5PN and the SS corrections up to 3PN are reported in Refs. [91, 92, 115, 116].

In alternative theories of gravity, along with the deformations at the level of multipole moments, we expect the conserved orbital energy to be different as well. In order to incorporate theses effects, we introduce free parameters, α_k, characterizing the deviations at different PN orders in the conserved energy defined in GR for compact binaries in aligned (or anti-aligned)-spin configuration. For spin contributions to the conservative dynamics we consider SO corrections up to 3.5PN and SS corrections at 3PN to the energy. The 3.5PN closed-form expression for the parametrized conserved energy reads as,

$$\begin{aligned} E(v) \;=\; & -\frac{1}{2}\eta\alpha_0 v^2\Bigg[1-\left(\frac{3}{4}+\frac{1}{12}\eta\right)\hat{\alpha}_2 v^2+\left\{\frac{14}{3}S_L+2\delta\Sigma_L\right\}\frac{\hat{\alpha}_3}{Gm^2}v^3-\left\{\frac{27}{8}-\frac{19}{8}\eta+\frac{1}{24}\eta^2\right. \\ & +\frac{S_L^2}{G^2m^4}(\kappa_++2)+\frac{S_L\Sigma_L}{G^2m^4}(\delta\kappa_++2\delta-\kappa_-)+\frac{\Sigma_L^2}{G^2m^4}\left(\frac{1}{2}\kappa_+-\frac{\delta}{2}\kappa_--\eta[\kappa_++2]\right)\bigg\}\hat{\alpha}_4 v^4 \\ & +\left\{\left[11-\frac{61}{9}\eta\right]S_L+\left[3-\frac{10}{3}\eta\right]\delta\Sigma_L\right\}\frac{\hat{\alpha}_5}{Gm^2}v^5-\left\{\frac{675}{64}-\left(\frac{34445}{576}-\frac{205}{96}\pi^2\right)\eta+\frac{155}{96}\eta^2\right. \\ & +\frac{35}{5184}\eta^3+\frac{S_L^2}{G^2m^4}\left(\left[\frac{5}{3}\delta\kappa_-+\frac{25}{6}\kappa_+-\frac{50}{9}\right]-\eta\left[\frac{5}{6}\kappa_++\frac{5}{3}\right]\right)+\frac{S_L\Sigma_L}{G^2m^4}\left(\left[\frac{5}{2}\delta\kappa_+-\frac{25}{3}\delta-\frac{5}{2}\kappa_-\right]\right. \\ & \left.-\eta\left[\frac{5}{6}\delta\kappa_++\frac{5}{3}\delta+\frac{35}{6}\kappa_-\right]\right)+\frac{\Sigma_L^2}{G^2m^4}\left(\left[\frac{5}{4}\kappa_+-\frac{5}{4}\delta\kappa_--5\right]-\eta\left[\frac{5}{4}\kappa_++\frac{5}{4}\delta\kappa_--10\right]\right. \\ & \left.\left.+\eta^2\left[\frac{5}{6}\kappa_++\frac{5}{3}\right]\right)\right\}\hat{\alpha}_6 v^6+\left\{\left(\frac{135}{4}-\frac{367}{4}\eta+\frac{29}{12}\eta^2\right)S_L+\left(\frac{27}{4}-39\eta+\frac{5}{4}\eta^2\right)\delta\Sigma_L\right\}\frac{\hat{\alpha}_7}{Gm^2}v^7\Bigg], \end{aligned} \tag{4.3.1}$$

with $\hat{\alpha}_i=\alpha_i/\alpha_0$. To obtain the gravitational waveform in frequency domain under the SPA [269], we use the standard prescription outlined in Refs. [122, 143] as assumed in chapter 3 also. The important difference here is that we use the parametrized expressions for the GW flux and conserved energy given by Eq. (4.2.3) and (4.3.1) respectively. Further we consider the amplitude to be at the leading quadrupolar order following chapter 3. The standard *restricted* PN waveform in frequency domain, thus, reads as

$$\tilde{h}_S(f)=\mathcal{A}\mu_2\,f^{-7/6}e^{i\psi_S(f)}, \tag{4.3.2}$$

with the amplitude $\mathcal{A} = \mathcal{M}_c^{5/6}/\sqrt{30}\pi^{2/3}D_L$; Chirp mass, $\mathcal{M}_c = (m_1 m_2)^{3/5}/(m_1+m_2)^{1/5}$ and the luminosity distance to be D_L. In the case of LISA, to account for its triangular geometry, we multiply the gravitational waveform by a factor of $\sqrt{3}/2$ while calculating the Fisher matrix for LISA [134]. The parametrized multipolar phasing, $\psi_S(f)$, has the same structure as that of the energy flux (see Eq. (4.2.3)). Schematically the parametrized phasing formula can be written as,

$$\psi_S(f) = 2\pi f t_c - \phi_c - \frac{\pi}{4} + \frac{3\alpha_0}{128\eta v^5 \mu_2^2}\Big[\psi_{\rm NS}(f) + \psi_{\rm SO}(f) + \psi_{\rm SS}(f)\Big], \tag{4.3.3}$$

where the parametrized non-spinning part, $\psi_{\rm NS}(f)$ is given by,

$$\begin{aligned}
\psi_{\rm NS} = {} & 1 + v^2\bigg(\frac{2140}{189} - \frac{1100}{189}\eta - \hat\alpha_2\bigg[\frac{10}{3} + \frac{10}{27}\eta\bigg] + \hat\mu_3^2\bigg[-\frac{6835}{2268} + \frac{6835}{567}\eta\bigg] + \hat\epsilon_2{}^2\bigg[-\frac{5}{81} + \frac{20}{81}\eta\bigg]\bigg) \\
& -16\pi v^3 + v^4\bigg(\frac{295630}{1323} - \frac{267745}{2646}\eta + \frac{32240}{1323}\eta^2 + \hat\alpha_2\bigg[-\frac{535}{7} + \frac{1940}{63}\eta + \frac{275}{63}\eta^2\bigg] \\
& + \hat\alpha_4\bigg[-\frac{405}{4} + \frac{285}{4}\eta - \frac{5}{4}\eta^2\bigg] + \hat\mu_3^2\bigg[-\frac{104815}{3528} + \frac{8545}{63}\eta - \frac{29630}{441}\eta^2 + \hat\alpha_2\bigg(\frac{6835}{336} - \frac{34175}{432}\eta \\
& - \frac{6835}{756}\eta^2\bigg)\bigg] + \hat\mu_3^2\hat\epsilon_2{}^2\bigg[\frac{6835}{9072} - \frac{6835}{1134}\eta + \frac{6835\eta^2}{567}\bigg] + \hat\mu_3^4\bigg[\frac{9343445}{508032} - \frac{9343445}{63504}\eta + \frac{9343445}{31752}\eta^2\bigg] \\
& + \hat\mu_4^2\bigg[-\frac{89650}{3969} + \frac{179300}{1323}\eta - \frac{89650}{441}\eta^2\bigg] + \hat\epsilon_2{}^2\bigg[-\frac{1885}{756} + \frac{695}{63}\eta - \frac{800}{189}\eta^2 + \hat\alpha_2\bigg(\frac{5}{12} - \frac{175}{108}\eta \\
& - \frac{5}{27}\eta^2\bigg)\bigg] + \hat\epsilon_2{}^4\bigg[\frac{5}{648} - \frac{5}{81}\eta + \frac{10}{81}\eta^2\bigg] + \hat\epsilon_3{}^2\bigg[-\frac{50}{63} + \frac{100}{21}\eta - \frac{50}{7}\eta^2\bigg]\bigg) \\
& + \pi v^5\bigg(3\log\bigg[\frac{v}{v_{\rm LSO}}\bigg] + 1\bigg)\bigg(\frac{80}{189}\big[214 - 131\eta\big] - \frac{80}{27}\hat\alpha_2\big[9+\eta\big] - \frac{9115}{756}\hat\mu_3^2\big[1-4\eta\big] - \frac{20}{27}\hat\epsilon_2{}^2\big[1-4\eta\big]\bigg) \\
& + v^6\bigg(\frac{36847016}{509355} - \frac{640}{3}\pi^2 - \frac{6848}{21}\gamma_E - \frac{6848}{21}\log[4v] + \bigg[\frac{28398155}{67914} + \frac{205}{12}\pi^2\bigg]\eta - \frac{563225}{3773}\eta^2 \\
& + \frac{3928700}{305613}\eta^3 + \hat\alpha_2\bigg[\frac{295630}{441} - \frac{1818445}{7938}\eta + \frac{312575}{7938}\eta^2 + \frac{32240}{3969}\eta^3\bigg] + \hat\alpha_4\bigg[\frac{14445}{14} - \frac{8795}{7}\eta \\
& + \frac{8105}{21}\eta^2 - \frac{275}{42}\eta^3\bigg] + \hat\alpha_6\bigg[\frac{3375}{4} + \bigg(-\frac{172225}{36} + \frac{1025}{6}\pi^2\bigg)\eta + \frac{775}{6}\eta^2 + \frac{175}{324}\eta^3\bigg] \\
& + \hat\mu_3^2\bigg[\frac{732782515}{3667356} - \frac{1061322545}{1222452}\eta + \frac{1027073335}{3667356}\eta^2 - \frac{15723035}{916839}\eta^3 + \hat\alpha_2\bigg(-\frac{104815}{1176} \\
& + \frac{4201865}{10584}\eta - \frac{206855}{1323}\eta^2 - \frac{29630}{1323}\eta^3\bigg) + \hat\alpha_4\bigg(-\frac{61515}{224} + \frac{868045}{672}\eta - \frac{1565215}{2016}\eta^2 + \frac{6835}{504}\eta^3\bigg)\bigg] \\
& + \hat\mu_3^2\hat\epsilon_2{}^2\bigg[-\frac{1742995}{190512} + \frac{1045805}{13608}\eta - \frac{2091650}{11907}\eta^2 + \frac{697310}{11907}\eta^3 + \hat\alpha_2\bigg(\frac{6835}{3024} - \frac{485285}{27216}\eta
\end{aligned}$$

$$
\begin{aligned}
&+\frac{116195}{3402}\eta^2+\frac{6835}{1701}\eta^3\Big)\Big]+\hat{\mu}_3^2\hat{\epsilon}_2^{4}\Big[\frac{6835}{108864}-\frac{6835}{9072}\eta+\frac{6835}{2268}\eta^2-\frac{6835}{1701}\eta^3\Big]+\hat{\mu}_3^2\hat{\epsilon}_3^{2}\Big[-\frac{34175}{7938}\\
&+\frac{170875}{3969}\eta-\frac{375925}{2646}\eta^2+\frac{68350}{441}\eta^3\Big]+\hat{\mu}_3^2\hat{\mu}_4^2\Big[-\frac{61275775}{500094}+\frac{306378875}{250047}\eta-\frac{674033525}{166698}\eta^2\\
&+\frac{122551550}{27783}\eta^3\Big]+\hat{\mu}_3^4\Big[\frac{140055985}{5334336}-\frac{1148286835}{5334336}\eta+\frac{307950925}{666792}\eta^2-\frac{27838955}{333396}\eta^3\\
&+\hat{\alpha}_2\Big(\frac{9343445}{169344}-\frac{663384595}{1524096}\eta+\frac{158838565}{190512}\eta^2+\frac{9343445}{95256}\eta^3\Big)\Big]+\hat{\mu}_3^4\hat{\epsilon}_2^{2}\Big[\frac{9343445}{3048192}\\
&-\frac{9343445}{254016}\eta+\frac{9343445}{63504}\eta^2-\frac{9343445}{47628}\eta^3\Big]+\hat{\mu}_3^6\Big[\frac{12772489315}{256048128}-\frac{12772489315}{21337344}\eta\\
&+\frac{12772489315}{5334336}\eta^2-\frac{12772489315}{4000752}\eta^3\Big]+\hat{\mu}_4^2\Big[-\frac{24426860}{916839}+\frac{62508560}{305613}\eta-\frac{12980600}{33957}\eta^2\\
&+\frac{286700}{11319}\eta^3+\hat{\alpha}_2\Big(-\frac{89650}{1323}+\frac{4751450}{11907}\eta-\frac{2241250}{3969}\eta^2-\frac{89650}{1323}\eta^3\Big)\Big]+\hat{\mu}_4^2\hat{\epsilon}_2^{2}\Big[-\frac{89650}{35721}\\
&+\frac{896500}{35721}\eta-\frac{986150}{11907}\eta^2+\frac{358600\eta^3}{3969}\Big]+\hat{\mu}_5^2\Big[\frac{1002569}{12474}-\frac{4010276}{6237}\eta+\frac{10025690}{6237}\eta^2\\
&-\frac{8020552}{6237}\eta^3\Big]+\hat{\epsilon}_2^{2}\Big[\frac{6134935}{190512}-\frac{2353285}{15876}\eta+\frac{550075}{6804}\eta^2-\frac{150845}{11907}\eta^3+\hat{\alpha}_2\Big(-\frac{1885}{252}\\
&+\frac{73175}{2268}\eta-\frac{1705}{189}\eta^2-\frac{800}{567}\eta^3\Big)+\hat{\alpha}_4\Big(-\frac{45}{8}+\frac{635}{24}\eta-\frac{1145}{72}\eta^2+\frac{5}{18}\eta^3\Big)\Big]+\hat{\epsilon}_2^{2}\hat{\epsilon}_3^{2}\Big[-\frac{50}{567}\\
&+\frac{500}{567}\eta-\frac{550}{189}\eta^2+\frac{200}{63}\eta^3\Big]+\hat{\epsilon}_2^{4}\Big[-\frac{25}{126}+\frac{3775}{2268}\eta-\frac{2150}{567}\eta^2+\frac{100}{81}\eta^3+\hat{\alpha}_2\Big(\frac{5}{216}-\frac{355}{1944}\eta\\
&+\frac{85}{243}\eta^2+\frac{10}{243}\eta^3\Big)\Big]+\hat{\epsilon}_2^{6}\Big[\frac{5}{11664}-\frac{5}{972}\eta+\frac{5}{243}\eta^2-\frac{20}{729}\eta^3\Big]+\hat{\epsilon}_3^{2}\Big[\frac{37180}{3969}-\frac{235640}{3969}\eta\\
&+\frac{420200}{3969}\eta^2-\frac{47900}{1323}\eta^3+\hat{\alpha}_2\Big(-\frac{50}{21}+\frac{2650}{189}\eta-\frac{1250}{63}\eta^2-\frac{50}{21}\eta^3\Big)\Big]+\hat{\epsilon}_4^{2}\Big[\frac{5741}{1764}-\frac{11482}{441}\eta\\
&+\frac{28705}{441}\eta^2-\frac{22964}{441}\eta^3\Big]\Big)+\pi v^7\Big(\frac{2365040}{1323}-\frac{1300930}{1323}\eta+\frac{400930}{1323}\eta^2+\hat{\alpha}_2\Big[-\frac{4280}{7}+\frac{19300}{63}\eta\\
&+\frac{2620}{63}\eta^2\Big]+\hat{\alpha}_4\big(-810+570\eta-10\eta^2\big)+\hat{\mu}_3^2\Big[-\frac{69905}{588}+\frac{191495}{336}\eta-\frac{73995}{196}\eta^2\\
&+\hat{\alpha}_2\Big(\frac{9115}{112}-\frac{45575}{144}\eta-\frac{9115}{252}\eta^2\Big)\Big]+\hat{\mu}_3^2\hat{\epsilon}_2^{2}\Big[\frac{54685}{9072}-\frac{54685}{1134}\eta+\frac{54685}{567}\eta^2\Big]\\
&+\hat{\mu}_3^4\Big[\frac{6835}{254016}-\frac{6835}{31752}\eta+\frac{6835}{15876}\eta^2\Big]+\hat{\mu}_4^2\Big[-\frac{400}{3969}+\frac{800}{1323}\eta\\
&-\frac{400}{441}\eta^2\Big]+\hat{\epsilon}_2^{2}\Big[-\frac{1885}{63}+\frac{2815}{21}\eta-\frac{3620}{63}\eta^2+\hat{\alpha}_2\Big(5-\frac{175}{9}\eta-\frac{20}{9}\eta^2\Big)\Big]\\
&+\hat{\epsilon}_3^{2}\Big[-\frac{400}{63}+\frac{800}{21}\eta-\frac{400}{7}\eta^2\Big]+\hat{\epsilon}_2^{4}\Big[\frac{10}{81}-\frac{80}{81}\eta+\frac{160}{81}\eta^2\Big]\Big).
\end{aligned}
\tag{4.3.4}
$$

Now to obtain the additional contribution to the parametrized TaylorF2 phasing for aligned spin binaries, we use the conventional notations for the spin variables $(\boldsymbol{\chi_1}, \boldsymbol{\chi_2})$, with the following re-definitions,

$$\boldsymbol{\chi_1} = Gm_1^2\mathbf{S}_1, \tag{4.3.5}$$

$$\boldsymbol{\chi_2} = Gm_2^2\mathbf{S}_2. \tag{4.3.6}$$

Furthermore, we use $\chi_s = (\chi_1+\chi_2)/2$ and $\chi_a = (\chi_1-\chi_2)/2$ to present the phasing formula, where χ_1 and χ_2 are the projections of $\boldsymbol{\chi_1}$ and $\boldsymbol{\chi_2}$ along the orbital angular momentum, respectively. These spin variables have the following relations,

$$S_L = Gm^2[\delta\chi_a + (1-2\eta)\chi_s]\,, \tag{4.3.7}$$

$$\Sigma_L = -Gm^2[\delta\chi_s + \chi_a]\,. \tag{4.3.8}$$

As mentioned earlier, we do not account for the partial contribution due to the spin-spin interactions to the phasing formula at the 3.5PN order. Finally we write down the expressions for $\psi_{\rm SO}$ and $\psi_{\rm SS}$ below,

$$\begin{aligned}
\psi_{\rm SO} \;=\;& v^3\Bigg\{\Bigg[\frac{32}{3}+\frac{80}{3}\hat{\alpha}_3+\frac{1}{3}\hat{\epsilon}_2^2-\Bigg(\frac{32}{3}+\frac{40}{3}\hat{\alpha}_3+\frac{4}{3}\hat{\epsilon}_2^2\Bigg)\eta\Bigg]\chi_s+\Bigg[\frac{32}{3}+\frac{80}{3}\hat{\alpha}_3+\frac{1}{3}\hat{\epsilon}_2^2\Bigg]\delta\chi_a\Bigg\}\\
&+v^5\Bigg(1+3\log[v/v_{\rm LSO}]\Bigg)\Bigg\{\Bigg[-\frac{64160}{567}+\frac{93920}{567}\eta-\frac{1760}{189}\eta^2+\hat{\alpha}_2\Bigg(\frac{160}{9}-\frac{1280}{81}\eta-\frac{160}{81}\eta^2\Bigg)\\
&+\hat{\alpha}_3\Bigg(-\frac{85600}{567}+\frac{12400}{81}\eta-\frac{22000}{567}\eta^2\Bigg)+\hat{\alpha}_5\Bigg(-\frac{1120}{9}+\frac{16940}{81}\eta-\frac{280}{81}\eta^2\Bigg)+\Bigg(\frac{13670}{1701}\\
&-\frac{58090}{1701}\eta+\frac{13640}{1701}\eta^2+\hat{\alpha}_3\Bigg[\frac{68350}{1701}-\frac{34175}{189}\eta+\frac{136700}{1701}\eta^2\Bigg]\Bigg)\hat{\mu}_3^2+\Bigg(\frac{6835}{6804}-\frac{13670}{1701}\eta\\
&+\frac{27340}{1701}\eta^2\Bigg)\hat{\mu}_3^2\hat{\epsilon}_2^2+\Bigg(-\frac{1465}{486}+\frac{23230}{1701}\eta-\frac{10880}{1701}\eta^2+\hat{\alpha}_2\Bigg[\frac{5}{9}-\frac{175}{81}\eta-\frac{20}{81}\eta^2\Bigg]+\hat{\alpha}_3\Bigg[\frac{200}{243}-\frac{100}{27}\eta\\
&+\frac{400}{243}\eta^2\Bigg]\Bigg)\hat{\epsilon}_2^2+\Bigg(\frac{5}{243}-\frac{40}{243}\eta+\frac{80}{243}\eta^2\Bigg)\hat{\epsilon}_2^4+\Bigg(\frac{1600}{567}\eta-\frac{1600}{189}\eta^2\Bigg)\hat{\epsilon}_3^2\Bigg]\chi_s+\Bigg[-\frac{64160}{567}+\frac{17440}{567}\eta\\
&+\hat{\alpha}_2\Bigg(\frac{160}{9}+\frac{160}{81}\eta\Bigg)-\hat{\alpha}_3\Bigg(\frac{85600}{567}-\frac{44000}{567}\eta\Bigg)-\hat{\alpha}_5\Bigg(\frac{1120}{9}-\frac{4340}{81}\eta\Bigg)+\Bigg(\frac{13670}{1701}-\frac{23930}{1701}\eta+
\end{aligned}$$

$$
\begin{aligned}
&\hat{\alpha}_3\left[\frac{68350}{1701}-\frac{273400}{1701}\eta\right]\Big)\hat{\mu}_3^2+\left(\frac{6835}{6804}-\frac{6835}{1701}\eta\right)\hat{\mu}_3^2\hat{\epsilon}_2^2+\Big(-\frac{1465}{486}+\frac{4520}{1701}\eta+\hat{\alpha}_2\left[\frac{5}{9}+\frac{5}{81}\eta\right]\\
&+\hat{\alpha}_3\left[\frac{200}{243}-\frac{800}{243}\eta\right]\Big)\hat{\epsilon}_2^2+\left(\frac{5}{243}-\frac{20}{243}\eta\right)\hat{\epsilon}_2^4\Big]\delta\chi_a\Big\}+\pi v^6\Big\{\Big[\frac{640}{3}-\frac{640}{3}\eta+\hat{\alpha}_3\left(\frac{1600}{3}-\frac{800}{3}\eta\right)\\
&+(10-40\eta)\hat{\epsilon}_2^2\Big]\chi_s+\left[\frac{640}{3}+10\hat{\epsilon}_2^2+\frac{1600}{3}\hat{\alpha}_3\right]\delta\chi_a\Big\}+v^7\Big\{\Big[-\frac{175520}{63}+\frac{7871090}{1323}\eta-\frac{4100}{3}\eta^2\\
&-\frac{199520}{1323}\eta^3+\hat{\alpha}_2\left(\frac{16040}{21}-\frac{195280}{189}\eta-\frac{11600}{189}\eta^2+\frac{440}{63}\eta^3\right)+\hat{\alpha}_3\Big(-\frac{11825200}{3969}+\frac{11267500}{3969}\eta\\
&-\frac{1322350}{1323}\eta^2+\frac{644800}{3969}\eta^3\Big)+\hat{\alpha}_4\left(540-920\eta+\frac{1160}{3}\eta^2-\frac{20}{3}\eta^3\right)+\hat{\alpha}_5\Big(-\frac{8560}{3}+\frac{169070}{27}\eta\\
&-\frac{68690}{27}\eta^2+\frac{1100}{27}\eta^3\Big)+\hat{\alpha}_7\left(-2430+\frac{16785}{2}\eta-2580\eta^2-15\eta^3\right)+\hat{\mu}_3^2\Big(\frac{58105}{189}-\frac{22900195}{15876}\eta\\
&+\frac{8056835}{10584}\eta^2+\frac{2844815}{7938}\eta^3\Big)+\hat{\mu}_3^2\hat{\alpha}_2\left(-\frac{6835}{126}+\frac{127285}{567}\eta-\frac{32335}{1134}\eta^2-\frac{3410}{567}\eta^3\right)\\
&+\hat{\mu}_3^2\hat{\alpha}_3\left(\frac{524075}{1323}-\frac{5309275}{2646}\eta+\frac{2381500}{1323}\eta^2-\frac{592600}{1323}\eta^3\right)+\hat{\mu}_3^2\hat{\alpha}_5\Big(\frac{6835}{9}-\frac{2795515}{648}\eta\\
&+\frac{20505}{4}\eta^2-\frac{6835}{81}\eta^3\Big)+\hat{\mu}_3^2\hat{\epsilon}_2^2\left(\frac{3260435}{127008}-\frac{7054105}{31752}\eta+\frac{4326905}{7938}\eta^2-\frac{355490}{1323}\eta^3\right)\\
&+\hat{\mu}_3^2\hat{\epsilon}_2^2\hat{\alpha}_2\left(-\frac{6835}{1008}+\frac{485285}{9072}\eta-\frac{116195}{1134}\eta^2-\frac{6835}{567}\eta^3\right)+\hat{\mu}_3^2\hat{\epsilon}_2^2\hat{\alpha}_3\Big(-\frac{34175}{3402}+\frac{580975}{6804}\eta\\
&-\frac{341750}{1701}\eta^2+\frac{136700}{1701}\eta^3\Big)+\hat{\mu}_3^2\hat{\epsilon}_2^4\left(-\frac{6835}{18144}+\frac{6835}{1512}\eta-\frac{6835}{378}\eta^2+\frac{13670}{567}\eta^3\right)\\
&+\hat{\mu}_3^2\hat{\epsilon}_3^2\left(-\frac{136700}{3969}\eta+\frac{136700}{567}\eta^2-\frac{546800}{1323}\eta^3\right)+\hat{\mu}_3^4\left(-\frac{129865}{1764}\eta+\frac{259730}{441}\eta^2-\frac{519460}{441}\eta^3\right)\\
&+\hat{\mu}_3^4\hat{\epsilon}_2^2\left(-\frac{9343445}{1016064}+\frac{9343445}{84672}\eta-\frac{9343445}{21168}\eta^2+\frac{9343445}{15876}\eta^3\right)+\hat{\mu}_3^4\hat{\alpha}_3\Big(-\frac{46717225}{190512}\\
&+\frac{794192825}{381024}\eta-\frac{233586125}{47628}\eta^2+\frac{46717225}{23814}\eta^3\Big)+\hat{\mu}_4^2\left(\frac{289760}{11907}\eta-\frac{205600}{567}\eta^2+\frac{1149440}{1323}\eta^3\right)\\
&+\hat{\mu}_4^2\hat{\alpha}_3\left(\frac{3586000}{11907}-\frac{23309000}{11907}\eta+\frac{14344000}{3969}\eta^2-\frac{1793000}{1323}\eta^3\right)+\hat{\mu}_4^2\hat{\epsilon}_2^2\Big(\frac{89650}{11907}-\frac{896500}{11907}\eta\\
&+\frac{986150}{3969}\eta^2-\frac{358600}{1323}\eta^3\Big)+\hat{\epsilon}_2^2\left(-\frac{1193245}{15876}+\frac{938855}{2646}\eta-\frac{7469165}{31752}\eta^2+\frac{83995}{1134}\eta^3\right)\\
&+\hat{\epsilon}_2^2\hat{\alpha}_2\left(\frac{1465}{72}-\frac{407885}{4536}\eta+\frac{5335}{162}\eta^2+\frac{2720}{567}\eta^3\right)+\hat{\epsilon}_2^2\hat{\alpha}_3\Big(\frac{18850}{567}-\frac{92825}{567}\eta+\frac{73700}{567}\eta^2\\
&-\frac{16000}{567}\eta^3\Big)+\hat{\epsilon}_2^2\hat{\alpha}_4\left(\frac{135}{8}-\frac{635}{8}\eta+\frac{1145}{24}\eta^2-\frac{5}{6}\eta^3\right)+\hat{\epsilon}_2^2\hat{\alpha}_5\left(\frac{140}{9}-\frac{14315}{162}\eta+105\eta^2-\frac{140}{81}\eta^3\right)\\
&+\hat{\epsilon}_2^2\hat{\epsilon}_3^2\left(\frac{50}{189}-\frac{1900}{567}\eta+\frac{7750}{567}\eta^2-\frac{3400}{189}\eta^3\right)+\hat{\epsilon}_2^4\left(\frac{1745}{1512}-\frac{1585}{162}\eta+\frac{12970}{567}\eta^2-\frac{5000}{567}\eta^3\right)
\end{aligned}
$$

$$
\begin{aligned}
&+\hat{\epsilon}_2^4\hat{\alpha}_2\bigg(-\frac{5}{36}+\frac{355}{324}\eta-\frac{170}{81}\eta^2-\frac{20}{81}\eta^3\bigg)+\hat{\epsilon}_2^4\hat{\alpha}_3\bigg(-\frac{25}{243}+\frac{425}{486}\eta-\frac{500}{243}\eta^2+\frac{200}{243}\eta^3\bigg)\\
&+\hat{\epsilon}_2^6\bigg(-\frac{5}{1296}+\frac{5}{108}\eta-\frac{5}{27}\eta^2+\frac{20}{81}\eta^3\bigg)+\hat{\epsilon}_3^2\bigg(\frac{258520}{3969}\eta-\frac{966200}{3969}\eta^2+\frac{612800}{3969}\eta^3\bigg)\\
&+\hat{\epsilon}_3^2\hat{\alpha}_2\bigg(-\frac{400}{21}\eta+\frac{10400}{189}\eta^2+\frac{400}{63}\eta^3\bigg)+\hat{\epsilon}_3^2\hat{\alpha}_3\bigg(\frac{2000}{189}-\frac{13000}{189}\eta+\frac{8000}{63}\eta^2-\frac{1000}{21}\eta^3\bigg)\\
&+\hat{\epsilon}_4^2\bigg(\frac{28705}{1764}\eta-\frac{28705}{294}\eta^2+\frac{57410}{441}\eta^3\bigg)\bigg]\chi_s+\bigg[-\frac{175520}{63}+\frac{3039410}{1323}\eta+\frac{29300}{1323}\eta^2\\
&+\hat{\alpha}_2\bigg(\frac{16040}{21}-\frac{23200}{189}\eta-\frac{4360}{189}\eta^2\bigg)+\hat{\alpha}_3\bigg(-\frac{11825200}{3969}+\frac{5354900}{3969}\eta-\frac{1289600}{3969}\eta^2\bigg)\\
&+\hat{\alpha}_4\bigg(540-380\eta+\frac{20}{3}\eta^2\bigg)+\hat{\alpha}_5\bigg(-\frac{8560}{3}+\frac{72770}{27}\eta-\frac{17050}{27}\eta^2\bigg)+\hat{\alpha}_7\bigg(-2430+\frac{9495}{2}\eta\\
&-105\eta^2\bigg)+\hat{\mu}_3^2\bigg(\frac{58105}{189}-\frac{15599425}{15876}\eta-\frac{5525}{24}\eta^2\bigg)+\hat{\mu}_3^2\hat{\alpha}_2\bigg(-\frac{6835}{126}+\frac{50425}{567}\eta+\frac{11965}{1134}\eta^2\bigg)\\
&+\hat{\mu}_3^2\hat{\alpha}_3\bigg(\frac{524075}{1323}-\frac{341800}{189}\eta+\frac{1185200}{1323}\eta^2\bigg)+\hat{\mu}_3^2\hat{\alpha}_5\bigg(\frac{6835}{9}-\frac{2180365}{648}\eta+\frac{211885}{162}\eta^2\bigg)\\
&+\hat{\mu}_3^2\hat{\epsilon}_2^2\bigg(\frac{3260435}{127008}-\frac{2245385}{15876}\eta+\frac{1230335}{7938}\eta^2\bigg)+\hat{\mu}_3^2\hat{\epsilon}_2^2\hat{\alpha}_2\bigg(-\frac{6835}{1008}+\frac{34175}{1296}\eta+\frac{6835}{2268}\eta^2\bigg)\\
&+\hat{\mu}_3^2\hat{\epsilon}_2^2\hat{\alpha}_3\bigg(-\frac{34175}{3402}+\frac{136700}{1701}\eta-\frac{273400}{1701}\eta^2\bigg)+\hat{\mu}_3^2\hat{\epsilon}_2^4\bigg(-\frac{6835}{18144}+\frac{6835}{2268}\eta-\frac{6835}{1134}\eta^2\bigg)\\
&+\hat{\mu}_3^4\bigg(-\frac{7005875}{31752}\eta+\frac{7005875}{7938}\eta^2\bigg)+\hat{\mu}_3^4\hat{\alpha}_3\bigg(-\frac{46717225}{190512}+\frac{46717225}{23814}\eta-\frac{46717225}{11907}\eta^2\bigg)\\
&+\hat{\mu}_3^4\hat{\epsilon}_2^2\bigg(-\frac{9343445}{1016064}+\frac{9343445}{127008}\eta-\frac{9343445}{63504}\eta^2\bigg)+\hat{\mu}_4^2\bigg(\frac{31840}{147}\eta-\frac{31840}{49}\eta^2\bigg)\\
&+\hat{\mu}_4^2\hat{\alpha}_3\bigg(\frac{3586000}{11907}-\frac{7172000}{3969}\eta+\frac{3586000}{1323}\eta^2\bigg)+\hat{\mu}_4^2\hat{\epsilon}_2^2\bigg(\frac{89650}{11907}-\frac{179300}{3969}\eta+\frac{89650}{1323}\eta^2\bigg)\\
&+\hat{\epsilon}_2^2\bigg(-\frac{1193245}{15876}+\frac{65255}{882}\eta-\frac{1742365}{31752}\eta^2\bigg)+\hat{\epsilon}_2^2\hat{\alpha}_2\bigg(\frac{1465}{72}-\frac{71105}{4536}\eta-\frac{1130}{567}\eta^2\bigg)\\
&+\hat{\epsilon}_2^2\hat{\alpha}_3\bigg(\frac{18850}{567}-\frac{27800}{189}\eta+\frac{32000}{567}\eta^2\bigg)+\hat{\epsilon}_2^2\hat{\alpha}_4\bigg(\frac{135}{8}-\frac{95}{8}\eta+\frac{5}{24}\eta^2\bigg)+\hat{\epsilon}_2^2\hat{\alpha}_5\bigg(\frac{140}{9}-\frac{11165}{162}\eta\\
&+\frac{2170}{81}\eta^2\bigg)+\hat{\epsilon}_2^2\hat{\epsilon}_3^2\bigg(\frac{50}{189}-\frac{100}{63}\eta+\frac{50}{21}\eta^2\bigg)+\hat{\epsilon}_2^4\bigg(\frac{1745}{1512}-\frac{50}{9}\eta+\frac{710}{189}\eta^2\bigg)+\hat{\epsilon}_2^4\hat{\alpha}_2\bigg(-\frac{5}{36}+\frac{175}{324}\eta\\
&+\frac{5}{81}\eta^2\bigg)+\hat{\epsilon}_2^4\hat{\alpha}_3\bigg(-\frac{25}{243}+\frac{200}{243}\eta-\frac{400}{243}\eta^2\bigg)-\hat{\epsilon}_2^6\bigg(\frac{5}{1296}-\frac{5}{162}\eta+\frac{5}{81}\eta^2\bigg)+\hat{\epsilon}_3^2\bigg(\frac{3800}{189}\eta\\
&-\frac{3800}{63}\eta^2\bigg)+\hat{\epsilon}_3^2\hat{\alpha}_3\bigg(\frac{2000}{189}-\frac{4000}{63}\eta+\frac{2000}{21}\eta^2\bigg)-\hat{\epsilon}_4^2\bigg(\frac{28705}{1764}\eta-\frac{28705}{882}\eta^2\bigg)\bigg]\delta\chi_a\bigg\}
\end{aligned}
\tag{4.3.9}
$$

$$
\begin{aligned}
\psi_{\rm SS}(f) \quad &= v^4\Bigg\{\Bigg[-10\kappa_+ - \frac{5}{8}\hat{\epsilon}_2^2 - 15\kappa_+\hat{\alpha}_4 - \delta\kappa_-\Big(10 + 15\hat{\alpha}_4\Big) + \Big(-40 + 20\kappa_+ + \frac{5}{2}\hat{\epsilon}_2^2 - \hat{\alpha}_4[60 \\
&-30\kappa_+]\Big)\eta\Bigg]\chi_s^2 + \Bigg[-20\kappa_- - 30\kappa_-\hat{\alpha}_4 - \delta\Big(20\kappa_+ + 30\kappa_+\hat{\alpha}_4 + \frac{5}{4}\hat{\epsilon}_2^2\Big) + \eta\kappa_-\Big(40 + 60\hat{\alpha}_4\Big)\Bigg]\chi_s\chi_a \\
&+\Bigg[-10\kappa_+ - \frac{5}{8}\hat{\epsilon}_2^2 - 15\kappa_+\hat{\alpha}_4 - \delta\kappa_-\Big(10 + 15\hat{\alpha}_4\Big) + \Big(40 + 20\kappa_+ + \hat{\alpha}_4[60 + 30\kappa_+]\Big)\eta\Bigg]\chi_a^2\Bigg\} \\
&+v^6\Bigg\{\Bigg[-\frac{1120}{9} + \frac{1150}{7}\kappa_+ + \kappa_-\delta\Big(\frac{1150}{7} - \frac{690}{7}\eta\Big) + \Big(\frac{38600}{63} - \frac{2990}{7}\kappa_+\Big)\eta - \Big(\frac{3880}{21} - \frac{1940}{21}\kappa_+\Big)\eta^2 \\
&+\frac{1600}{63}\eta^2\hat{\epsilon}_3^2 + \hat{\alpha}_2\Big(-30\kappa_+ - \Big[30 + \frac{10}{3}\eta\Big]\delta\kappa_- + \Big[-120 + \frac{170}{3}\kappa_+\Big]\eta + \Big[-\frac{40}{3} + \frac{20}{3}\kappa_+\Big]\eta^2\Big) \\
&-\hat{\alpha}_3\Big(\frac{3200}{9} - \frac{1600}{3}\eta + \frac{1600}{9}\eta^2\Big) + \hat{\alpha}_4\Big(\frac{1070}{7}\kappa_+ + \Big[\frac{1070}{7} - \frac{550}{7}\eta\Big]\delta\kappa_- + \Big[\frac{4280}{7} - \frac{2690}{7}\kappa_+\Big]\eta \\
&-\Big[\frac{2200}{7} - \frac{1100}{7}\kappa_+\Big]\eta^2\Big) + \hat{\alpha}_6\Big(-\frac{1600}{9} + \frac{700}{3}\kappa_+ + \Big[\frac{700}{3} - \frac{500}{3}\eta\Big]\delta\kappa_- + \Big[\frac{1600}{9} - \frac{1900}{3}\kappa_+\Big]\eta \\
&+\Big[\frac{2000}{9} + \frac{200}{3}\kappa_+\Big]\eta^2\Big) + \hat{\mu}_3^2\Big(-\frac{95}{7}\kappa_+ + \Big[-\frac{95}{7} + \frac{13675}{252}\eta\Big]\delta\kappa_- + \Big[-\frac{6835}{126} + \frac{20515}{252}\kappa_+\Big]\eta \\
&+\Big[\frac{13670}{63} - \frac{6835}{63}\kappa_+\Big]\eta^2\Big) + \hat{\mu}_3^2\hat{\alpha}_4\Big(-\frac{6835}{168}\kappa_+ - \Big[\frac{6835}{168} - \frac{6835}{42}\eta\Big]\delta\kappa_- + \Big[\frac{13670}{21} - \frac{6835}{21}\kappa_+\Big]\eta^2\Big) \\
&-\hat{\mu}_3^2\hat{\epsilon}_2^2\Big(\frac{6835}{2016} - \frac{6835}{252}\eta + \frac{6835}{126}\eta^2\Big) + \hat{\epsilon}_2^2\Big(\frac{470}{63} - \frac{5}{6}\kappa_+ - \Big[\frac{5}{6} - \frac{20}{9}\eta\Big]\delta\kappa_- - \Big[\frac{730}{21} - \frac{35}{9}\kappa_+\Big]\eta \\
&+\Big[\frac{1240}{63} - \frac{20}{9}\kappa_+\Big]\eta^2\Big) - \hat{\epsilon}_2^2\hat{\alpha}_2\Big(\frac{15}{8} - \frac{175}{24}\eta - \frac{5}{6}\eta^2\Big) - \hat{\epsilon}_2^2\hat{\alpha}_3\Big(\frac{100}{9} - 50\eta + \frac{200}{9}\eta^2\Big) + \hat{\epsilon}_2^2\hat{\alpha}_4\Big(-\frac{5}{6}\kappa_+ \\
&-\Big[\frac{5}{6} - \frac{10}{3}\eta\Big]\delta\kappa_- - \Big[\frac{10}{3} - 5\kappa_+\Big]\eta + \Big[\frac{40}{3} - \frac{20}{3}\kappa_+\Big]\eta^2\Big) - \hat{\epsilon}_2^4\Big(\frac{5}{24} - \frac{5}{3}\eta + \frac{10}{3}\eta^2\Big)\Bigg]\chi_s^2 \\
&+\Bigg[\Big(\frac{2300}{7} - \frac{5980}{7}\eta + \frac{3880}{21}\eta^2\Big)\kappa_- + \Big(-\frac{2240}{9} + \frac{2300}{7}\kappa_+ + \Big(\frac{560}{9} - \frac{1380}{7}\kappa_+\Big)\eta\Big)\delta \\
&+\hat{\alpha}_2\Big(\Big[-60 + \frac{340}{3}\eta + \frac{40}{3}\eta^2\Big]\kappa_- - \Big(60 + \frac{20}{3}\eta\Big)\delta\kappa_+\Big) - \hat{\alpha}_3\delta\Big(\frac{6400}{9} - \frac{1600}{3}\eta\Big) + \hat{\alpha}_4\Big(\Big[\frac{2140}{7} \\
&-\frac{5380}{7}\eta + \frac{2200}{7}\eta^2\Big]\kappa_- + \Big[\frac{2140}{7} - \frac{1100}{7}\eta\Big]\kappa_+\delta\Big) + \hat{\alpha}_6\Big(\Big[\frac{1400}{3} - \frac{3800}{3}\eta + \frac{400}{3}\eta^2\Big]\kappa_- \\
&+\Big[-\frac{3200}{9} + \frac{1400}{3}\kappa_+ - \Big(\frac{5600}{9} + \frac{1000}{3}\kappa_+\Big)\eta\Big]\delta\Big) + \hat{\mu}_3^2\Big(\Big[-\frac{190}{7} + \frac{20515}{126}\eta - \frac{13670}{63}\eta^2\Big]\kappa_- \\
&+\Big[-\frac{190}{7} + \frac{13675}{126}\eta\Big]\delta\kappa_+\Big) + \hat{\mu}_3^2\hat{\alpha}_4\Big(\Big[-\frac{6835}{84} + \frac{6835}{14}\eta - \frac{13670}{21}\eta^2\Big]\kappa_- - \Big[\frac{6835}{84} - \frac{6835}{21}\eta\Big]\delta\kappa_+\Big) \\
&-\hat{\mu}_3^2\hat{\epsilon}_2^2\delta\Big(\frac{6835}{1008} - \frac{6835}{252}\eta\Big) + \hat{\epsilon}_2^2\Big(\Big[-\frac{5}{3} + \frac{70}{9}\eta - \frac{40}{9}\eta^2\Big]\kappa_- + \Big[\frac{940}{63} - \frac{5}{3}\kappa_+ - \Big(\frac{650}{63} - \frac{40}{9}\kappa_+\Big)\eta\Big]\delta\Big)
\end{aligned}
$$

$$
\begin{aligned}
&-\hat{\epsilon}_2^2\hat{\alpha}_2\delta\left(\frac{15}{4}+\frac{5}{12}\eta\right)-\hat{\epsilon}_2^2\hat{\alpha}_3\delta\left(\frac{200}{9}-50\eta\right)+\hat{\epsilon}_2^2\hat{\alpha}_4\left(\left[-\frac{5}{3}+10\eta-\frac{40}{3}\eta^2\right]\kappa_-+\left[-\frac{5}{3}+\frac{20}{3}\eta\right]\delta\kappa_+\right)\\
&-\hat{\epsilon}_2^4\delta\left(\frac{5}{12}-\frac{5}{3}\eta\right)\Bigg]\chi_s\chi_a+\left[-\frac{1120}{9}+\frac{1150}{7}\kappa_+-\left(\frac{3320}{63}+\frac{2990}{7}\kappa_+\right)\eta+\left(\frac{3880}{21}+\frac{1940}{21}\kappa_+\right)\eta^2\right.\\
&+\left(\frac{1150}{7}-\frac{690}{7}\eta\right)\delta\kappa_-+\hat{\alpha}_2\left(-30\kappa_++\left[120+\frac{170}{3}\kappa_+\right]\eta+\left[\frac{40}{3}+\frac{20}{3}\kappa_+\right]\eta^2-\left[30+\frac{10}{3}\eta\right]\delta\kappa_-\right)\\
&-\hat{\alpha}_3\left(\frac{3200}{9}-\frac{12800}{9}\eta\right)+\hat{\alpha}_4\left(\frac{1070}{7}\kappa_+-\left[\frac{4280}{7}+\frac{2690}{7}\kappa_+\right]\eta+\left[\frac{2200}{7}+\frac{1100}{7}\kappa_+\right]\eta^2\right.\\
&\left.+\left[\frac{1070}{7}-\frac{550}{7}\eta\right]\delta\kappa_-\right)+\hat{\alpha}_6\left(-\frac{1600}{9}+\frac{700}{3}\kappa_+-\left[\frac{800}{9}+\frac{1900}{3}\kappa_+\right]\eta+\left[\frac{400}{3}+\frac{200}{3}\kappa_+\right]\eta^2\right.\\
&\left.+\left[\frac{700}{3}-\frac{500}{3}\eta\right]\delta\kappa_-\right)+\hat{\mu}_3^2\left(-\frac{95}{7}\kappa_++\left[\frac{6835}{126}+\frac{20515}{252}\kappa_+\right]\eta-\left[\frac{13670}{63}+\frac{6835}{63}\kappa_+\right]\eta^2\right.\\
&\left.-\left[\frac{95}{7}-\frac{13675}{252}\eta\right]\delta\kappa_-\right)+\hat{\mu}_3^2\hat{\alpha}_4\left(-\frac{6835}{168}\kappa_++\left[\frac{6835}{42}+\frac{6835}{28}\kappa_+\right]\eta-\left[\frac{13670}{21}+\frac{6835}{21}\kappa_+\right]\eta^2\right.\\
&\left.-\left[\frac{6835}{168}-\frac{6835}{42}\eta\right]\delta\kappa_-\right)+\hat{\mu}_3^2\hat{\epsilon}_2^2\left(-\frac{6835}{2016}+\frac{6835}{504}\eta\right)+\hat{\epsilon}_2^2\left(\frac{470}{63}-\frac{5}{6}\kappa_+-\left[\frac{340}{63}-\frac{35}{9}\kappa_+\right]\eta\right.\\
&\left.-\left[\frac{40}{9}+\frac{20}{9}\kappa_+\right]\eta^2-\left[\frac{5}{6}-\frac{20}{9}\eta\right]\delta\kappa_-\right)-\hat{\epsilon}_2^2\hat{\alpha}_2\left(\frac{15}{8}+\frac{5}{24}\eta\right)-\hat{\epsilon}_2^2\hat{\alpha}_3\left(\frac{100}{9}-\frac{400}{9}\eta\right)\\
&+\hat{\epsilon}_2^2\hat{\alpha}_4\left(-\frac{5}{6}\kappa_++\left[\frac{10}{3}+5\kappa_+\right]\eta-\left[\frac{40}{3}+\frac{20}{3}\kappa_+\right]\eta^2-\left[\frac{5}{6}-\frac{10}{3}\eta\right]\delta\kappa_-\right)-\hat{\epsilon}_2^4\left(\frac{5}{24}-\frac{5}{6}\eta\right)\Bigg]\chi_a^2\Bigg\}
\end{aligned}
\tag{4.3.10}
$$

As a consistency check, we confirm the recovery of the corresponding expression for the TaylorF2 phasing in GR for aligned spin binaries (see Refs. [64, 238, 289]) in the limit, $\mu_2 = \mu_3 = \mu_4 = \mu_5 = \epsilon_2 = \epsilon_3 = \epsilon_4 = \alpha_0 = \alpha_2 = \alpha_3 = \alpha_4 = \alpha_5 = \alpha_6 = \alpha_7 = 1$. We also update table 3.1 given in chapter 3 (or Table I of Ref. [204]) to explicitly show the appearances of the parameters μ_l and ϵ_l at various PN order of the phasing formula (see Table 4.1).

One of the salient features of the parametrized multipolar phasing for spinning binaries derived here is the presence of ϵ_2 at 1.5PN order and ϵ_3 at 2.5PN order (logarithmic) due to the SO interactions and hence not present in the non-spinning phasing. At 2PN and 3PN, due to the spin-spin interactions, no additional multipole moments compared to the non-spinning systems appear. These are the orders at which $\kappa_\pm$ appear. This has interesting interpretation as $\kappa_\pm$ can parametrize the potential deviations from BH nature [214, 215] as binaries comprising of non-BHs will have $\kappa_\pm$ to be different from 2 and 0, respectively, which are the unique values corresponding to BBHs.

PN order	frequency dependences	Multipole coefficients
0 PN	$f^{-5/3}$	μ_2
1 PN	f^{-1}	μ_2, μ_3, ϵ_2
1.5 PN	$f^{-2/3}$	μ_2, $\underline{\epsilon_2}$
2 PN	$f^{-1/3}$	μ_2, μ_3, μ_4, ϵ_2, ϵ_3
2.5 PN log	$\log f$	μ_2, μ_3, ϵ_2, $\underline{\epsilon_3}$
3 PN	$f^{1/3}$	μ_2, μ_3, μ_4, μ_5, ϵ_2, ϵ_3, ϵ_4
3 PN log	$f^{1/3}\log f$	μ_2
3.5 PN	$f^{2/3}$	μ_2, μ_3, μ_4, ϵ_2, ϵ_3, $\underline{\epsilon_4}$

Table 4.1. Update of the summary given in table 3.1 of chapter 3 for the multipolar structure of the PN phasing formula. Contribution of various multipoles to different phasing coefficients and their frequency dependences are tabulated. The additional multipole coefficients appearing due to spin are underlined. Following the definitions introduced in chapter 3 [204], μ_l refer to mass-type multipole moments and ϵ_l refer to current-type multipole moments.

The cross-terms of the multipole coefficients with $\kappa_\pm$ showcase the degeneracy between BBHs in alternative theories and non-BHs in GR. As one can see from Eq. (4.3.10), μ_2, μ_3 and ϵ_2 are the multipole coefficients which are sensitive to the non-BH nature (vis-a-vis the above mentioned parametrization). As can be seen from the phasing formula, these imprints will be higher order corrections to the multipole coefficients and may not influence their estimates unless the values of $\kappa_\pm$ are sufficiently high.

4.4 Methodology for numerical analysis

We have discussed the the semi-analytical Fisher information matrix based parameter estimation scheme [67, 133, 136, 258] in section 1.4. We follow the same prescription to discuss the projected bounds on the multipolar deviation coefficients for the spinning binaries. We also discuss the leading order bounds on the systematics of the estimated parameters due to the difference between the spinning and non-spinning waveforms in the Appendix A for LISA.

For $\vec{\theta}$ being the set of parameters defining the GW signal $\tilde{h}(f; \vec{\theta})$, the Fisher information matrix is defined in Eq. (1.4.18). In the large signal-to-noise ratio (SNR) limit, the distribution of the inferred parameters follow a Gaussian distribution around their respective true values for which the variance-covariance matrix of the errors on the parameters is given in Eq. (1.4.19) and the 1σ statistical error bars on various parameters are given in Eq. (1.4.20).

Fisher information matrix method, by default, assumes a flat prior distribution in the range $[-\infty, \infty]$ on all the parameters to be estimated [136,283]. In contrast, in the large SNR limit, a Gaussian prior can also be implemented on the desired parameter as described in Ref. [136]. For our purpose, we employ a Gaussian prior on ϕ_c centered around $\phi_c = 0$ with a variance of about π^2. This choice is somewhat ad-hoc but ensures that the prior distribution is not a too narrow Gaussian to significantly influence the result but helps us dealing with the ill-conditionedness of the Fisher matrix. This also restricts the prior range to exceed to the unphysical domain beyond $\pm\pi$. Hence our modified Fisher matrix has the following form,

$$\Gamma' = \Gamma + \Gamma^{(0)}, \tag{4.4.1}$$

where $\Gamma^{(0)}$ is a diagonal matrix with only one non-zero element corresponding to $\Gamma^{(0)}_{\phi_c\phi_c}$ component. We use this modified Fisher matrix (Γ') for the estimation of 1σ upper bounds on any mulitpolar deviation of the coefficients from GR value.

We estimate the statistical errors on various multipole coefficients while considering an eight dimensional parameter space, $\{t_c, \phi_c, \log\mathcal{A}, \log\mathcal{M}_c, \log\eta, \chi_s, \chi_a, \mu_\ell$ or ϵ_ℓ or $\alpha_m\}$ to describe the true GW signal.

4.5 Detector configurations

We describe here the various detector configurations we considered in the present study.

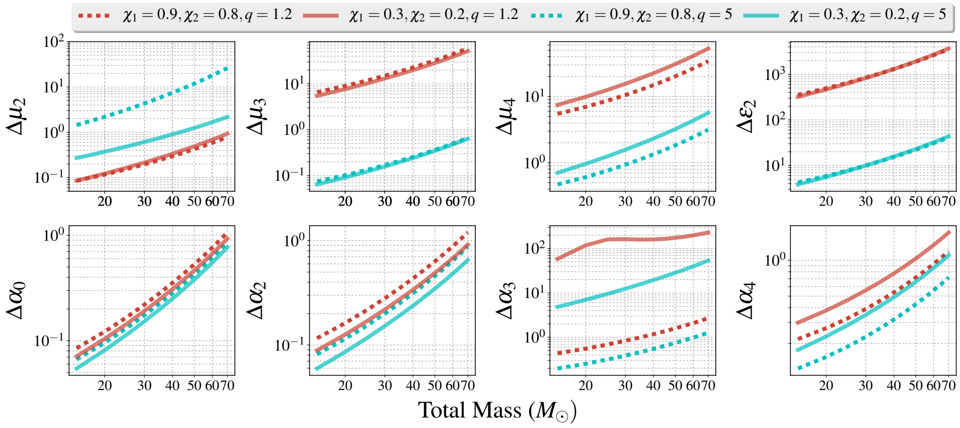

Figure 4.1. Projected 1σ errors on the multipole and the energy coefficients as a function of total mass for two different mass ratios $q = m_1/m_2 = 1.2, 5$ and two spin configurations, $\chi_1 = 0.9, \chi_2 = 0.8$ and $\chi_1 = 0.3, \chi_2 = 0.2$ for the second generation detector network. All the sources are at a fixed luminosity distance of 100 Mpc with the angular position and orientations to be $\theta = \pi/6, \phi = \pi/3, \psi = \pi/6, \iota = \pi/5$. To obtain the numerical estimates showed in this plot, we also consider a prior distribution on ϕ_c. To be precise, we assume the prior on ϕ_c for each detector in the network to follow a Gaussian distribution with a zero mean and a variance of $1/\pi^2$.

4.5.1 Ground-based second generation detector network

As a representative case, we consider a world-wide network of five second-generation ground based detectors: LIGO-Hanford, LIGO-Livingston, Virgo, KAGRA [69], and LIGO-India [201]. We assume the noise PSD for LIGO-Hanford, LIGO-Livingstone and LIGO-India to be the analytical fit given in Ref. [46] whereas the fit given in Eq. (1.4.6) is used for Virgo PSD. We consider the lower cut off frequency, $\mathrm{f_{low}} = 10$ Hz for these detectors. For the Japanese detector, KAGRA, we use the noise PSD given in Ref. [3] with $\mathrm{f_{low}} = 1$ Hz. For all the detectors, $f_{\rm high}$ is taken to be the frequency at the last stable orbit, $f_{\rm LSO} = 1/(\pi\, m\, 6^{3/2})$. As opposed to the single detector Fisher matrix analysis, for a network of detectors, Fisher matrix is evaluated for each detector and then added to obtain the network-Fisher-matrix. To estimate the individual Fisher matrices we use a waveform that is weighted with the correct antenna pattern functions $F_{+/\times}(\theta, \phi, \psi)$ of the detectors, where θ, ϕ and ψ are the declination, the right ascension and the polarization angle of the source in

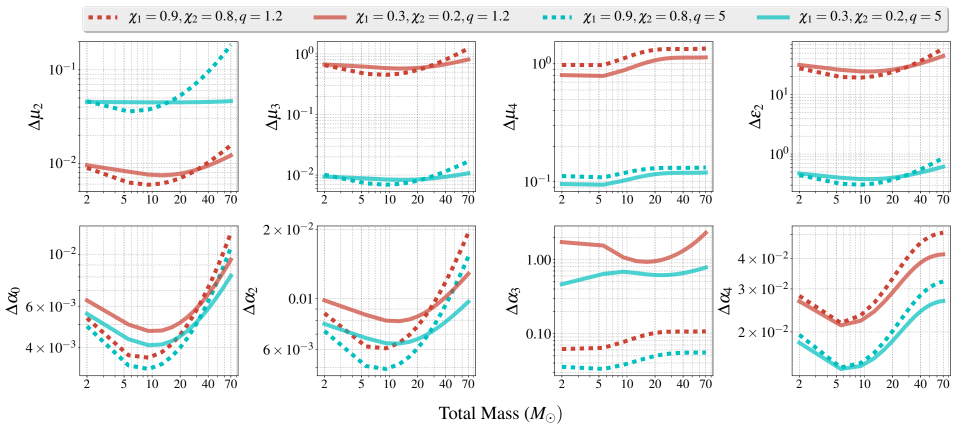

Figure 4.2. Projected 1σ errors on the multipole and the energy coefficients as a function of total mass for two different mass ratios $q = m_1/m_2 = 1.2, 5$ and two spin configurations, $\chi_1 = 0.9, \chi_2 = 0.8$ and $\chi_1 = 0.3, \chi_2 = 0.2$ for the third generation detector network. All the sources are at a fixed luminosity distance of 100 Mpc with the angular position and orientations to be $\theta = \pi/5, \phi = \pi/6, \psi = \pi/4, \iota = \pi/4$. To obtain the numerical estimates showed in this plot, we also consider a prior distribution on ϕ_c. To be precise, we assume the prior on ϕ_c for each detector in the network to follow a Gaussian distribution with a zero mean and a variance of $1/\pi^2$.

the sky. More precisely we use the following waveform

$$\tilde{h}(f) = \frac{1+\cos^2\iota}{2} F_+(\theta,\phi,\psi)\,\tilde{h}_+(f) + \cos\iota\, F_\times(\theta,\phi,\psi)\,\tilde{h}_\times(f) \tag{4.5.1}$$

with

$$\tilde{h}_+(f) = \mathcal{A}\mu_2\, f^{-7/6} e^{-i\Psi_s}\,, \tag{4.5.2}$$

$$\tilde{h}_\times(f) = -i\,\tilde{h}_+(f)\,. \tag{4.5.3}$$

The individual $F_{+/\times}(\theta,\phi,\psi)$ for each detector are estimated incorporating the location of the detectors on Earth as well as Earth's rotation as given in Ref. [4]. We calculate the Fisher matrix for each detector considering an eight dimensional parameter space, $\{t_c, \phi_c, \log\mathcal{A}, \log\mathcal{M}_c, \log\eta, \chi_s, \chi_a, \mu_\ell$ or ϵ_ℓ or $\alpha_m\}$, which specifies the true GW signal. Here we fix the four angles, $\theta, \phi, \psi, \iota$ to be $\pi/6, \pi/3, \pi/6, \pi/5$ respectively and do not treat them as parameters in the Fisher matrix estimation. These four angles, being the extrinsic parameters, have negligible correlations with the intrinsic ones, especially with the multipole or the energy coefficients, which are our primary interest.

4.5.2 Ground-based third generation detector network

As a representative case for the third generation ground-based detector network, we consider three detectors: one Cosmic Explorer-wide band (CE-wb) [24] in Australia, one CE-wb in Utah-USA and one Einstein Telescope-D (ET-D) [11] in Europe. We use the noise PSD given in Ref. [11] for ET-D and the analytical fit given in Eq. (1.4.7) for the CE-wb. We assume $f_{\rm low}$ to be 1 and 5 Hz for the ET-D and CE-wb, respectively. To evaluate the Fisher matrix for this network configuration we use the same waveform as given in Eq. (4.5.1) except for the estimation of Fisher matrix in case of ET-D, we multiply the waveform by $\sin(\pi/3)$ because of its triangular shape. We follow the same scheme as described in Sec. 4.5.1 to estimate the 1σ bounds on $\mu_2, \mu_3, \mu_4, \epsilon_2$ and $\alpha_0, \alpha_2, \alpha_3, \alpha_4$.

4.5.3 Space-based LISA detector

For the space based detector, LISA, we use analytical fit given in [70] and choose $f_{\rm low}$ in such a way that the signal stays in the detector band for one year or less depending on the frequency at the last stable orbit. More specifically, we assume $f_{\rm low}$ to be [83, 134]

$$f_{\rm low} = \max\left[10^{-5}, 4.149\times 10^{-5}\left(\frac{\mathcal{M}_c}{10^6 M_\odot}\right)^{-5/8}\left(\frac{T_{\rm obs}}{1\,{\rm yr}}\right)^{-3/8}\right], \tag{4.5.4}$$

where $T_{\rm obs}$ is the observation time which we consider to be one year. We assume the upper cut off frequency, $f_{\rm high}$, to be the minimum of $[0.1, f_{\rm LSO}]$. The waveform we employ for LISA is given in Eq. (4.3.2) except we multiply it by an additional factor of $\sqrt{3}/2$ in order to account for the triangular shape of the detector. We do not account for the orbital motion of LISA in our calculations and consider LISA to be a single detector.

We next discuss the Fisher matrix projections of the various deformation coefficients parametrizing the conservative and dissipative sectors in the context of the detector configurations described

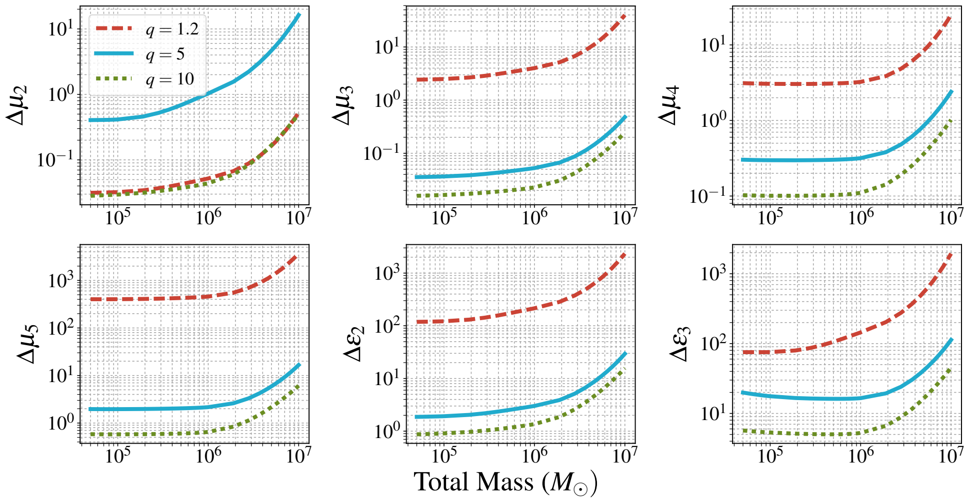

Figure 4.3. Projected 1σ errors on the multipole coefficients as a function of total mass for three different mass ratios $q = m_1/m_2 = 1.2, 5$ and 10 in case of LISA noise PSD. We assume $\chi_1 = 0.9, \chi_2 = 0.8$. All the sources are considered to be at a fixed luminosity distance of 3 Gpc. To obtain the numerical estimates showed in this plot, we also consider a prior distribution on ϕ_c. To be precise, we assume ϕ_c to follow a Gaussian distribution with a zero mean and a variance of $1/\pi^2$.

above.

4.6 Results

Our results for the ground-based detectors are depicted in Figs. 4.1 for second generation and 4.2 for third generation and those for the space-based LISA detector are presented in Figs. 4.3, 4.4, 4.5, 4.6 and 4.7. For the second and third generation ground-based detectors configurations, we choose the binary systems with two different mass ratios $q = 1.2, 5$ for two sets of spin configurations: high spin case with $\chi_1 = 0.9, \chi_2 = 0.8$ and low spin case with $\chi_1 = 0.3, \chi_2 = 0.2$. We also assume the luminosity distance to all these prototypical sources to be 100 Mpc. We consider these sources are detected with a network of second or third generation detectors as detailed in the last section. For LISA, we consider our prototypical supermassive BHs to be at the luminosity distance of 3 Gpc with three different mass ratios of $q = 1.2, 5, 10$. For these mass ratios, we investigate both high spin ($\chi_1 = 0.9, \chi_2 = 0.8$) and low spin ($\chi_1 = 0.3, \chi_2 = 0.2$) scenarios.

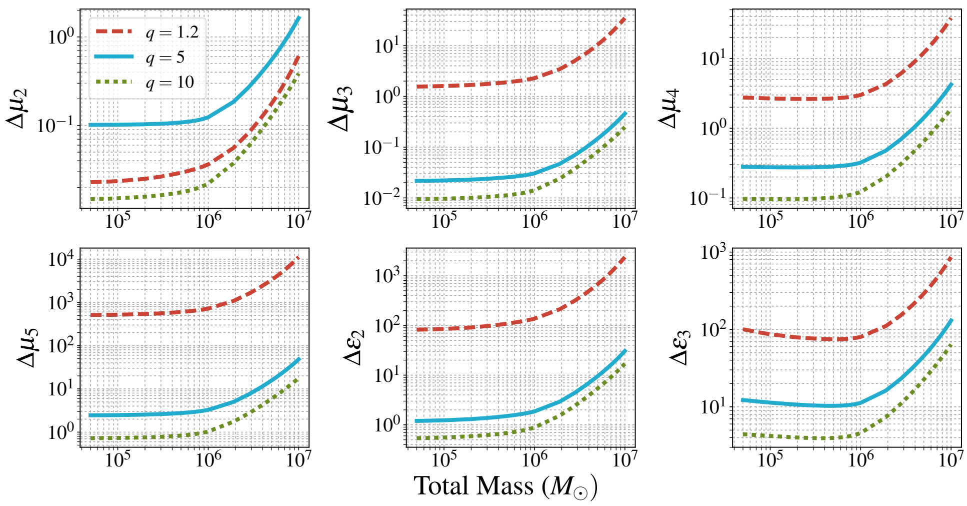

Figure 4.4. Projected 1σ errors on the multipole coefficients as a function of total mass for three different mass ratios $q = m_1/m_2 = 1.2, 5$ and 10 in case of LISA noise PSD. We assume $\chi_1 = 0.3, \chi_2 = 0.2$. All the sources are considered to be at a fixed luminosity distance of 3 Gpc. To obtain the numerical estimates showed in this plot, we also consider a prior distribution on ϕ_c. To be precise, we assume ϕ_c to follow a Gaussian distribution with a zero mean and a variance of $1/\pi^2$.

First we discuss the qualitative features in the plots. As expected, the third generation detector network which has better bandwidth and sensitivity does better than the second generation detectors. On the other hand LISA and third generation detectors perform comparably, though for totally different source configurations. The bounds on the multipole coefficients describing the dissipative dynamics broadly follow the trends seen in the non-spinning study carried out in chapter 3 [204]. The mass-type multipole moments are measured with better accuracies than the current-type ones appearing at the same PN order. Among all the coefficients, μ_2 (corresponding to the mass quadrupole) yields the best constraint as it is the dominant multipole contributing to the flux and the phasing. Due to the interplay between the sensitivity and mass dependent upper cut-off frequency, the errors increase as a function of mass in the regions of the parameter space we explore. The errors improve as the mass ratio increases for all cases except μ_2. As argued in chapter 3 [204], μ_2 is the only multipole parameter which appears both in the amplitude and the phase of the waveform and hence shows trends different from the other multipole coefficients. Inclusion of spins, on the whole, worsens the estimation of the multipole coefficients compared to the non-

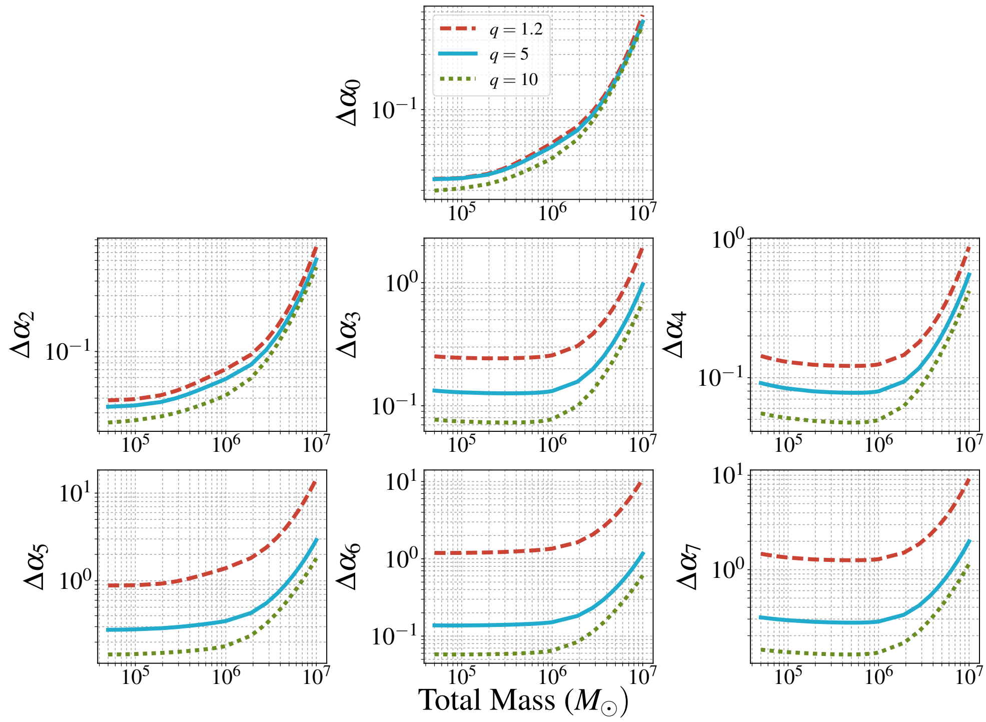

Figure 4.5. Projected 1σ errors on the energy coefficients as a function of total mass for three different mass ratios $q = m_1/m_2 = 1.2, 5$ and 10 in case of LISA noise PSD. We assume $\chi_1 = 0.9, \chi_2 = 0.8$. All the sources are considered to be at a fixed luminosity distance of 3 Gpc. To obtain the numerical estimates showed in this plot, we also consider a prior distribution on ϕ_c. To be precise, we assume the prior on ϕ_c to follow a Gaussian distribution with a zero mean and a variance of $1/\pi^2$.

spinning case. This is expected as the spins increase the dimensionality of the parameter space but do not give rise to any new features which may help the estimation. Effects such as spin-induced precession, which brings in a new time scale and associated modulations, may help counter this degradation in the parameter estimation. But this will be a topic for a future investigation. We also explore the bounds on the multipole coefficients as a function of the spin magnitudes in case of LISA (see fig. 4.7). Here we consider two mass ratio cases $q = 10, 20$ but fix the total mass of the system to be $2\times10^5 M_\odot$and plot the bounds as a function of primary spin χ_1. Since we vary the secondary spin, χ_2 as well, we get a spread on the bounds at each χ_1 along the y-axis due to different values of χ_2 in the limit $[-1, 1]$. We find that the parameter estimation improves with the spin mag-

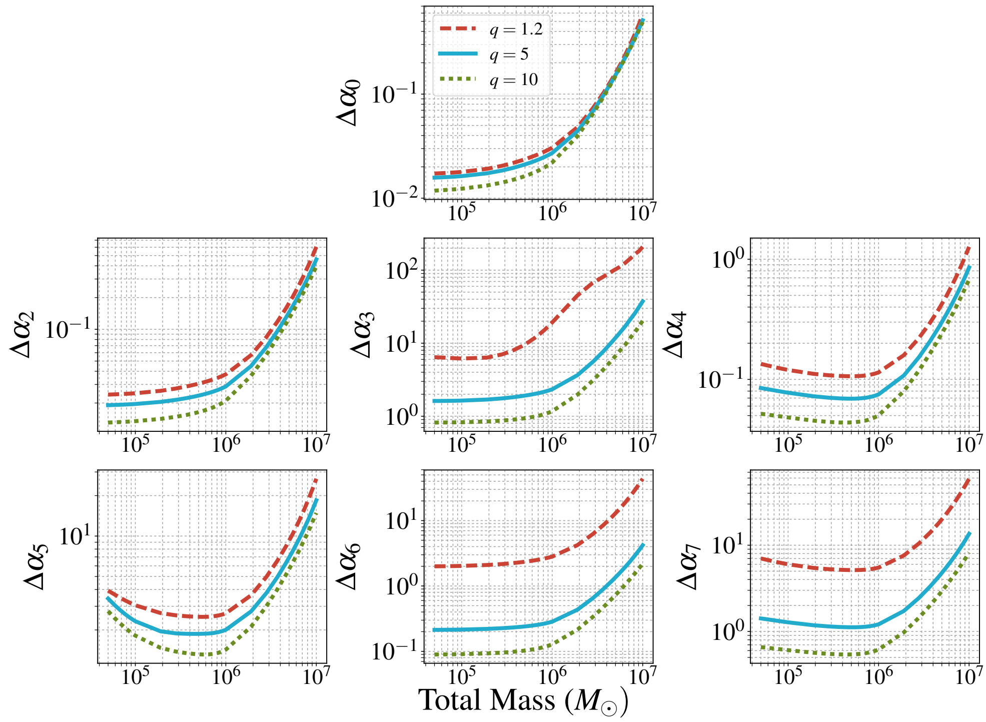

Figure 4.6. Projected 1σ errors on the energy coefficients as a function of total mass for three different mass ratios $q = m_1/m_2 = 1.2, 5$ and 10 in case of LISA noise PSD. We have considered $\chi_1 = 0.3, \chi_2 = 0.2$. All the sources are considered to be at a fixed luminosity distance of 3 Gpc. To obtain the numerical estimates showed in this plot, we also consider a prior distribution on ϕ_c. To be precise, we assume the prior on ϕ_c to follow a Gaussian distribution with a zero mean and a variance of $1/\pi^2$.

nitudes and hence highly spinning systems would yield stronger constraints on these coefficients. The estimations of various α_k, parametrizing the conservative dynamics, also broadly follow these trends. However, there is an important exception. The bounds on α_3 is consistently worse than those of α_4. This may be attributed to the important difference between them. α_3 parametrizes the 1.5PN term in the conserved energy which has only spin-dependent terms whereas the 2PN term contains both non-spinning and spinning contributions. Hence though α_4 is sub-leading in the PN counting, the bounds on it are better.

We now discuss the quantitative results from these plots. One of the most interesting results is the projected constraints on coefficients that parametrize conservative dynamics. For third generation

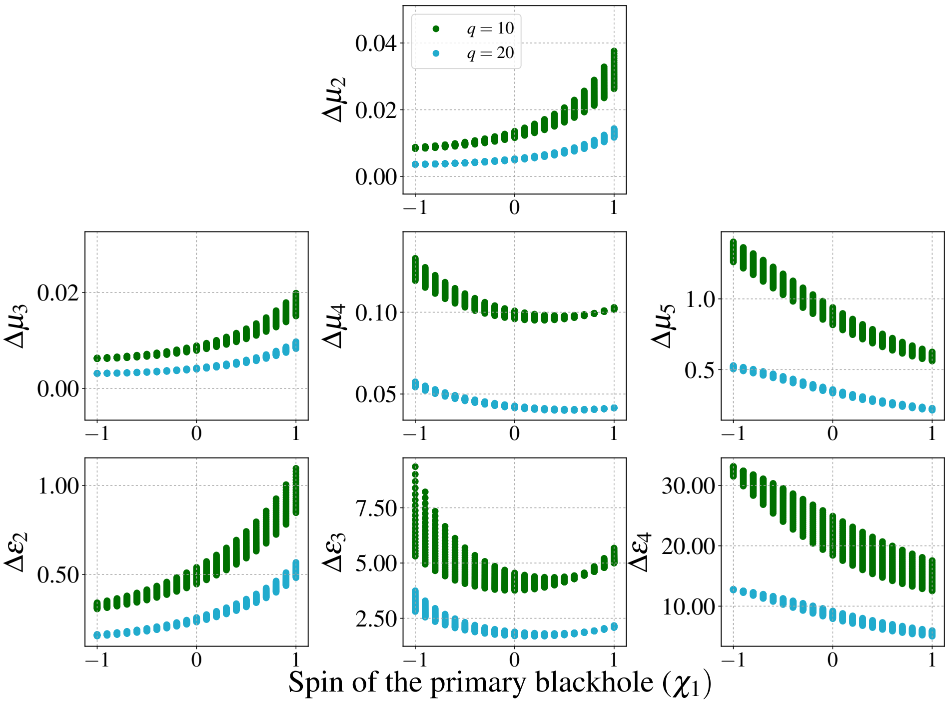

Figure 4.7. Projected 1σ errors on multipole coefficients as a function of the spin of the heavier black hole, χ_1, for LISA noise PSD. All the sources are considered to be at a fixed luminosity distance of 3 Gpc with a total mass of 2×10^5 $M_\odot$. The green dots are for mass ratio 10 and the cyan dots denotes mass ratio 20. The vertical spread in the bounds at each χ_1 value is due to different χ_2 in the range $[-1, 1]$.To obtain the numerical estimates showed in this plot, we also consider a prior distribution on ϕ_c. To be precise, we assume the prior on ϕ_c to follow a Gaussian distribution with a zero mean and a variance of $1/\pi^2$.

ground-based detectors and the prototypical source configurations, the bounds on 2PN conservative dynamics can be$\sim$ 10^{-2} which is comparable to or even better than the corresponding bounds expected from LISA. On the multipole coefficients side, the quadrupole coefficient μ_2 may be constrained to $\leq$ $10^{-1}(10^{-2})$ for second (third) generation detector network while the bounds from LISA are $\sim$ 10^{-2}. The best bounds on μ_3 are $\sim$ $10^{-1}, 10^{-2}, 10^{-2}$ for second generation, third generation and LISA, respectively, corresponding to highly spinning binaries. The projected bounds on the higher multipole coefficients from third generation detector network and LISA are comparable in all these cases, though one should keep in mind the specifications of the sources we consider for these two cases are very different.

4.7 Conclusion

We extend our parametrized tests of multipolar structure and conservative dynamics of CBC, developed in chapter 3, by including spin effects in the inspiral dynamics for non-precessing compact binaries in quasi-circular orbits. The SO contributions are computed up to 3.5PN order while the SS contributions are obtained up to 3PN order. We also provide the projected 1σ bounds on the multipole coefficients as well as the PN deviation parameters in the conserved energy for the second generation ground based detector network, the third generation ground based detector network and the space-based detector LISA, using the Fisher matrix approach. We find that the four leading order multipole coefficients and the four leading order PN conserved energy coefficients are measured with reasonable accuracies using these GW detectors.

As a follow-up, it will be interesting to compute the parametrized waveform within the effective-one-body formalism and investigate the possible bounds on these coefficients. Inclusion of higher modes of the gravitational waveforms, which contain these multipole coefficients in the amplitude of the waveform, will also be an interesting follow-up in the future.

5 Linear momentum flux from compact binaries in quasi-elliptical orbits at second post-Newtonian order

Asymmetric gravitational wave emission by a compact binary system leads to a flux of linear momentum from the system [244, 247]. In order to conserve the total linear momentum, the system recoils. The direction of recoil changes continuously over an orbit. As a result, for a perfectly circular trajectory, no net recoil builds up over an orbit. On the contrary, for inspiralling compact binaries, the recoil accumulates over the inspiralling orbits and imparts a kick to the merger.

A reasonably high kick imparted to the merger could be of great importance in understanding the structure formation of globular clusters. If the kick is greater than the escape velocity of the host galaxy, the remnant BH may even be ejected [211] from the galaxy. Even if the kick is not high enough to eject the merged BH from the galaxy, it might cause important dynamical changes at the core of the galaxy. A detailed discussion on various astrophysical aspects of BH kicks can be found in ref [233].

Although a compact binary merger may have significant eccentricity at the birth, due to the GW radiation, it gets circularized [249, 250]. By the time their GW frequency enters the sensitivity bands of the ground based interferometric GW detectors, they may have negligible eccentricity. On the contrary, there may be astrophysical processes which may retain their eccentricity even in the late stages of their dynamics. For example, in dense stellar clusters, interactions between pairs of binary black hole systems may eject one of the black holes leading to the formation of a stable hierarchical triple system. If the two orbital planes are tilted with respect to each other, the third body can increase the eccentricity of the inner binary via Kozai mechanism [213]. Binaries in such hierarchical triple systems may retain their eccentricities even towards the late stages of the inspiral. Further, binary neutron star systems in globular clusters may have a thermal distribution of eccentricities [80] if formed by exchange interactions as opposed to the scenario where the formation happens through the common envelope. Similarly, there have been mechanisms proposed for binaries consisting of supermassive BHs in the LISA band [183, 190, 191] which may have detectable eccentricities. Motivated by these scenarios, we study the gravitational recoils in the case of non-spinning compact binary systems in quasi-elliptical orbits.

The first formal treatment of GW recoil for a general self-gravitating system in linearized gravity is explored in refs. [77, 247]. It is valid for any kind of motion (rotational, vibrational or any other kind) given the source is localized within a finite volume. Later, within the post-Newtonian formalism, the leading order contribution (Newtonian) to the LMF and recoil of a compact binary system is discussed by Fitchett in refs. [168, 169]. The first PN correction of this was computed by Wiseman [300] and the circular orbit case was discussed as a special case. Much later, a closed form expression for the recoil in case of compact binary in quasi-circular orbit is quoted in [108] at the second post-Newtonian (PN) order. Its extension to 2.5PN order, accounting for the radiation reaction effects, is discussed in ref. [236]. According to these studies, the BH recoil for nonspinning systems could be in the range 74-250 km s^{-1}. Using the EOB approach, the recoil estimates for BBH is obtained considering the contributions from inspiral, plunge and ringdown phases in ref. [141]. The typical estimate obtained here, lies in the range 49-172 km s^{-1}. In ref. [167], BH perturbation theory is used to estimate the accumulated recoil up to the innermost stable circular orbit (ISCO) (10-100 km s^{-1}) for a system where a test particle inspirals into a BH. In principle, these estimates are valid for extreme mass ratio inspirals but they have extrapolated the results till mass ratio of about ~ 0.4.

Along with the various analytical and semi-analytical studies, the recent progress in NR has led to more accurate estimates for the recoil of the remnant BH. As quoted in refs. [73, 124, 179, 187], the recoil velocity can reach up to a few hundreds of km s^{-1} while the component masses are nonspinning. But for the spinning case [178, 188, 212], the recoil velocity can be of the order of few thousands km s^{-1}. In case of maximally spinning BHs, it could be as high as 4000 km s^{-1} [126]. Such a large recoil velocity may lead to ejection of the merged binary from its host galaxy. A detailed study on multipolar analysis of the gravitational recoil is also discussed in ref. [271]. They have explored the build up of the recoil through the different phases of the binary evolution, (inspiral+merger+ringdown) due to the relative amplitude and the phases of various modes of the GWs.

Using the MPM-PN formalism, discussed in chapter 2, the leading order Newtonian contribution to the LMF and the associated recoil of a compact binary system is explored by Fitchett in refs. [168, 169]. They assumed the inspiralling binary to be composed of two point particles moving in a Keplerian orbit. A rough estimate of maximum BH recoil quoted in these studies are ~ 1500km/s. Assuming the periastron advance to be small, a crude estimate of the recoil at 1PN is also quoted. The first formal extension of these estimates at 1PN for binaries moving in generic orbits is explored by Wiseman [300] and concluded that higher order correction reduces the net momentum ejection. As a special case, they also studied BNS systems moving in quasi-circular orbits. They found the upper bound on the velocity of the center of mass very near to the coalescence to be 1 km s^{-1}. In another study [274], the authors showed a 10% increase in the recoil estimate compared to the quasi-circular case for small eccentricities ($e < 0.1$) using close limit approximation. They also claimed that the maximum recoil takes place at the symmetric mass ratio of around $\eta \sim 0.19$ and the magnitude could be as high as $216 - 242$ km/s. Here we extend the above studies to 2PN and compute the linear momentum flux for the case of compact binaries moving in quasi-elliptical orbits. We first provide the instantaneous contribution to the LMF in terms of the dynamical variables for the compact binaries moving in a generic orbit. We then compute the 1.5PN hereditary contribution to the LMF assuming the quasi-Keplerian (QK) representation of the orbital dynamics. In order to obtain the complete closed form expression for 2PN LMF we add both the contributions. We further restrict in the small eccentricity regime ($e_t << 1$) by expanding the complete expression in series of e_t and truncate at $O(e_t^2)$. We finally quote the results in terms of the various QK parameters defining the quasi-elliptical orbits by the end of this chapter.

This chapter is organized as follows. In section 5.1 we discuss the multipolar decomposition of LMF in terms of the various source type multipole moments and their non-linear interactions. In sections 5.2 and 5.3, we describe the orbital dynamics and quote all the source multipole moments as functions of orbital parameters up to the accuracy needed for the present calculation of LMF at 2PN. In section 5.4 we quote the instantaneous contribution to the LMF. Furthermore, in section 5.5 we summarize the generalized quasi-keplerian representations (QKR) of the orbital dynamics and re-express the LMF in terms of the QK parameters. Finally in section 5.7 we derive the hereditary contributions and quote the complete LMF at 2PN.

5.1 Multipole decomposition of Linear momentum flux

For an isolated source, gravitational wave generation is well studied under the framework of multipolar decomposition [279]. Following [279], we explicitly write down the multipolar decomposition of far-zone linear momentum flux (LMF) for an isolated source at the second post-Newtonian order in terms symmetric trace-free (STF) radiative mass type and current type multipole moments as,

$$\begin{aligned}\mathcal{F}_P^i &= \frac{G}{c^7}\Bigg\{\left[\frac{2}{63}\,U^{(1)}_{ijk}\,U^{(1)}_{jk}+\frac{16}{45}\,\varepsilon_{ijk}U^{(1)}_{ja}\,V^{(1)}_{ka}\right]\\ &+\frac{1}{c^2}\left[\frac{1}{1134}\,U^{(1)}_{ijkl}\,U^{(1)}_{jkl}+\frac{1}{126}\,\varepsilon_{ijk}U^{(1)}_{jab}\,V^{(1)}_{kab}+\frac{4}{63}\,V^{(1)}_{ijk}\,V^{(1)}_{jk}\right]\\ &+\frac{1}{c^4}\left[\frac{1}{59400}\,U^{(1)}_{ijklm}\,U^{(1)}_{jklm}+\frac{2}{14175}\,\varepsilon_{ijk}U^{(1)}_{jabc}\,V^{(1)}_{kabc}+\frac{2}{945}\,V^{(1)}_{ijkl}\,V^{(1)}_{jkl}\right]+O\left(\frac{1}{c^5}\right)\Bigg\}, \end{aligned} \tag{5.1.1}$$

where $U^{(p)}_K$ and $V^{(p)}_K$ $\Big($ $K = i_1 i_2 \cdots i_k$ represents the multi-index structure of the tensors of order k in three dimension$\Big)$ are the p^{th} time derivative of mass-type and current-type radiative multipole moments respectively. ε_{ijk} is the usual three dimensional Levi-Civita tensor, with a value +1 in case of all even permutations and −1 for all the odd ones. The multipole moments in the formula, are functions of retarded time $(t-(r/c))$ in radiative coordinates, where r and t denote the distance of the source from the observer and the time of observation in radiative coordinates, respectively.

Using the MPM formalism [84, 85, 93–95, 97, 98, 100, 101, 106, 145, 277] the two types of radiative moments can be expressed in terms of two types of canonical moments (M_L, S_L) and eventually as a function of all the source multipole moments $(I_L, J_L, X_L, W_L, Y_L, Z_L)$ [103] at the 2PN order. All the radiative moments have two types of contributions. One of them is only a function of retarded time and hence called the *instantaneous* part. The other one depends on the dynamical behavior of the system throughout its entire past and referred to as the *hereditary* contributions. These contributions contain information about various multipolar interactions the wave undergoes as it propagates from the source to the detector.

Here, we explicitly quote all the radiative moments in terms of the source moments accurate up to the order necessary for the present calculation. Since the leading order term in the LMF expression (see Eq. 5.1.1) consists of the mass quadrupole moment (U_{ij}), the desired accuracy of (U_{ij}) is 2PN. Furthermore, the decomposition of mass quadrupole into instantaneous and hereditary parts is as follows,

$$U_{ij} = U_{ij}^{\text{inst}} + U_{ij}^{\text{hered}}, \tag{5.1.2}$$

where the instantaneous and the hereditary parts explicitly reads

$$U_{ij}^{\text{inst}} = I_{ij}^{(2)}(T_R) + O\left(\frac{1}{c^5}\right), \tag{5.1.3a}$$

$$U_{ij}^{\text{hered}}(T_R) = \frac{2Gm}{c^3}\int_{-\infty}^{T_R} d\tau \left[\ln\left(\frac{T_R-\tau}{2\tau_0}\right) + \frac{11}{12}\right] I_{ij}^{(4)}(\tau) + O\left(\frac{1}{c^5}\right) \tag{5.1.3b}$$

In the above expression, m represents the Arnowitt, Deser and Misner (ADM) mass of the source. The constant τ_0 is related to an arbitrary length scale r_0 by $\tau_0 = r_0/c$ and was originally introduced in the MPM formalism.

The required accuracy of mass octupole moment is 1.5PN which is,

$$U_{ijk} = U_{ijk}^{\text{inst}} + U_{ijk}^{\text{hered}}, \tag{5.1.4}$$

and both the parts separately read

$$U_{ijk}^{\text{inst}}(T_R) = I_{ijk}^{(3)}(T_R) + O\left(\frac{1}{c^4}\right), \tag{5.1.5a}$$

$$U_{ijk}^{\text{hered}}(T_R) = \frac{2Gm}{c^3}\int_{-\infty}^{T_R} d\tau \left[\ln\left(\frac{T_R-\tau}{2\tau_0}\right) + \frac{97}{60}\right] I_{ijk}^{(5)}(\tau) + O\left(\frac{1}{c^5}\right) \tag{5.1.5b}$$

As the other two mass type moments U_{ijkl} and U_{ijklm} appear in the LMF at 1PN and 2PN respectively, the desired accuracy for these two are 1PN and Newtonian respectively and have only instantaneous contributions, which read,

$$U_{ijkl}^{\text{inst}}(T_R) = I_{ijkl}^{(4)}(T_R) + O\left(\frac{1}{c^4}\right) \tag{5.1.6}$$

$$U_{ijklm}^{\text{inst}}(T_R) = I_{ijklm}^{(4)}(T_R) + O\left(\frac{1}{c^4}\right) \tag{5.1.7}$$

Among the current type moments, current quadrupole moment is needed to be evaluated at 2PN order.

$$V_{ij} = V_{ij}^{\text{inst}} + V_{ij}^{\text{hered}}, \tag{5.1.8}$$

The instantaneous and the hereditary parts in terms of the current quadrupole moments read

$$V_{ij}^{\text{inst}}(T_R) = J_{ij}^{(2)}(T_R) + O\left(\frac{1}{c^5}\right). \tag{5.1.9a}$$

$$V_{ij}^{\text{hered}}(T_R) = \frac{2Gm}{c^3}\int_{-\infty}^{T_R} d\tau \left[\ln\left(\frac{T_R-\tau}{2\tau_0}\right) + \frac{7}{6}\right] J_{ij}^{(4)}(\tau) + O\left(\frac{1}{c^4}\right). \tag{5.1.9b}$$

For all the other current type moments (V_{ijk}, V_{ijkl}), we need only the instantaneous parts to obtain

LMF at 2PN.

$$V^{\rm inst}_{ijk}(T_R) = J^{(3)}_{ijk}(T_R) + \mathcal{O}\left(\frac{1}{c^3}\right), \tag{5.1.10}$$

$$V^{\rm inst}_{ijkl}(T_R) = J^{(4)}_{ijkl}(T_R) + \mathcal{O}\left(\frac{1}{c^3}\right). \tag{5.1.11}$$

Using Eqs. (5.1.2)-(5.1.11) we obtain the closed form expression for LMF at 2PN in terms of the source multipole moments. The LMF also admits a decomposition into instantaneous and hereditary parts like the radiative moments. The instantaneous and the hereditary parts indicate two distinct physical processes and their evaluations need separate treatments. Thus, for our convenience, we explicitly write the two types of contributions (instantaneous and hereditary) to linear momentum flux separately as follows,

$$\mathcal{F}_i = \mathcal{F}^{\rm inst}_i + \mathcal{F}^{\rm hered}_i, \tag{5.1.12}$$

where the instantaneous part up to 2PN in terms of the source multipole moments is [236]

$$\begin{aligned}\mathcal{F}^{\rm inst}_i \quad = \quad & \frac{G}{c^7}\left\{\frac{2}{63}\, I^{(4)}_{ijk}\, I^{(3)}_{jk} + \frac{16}{45}\,\varepsilon_{ijk} I^{(3)}_{ja}\, J^{(3)}_{ka}\right.\\ & +\frac{1}{c^2}\left[\frac{1}{1134}\, I^{(5)}_{ijkl}\, I^{(4)}_{jkl} + \frac{4}{63}\, J^{(4)}_{ijk}\, J^{(3)}_{jk} + \frac{1}{126}\,\varepsilon_{ijk} I^{(4)}_{jab}\, J^{(4)}_{kab}\right]\\ & \left.+\frac{1}{c^4}\left[\frac{1}{59400}\, I^{(6)}_{ijklm}\, I^{(5)}_{jklm} + \frac{2}{945}\, J^{(5)}_{ijkl}\, J^{(4)}_{jkl} + \frac{2}{14175}\,\varepsilon_{ijk} I^{(5)}_{jabc}\, J^{(5)}_{kabc}\right]\right\},\end{aligned} \tag{5.1.13}$$

and the hereditary contribution at 1.5PN is

$$\begin{aligned}\mathcal{F}^{\rm hered}_i = & \frac{4\,G^2\,m}{63\,c^{10}}\, I^{(4)}_{ijk}(t) \int_0^\infty d\tau\left[\ln\left(\frac{\tau}{2\tau_0}\right) + \frac{11}{12}\right] I^{(5)}_{jk}(t-\tau)\\ & + \frac{4\,G^2\,m}{63\,c^{10}}\, I^{(3)}_{jk}(t) \int_0^\infty d\tau\left[\ln\left(\frac{\tau}{2\tau_0}\right) + \frac{97}{60}\right] I^{(6)}_{ijk}(t-\tau)\\ & + \frac{32\,G^2\,m}{45\,c^{10}}\,\varepsilon_{ijk}\, I^{(3)}_{ja}(t) \int_0^\infty d\tau\left[\ln\left(\frac{\tau}{2\tau_0}\right) + \frac{7}{6}\right] J^{(5)}_{ka}(t-\tau)\end{aligned}$$

$$+\frac{32\,G^2\,m}{45\,c^{10}}\,\varepsilon_{ijk}\,J^{(3)}_{ka}(t)\int_0^\infty d\tau\left[\ln\left(\frac{\tau}{2\tau_0}\right)+\frac{11}{12}\right]I^{(5)}_{ja}(t-\tau). \tag{5.1.14}$$

5.2 Orbital dynamics of the compact binary source

In the previous section, we have provided an explicit closed form expression of the far-zone linear momentum flux from a compact binary system in terms of various source multipole moments. Here we specialize to the case of a non-spinning compact binary system in quasi-elliptical orbits, with the component masses m_1 and m_2 respectively with $m_1 \geq m_2$, the total mass $m = m_1 + m_2$, and the symmetric mass ratio, $\eta = m_1 m_2/m^2$. Since the binary constituents are nonspinning, its motion is completely confined in a plane with a relative separation,

$$\mathbf{x} = \mathbf{x_1} - \mathbf{x_2} = r\,\hat{\mathbf{n}}, \tag{5.2.1}$$

with $r = |\mathbf{x}|$, $\mathbf{x_1}$ and $\mathbf{x_2}$ are the position vectors of the component masses, and $\hat{\mathbf{n}}$ is the unit vector along the relative separation vector. In polar coordinates,

$$\hat{\mathbf{n}} = \frac{\mathbf{x}}{r} = \cos\phi\,\hat{\mathbf{e}}_\mathbf{x} + \sin\phi\,\hat{\mathbf{e}}_\mathbf{y}\,, \tag{5.2.2}$$

where ϕ is the orbital phase of the binary, and $\hat{\mathbf{e}}_\mathbf{x}$ and $\hat{\mathbf{e}}_\mathbf{y}$ are the unit vectors along x and y axes. The relative velocity and acceleration for the system are the following,

$$\mathbf{v} = \frac{\mathrm{d}\mathbf{x}}{\mathrm{d}t}, \tag{5.2.3}$$

$$\mathbf{a} = \frac{\mathrm{d}\mathbf{v}}{\mathrm{d}t} = \frac{\mathrm{d}^2\mathbf{x}}{\mathrm{d}^2 t}. \tag{5.2.4}$$

To calculate the 2PN accurate LMF, we need the time derivative of the source multipole moments. Hence we need 2PN accurate equations of motion for the compact binary system in the center of mass frame, which is quoted below [104]:

$$a^i = -\frac{G\,m}{r^2}\left\{\left[P_1 - \frac{\eta}{c^5}\left(\frac{136}{15}\frac{G^2\,m^2}{r^2}\dot{r} + \frac{24}{5}\frac{G\,m}{r}\dot{r}v^2\right)\right]n^i + \left[P_2\,\frac{\dot{r}}{c^2} + \frac{\eta}{c^5}\left(\frac{24}{5}\frac{G^2\,m^2}{r^2} + \frac{8}{5}\frac{G\,m}{r}v^2\right)\right]v^i\right\}, \tag{5.2.5}$$

where,

$$\begin{aligned}
P_1 =\ & 1 + \frac{1}{c^2}\left[\frac{G\,m}{r}(-4-2\eta) - \frac{3\dot{r}^2\eta}{2} + v^2(1+3\eta)\right] + \frac{1}{c^4}\left[\frac{G^2\,m^2}{r^2}\left(9 + \frac{87\eta}{4}\right) + \dot{r}^4\left(\frac{15\eta}{8} - \frac{45\eta^2}{8}\right)\right. \\
& \left. + v^4\left(3\eta - 4\eta^2\right) + \frac{G\,m}{r}\dot{r}^2\left(-2 - 25\eta - 2\eta^2\right) + v^2\left(\frac{G\,m}{r}\left(-\frac{13\eta}{2} + 2\eta^2\right) + \dot{r}^2\left(-\frac{9\eta}{2} + 6\eta^2\right)\right)\right] \\
& + \frac{1}{c^6}\left[\frac{G^3\,m^3}{r^3}\left(-16 - \frac{1399\eta}{12} + \frac{41\pi^2\eta}{16} - \frac{71\eta^2}{2}\right) + \frac{G\,m}{r}\dot{r}^4\left(79\eta - \frac{69\eta^2}{2} - 30\eta^3\right) + \dot{r}^6\left(-\frac{35\eta}{16}\right.\right. \\
& \left. + \frac{175\eta^2}{16} - \frac{175\eta^3}{16}\right) + \frac{G^2\,m^2}{r^2}\dot{r}^2\left(1 + \frac{22717\eta}{168} + \frac{615\pi^2\eta}{64} + \frac{11\eta^2}{8} - 7\eta^3\right) + v^6\left(\frac{11\eta}{4} - \frac{49\eta^2}{4}\right. \\
& \left. + 13\eta^3\right) + v^4\left(\dot{r}^2\left(-\frac{15\eta}{2} + \frac{237\eta^2}{8} - \frac{45\eta^3}{2}\right) + \frac{G\,m}{r}\left(\frac{75\eta}{4} + 8\eta^2 - 10\eta^3\right)\right) + v^2\left(\frac{G^2\,m^2}{r^2}\times\right. \\
& \times\left(-\frac{20827\eta}{840} - \frac{123\pi^2\eta}{64} + \eta^3\right) + \frac{G\,m}{r}\dot{r}^2\left(-121\eta + 16\eta^2 + 20\eta^3\right) + \dot{r}^4\left(\frac{15\eta}{2} - \frac{135\eta^2}{4}\right. \\
& \left.\left.\left. + \frac{255\eta^3}{8}\right)\right)\right],
\end{aligned} \tag{5.2.6a}$$

$$\begin{aligned}
P_2 =\ & -4 + 2\eta + \frac{1}{c^2}\left[v^2\left(-\frac{15\eta}{2} - 2\eta^2\right) + \dot{r}^2\left(\frac{9\eta}{2} + 3\eta^2\right) + \frac{G\,m}{r}\left(2 + \frac{41\eta}{2} + 4\eta^2\right)\right] \\
& + \frac{1}{c^4}\left[\dot{r}^4\left(-\frac{45\eta}{8} + 15\eta^2 + \frac{15\eta^3}{4}\right) + v^4\left(-\frac{65\eta}{8} + 19\eta^2 + 6\eta^3\right) + \frac{G^2\,m^2}{r^2}\left(-4 - \frac{5849\eta}{840} - \frac{123\pi^2\eta}{32}\right.\right. \\
& \left. + 25\eta^2 + 8\eta^3\right) + \frac{G\,m}{r}\dot{r}^2\left(\frac{329\eta}{6} + \frac{59\eta^2}{2} + 18\eta^3\right) + v^2\left(\dot{r}^2\left(12\eta - \frac{111\eta^2}{4} - 12\eta^3\right) + \frac{G\,m}{r}\left(-15\eta\right.\right. \\
& \left.\left.\left. - 27\eta^2 - 10\eta^3\right)\right)\right],
\end{aligned} \tag{5.2.6b}$$

where the $\dot{r}$ and $\ddot{r}$ denote the first and the second time derivatives of the orbital separation r respectively. Furthermore, the above equation of motion can be used to write down the following expressions in order to obtain the derivatives of the multipole moments,

$$\dot{v} = \frac{\mathbf{a}\cdot\mathbf{v}}{v}, \tag{5.2.7}$$

$$\ddot{r} = \frac{1}{r}\left[\left(v^2 - \dot{r}^2\right) + \mathbf{a}\cdot\mathbf{x}\right], \tag{5.2.8}$$

with the magnitude of the orbital velocity being, $v = |\mathbf{v}|$.

5.3 Source multipole moments

To evaluate the instantaneous and the hereditary contributions to the LMF, we need the explicit expressions for the various multipole moments for compact binaries moving in quasi-elliptical orbits. These are obtained from the long algebraic computations (see ref. [106] for details) using MPM-PN formalism, briefly described in chapter 2. In this section, we explicitly quote all the source multipole moments in terms of dynamical variables $(r, \dot{r}, \mathbf{x}, \mathbf{v})$ at second Post-Newtonian (PN) order [61, 105]. The mass-quadrupole moment is first computed in ref. [105] and also quoted in ref. [61] in the center of mass frame in harmonic coordinates. At 2PN accuracy this reads,

$$I_{ij} = \eta m \left[A_1\, x_{\langle i}x_{j\rangle} + A_2\, \frac{r\dot{r}}{c^2}\, x_{\langle i}v_{j\rangle} + A_3\, \frac{r^2}{c^2}\, v_{\langle i}v_{j\rangle}\right] + O\left(\frac{1}{c^5}\right), \tag{5.3.1}$$

where,

$$\begin{aligned} A_1 =\; & 1 + \frac{1}{c^2}\left[v^2\left(\frac{29}{42} - \frac{29\,\eta}{14}\right) + \frac{G\,m}{r}\left(-\frac{5}{7} + \frac{8\,\eta}{7}\right)\right] + \frac{1}{c^4}\left[\frac{G\,m}{r}v^2\left(\frac{2021}{756} - \frac{5947\,\eta}{756} - \frac{4883\,\eta^2}{756}\right)\right. \\ & + \frac{G\,m}{r}\dot{r}^2\left(-\frac{131}{756} + \frac{907\,\eta}{756} - \frac{1273\,\eta^2}{756}\right) + \frac{G^2\,m^2}{r^2}\left(-\frac{355}{252} - \frac{953\,\eta}{126} + \frac{337\,\eta^2}{252}\right) + v^4\left(\frac{253}{504} - \frac{1835\,\eta}{504}\right. \\ & \left.\left. + \frac{3545\,\eta^2}{504}\right)\right], \end{aligned} \tag{5.3.2a}$$

$$A_2 = -\frac{4}{7} + \frac{12\,\eta}{7} + \frac{1}{c^2}\left[v^2\left(-\frac{26}{63} + \frac{202\,\eta}{63} - \frac{418\,\eta^2}{63}\right) + \frac{G\,m}{r}\left(-\frac{155}{54} + \frac{4057\,\eta}{378} + \frac{209\,\eta^2}{54}\right)\right], \tag{5.3.2b}$$

$$\begin{aligned} A_3 =\; & \frac{11}{21} - \frac{11\,\eta}{7} + \frac{1}{c^2}\left[\frac{G\,m}{r}\left(\frac{106}{27} - \frac{335\,\eta}{189} - \frac{985\,\eta^2}{189}\right) + \dot{r}^2\left(\frac{5}{63} - \frac{25\,\eta}{63} + \frac{25\,\eta^2}{63}\right) + v^2\left(\frac{41}{126}\right.\right. \\ & \left.\left. - \frac{337\,\eta}{126} + \frac{733\,\eta^2}{126}\right)\right]. \end{aligned} \tag{5.3.2c}$$

Mass octupole moment, I_{ijk}, at 2PN, the higher order mass-type moment I_{ijkl} at 1PN and I_{ijklm} at Newtonian order, are as follows [61]:

$$I_{ijk} = -\eta\, m\, \sqrt{1-4\eta}\left\{\left[B_1 - \frac{56}{9}\frac{\eta}{c^5}\frac{G^2 m^2}{r^2}\,\dot{r}\right] x_{\langle ijk\rangle} + \left[B_2\,\frac{r\,\dot{r}}{c^2} + \frac{\eta\, r}{c^5}\left(\frac{232}{15}\frac{G^2 m^2}{r^2} - \frac{12}{5}\frac{G\,m}{r}\,v^2\right)\right] x_{\langle ij}v_{k\rangle} + B_3\,\frac{r^2}{c^2}\,x_{\langle i}v_{jk\rangle} + B_4\,\frac{r^3\,\dot{r}}{c^4}\,v_{\langle ijk\rangle}\right\} + O\left(\frac{1}{c^6}\right), \quad (5.3.3)$$

where,

$$B_1 = 1 + \frac{1}{c^2}\left[v^2\left(\frac{5}{6} - \frac{19\,\eta}{6}\right) + \frac{G\,m}{r}\left(-\frac{5}{6} + \frac{13\,\eta}{6}\right)\right] + \frac{1}{c^4}\left[\frac{G\,m}{r}v^2\left(\frac{3853}{1320} - \frac{14257\,\eta}{1320} - \frac{17371\,\eta^2}{1320}\right) + \frac{G^2 m^2}{r^2}\left(-\frac{47}{33} - \frac{1591\,\eta}{132} + \frac{235\,\eta^2}{66}\right) + v^4\left(\frac{257}{440} - \frac{7319\,\eta}{1320} + \frac{5501\,\eta^2}{440}\right) + \frac{G\,m}{r}\,\dot{r}^2\left(-\frac{247}{1320} + \frac{531\,\eta}{440} - \frac{1347\,\eta^2}{440}\right)\right], \quad (5.3.4a)$$

$$B_2 = -(1-2\,\eta) + \frac{1}{c^2}\left[v^2\left(-\frac{13}{22} + \frac{107\,\eta}{22} - \frac{102\,\eta^2}{11}\right) + \frac{G\,m}{r}\left(-\frac{2461}{660} + \frac{8689\,\eta}{660} + \frac{1389\,\eta^2}{220}\right)\right], \quad (5.3.4b)$$

$$B_3 = 1 - 2\,\eta + \frac{1}{c^2}\left[\frac{G\,m}{r}\left(\frac{1949}{330} + \frac{62\,\eta}{165} - \frac{483\,\eta^2}{55}\right) + v^2\left(\frac{61}{110} - \frac{519\,\eta}{110} + \frac{504\,\eta^2}{55}\right) + \dot{r}^2\left(-\frac{1}{11} + \frac{4\,\eta}{11} - \frac{3\,\eta^2}{11}\right)\right], \quad (5.3.4c)$$

$$B_4 = \left(\frac{13}{55} - \frac{52\,\eta}{55} + \frac{39\,\eta^2}{55}\right), \quad (5.3.4d)$$

$$I_{ijkl} = \eta\, m\left\{x_{\langle ijkl\rangle}\left[1 - 3\,\eta + \frac{1}{c^2}\left[\frac{G\,m}{r}\left(-\frac{10}{11} + \frac{61\,\eta}{11} - \frac{105\,\eta^2}{11}\right) + v^2\left(\frac{103}{110} - \frac{147\,\eta}{22} + \frac{279\,\eta^2}{22}\right)\right]\right] + x_{\langle ijk}v_{l\rangle}\frac{r\,\dot{r}}{c^2}\left[-\frac{72}{55} + \frac{72\,\eta}{11} - \frac{72\,\eta^2}{11}\right] + x_{\langle ij}v_{kl\rangle}\frac{r^2}{c^2}\left[\frac{78}{55} - \frac{78\,\eta}{11} + \frac{78\,\eta^2}{11}\right]\right\} + O\left(\frac{1}{c^3}\right), \quad (5.3.5)$$

$$I_{ijklm} = -\eta\, m\,\sqrt{1-4\eta}\,x_{\langle ijklm\rangle}\left[1 - 2\,\eta\right] + O\left(\frac{1}{c^2}\right). \quad (5.3.6)$$

The accuracy of the current quadrupole moment needed for present purpose is 2PN, whereas J_{ijk} is needed at 1PN and J_{ijkl} at Newtonian order. They are quoted below [61]:

$$J_{ij} = -\eta m \sqrt{1-4\eta}\left\{\left[C_1 - \frac{62}{7}\frac{\dot{r}\,\eta}{c^5}\frac{G^2m^2}{r^2}\right]\epsilon_{ab\langle i}x_{j\rangle a}v_b + \left[C_2\frac{r\,\dot{r}}{c^2} + \frac{r\,\eta}{c^5}\frac{G\,m}{r}\left(\frac{216}{35}\frac{G\,m}{r} - \frac{4}{5}v^2\right)\right]\epsilon_{ab\langle i}v_{j\rangle b}x_a\right\} + O\left(\frac{1}{c^6}\right), \tag{5.3.7}$$

where,

$$C_1 = 1 + \frac{1}{c^2}\left[v^2\left(\frac{13}{28} - \frac{17\,\eta}{7}\right) + \frac{G\,m}{r}\left(\frac{27}{14} + \frac{15\,\eta}{7}\right)\right] + \frac{1}{c^4}\left[\frac{G\,m}{r}v^2\left(\frac{671}{252} - \frac{1297\,\eta}{126} - \frac{121\,\eta^2}{12}\right) + \frac{G\,m}{r}\dot{r}^2\left(-\frac{5}{252} - \frac{241\,\eta}{252} - \frac{335\,\eta^2}{84}\right) + \frac{G^2m^2}{r^2}\left(-\frac{43}{252} - \frac{1543\,\eta}{126} + \frac{293\,\eta^2}{84}\right) + v^4\left(\frac{29}{84} - \frac{11\,\eta}{3} + \frac{505\,\eta^2}{56}\right)\right], \tag{5.3.8a}$$

$$C_2 = \frac{5}{28}(1-2\,\eta) + \frac{1}{504}\frac{1}{c^2}\left[\frac{G\,m}{r}\left(824 + 1348\,\eta - 1038\,\eta^2\right) + 75v^2\left(1 - 7\,\eta + 12\,\eta^2\right)\right], \tag{5.3.8b}$$

$$J_{ijk} = \eta\, m\, \epsilon_{ab\langle i}\left\{x_{jk\rangle a}v_b\left[1 - 3\,\eta + \frac{1}{c^2}\left[\frac{G\,m}{r}\left(\frac{14}{9} - \frac{16\,\eta}{9} - \frac{86\,\eta^2}{9}\right) + v^2\left(\frac{41}{90} - \frac{77\,\eta}{18} + \frac{185\,\eta^2}{18}\right)\right]\right] + x_j v_{k\rangle b}x_a\frac{r\,\dot{r}}{c^2}\left[\frac{2}{9} - \frac{10\,\eta}{9} + \frac{10\,\eta^2}{9}\right] + v_{jk\rangle b}x_a\frac{r^2}{c^2}\left[\frac{7}{45}\left(1 - 5\,\eta + 5\,\eta^2\right)\right]\right\} + O\left(\frac{1}{c^3}\right), \tag{5.3.9a}$$

$$J_{ijkl} = -\eta\, m\sqrt{1-4\eta}\,\epsilon_{ab\langle i}x_{jkl\rangle a}v_b\left[1 - 2\,\eta\right] + O\left(\frac{1}{c^2}\right). \tag{5.3.9b}$$

In the above expressions, $x_{ijk\ldots} = x_i x_j x_k \ldots$, $v_{ijk\ldots} = v_i v_j v_k \ldots$ and $\langle\rangle$ denotes that the terms are symmetric and trace-free w.r.t the indices listed inside the brackets.

5.4 Instantaneous contribution to the Linear momentum flux

With all the ingredients provided in the previous sections we now compute the instantaneous contribution to the LMF using Eq. (5.1.13). First we calculate all the time derivatives of the source multipole moments given in Eqs. (5.3.1)-(5.3.9b) using 2PN equation of motion as quoted in Eq. (5.2.5). Next we perform all the contractions in Eq. (5.1.13) and the resulting instantaneous linear momentum flux in terms of dynamical variables $(r, \dot{r}, v, \mathbf{v}, \mathbf{x})$ is given by,

$$
\begin{aligned}
\mathcal{F}_i^{\rm inst} = {} & \frac{G^2 m^4 \dot{r}}{r^5}\sqrt{1-4\eta}\eta^2 \mathbf{x}_i \Big(\frac{32}{35}\frac{Gm}{r} - \frac{24}{7}\dot{r}^2 + \frac{88}{21}v + \frac{1}{c^2}\Big(\frac{G^2m^2}{r^2}\Big[-\frac{472}{63} + \frac{16}{315}\eta\Big] + v^4\Big[\frac{6808}{315} - \frac{6232}{315}\eta\Big] \\
& + \dot{r}^2 v^2\Big[-\frac{22672}{315} + \frac{15016}{315}\eta\Big] + \frac{4}{945}\frac{Gm}{r}\Big[3(956\eta - 4385)v^2 + (12301 - 1168\eta)\dot{r}^2\Big] + \Big[\frac{14744}{315} \\
& - \frac{1184}{45}\eta\Big]\dot{r}^4\Big) + \frac{1}{c^4}\Big(\frac{G^3m^3}{r^3}\Big[\frac{211124}{10395} + \frac{126184}{3465}\eta - \frac{4856}{3465}\eta^2\Big] + v^6\Big[\frac{272}{231} - \frac{75178\eta}{693} + \frac{299872\eta^2}{3465}\Big] \\
& + v^4\dot{r}^2\Big[\frac{84928}{3465} + \frac{1800718}{3465}\eta - \frac{67072}{231}\eta^2\Big] - v^2\dot{r}^4\Big[\frac{85808}{3465} + \frac{2411504}{3465}\eta - \frac{4544}{15}\eta^2\Big] + \dot{r}^6\Big[\frac{32}{33} \\
& + \frac{197704}{693}\eta - \frac{10048}{99}\eta^2\Big] + \frac{G^2m^2}{r^2}\Big[\Big(-\frac{3213692}{10395} + \frac{758}{7}\eta - \frac{57748}{3465}\eta^2\Big)\dot{r}^2 + v^2\Big(\frac{432944}{1485} \\
& - \frac{1508722}{10395}\eta + \frac{424432}{10395}\eta^2\Big)\Big] + \frac{Gm}{r}\Big[\dot{r}^4\Big(-\frac{57608\eta^2}{385} + \frac{205162\eta}{315} - \frac{263524}{693}\Big) + \dot{r}^2v^2\Big(\frac{927602\eta^2}{3465} \\
& - \frac{905864\eta}{945} + \frac{585394}{1155}\Big) - v^4\Big(\frac{357746\eta^2}{3465} - \frac{917366\eta}{3465} + \frac{152818}{1155}\Big)\Big]\Big)\Big) + \frac{G^2m^4}{r^4}\sqrt{1-4\eta}\eta^2\mathbf{v}_i\Big(-\frac{64}{105}\frac{Gm}{r} \\
& + \frac{304}{105}\dot{r}^2 - \frac{80}{21}v^2 + \frac{1}{c^2}\Big[\frac{G^2m^2}{r^2}\Big(\frac{32}{5} + \frac{544}{945}\eta\Big) + v^4\Big(\frac{592\eta}{45} - \frac{740}{63}\Big) + \frac{Gm}{r}\Big(\dot{r}^2\Big[-\frac{10796}{315} - \frac{8}{63}\eta\Big] \\
& + v^2\Big[\frac{3628}{105} - \frac{216}{35}\eta\Big]\Big) + \dot{r}^2v^2\Big(\frac{448}{9} - \frac{2056}{63}\eta\Big) + \dot{r}^4\Big(\frac{5576\eta}{315} - \frac{10652}{315}\Big)\Big] + \frac{1}{c^4}\Big[\frac{G^3m^3}{r^3}\Big(-\frac{945388}{31185} \\
& - \frac{30608}{1155}\eta + \frac{17648}{10395}\eta^2\Big) + v^6\Big(-\frac{61928}{3465} + \frac{6196}{99}\eta - \frac{183712}{3465}\eta^2\Big) + \dot{r}^2v^4\Big(\frac{293756}{3465} - \frac{245792}{693}\eta \\
& + \frac{13616}{77}\eta^2\Big) + \dot{r}^4v^2\Big(-\frac{484336}{3465} + \frac{31268}{63}\eta - \frac{204856}{1155}\eta^2\Big) + \dot{r}^6\Big(\frac{245356}{3465} - \frac{142280}{693}\eta + \frac{195128}{3465}\eta^2\Big) \\
& + \frac{G^2m^2}{r^2}\Big(\dot{r}^2\Big[\frac{1524524}{10395} - \frac{49684}{2079}\eta - \frac{8684}{2079}\eta^2\Big] + v^2\Big[-\frac{764668}{6237} + \frac{32188}{945}\eta - \frac{4436}{385}\eta^2\Big]\Big) \\
& + \frac{Gm}{r}\Big(\dot{r}^4\Big[\frac{965896}{3465} - \frac{1388906\eta}{3465} + \frac{672464\eta^2}{10395}\Big] + \dot{r}^2v^2\Big(-\frac{63386\eta^2}{495} + \frac{93284\eta}{165} - \frac{399986}{1155}\Big) \\
& + v^4\Big(\frac{160346\eta^2}{3465} - \frac{429626\eta}{3465} + \frac{94214}{1155}\Big)\Big)\Big]\Big).
\end{aligned}
\tag{5.4.1}
$$

Eq. (5.4.1) reduces to the instantaneous part of Eq. (1) of [108] in the circular orbit limit where $\dot{r} \to 0$. One may notice here that the component of the linear momentum flux along the radial direction (i.e. the term associated to the radial direction, $\mathbf{x}$) depends on $\dot{r}$ and hence in case of circular orbit contributions from these terms are 0 and the emission of linear momentum is along the direction of the relative velocity vector, $\mathbf{v}$ only.

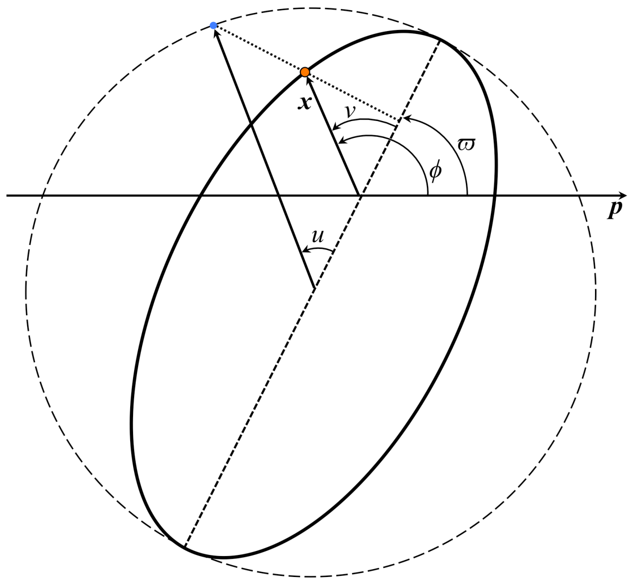

Figure 5.1. **p** is a unit vector along a reference axis. **x** is the relative separation vector joining the focus of the ellipse to the position of the reduced mass making an angle ϕ with **p** and an angle v with the semi-major axis of the ellipse. Eccentric anomaly u is the angle between the semi-major axis and the line drawn from the center to a point on the auxiliary circle, i.e. the point on the circle made by extended perpendicular line drawn from the semi-major axis to the reduced mass. Figure courtesy ref. [239]

The above expression for linear momentum flux is given in terms of generic dynamical variables $r, \dot{r}, \phi$ and $\dot{\phi}$. While specializing to the case of quasi-elliptical orbits, it is usually convenient to express these dynamical variables in terms of the parameters associated with quasi-elliptical orbits, namely the generalized quasi-Keplerian representation (QKR) of the orbital dynamics. One needs 2PN QKR to compute the 2PN LMF in terms of the orbital parameters. In the next section we briefly start with the description of the parametrization of Keplerian orbits followed by its PN generalization, the quasi-Keplerian (QK) representation.

5.5 Keplerian and Quasi-Keplerian parametrization

The Keplerian parametrization for the Newtonian motion of a compact binary system is widely used in describing celestial mechanics. In polar coordinates and in the center of mass frame, the parametrization is given by,

$$r_{\mathrm{N}} = a(1 - e\cos u)\,, \tag{5.5.1a}$$

$$\phi_{\mathrm{N}} = V_N\,, \tag{5.5.1b}$$

$$l_{\mathrm{N}} = n(t - t_0) = u - e\sin u\,, \tag{5.5.1c}$$

$$v = V_{\mathrm{N}}(u) \equiv 2\arctan\left[\left(\frac{1+e}{1-e}\right)^2 \tan\left(\frac{u}{2}\right)\right]\,, \tag{5.5.1d}$$

where subscript N denotes the Newtonian quantities. r_N and ϕ_N together define the relative separation vector, $\mathbf{r_N} = r_N(\cos\phi_n, \sin\phi_n, 0)$. The semi-major axis of the orbit is a with an eccentricity e. Both of these can be written in terms of the conserved orbital energy and angular momentum which completely define the orbits. Here u, v, l are the eccentric, true, and mean anomalies and n is the mean motion, $n = 2\pi/P$, where P is the radial orbital (periastron to periastron) period. Geometrical interpretation of various angles are given in fig. 5.1. To describe the complete parametrization, a circle has been drawn circumscribing the ellipse with a radius the same as the semi-major axis. This is called the auxiliary circle. The eccentric anomaly is defined w.r.t. the auxiliary circle.

Having discussed the Keplerian representation (KR), we now describe the PN extension of the KR, the quasi-Keplerian representation at 2PN. In 1985, Damour and Deruelle generalized this parametrization up to 1PN [140] and proposed a "Keplerian like parametrization". Later in refs. [147, 270, 294] the 2PN extension of the parametric solution has been quoted. QK parametrization is obtained considering 2PN conservative contributions to the binary motion and it admits very similar expressions as the Keplerian one but with more complex structure. The extension of Eq. (5.5.1) to 2PN has the following form,

$$r = a_r(1 - e_r\cos u)\,, \tag{5.5.2a}$$

$$\phi = \lambda + W(l; n, e_t)\,, \tag{5.5.2b}$$

$$\lambda = (1 + k)n(t - t_0) + c_\lambda\,, \tag{5.5.2c}$$

$$W(l; n, e_t) = (1 + k)(v - l) + \frac{f_{4\phi}}{c^4}\sin 2v + \frac{g_{4\phi}}{c^4}\sin 3v\,, \tag{5.5.2d}$$

$$l = n(t-t_0) + c_l = u - e_t \sin u + \frac{g_{4t}}{c^4}(v-u) + \frac{f_{4t}}{c^4}\sin v\,, \tag{5.5.2e}$$

$$v = V(u) \equiv 2\arctan\left[\left(\frac{1+e_\phi}{1-e_\phi}\right)^2 \tan\left(\frac{u}{2}\right)\right]. \tag{5.5.2f}$$

The expressions of the functions f_{4t}, g_{4t}, $f_{4\phi}$, $f_{6\phi}$ and $g_{4\phi}$ are given in ref. [232]. a_r is some 2PN equivalent "semi-major axis". Unlike the KR, in QKR, there appear three eccentricities e_r, e_t and e_ϕ instead of one to completely parameterize the motion. These eccentricities can also be written in terms of the 2PN conserved energy and the angular momentum. We find it convenient to use e_t and the mean motion n as the constants of motion and express all the dynamical variables in terms of these two. We have used a combination of total mass and n given by $\xi = Gmn/c^3$, as a PN expansion parameter. Here we quote all the dynamical variables correct up to 2PN in terms of e_t, eccentric anomaly u, and the post-Newtonian expansion parameter ξ [239].

$$r = m\xi^{-2/3}(1-e_t\cos u)\Bigg(1+[-18+2\eta-(6-7\eta)e_t\cos u]\frac{\xi^{2/3}}{6(1-e_t\cos u)}+\Big\{-72(4-7\eta)+[72+30\eta+8\eta^2 -(72-231\eta+35\eta^2)e_t\cos u](1-e_t^2)-36(5-2\eta)(2+e_t\cos u)\sqrt{1-e_t^2}\Big\}\frac{\xi^{4/3}}{72(1-e_t^2)(1-e_t\cos u)}+O(\xi^2)\Bigg), \tag{5.5.3a}$$

$$\begin{aligned}\dot{r} = {}& \frac{\xi^{1/3}}{(1-e_t\cos u)}e_t\sin u\Bigg\{1+(6-7\eta)\frac{\xi^{2/3}}{6}+\Big[-468-15\eta+35\eta^2+(135\eta-9\eta^2)e_t^2+(324+342\eta \\ & -96\eta^2)e_t\cos u+(216-693\eta+105\eta^2)(e_t\cos u)^2-(72-231\eta+35\eta^2)(e_t\cos u)^3 \\ & +\frac{36}{\sqrt{1-e_t^2}}(1-e_t\cos u)^2(4-e_t\cos u)(5-2\eta)\Big]\frac{\xi^{4/3}}{72(1-e_t\cos u)^3}+O(\xi^2)\Bigg\},\end{aligned} \tag{5.5.3b}$$

$$\phi(\lambda, l) = \lambda + W(l)\,, \tag{5.5.3c}$$

$$\lambda = (1+k)l\,, \tag{5.5.3d}$$

$$k = \frac{3\xi^{2/3}}{1-e_t^2} + \left[78 - 28\eta + (51 - 26\eta)e_t^2\right]\frac{\xi^{4/3}}{4(1-e_t^2)^2} + \Big\{18240 - 25376\eta + 492\pi^2\eta + 896\eta^2$$
$$+ (28128 - 27840\eta + 123\pi^2\eta + 5120\eta^2)e_t^2 + (2496 - 1760\eta + 1040\eta^2)e_t^4$$
$$+ \left[1920 - 768\eta + (3840 - 1536\eta)e_t^2\right]\sqrt{1-e_t^2}\Big\}\frac{\xi^2}{128(1-e_t^2)^3}\,, \quad (5.5.3e)$$

$$l = u - e_t\sin u + \left[(15\eta - \eta^2)e_t\sin u\sqrt{1-e_t^2} + 12(5-2\eta)(v-u)(1-e_t\cos u)\right]\frac{\xi^{4/3}}{8\sqrt{1-e_t^2}(1-e_t\cos u)}$$
$$+ O(\xi^2), \quad (5.5.3f)$$

$$W(l) = (v - u + e_t\sin u) + (v - u + e_t\sin u)\frac{3\xi^{2/3}}{1-e_t^2} + \Big(8\left[78 - 28\eta + (51-26\eta)e_t^2 - 6(5-2\eta)(1-e_t^2)^{3/2}\right]$$
$$(v-u)(1-e_t\cos u)^3 + \Big\{624 - 284\eta + 4\eta^2 + (408 - 88\eta - 8\eta^2)e_t^2 - (60\eta - 4\eta^2)e_t^4 + [-1872 + 792\eta$$
$$-8\eta^2 - (1224 - 384\eta - 16\eta^2)e_t^2 + (120\eta - 8\eta^2)e_t^4\Big]e_t\cos u + \Big[1872 - 732\eta + 4\eta^2 + (1224 - 504\eta$$
$$-8\eta^2)e_t^2 - (60\eta - 4\eta^2)e_t^4\Big](e_t\cos u)^2 + \left[-624 + 224\eta - (408 - 208\eta)e_t^2\right](e_t\cos u)^3\Big\}e_t\sin u$$
$$+ \Big\{-(8 + 153\eta - 27\eta^2)e_t^2 + (4\eta - 12\eta^2)e_t^4 + \left[8 + 152\eta - 24\eta^2 + (8 + 146\eta - 6\eta^2)e_t^2\right]e_t\cos u$$
$$+ \left[-8 - 148\eta + 12\eta^2 - (\eta - 3\eta^2)e_t^2\right](e_t\cos u)^2\Big\}e_t\sin u\sqrt{1-e_t^2}\Big)\frac{\xi^{4/3}}{32(1-e_t^2)^2(1-e_t\cos u)^3} + O(\xi^2)\,,$$
$$(5.5.3g)$$

$$\dot{\phi} = \frac{(\xi/M)\sqrt{1-e_t^2}}{(1-e_t\cos u)^2}\Big(1 + \left[3 - (4-\eta)e_t^2 + (1-\eta)e_t\cos u\right]\frac{\xi^{2/3}}{(1-e_t^2)(1-e_t\cos u)}$$
$$+ \Big\{144 - 48\eta - (162 + 68\eta - 2\eta^2)e_t^2 + (60 + 26\eta - 20\eta^2)e_t^4 + (18\eta + 12\eta^2)e_t^6 + \Big[-216 + 125\eta + \eta^2$$
$$+(102 + 188\eta + 16\eta^2)e_t^2 - (12 + 97\eta - \eta^2)e_t^4\Big]e_t\cos u + \Big[108 - 97\eta - 5\eta^2 + (66 - 136\eta + 4\eta^2)e_t^2$$
$$-(48 - 17\eta + 17\eta^2)e_t^4\Big](e_t\cos u)^2 + \left[-36 + 2\eta - 8\eta^2 - (6 - 70\eta - 14\eta^2)e_t^2\right](e_t\cos u)^3$$
$$+ 18(1-e_t\cos u)^2(1 - 2e_t^2 + e_t\cos u)(5-2\eta)\sqrt{1-e_t^2}\Big\}\frac{\xi^{4/3}}{12(1-e_t^2)^2(1-e_t\cos u)^3} + O(\xi^2)\Big)\,.$$
$$(5.5.3h)$$

We have quoted the above expressions in terms the radial frequency $\omega_r = n = \xi/m$ (related to the time to return to the periastron), convenient for the binary motion in quasi-elliptical orbits at 2PN. In contrast to this, the convenient choice for a binary moving in circular orbit would be to use the azimuthal frequency $\omega_\phi \equiv \xi_\phi/m$ (which is related to the time to come back to the same azimuthal angular position in the orbit). The relation between these two variables can easily be obtained by taking the orbital average of the quantity $\dot{\phi}$,

$$\begin{aligned}\xi_\phi &= M\langle\dot{\phi}\rangle = M\frac{d\lambda}{dt} = (1+k)\xi \\ &= \xi\Bigg(1 + \frac{3\xi^{2/3}}{1-e_t^2} + \Big[78 - 28\eta + (51-26\eta)e_t^2\Big]\frac{\xi^{4/3}}{4(1-e_t^2)^2} + \Big\{18240 - (25376 - 492\pi^2)\eta + 896\eta^2 \\ &\qquad + [28128 - (27840 - 123\pi^2)\eta + 5120\eta^2]e_t^2 + (2496 - 1760\eta + 1040\eta^2)e_t^4 \\ &\qquad + \Big[1920 - 768\eta + (3840 - 1536\eta)e_t^2\Big]\sqrt{1-e_t^2}\Big\}\frac{\xi^2}{128(1-e_t^2)^3}\Bigg). \end{aligned} \tag{5.5.4}$$

Inverting the above equation we obtain ξ_ϕ in terms of ξ, which has been used in further calculations,

$$\begin{aligned}\xi &= \xi_\phi\Bigg(1 - \frac{3\xi_\phi^{2/3}}{1-e_t^2} - \Big[18 - 28\eta + (51-26\eta)e_t^2\Big]\frac{\xi_\phi^{4/3}}{4(1-e_t^2)^2} - \Big\{-192 - (14624 - 492\pi^2)\eta + 896\eta^2 \\ &\qquad + [8544 - (17856 - 123\pi^2)\eta + 5120\eta^2]e_t^2 + (2496 - 1760\eta + 1040\eta^2)e_t^4 \\ &\qquad + \Big[1920 - 768\eta + (3840 - 1536\eta)e_t^2\Big]\sqrt{1-e_t^2}\Big\}\frac{\xi_\phi^2}{128(1-e_t^2)^3}\Bigg). \end{aligned} \tag{5.5.5}$$

In the previous chapters of this thesis, we have used x or v to express the PN quantities. For convenience, in this chapter we use azimuthal frequency, ξ_ϕ as the expansion parameter. ξ_ϕ/m, is directly related to the usual PN expansion parameter x or v by the following relation,

$$\xi_\phi = M\omega_\phi = x^{3/2} = v^3\,. \tag{5.5.6}$$

5.6 Instantaneous LMF for compact binaries in terms of quasi-Keplerian parameters in the small eccentricity limit

We have provided all the necessary ingredients to compute LMF from a compact binary moving in quasi-elliptical orbit in terms of its orbital elements. As a next step, we re-express the instantaneous contribution to the LMF in terms of QK parameters. To be precise, we use Eqs. (5.5.3) to re-express Eq. (5.4.1) in terms of $\{\xi_\phi, e_t, u\}$. To re-write a closed form expression of the flux in terms of the orbital phase ϕ, we invert Eq. (5.5.3c), which further requires a re-expansion of the same in a series w.r.t. e_t. We keep the terms only up to $O(e_t^2)$ to obtain u in terms of ϕ. Finally, we give the instantaneous contribution to the LMF emitted by a non-spinning compact binary system in an quasi-elliptical orbit in Eqs. (5.6.1a) and (5.6.1b) in the small eccentricity limit. The emission of linear momentum is more towards the merger of the binary where the eccentricity is expected to be small. Hence we provide all our results here, retaining the terms only up to $O(e_t^2)$.

$$
\begin{aligned}
\mathcal{F}_x^{\text{inst}} = {} & \frac{464}{105}\frac{c^4}{G}\sqrt{1-4\eta}\eta^2\xi_\phi^{11/3}\Big(\sin\phi + \frac{407}{116}e_t\sin 2\phi + e_t^2\Big[\frac{633}{58}\sin\phi + \frac{151}{29}\sin 3\phi\Big] + \xi_\phi^{2/3}\Big[\Big(-\frac{452}{87} - \frac{1139}{522}\eta\Big)\sin\phi \\
& + e_t\Big(\Big[-\frac{1094}{87} - \frac{2883}{232}\eta\Big]\sin 2\phi - \frac{1221}{116}\phi\cos 2\phi + \frac{1167}{116}\phi\Big) + e_t^2\Big(\Big[-\frac{2599}{116} - \frac{12683}{261}\eta\Big]\sin\phi - \Big[\frac{4213}{348} \\
& + \frac{9767}{348}\eta\Big]\sin 3\phi + \frac{831}{29}\phi\cos\phi - \frac{906}{29}\phi\cos 3\phi\Big)\Big] + \xi_\phi^{4/3}\Big[\Big(-\frac{71345}{22968} + \frac{36761}{2088}\eta + \frac{147101}{68904}\eta^2\Big)\sin\phi \\
& + e_t\Big(\Big[-\frac{2808541}{68904} + \frac{6878125}{91872}\eta + \frac{622681}{30624}\eta^2 - \frac{3663}{232}\phi^2\Big]\sin 2\phi + \Big[\frac{5089}{232} + \frac{14347}{232}\eta\Big]\phi\cos 2\phi \\
& - \Big[\frac{3665}{232} + \frac{41531}{696}\eta\Big]\phi\Big) + e_t^2\Big(\Big[-\frac{931021}{6264} + \frac{1108915}{5742}\eta + \frac{7192771}{68904}\eta^2 + \frac{2493}{29}\phi^2\Big]\sin\phi \\
& + \Big[-\frac{23717}{176} + \frac{2249135}{15312}\eta + \frac{3092275}{45936}\eta^2 - \frac{2718}{29}\phi^2\Big]\sin 3\phi + \Big[\frac{201}{29} - \frac{12877}{58}\eta\Big]\phi\cos\phi \\
& + \Big[\frac{1495}{58} + \frac{13995}{58}\eta\Big]\phi\cos 3\phi\Big)\Big]\Big)
\end{aligned} \tag{5.6.1a}
$$

$$
\begin{aligned}
\mathcal{F}_y^{\text{inst}} = {} & \frac{464}{105}\frac{c^4}{G}\sqrt{1-4\eta}\eta^2\xi_\phi^{11/3}\Big(-\cos\phi - e_t\Big[\frac{389}{116} + \frac{407}{116}\cos 2\phi\Big] - e_t^2\Big[\frac{1187}{58}\cos\phi + \frac{151}{29}\cos 3\phi\Big] \\
& + \xi_\phi^{2/3}\Big[\Big(\frac{452}{87} + \frac{1139}{522}\eta\Big)\cos\phi + e_t\Big(\frac{3583}{348} + \frac{25193}{2088}\eta + \Big[\frac{1094}{87} + \frac{2883}{232}\eta\Big]\cos 2\phi - \frac{1221}{116}\phi\sin 2\phi\Big) \\
& + e_t^2\Big(\Big[\frac{3993}{116} + \frac{52363}{522}\eta\Big]\cos\phi + \Big[\frac{4213}{348} + \frac{9767}{348}\eta\Big]\cos 3\phi - \frac{831}{29}\phi\sin\phi - \frac{906}{29}\phi\sin 3\phi\Big)\Big] \\
& + \xi_\phi^{4/3}\Big[\Big(\frac{71345}{22968} - \frac{36761\eta}{2088} - \frac{147101\eta^2}{68904}\Big)\cos\phi + e_t\Big(\frac{3212437}{68904} - \frac{185195}{2784}\eta - \frac{5567939}{275616}\eta^2 \\
& + \Big[\frac{2808541}{68904} - \frac{6878125}{91872}\eta - \frac{622681}{30624}\eta^2 + \frac{3663}{232}\phi^2\Big]\cos 2\phi + \frac{3501}{232}\phi^2 + \Big[\frac{5089}{232} + \frac{14347}{232}\eta\Big]\phi\sin 2\phi\Big)
\end{aligned}
$$

$$
+ e_t^2\Big(\Big[\frac{660155}{1566} - \frac{1039069}{2552}\eta - \frac{4040725}{17226}\eta^2 + \frac{2493}{29}\phi^2\Big]\cos\phi - \Big[\frac{201}{29} - \frac{12877}{58}\eta\Big]\phi\sin\phi
+ \Big[\frac{23717}{176} - \frac{2249135}{15312}\eta - \frac{3092275}{45936}\eta^2 + \frac{2718}{29}\phi^2\Big]\cos 3\phi + \Big[\frac{1495}{58} + \frac{13995}{58}\eta\Big]\phi\sin 3\phi\Big)\Big]\Big) \tag{5.6.1b}
$$

Next, we cross check various limiting cases of these results. In the Newtonian limit, Eq. (5.6.1a) & (5.6.1b) represent Eq. (2.23) of ref. [168]. Furthermore Eqs. (5.6.1a) & (5.6.1b) reduce to the instantaneous part of LMF from a compact binary in circular orbit, in the limit $e_t \to 0$ (see Eq.(1) of ref. [108]). In contrast to the circular orbit case, instantaneous contribution to the LMF consists of aperiodic terms, having linear or quadratic dependence on ϕ along with all the periodic terms in ϕ. Only the periodic terms in ϕ contributes to the expression of the recoil for circular orbits, as the other contributions are functions of eccentricity, hence 0. The aperiodic terms arise due to the fact that along with the mass asymmetry that gives rise to the emission of LMF in the first place, in case of elliptical orbits there is another asymmetry in the orbital motion along the y-axis. Since the origin of the reference frame is at one of the foci of the ellipse, the velocity at the pericenter is not the same as the velocity at the apocenter. As a result, there is a flux of linear momenta emitted along the y-direction. This effect is there starting from the Newtonian order (see Eq. (2.23) of ref. [168]). In the next section we focus on the hereditary contribution at 1.5PN.

5.7 Hereditary contribution to the linear momentum flux

Giving a detailed prescription to calculate the instantaneous contribution to LMF in the previous section, we now focus on the hereditary contribution. Due to non-linearity of the Einstein's field equations, the time varying source moments couple to themselves and to others giving rise to the hereditary contributions which depend on the entire history of the system [98]. The leading order hereditary interaction between the mass quadrupole moment (I_{ij}) and mass monopole (M or the ADM mass) appears at relative 1.5PN order. In order to estimate the 2PN accurate LMF, we need to calculate the 1.5PN hereditary contribution to it.

We adopt a semi-analytical method in the frequency domain to calculate the hereditary contribution as proposed in ref. [62]. It is based on the Fourier decomposition of Keplerian motion [248]. Though the general prescription of this decomposition at arbitrary order is quoted in [62], to obtain the 1.5 PN hereditary contribution to the LMF, we need the Fourier decomposition of the multipole moments at Newtonian order only, which simply read,

$$I_L(U) = \sum_{p=-\infty}^{\infty} \mathcal{I}_L e^{ip\ell}, \tag{5.7.1}$$

$$J_{L-1}(U) = \sum_{p=-\infty}^{\infty} \mathcal{J}_{L-1} e^{ip\ell}, \tag{5.7.2}$$

with the inverse relation to be

$$\mathcal{I}_L = \frac{1}{2\pi}\int_0^{2\pi} d\ell I_L(U) e^{-ip\ell} \tag{5.7.3}$$

$$\mathcal{J}_{L-1} = \frac{1}{2\pi}\int_0^{2\pi} d\ell J_{L-1}(U) e^{-ip\ell}. \tag{5.7.4}$$

All the Fourier coefficients in Eqs. (5.7.3) & (5.7.4) can easily be obtained as combinations of Bessel functions. With the correct normalization factors depicted in Eqs (5.1a) & (5.1b) of ref. [62], these coefficients are quoted in Appendix A of the same.

The closed form expressions of the 1.5 PN hereditary contributions, given in Eq. (5.1.14), consist of four integrations on the various combinations of the source moments over time starting from the remote past to the current retarded time. All four terms are evaluated following a similar semi-analytical scheme. Using the Fourier decomposition introduced in Eq. (5.7.1) & (5.7.2) we rewrite the first integral as a sum over all the Fourier indices multiplied with an integration (see Eq. 5.7.7) on a quantity, independent of the Fourier coefficients as well as any other parameters defining the orbital motion, over time. Furthermore we also use the fact that if $\ell(t) = n(t - t_0)$ at the current time t, then at a retarded time $(t-\tau)$, $\ell(t-\tau)$ is simply $(\ell(t) - n\tau)$ where n is the mean motion.

For convenience, we explicitly write the complete expression in Eq. (5.1.14) in terms of the four integrals as defined below,

$$\mathcal{F}_i^{\text{hered}} = \left(\mathcal{F}_i^{\text{hered}}\right)_1 + \left(\mathcal{F}_i^{\text{hered}}\right)_2 + \left(\mathcal{F}_i^{\text{hered}}\right)_3 + \left(\mathcal{F}_i^{\text{hered}}\right)_4. \tag{5.7.5}$$

Now each of the above terms on the right hand side of Eq. (5.7.5), can be written as an infinite sum on the indices of the Bessel functions given by,

$$\begin{aligned}\left(\mathcal{F}_i^{\text{hered}}\right)_1 &= \frac{4\,G^2\,m}{63\,c^{10}}\, I^{(4)}_{ijk}(t) \int_0^\infty d\tau \left[\ln\left(\frac{\tau}{2\tau_0}\right) + \frac{11}{12}\right] I^{(5)}_{jk}(t-\tau) \\ &= \frac{4\,G^2\,m}{63\,c^{10}} \sum_{p=-\infty}^{\infty} (ipn)^4 \underset{(p)}{\mathcal{I}_{ijk}} e^{ip\ell(t)} \sum_{q=-\infty}^{\infty} (iqn)^5 \underset{(q)}{\mathcal{I}_{jk}} e^{iq\ell(t)} \int_0^\infty d\tau \left[\ln\left(\frac{\tau}{2\tau_0}\right) + \frac{11}{12}\right] e^{-iqn\tau} \\ &= \frac{4\,G^2\,m}{63\,c^{10}} \sum_{p,q=-\infty}^{\infty} n^8 (pq)^4 e^{i(p+q)\ell} \underset{(p)}{\mathcal{I}_{ijk}} \underset{(q)}{\mathcal{I}_{jk}} \Big[\frac{i\pi}{2} Sign(-qn) - \Big(\ln(2|-qn|\tau_0 e^{-11/12}) + \gamma_E\Big)\Big], \end{aligned} \tag{5.7.6}$$

where γ_E is the Euler constant, p, q are the Bessel function indices running from 0 to ∞ and the function $Sign(qn) = \pm 1$. To evaluate the time integration in the above expression we use the standard integral quoted below,

$$\int_0^\infty d\tau e^{i\sigma\tau} \ln\left(\frac{\tau}{2r_0}\right) = -\frac{1}{\sigma}\Big[\frac{\pi}{2} Sign(\sigma) + i\Big(\ln(2|\sigma|r_0) + \gamma_E\Big)\Big]. \tag{5.7.7}$$

Following the very similar method we obtain the other integrals in Eq. (5.7.5) as well.

$$\begin{aligned}\left(\mathcal{F}_i^{\text{hered}}\right)_2 &= \frac{4\,G^2\,m}{63\,c^{10}}\, I^{(3)}_{jk}(t) \int_0^\infty d\tau \left[\ln\left(\frac{\tau}{2\tau_0}\right) + \frac{97}{60}\right] I^{(6)}_{ijk}(t-\tau) \\ &= \frac{4\,G^2\,m}{63\,c^{10}} \sum_{p,q=-\infty}^{\infty} n^9 p^5 q^3 e^{i(p+q)\ell} \underset{(q)}{\mathcal{I}_{jk}} \underset{(p)}{\mathcal{I}_{ijk}} \Big[i\frac{\pi}{2} Sign(-pn) - \Big(\ln(2|-pn|\tau_0 e^{-97/60}) + \gamma_E\Big)\Big] \end{aligned} \tag{5.7.8}$$

$$\begin{aligned}\left(\mathcal{F}_i^{\text{hered}}\right)_3 &= \frac{32\,G^2\,m}{45\,c^{10}}\, \varepsilon_{ijk}\, I^{(3)}_{ja}(t) \int_0^\infty d\tau \left[\ln\left(\frac{\tau}{2\tau_0}\right) + \frac{7}{6}\right] J^{(5)}_{ka}(t-\tau) \\ &= \frac{32\,G^2\,m}{45\,c^{10}} \sum_{p,q=-\infty}^{\infty} n^7 p^3 q^4 e^{i(p+q)\ell} \varepsilon_{ijk} \underset{(p)}{\mathcal{I}_{ja}} \underset{(q)}{\mathcal{J}_{ka}} \Big[\frac{\pi}{2} Sign(-qn) + i\Big(\ln(2|-qn|\tau_0 e^{-7/6}) + \gamma_E\Big)\Big] \end{aligned} \tag{5.7.9}$$

$$\begin{aligned}\left(\mathcal{F}_i^{\text{hered}}\right)_4 &= \frac{32\,G^2\,m}{45\,c^{10}}\, \varepsilon_{ijk}\, J^{(3)}_{ka}(t) \int_0^\infty d\tau \left[\ln\left(\frac{\tau}{2\tau_0}\right) + \frac{11}{12}\right] I^{(5)}_{ja}(t-\tau) \\ &= \frac{32\,G^2\,m}{45\,c^{10}} \sum_{p,q=-\infty}^{\infty} n^7 p^4 q^3 e^{i(p+q)\ell} \varepsilon_{ijk} \underset{(p)}{\mathcal{I}_{ja}} \underset{(q)}{\mathcal{J}_{ka}} \Big[\frac{\pi}{2} Sign(-pn) + i\Big(\ln(2|-pn|\tau_0 e^{-11/12}) + \gamma_E\Big)\Big] \end{aligned} \tag{5.7.10}$$

Finally explicitly expressing all the Fourier components $(\mathcal{I}_L, \mathcal{J}_L)$ (quoted in Appendix A of ref. [62]) in Eqs. (5.7.6-5.7.10) in terms of the Bessel functions and performing the summation, one can obtain the total hereditary contribution. In principle, one can keep adding the infinite number of terms to get a more accurate result, but since we are interested in the small eccentricity limit, the infinite sum boils down to a finite closed form expression. The two non-zero components of the hereditary contributions to the linear momentum flux in the small eccentricity limit read as,

$$\begin{aligned}
\mathcal{F}_x^{\text{hered}} =& -\frac{464}{105}\frac{c^4}{G}\sqrt{1-4\eta}\eta^2\xi_\phi^{\frac{14}{3}}\Bigg(-\frac{309}{58}\pi\sin\phi+2\log\left(\frac{n}{\omega_0}\right)\cos\phi+e_t\Bigg[-\frac{8211}{580}-\frac{5517}{232}\pi\sin2\phi+2\log\left(\frac{n}{\omega_0}\right)+\\
&+\Big(\frac{260673}{16820}+\frac{95951}{841}\log2-\frac{463563}{6728}\log3+\frac{465}{29}\log\Big[\frac{n}{\omega_0}\Big]\Big)\cos2\phi\Bigg]+e_t^2\Bigg[-\frac{2454}{29}\pi\sin\phi-\frac{21847}{464}\pi\sin3\phi\\
&+\Big(-\frac{428169}{8410}+\frac{356305}{841}\log2-\frac{215703}{841}\log3+\frac{2341}{58}\log\Big[\frac{n}{\omega_0}\Big]\Big)\cos\phi+\Big(\frac{515501}{8410}-\frac{115529}{841}\log2\\
&-\frac{1908603}{13456}\log3+\frac{78125}{464}\log5+\frac{2655}{58}\log\Big[\frac{n}{\omega_0}\Big]\Big)\cos3\phi\Bigg]\Bigg)
\end{aligned} \tag{5.7.11a}$$

$$\begin{aligned}
\mathcal{F}_y^{\text{hered}} =& -\frac{464}{105}\frac{c^4}{G}\sqrt{1-4\eta}\eta^2\xi_\phi^{\frac{14}{3}}\Bigg(\frac{309}{58}\pi\cos\phi+2\log\left(\frac{n}{\omega_0}\right)\sin\phi+e_t\Bigg[\frac{5205}{232}\pi+\frac{5517}{232}\pi\cos2\phi\\
&+\Big(\frac{260673}{16820}+\frac{95951}{841}\log2-\frac{463563}{6728}\log3+\frac{465}{29}\log\Big[\frac{n}{\omega_0}\Big]\Big)\sin2\phi\Bigg]+e_t^2\Bigg[\frac{4878}{29}\pi\cos\phi+\frac{21847}{464}\pi\cos3\phi+\\
&+\Big(\frac{488103}{8410}+\frac{684787}{841}\log2-\frac{830169}{1682}\log3+\frac{3391}{58}\log\Big[\frac{n}{\omega_0}\Big]\Big)\sin\phi+\Big(\frac{515501}{8410}-\frac{115529}{841}\log2\\
&-\frac{1908603}{13456}\log3+\frac{78125}{464}\log5+\frac{2655}{58}\log\Big[\frac{n}{\omega_0}\Big]\Big)\sin3\phi\Bigg]\Bigg),
\end{aligned} \tag{5.7.11b}$$

where

$$\omega_0=\frac{1}{\tau_0}\exp\left[\frac{5921}{1740}+\frac{48}{29}\log2-\frac{405}{116}\log3-\gamma_E\right]$$

It should be noted here that, a simple redefinition of phase variable by, $\psi=\phi-\frac{2Gm}{c^3}\dot{\phi}\log\left(\frac{n}{\omega_0}\right)$, absorbs all the terms involving the logarithm of the mean motion ($\log[n]$) in Eq. (5.7.11a) & (5.7.11b), which practically introduces only a very small modulation in the phase. As a result of this redefinition, Eq. (5.7.11a) & (5.7.11b) together with the instantaneous parts in Eqs. (5.6.1b) & (5.6.1b) give rise to the total LMF from the system, given in Eq. (5.7.12) & (5.7.13) below:

$$\begin{aligned}
\mathcal{F}_x =& -\frac{464}{105}\frac{c^4}{G}\sqrt{1-4\eta}\eta^2\xi_\phi^{\frac{11}{3}}\Bigg(-\sin\psi-\frac{407}{116}e_t\sin2\psi+e_t^2\Big[-\frac{633}{58}\sin\psi-\frac{151}{29}\sin3\psi\Big]\\
&+\xi_\phi^{2/3}\Big(\Big[\frac{1139\eta}{522}+\frac{452}{87}\Big]\sin\psi+e_t\Big[\Big(\frac{2883\eta}{232}+\frac{1094}{87}\Big)\sin2\psi+\frac{1221}{116}\psi\cos2\psi-\frac{1167}{116}\psi\Big]\\
&+e_t^2\Big[\Big(\frac{12683\eta}{261}+\frac{2599}{116}\Big)\sin\psi+\Big(\frac{9767\eta}{348}+\frac{4213}{348}\Big)\sin3\psi-\frac{831}{29}\psi\cos\psi+\frac{906}{29}\psi\cos3\psi\Big]\Big)\\
&+\xi_\phi\Big(-\frac{309}{58}\pi\sin\psi+e_t\Big[-\frac{8211}{580}-\frac{5517}{232}\pi\sin2\psi+\Big(\frac{260673}{16820}+\frac{95951}{841}\log2-\frac{463563}{6728}\log3\Big)\cos2\psi\Big]\\
&+e_t^2\Big[-\frac{2454}{29}\pi\sin\psi-\frac{21847}{464}\pi\sin3\psi+\Big(-\frac{428169}{8410}+\frac{356305}{841}\log2-\frac{215703}{841}\log3\Big)\cos\psi\\
&+\Big(\frac{515501}{8410}-\frac{115529}{841}\log2-\frac{1908603}{13456}\log3+\frac{78125}{464}\log5\Big)\cos3\psi\Big]\Big)
\end{aligned}$$

$$
\begin{aligned}
&+\xi_\phi^{4/3}\Big(\Big[\frac{71345}{22968}-\frac{36761\eta}{2088}-\frac{147101\eta^2}{68904}\Big]\sin\psi+e_t\Big[\Big(\frac{3665}{232}+\frac{41531\eta}{696}\Big)\psi-\Big(\frac{14347\eta}{232}+\frac{5089}{232}\Big)\psi\cos 2\psi\\
&+\Big(\frac{2808541}{68904}-\frac{6878125\eta}{91872}-\frac{622681\eta^2}{30624}+\frac{3663\psi^2}{232}\Big)\sin 2\psi\Big]+e_t^2\Big[\Big(\frac{12877\eta}{58}-\frac{201}{29}\Big)\psi\cos\psi\\
&-\Big(\frac{13995\eta}{58}+\frac{1495}{58}\Big)\psi\cos 3\psi+\Big(\frac{931021}{6264}-\frac{1108915\eta}{5742}-\frac{7192771\eta^2}{68904}-\frac{2493\psi^2}{29}\Big)\sin\psi\\
&\left(\frac{23717}{176}-\frac{2249135\eta}{15312}-\frac{3092275\eta^2}{45936}+\frac{2718\psi^2}{29}\right)\sin 3\psi\Big]\Big)\Big), \qquad (5.7.12)
\end{aligned}
$$

$$
\begin{aligned}
\mathcal{F}_y=&-\frac{464}{105}\frac{c^4}{G}\sqrt{1-4\eta}\eta^2\xi_\phi^{\frac{11}{3}}\Big(\cos\psi+e_t\Big[\frac{389}{116}+\frac{407}{116}\cos 2\psi\Big]+e_t^2\Big[\frac{1187}{58}\cos\psi+\frac{151}{29}\cos 3\psi\Big]\\
&+\xi_\phi^{2/3}\Big(\Big[-\frac{452}{87}-\frac{1139\eta}{522}\Big]\cos\psi+e_t\Big[-\frac{3583}{348}-\frac{25193\eta}{2088}-\Big(\frac{2883\eta}{232}+\frac{1094}{87}\Big)\cos 2\psi+\frac{1221}{116}\psi\sin 2\psi\Big]\\
&+e_t^2\Big[\Big(-\frac{52363\eta}{522}-\frac{3993}{116}\Big)\cos\psi-\Big(\frac{9767\eta}{348}+\frac{4213}{348}\Big)\cos 3\psi+\frac{831}{29}\psi\sin\psi+\frac{906}{29}\psi\sin 3\psi\Big]\Big)\\
&+\xi_\phi\Big(\frac{309}{58}\pi\cos\psi+e_t\left[\frac{5205}{232}\pi+\frac{5517}{232}\pi\cos 2\psi+\Big(\frac{260673}{16820}+\frac{95951}{841}\log 2-\frac{463563}{6728}\log 3\Big)\sin 2\psi\right]\\
&+e_t^2\Big[\frac{4878}{29}\pi\cos\psi+\frac{21847}{464}\pi\cos 3\psi+\Big(\frac{488103}{8410}+\frac{684787}{841}\log 2-\frac{830169}{1682}\log 3\Big)\sin\psi\\
&+\Big(\frac{515501}{8410}-\frac{115529}{841}\log 2-\frac{1908603}{13456}\log 3+\frac{78125}{464}\log 5\Big)\sin 3\psi\Big]\Big)+\xi_\phi^{4/3}\Big(\Big[\frac{147101\eta^2}{68904}+\frac{36761\eta}{2088}\\
&-\frac{71345}{22968}\Big]\cos\psi+e_t\Big[-\frac{3212437}{68904}+\frac{185195\eta}{2784}+\frac{5567939\eta^2}{275616}-\frac{3501\psi^2}{232}+\Big(\frac{622681\eta^2}{30624}+\frac{6878125\eta}{91872}\\
&-\frac{3663\psi^2}{232}-\frac{2808541}{68904}\Big)\cos 2\psi-\Big(\frac{14347\eta}{232}+\frac{5089}{232}\Big)\psi\sin 2\psi\Big]+e_t^2\Big[\Big(\frac{4040725\eta^2}{17226}+\frac{1039069\eta}{2552}-\frac{2493\psi^2}{29}\\
&-\frac{660155}{1566}\Big)\cos\psi+\Big(\frac{3092275\eta^2}{45936}+\frac{2249135\eta}{15312}-\frac{2718\psi^2}{29}-\frac{23717}{176}\Big)\cos 3\psi+\Big(\frac{201}{29}-\frac{12877\eta}{58}\Big)\psi\sin\psi\\
&-\left(\frac{13995\eta}{58}+\frac{1495}{58}\right)\psi\sin 3\psi\Big]\Big)\Big). \qquad (5.7.13)
\end{aligned}
$$

As a consistency check, in the limit $e_t \to 0$, above expression reduces to the estimate of LMF from a binary moving in a quasi-circular orbit (see Eq. (1) of ref. [108]).

5.8 Summary

In this chapter we extended the LMF computation presented in ref. [168] at 2PN for a non-spinning compact binary system moving in a quasi-elliptical orbit. We first discuss the instantaneous contribution and quote the 2PN equivalent of the same in terms of orbital elements $r, \dot{r}, \phi, \dot{\phi}$. We then use the 2PN QK parametrization to obtain the hereditary contribution at 1.5PN and re-express the complete LMF in terms of the QK parameters of the compact binary inspiral. This 2PN LMF expression can further be used to compute the recoil of the system. To be noted here, along with all the periodic terms appearing in the LMF expressions, aperiodic terms also appear with explicit dependences on eccentricity. These features start appearing from the Newtonian order itself and are discussed in ref. [168]. These terms give rise to a continuous drift of the center of mass over an orbit. At 2PN, the complete closed form expression of the LMF, retaining the terms only up to $O(e_t^2)$, is obtained in Eqs. (5.7.12) & (5.7.13). These flux components can further be used to estimate the associated recoil of the compact binary system at 2PN. However, all the aperiodic terms in the orbital phase, ψ, explicitly depend on the eccentricity parameter e_t. Hence, in order to obtain realistic estimates for the complete accumulated recoil of the binary over its inspiralling orbits, one needs to consider the evolution of the orbital parameters (e_t, ψ and ξ_ϕ). This we postpone for the future.

6 Imprints of the redshift evolution of the double neutron star merger rate on their signal to noise ratio distribution

6.1 Introduction

We have already seen how useful the parameter estimation of gravitational signals are for understanding source properties and performing tests of strong-field gravity. In this chapter we consider how the SNR distribution of compact binaries carries a wealth of astrophysical information and how this may facilitate unique probes of the evolution of the star formation rate as a function of redshift. Recently, on very general grounds, Schutz [272] pointed out that the observed SNRs of the GW events detected by GW detectors should follow a universal distribution if the underlying source population is uniform within the volume accessible to the detectors. This distribution is independent of the type of the sources and hence referred to as universal. As argued by Schutz [272], the universality lies in the fact that the SNR of the GW events are inversely proportional to the luminosity distance ($\rho \propto \frac{1}{D_L}$) and at relatively low redshifts (say, $z \lesssim 0.1$) the luminosity distance and co-moving distance are roughly the same. More precisely, following Chen and Holz [129], for a source population following a constant co-moving number density, the probability density function, f_D, of the source (say a compact binary merger) distribution at a co-moving distance of D, is proportional to D^2, i.e. $f_D dD \propto D^2\, dD$. Since $\rho \propto \frac{1}{D}$, the distribution of SNR corresponding to the particular source distribution, can easily be shown to follow $p(\rho) = f_D\left|\frac{dD}{d\rho}\right| \propto \frac{1}{\rho^4}$. After normalization, we obtain

$$p(\rho) = \frac{3\rho_{th}^3}{\rho^4}, \tag{6.1.1}$$

where ρ_{th} is the SNR threshold used for detection. The above derivation crucially assumes that the properties of the source population (such as the mass distribution) do not evolve with redshift. Chen and Holz [129] explored various implications of this universal distribution for the sources detectable by second generation detectors such as advanced LIGO/Virgo. This universal distribution is also an ingredient used in [21] to derive a bound on the rate of the binary black hole mergers from the first observation run of LIGO [17].

Motivated by [272] and [129], in this chapter we study the SNR distribution of compact binary mergers for cosmological sources. In the case of BBH mergers, their mass distribution is likely to influence the SNR distribution as much as the cosmological evolution (see for instance [288]) which makes it difficult to disentangle the two effects. However, that is not the case with DNS mergers as the masses are expected to vary over a relatively smaller range compared to BBH mergers.

The proposed third generation GW detector, Cosmic Explorer (CE) will have the sensitivity to observe DNS mergers up to a redshift of ~ 5 with high SNRs. Hence considering CE's sensitivity as representative of a third generation GW detector, in this chapter we study how the SNR distribution of DNS mergers observed by CE gets affected by the redshift evolution of their rate density and hence use the detected SNR distribution to probe the underlying redshift evolution of DNS mergers. Considering astrophysically motivated models for the redshift evolution of the DNS merger rate density, we study how distinguishable the resulting SNR distributions are from each other. The novelty of the proposed method is that it does not rely on the direct measurement of distance or redshift but requires only the SNRs. We find that detections of the order of a few hundreds of DNS mergers are sufficient to distinguish between different redshift evolution models. As the projected detection rate of DNS mergers per year by the third generation GW detectors is of the order a few hundreds to thousands [39], one year of observation by CE may itself be sufficient to track the redshift evolution of DNS using this method.

This chapter is organized in the following way. In section 6.2 we consider the cosmological effects on the optimal SNR of compact binary sources. In section 6.3 we explore how the different DNS merger rate densities affect the SNR distributions. In section 6.4 we discuss whether the distributions corresponding to all the merger rate densities are distinguishable from each other.

6.2 Effects of cosmological expansion on the signal to noise ratio of compact binaries

The optimal SNR, discussed in detail in chapter 1, is defined as

$$\rho = \sqrt{4\int_0^\infty \frac{|\tilde{h}(f)|^2}{S_h(f)}df}, \tag{6.2.1}$$

where $S_h(f)$ is the detector's power spectral density (PSD) and $\tilde{h}(f)$ is the frequency domain gravitational waveform (for instance, Sec. (5.1) of [268] for details) or the optimal template. We employ the restricted post-Newtonian (PN) waveform (RWF) here, $\tilde{h}(f) = \mathcal{A} f^{-7/6} e^{i\psi(f)}$, where $\mathcal{A}$ is the amplitude and $\psi(f)$ is the frequency domain GW phase. In RWF, the PN corrections to the amplitude of the gravitational waveform are ignored but the phase is accounted for to the maximum available accuracy. Using the RWF, the optimal SNR for GW events of compact binary systems can be expressed as [136]

$$\rho(m_1, m_2, D_L, \theta, \phi, \psi, \iota) = \sqrt{4\frac{\mathcal{A}^2}{D_L^2}\left[F_+^2(\theta,\phi,\psi)(1+\cos^2\iota)^2 + 4F_\times^2(\theta,\phi,\psi)\cos^2\iota\right] I(M)}, \tag{6.2.2}$$

where $F_{+,\times}(\theta,\phi,\psi)$ are the antenna pattern functions for the 'plus' and 'cross' polarizations of gravitational waves, $\mathcal{A} = \sqrt{5/96}\pi^{-2/3}\mathcal{M}^{5/6}$, $\mathcal{M}$ is the chirp mass, which is related to the total mass M by $\mathcal{M} = M\eta^{3/5}$, where $\eta = \frac{m_1 m_2}{M^2}$ is the symmetric mass ratio of the system and m_1, m_2 are the component masses. The four angles $\{\theta, \phi, \psi, \iota\}$ describe the location and orientation of the source with respect to the detector. $I(M)$ is the frequency integral defined as

$$I(M) = \int_0^\infty \frac{f^{-7/3}}{S_h(f)}df \simeq \int_{f_{low}}^{f_{\rm LSO}} \frac{f^{-7/3}}{S_h(f)}df. \tag{6.2.3}$$

In the last step, we have replaced the lower and upper limit of the integral by the seismic cut off, f_{low}, of the detector and the frequency at the last stable orbit. The GW frequency at the last stable orbit (LSO) up to which the PN approximation is validis, $f_{\rm LSO} = \frac{1}{6^{3/2}\pi M}$. This is the expression for the frequency at the LSO of a Schwarzschild BH with total mass M.

As we use CE as a proxy for third generation detectors in this chapter, the SNR computation uses the analytical fit given in section 1.3.2 of chapter 1 as the Cosmic Explorer wide band (CE-wb) sensitivity curve [24]. Next we discuss the effect of cosmology on the gravitational waveform and hence the expression for SNR.

6.2.1 Effects of cosmological expansion

Assuming a flat Λ-CDM cosmological model [43, 45] of the universe, we explore the modification to the SNR for compact binary systems at cosmological distances. Cosmological expansion of the universe affects the gravitational waveforms in two ways. GW amplitude is inversely proportional to the co-moving distance D, which is related to the luminosity distance D_L by $D_L = D\,(1+z)$, where z is the redshift to the source. Secondly, due to the cosmological expansion, the GW frequency gets redshifted. This results in redefining the chirp mass in such a way that the observed chirp mass ($\mathcal{M}$) is related to the corresponding chirp mass in the source frame ($\mathcal{M}_{\rm source}$), by $\mathcal{M} = \mathcal{M}_{\rm source}\,(1+z)$. In order to explicitly incorporate these effects, we re-write the expression for SNR in Eq. 6.2.2 as

$$\rho = \frac{\mathcal{M}_{\rm source}^{5/6}}{D(1+z)^{1/6}}\, g(\theta,\phi,\psi,\iota)\;\sqrt{I(M)}, \tag{6.2.4}$$

where all the angular dependencies in the waveform are captured into the definition of $g(\theta,\phi,\psi,\iota)$ and all other variables have their usual meanings.

In a flat FLRW cosmology, the comoving distance (following $c = G = 1$ units), corresponding to a redshift z (Ref. [193, 301]) is given by

$$D(z) = \frac{1}{H_0}\int_0^z \frac{dz'}{E(z')}, \tag{6.2.5}$$

where H_0 is the Hubble constant and

$$E(z) = \sqrt{\Omega_m(1+z)^3 + \Omega_\Lambda}, \tag{6.2.6}$$

with the total density parameter (Ω) consisting of matter (dark and baryonic) density (Ω_m) and cosmological constant (Ω_Λ). Throughout this chapter, we consider a cosmology with $\Omega_\Lambda = 0.7$ and $\Omega_m = 0.3$ and $H_0 = 72$km/Mpc/sec [43, 45].

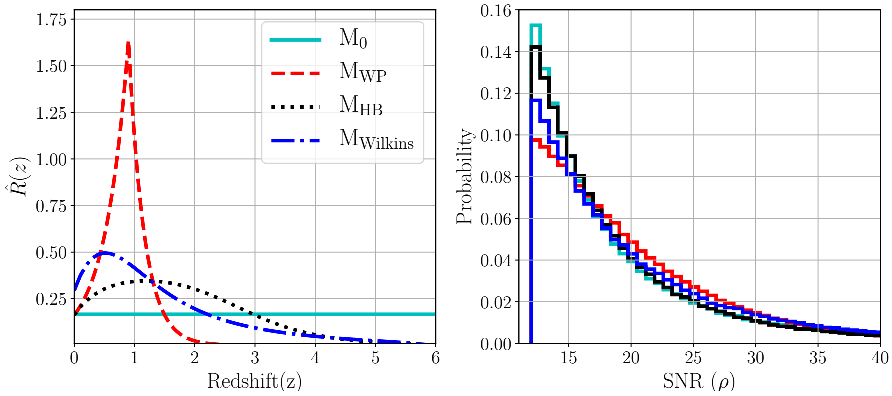

Figure 6.1. Figure on the left panel shows the evolution of co-moving merger rate density with redshift for four different models, M_0 stands for the constant comoving merger rate, $M_{\rm WP}$ represents the model for rate density evolution obtained by Wandermann & Piran [291], $M_{\rm HB}$ and $M_{\rm Wilkins}$ denote the merger rate models obtained in Ref. [259, 284] following the star formation rates given in ref. [195] and [295] respectively. The figure on the right most panel contains the corresponding normalized SNR distributions.

Given that z is a function of co-moving distance, D (Eq. 6.2.5), it is clear from Eq. 6.2.4 that the simple scaling relation for SNR ($\rho \propto 1/D$) would no longer hold. Hence it is obvious that the universal SNR distribution, given in Eq. 6.1.1, does not apply any more. In the next section we discuss the effect of redshift evolution of the DNS merger rate on the SNR distribution.

6.3 Imprints of co-moving merger rate density evolution of DNS systems on the SNR distribution

Usually it is assumed that the DNS formation rate follows the star formation rate, whereas their merger rate will depend also on the delay time distribution, i.e. the distribution of the time delay between the formation and the merger. Hence, following Ref. [259], the binary merger rate density can be written as

$$R(z) \propto \int_{t_d^{\rm min}}^{\infty} \frac{\dot{\rho}_*(z_f(z,t_d))}{1+z_f(z,t_d)} P(t_d)\, dt_d, \tag{6.3.1}$$

where $\dot{\rho}_*$ is the star formation rate, t_d is the delay time and $t_d^{\rm min}$ is the minimum delay time for a binary to merge since its formation. The redshift z describes the epoch at which the compact binary merges and z_f is the redshift at which its progenitor binary forms and they are related by a delay time t_d. The factor $P(t_d)$ is the distribution of the delay time. According to various population synthesis models [53,79,150,222,242,281], the delay time follows a power-law distribution, $P(t_d) \propto 1/t_d$, with $t_d > t_d^{\rm min}$. The factor $(1+z_f)^{-1}$ in Eq. (6.3.1) takes into account the cosmological time dilation between the star formation and the merger.

For our analysis in this chapter, we use two merger rate models, following the two star formation rate models proposed in refs. [195] and [295], and denote them as $M_{\rm HB}$ and $M_{\rm Wilkins}$, respectively. In both cases we consider [78, 79] $t_d^{\rm min} \sim 20$Myr. As discussed in Ref. [155], the redshift evolution of the host galaxy affects the merger rate of DNS binaries (see their top panel of Figures 3 and 4). For higher metallicities, the peak of the merger rate density shifts towards lower redshifts. From this perspective, our $\rm M_{Wilkins}$ is representative of the case where the DNS mergers primarily happen in high metallicity environments. We also consider another model of rate density evolution, obtained in ref. [291],

$$R_{WP}(z) = 45 Mpc^{-3} Gyr^{-1}. \begin{cases} e^{(z-0.9)/0.39} & z \leq 0.9 \\ e^{-(z-0.9)/0.26} & z > 0.9. \end{cases}$$

This is a model (denoted as $\rm M_{WP}$) derived based on the short Gamma-Ray Bursts (GRBs) observed by the Gamma-Ray satellites accounting for the effect of beaming. Though some what indirect, we use this model to have enough diversity in the set of models we compare against.

Along with these models, we also consider a case with constant comoving rate density, M_0, characterized by $R(z) = R_0 = 1 Mpc^{-3} Myr^{-1}$. The left panel of Fig. 6.1 shows the normalized merger rate density models discussed above.

Given the merger rate density $R(z)$ (in units of $Mpc^{-3}Myr^{-1}$), the total number of sources (in units of Myr^{-1}) in a co-moving volume of radius D is,

$$N(D) \propto \int_0^D \frac{R(z(D'))}{1+z(D')} D'^2 dD', \tag{6.3.2}$$

where z can be numerically inverted to obtain the corresponding co-moving distance D. The $(1+z)$ factor in the denominator accounts for the time dilation between the source-frame and the observer-frame.

Considering the above proposed models to be the underlying source distribution within the co-moving volume and assuming isotropy, we obtain the optimal SNR distribution of DNS mergers for CE (right panel of

Fig. 6.1). To generate the source population in order to obtain the optimal SNR distributions corresponding to different $R(z)$ (left panel of Fig 6.1), first the sources are assumed to be uniformly located and oriented on the sphere parametrized by the comoving distance. This is achieved by making sure that the azimuth angles ϕ, ψ are drawn from a distribution uniform in the limit $[0, 2\pi]$ and the polar angles θ, ι are chosen such that their cosines are uniformly distributed between $[-1, 1]$. These choices ensure that at any radius, the source population is uniformly located and oriented on the surface of the sphere. Further, we need to distribute the sources *within* the detection volume specified by the maximum radius $D_{max}(\rho_{th}, M)$ (or $z_{max}(\rho_{th}, M)$), which depends on the SNR threshold ($\rho_{th} = 12$ considered here). Hence we choose $N(D)$ to be uniformly distributed between $N(1)$ and $N(D_{max})$ and for each realization we numerically solve Eq (6.3.2) to obtain the corresponding D value from $N(D)$.

Using the procedure outlined above, we compute the optimal SNR distributions for the different models by imposing the SNR threshold of 12 which is shown in the right panel of Fig 6.1. Next we discuss how many detections are required for these models to be statistically distinguishable from each other.

6.4 Statistical tests of distinguishability of various models

In this section, we demonstrate the distinguishability of the SNR distributions corresponding to all the merger rate density models discussed in the previous section. First of all, we discuss how to account for the uncertainty on the SNRs associated with GW detections and then we discuss the distinguishability of different models.

6.4.1 Uncertainties on the SNRs

In reality, GW detections are made applying a certain pre-determined detection threshold on the matched filtered SNRs which are calculated by matching the observed data and a template bank of precomputed GW waveforms. However, the SNR distributions in the right panel of Fig. 6.1 are produced using optimal SNRs for each source, where optimal SNR is a point estimate (SNR of the best fit template from matched filtering). Therefore it is important to fold in the uncertainties to the point estimates of SNRs to account for the usage of matched-filtering in the process of GW detections.

Under the assumption of zero mean Gaussian random noise in the detectors, the matched filter SNR (σ) follows the Rice distribution [263] (see Eq. (1.4.5)) discussed in chapter 1. In order to account for the errors on SNRs in our distributions, we first calculate the optimal SNR (say ρ_i) for each source and then replace it with a number chosen at random from the distribution $f(\sigma, \rho_i)$ (Eq. 1.4.5).

6.4.2 Statistical tests

Now we quantify the distinguishability of the different SNR distributions by employing the Anderson-Darling (AD) [51] test. The AD test is a well-known tool used to assess whether a sample data belongs to a reference distribution. The test returns a probability value (p value) for the “null" hypothesis that the *sample belongs to the reference distribution*. If the null hypothesis is true, the p value distribution obtained by performing the experiment multiple times is uniform between 0 and 1 with a median p value of 0.5. If the sample does not belong to the reference distribution, the p value distribution will sharply peak around 0. A p value distribution weighted more towards 0, implies a stronger evidence of rejecting the null hypothesis or ability to distinguish the two distributions.

In order to quantify the distinguishability between two arbitrary merger rate density models M and N, we follow the procedure below. First we synthesize a fiducial data of SNR distribution of size n (number of detections) assuming that the model M is the true merger rate distribution. We will account for the uncertainties on each of the SNRs in the synthesized data along the lines mentioned earlier in section 6.4.1. This noisy *data* is labeled as data$_M$, where the subscript refers to the underlying merger rate model. Then, we carry out the AD test between data$_M$ and the reference distribution $p_N(\rho)$ which is the predicted SNR distribution corresponding to the merger rate model N. In the above step, since $p_N(\rho)$ is the theoretical prediction, it is always free of errors which is ensured by using a sufficiently large number of samples consisting of optimal SNRs to generate that.

The test returns a p value which is denoted as $\mathcal{P}(M|N)$. Due to the limited number (n) of synthesized samples, the data$_M$ may not capture the essence of the model M and hence affects the p value. To account for this, we repeat the p value estimation 100 times, each time synthesizing the data$_M$ randomly and then computing the median of the resulting p value distribution. The median of p values is denoted as $\bar{\mathcal{P}}(M|N)$.

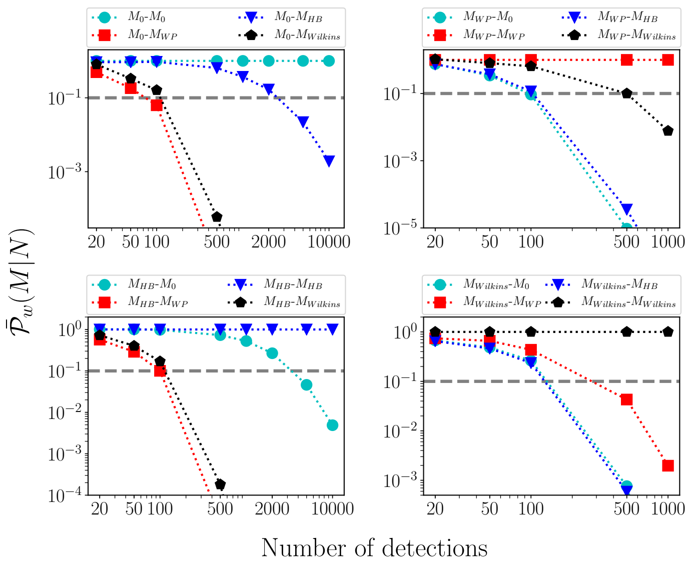

Figure 6.2. Weighted p-values ($\bar{\mathcal{P}}_w(M|N)$) from Anderson-Darling test performed on the data obtained from the four models as functions of the number of detections. The first argument in each legend represents the data generated by following a particular model M (denoted as data$_M$ in the main text), whereas the second argument is the theoretical model with which the data is compared to. We put a gray horizontal line in every panel corresponding to the threshold on $\bar{\mathcal{P}}_w(M|N)$ (see main text for details).

6.4.3 Weighted *p*-values

As mentioned earlier (in section 6.4.1), we have used Rice distribution to model the errors in SNR. The presence of these errors in the data will affect the p values which in turn can lead to false detection or false rejection. For example, the median of the p value distribution resulting from AD test of data$_M$ with the model M, in principle, should be 0.5. But due to the errors, the test may return a lower median which may even lead to the rejection of the null hypothesis when it is actually true. In our case, we have multiple models {N} to be tested against the data$_M$ and p value for each model ($\bar{\mathcal{P}}(M|N)$) will decrease due to the errors thereby reducing the ability to distinguish between various models.

In order to quantify the distinguishability between the data and a model along the lines described earlier, we introduce the notion of *weighted* p values. For a given data$_M$, we define a weighting function $\mathcal{W}$ as

$$\mathcal{W} = \frac{1}{\bar{\mathcal{P}}(M|M)}. \tag{6.4.1}$$

where $\bar{P}(M|M)$ is the median of p values between data$_M$ and the underlying model M (which, in the absence of noise, is 0.5). We now define the weighted p value between models data$_M$ and N as

$$\bar{\mathcal{P}}_w(M|N) = \mathcal{W} \times \bar{\mathcal{P}}(M|N). \tag{6.4.2}$$

The weighting factor $\mathcal{W}$ is chosen in such a way that the weighted p value for data$_M$ with the model M itself always returns unity ((*i.e,* $\bar{\mathcal{P}}_w(M|M) = 1$)). Weighted p values have been extensively discussed in the literature in the context of testing multiple hypotheses (for example, see the references [81, 156, 194]). The definition we use here may be thought of as an adaptation of this generic definition to our problem.

Based on our previous discussion, it is clear that if two distributions are distinguishable, $\bar{\mathcal{P}}_w(M|N)$ will always be smaller than 1. Using a threshold on the median of the p-value distribution of 0.05 while performing the AD test (i.e. 95% of the time the model is rejected), we set a rejection threshold on $\bar{\mathcal{P}}_w(M|N)$ to be 0.05/0.5=0.1.

6.4.4 Results and discussion

We present our results in Fig. 6.2 where, in the x-axis, we show the number of detections n (for n= 20, 50, 100, 200, 500, 1000, 2000, 5000, 10000 etc.) and in the y-axis, we show the distinguishability of each of the four rate models ($M_0, M_{\rm HB}, M_{\rm Wilkins}, M_{\rm WP}$) from each other by computing the *weighted p* values $\bar{\mathcal{P}}_w(M|N)$ among them. Each panel corresponds to a particular model for the data and the different curves in each panel correspond to $\bar{\mathcal{P}}_w(M|N)$ estimated for all the four models. For example, in the top-left panel of Fig. 6.2 we synthesize the data following constant co-moving rate density and compare against the theoretical distributions of all four models. By construction, the *weighted p* value $\bar{\mathcal{P}}_w(M_0|M_0)$, when the data containing M_0 is compared with model M_0 itself, represented by the cyan line, is constant and is 1. As opposed to this scenario, all the other ratio falls off as a function of the number of detections. Hence the data can be distinguished from the other models. In the top-left panel, we also see that a low number of detections ($\sim$ 500) is sufficient to distinguish between data$_{M_0}$ and the model $M_{\rm WP}$ or $M_{\rm Wilkins}$ whereas we need at least thousands of detections to distinguish between the data$_{M_0}$ and the model $M_{\rm HB}$.

In the remaining three panels, we perform the same exercise for the rest of the three models. In the top right panel the data ($\mathrm{data}_{\mathrm{M_{WP}}}$) is generated from the merger rate density model, $\mathrm{M_{WP}}$. As expected, $\bar{\mathcal{P}}_w(M_{\mathrm{WP}}|M_{\mathrm{WP}})$ is unity (red curve). The cyan, blue and the black curves represent the comparison with models $\mathrm{M_0}$, $\mathrm{M_{HB}}$, $\mathrm{M_{Wilkins}}$ respectively. We find that for a few hundreds of detections, all three models are distinguishable from $\mathrm{M_{WP}}$. This is not surprising given how different this distribution is from others in the left panel of Fig. 6.1.

Similarly in the bottom left panel the data is generated following the merger rate density model, $\mathrm{M_{HB}}$ and in the bottom right panel the data is generated following the merger rate density model, $\mathrm{M_{Wilkins}}$. In case of data containing M_{HB} (bottom left panel) we find that a larger number of detections ($\sim$ few thousands) of DNS mergers are needed in order to distinguish this model especially from $\mathrm{M_0}$. As opposed to this scenario, in the bottom right panel, $\mathrm{M_{Wilkins}}$ is distinguishable from other models given a few hundreds of detections.

Therefore it is evident that $\mathrm{M_{WP}}$ and $\mathrm{M}_{Wilkins}$ can be distinguished from all other models with high confidence with a few hundreds of detections, whereas $\mathrm{M_{HB}}$ is difficult to distinguish from the M_0 using this method with low number of detections. However, with a large number of detections (say 5,000) $\mathrm{M_{HB}}$ is distinguishable from the other models. Given a sufficiently large number of detections, we expect $\bar{\mathcal{P}}_w(M|N)$ to be either 0 or 1 given the two distributions are different or the same respectively. Hence we do not show any $\bar{\mathcal{P}}_w(M|N) < 10^{-4}$ in Figure 6.2 and treat them as a scenario where the two distributions are completely distinguishable.

As shown in [39] and the most recent work in [71], the fore-casted DNS detection rates by the third generation detectors ET-B and CE ranges from one thousand to tens of thousands per year. Given this rate, it is clear that the SNR data collected from less than a year of observation will be sufficient to test various merger rate density models. As discussed before, the proposed method does not rely on the measurements of distance or redshift measurements which are usually obtained using computationally expensive parameter estimation algorithms. Instead, this method requires only the signal-to-noise ratios which are outcomes of the detection (or search) algorithms. Hence, the test based on SNR distributions offers a novel and computationally cheaper method to distinguish between various predicted merger rate density models in the era of third generation gravitational wave detectors.

A Systematic bias estimates for LISA

The use of inaccurate waveform model may lead to systematic biases in the parameter estimation [138,166]. For a detector data stream, s, consisting of a true waveform $\tilde{h}_{\rm T}(f;\vec{\theta}^{\rm T})$ and recovered with an approximate waveform $\tilde{h}_{\rm AP}(f;\vec{\theta}^{\rm best\ fit})$, the systematic errors on various parameters can be obtained by minimizing $\left\langle [\tilde{h}_{\rm T}(f;\vec{\theta}^{\rm T}) - \tilde{h}_{\rm AP}(f;\vec{\theta}^{\rm best\ fit})], [\tilde{h}_{\rm T}(f;\vec{\theta}^{\rm T}) - \tilde{h}_{\rm AP}(f;\vec{\theta}^{\rm best\ fit})]\right\rangle$ [138]. Since we are interested in quantifying the systematics due to the difference between the spinning and non-spinning waveforms, we adopt the minimization scheme developed in Ref. [138]. The basic assumption behind this scheme is to define a one parameter family of waveform models $(\tilde{h}^{\lambda}(f;\theta))$ that interpolate between both $\tilde{h}_{\rm T}(f;\vec{\theta}^{\rm T}) \equiv \tilde{h}^{\lambda=1}(f;\theta)$ and $\tilde{h}_{\rm AP}(f;\vec{\theta}) \equiv \tilde{h}^{\lambda=0}(f;\theta)$. As it turns out, after a set of approximations, the linearized estimate for the systematic error is (see Eq. (29) in Ref. [138])

$$\Delta_{\rm sys}\theta_m = \left(\Gamma^{-1}_{\rm AP}\right)_{mk}\left\langle i\mathcal{A}\mu_2 f^{-7/6}\Delta\psi e^{i\psi}\Big|_{\theta=\theta^{\rm best\,fit}}, \frac{\partial\tilde{h}_{\rm AP}(f;\vec{\theta}^{\rm best\ fit})}{\partial\theta_k}\right\rangle, \tag{A.0.1}$$

where $(\Gamma_{AP})_{mk}$ is the Fisher matrix obtained from the approximate waveform $\tilde{h}_{\rm AP}(f;\vec{\theta})$ and $\Delta\psi = \psi_T - \psi_{\rm AP}$. All the quantities are evaluated at the best fit values of the parameters which coincide with the true values in the large SNR limit.

To quantify the systematic bias, we consider a six dimensional parameter space consists of $\{t_c, \phi_c, \ln\mathcal{A}, \ln\mathcal{M}_c$, $\ln\eta, \mu_\ell$ or $\epsilon_\ell\}$ to completely specify the approximate waveform $\tilde{h}_{\rm AP}(f;\vec{\theta}^{\rm best\ fit})$, for our purpose the parametrized non-spinning TaylorF2 waveform. We use the same approximate waveform to estimate the six dimensional Fisher matrix, $\Gamma_{\rm AP}$. On the other hand, we consider the parametrized non-precessing TaylorF2 waveform to be our true waveform model.

In Fig. A.1 we show the systematic biases on μ_2 and μ_3 for binaries with three different total masses, $M = 10^5$

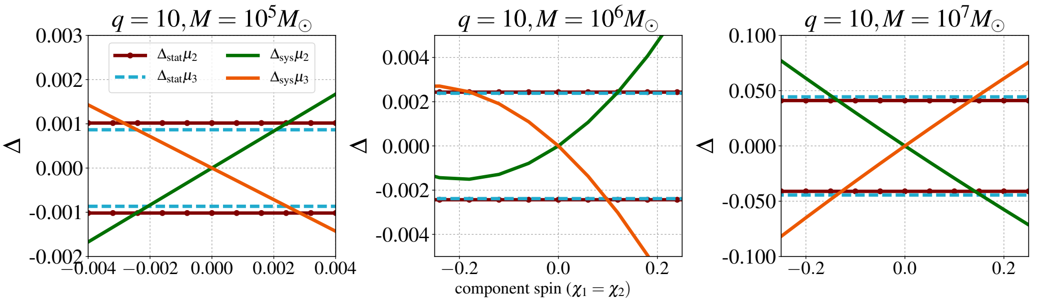

Figure A.1. Numerical estimates of systematic biases on the two leading multipole coefficients μ_2 and μ_3 as a function of $\chi_1 = \chi_2 = \chi$ for LISA noise PSD. We consider systems with three different total masses, $m = 10^5, 10^6, 10^7 M_\odot$ having mass ratio $q = 10$. All the sources are considered to be at a fixed luminosity distance of 3 Gpc.

$\mathrm{M}_\odot$, 10^6 $\mathrm{M}_\odot$, 10^7 $\mathrm{M}_\odot$ and mass ratio $q = 10$ as a function of individual spin parameter $\chi_1 = \chi_2 = \chi$ for LISA. Due to a smaller total mass ($M = 10^5\mathrm{M}_\odot$) a large number of inspiral cycles reside in the LISA band. Hence even with very small spin values $\chi \sim O(10^{-3})$, the systematic errors become larger than the statistical errors, which demands a parametrized spinning waveform model. In contrast, for larger total masses of about 10^6 $\mathrm{M}_\odot$ or 10^7 $\mathrm{M}_\odot$, the systematics affect the parameter estimation when the spin magnitude is slightly larger $\sim O(10^{-1})$, as expected. Hence it is very crucial to incorporate the spin corrections in the waveform to reduce the effects of systematics when extracting the information about the multipole coefficients. We also find that as the total mass of binary increases the slope of the systematic bias curves changes from positive to negative for μ_2 and vice-versa for μ_3. This could be due to the nature of the correlation (positive or negative) between these multipole coefficients and the binary parameters (such as masses and spins) with increasing total mass. We quote the leading order estimates for the systematic biases in case of LISA only. Since the Fisher matrix-based leading order estimation of systematic biases for network configuration demands reformulation of the prescription, we postpone these for future study in a more rigorous and accurate Bayesian framework.

LIST OF PUBLICATIONS ARISING FROM THE THESIS

1. **Testing the multipole structure of compact binaries using gravitational wave observations**

   Shilpa Kastha , Anuradha Gupta, K G Arun, B S Sathyaprakash and Chris Van Den Broeck

   Physical Review D. 98, 124033 (2018)

   arXiv:1809.10465 [gr-qc]

2. **Testing the multipole structure and conservative dynamics of compact binaries using gravitational wave observations: The spinning case**

   Shilpa Kastha , Anuradha Gupta, K G Arun, B S Sathyaprakash and Chris Van Den Broeck

   Physical Review D. 100, 044007 (2019)

   arXiv:1905.07277 [gr-qc]

3. **Imprints of the redshift evolution of double neutron star merger rate on the signal to noise ratio distribution**

   Shilpa Kastha, M. Saleem and K G Arun

   Communicated

   arXiv:1801.05942v2 [gr-qc]

4. **Linear momentum flux from inspiralling compact binaries in quasi-elliptical orbits at second post-Newtonian order**

   Shilpa Kastha , Chandra Kant Mishra, K G Arun

   In preparation

Shilpa Kastha

WORKSHOPS ATTENDED AND POSTER PRESENTED

1. 7 - 10 August 2018 : **Physics and Astrophysics at the eXtreme**, IUCAA, Pune, India .

2. 5 - 9 February 2018 : **XXXVI Meeting of Astronomical Society of India (ASI 2018)** , Osmania University, Hyderabad, India.

3. 18 - 20 May 2017 : **29th meeting of IAGRG.**, IIT Guwahati, Asam, India.

   Poster : *Gravitational recoil of eccentric compact binaries*

4. *18 - 20 May 2016 :* **The Future of Gravitational Wave Astronomy (FGWA 2016)***, International Centre for Theoretical Sciences, Bangalore, India.*

5. *10 - 13 May 2016 :* **XXXIV Meeting of Astronomical Society of India (ASI 2016)***, University of Kashmir, Srinagar, India.*

   Poster : *Tracking the merger rate density evolution of double Neutron star binaries.*

6. *14 - 18 December 2015 :* **8th International Conference on Gravitation and Cosmology (ICGC 2015)***, ISER Mohali, India.*

   Poster : *Probing the inhomogeneity in the spatial distribution of Double Neutron Star mergers Through Gravitational wave observations*

SEMINARS PRESENTED

1. ***Testing The Multipole Structure Of Compact Binaries Using Gravitational Wave Observations***

   22nd International Conference on General Relativity and Gravitation,

   13th Edoardo Amaldi Conference on Gravitational Waves, 2019 at Valencia, Spain.

2. ***Testing the multipolar structure of compact binary spacetimes***

   XXXVI Meeting of Astronomical Society of India, 2018 at Osmania University, India.

3. ***Testing Post-Newtonian multipole structure of general relativity***

   Seminar at the Institute of Gravitation & Cosmos, Penn State, USA (2017)

4. ***Probing Inhomogeneity in the Spatial distribution of double neutron star binaries using Gravitational-Wave Observations***

   The Future of Gravitational Wave Astronomy, ICTS-TIFR, Bangalore, India (2016).

Thesis Highlight

Name of the Student: Shilpa Kastha
Enrolment No.: PHYS10201404001
Name of the CI/OCC:
Thesis Title: Gravitational waves from compact binary coalescences: Tests of General Relativity and Astrophysics
Discipline: Theoretical physics
Sub-Area of Discipline: Gravitational waves Astrophysics
Date of viva voce: 06/02/2020

The recent detections of Gravitational waves (GWs) from binary blackholes and binary neutron star systems have provided an unprecedented opportunity for astrophysical measurements and testing general relativity in the strong-field regime.

In this thesis we propose a model-independent method to test general relativity by parametrizing the gravitational waveform from a compact binary system in terms of the multipole moments within the Post-Newtonian (PN) framework. We develop the parametrized multipolar GW phasing formula for compact binaries in quasi-circular orbit including the important effects of spins in the inspiral dynamics at 3.5PN order and deviations to the PN coefficients in the conserved energy. We also discuss the projected bounds on the multipole and the energy coefficients in the context of various GW detectors. The waveform we present here would be extremely useful not only in deriving the first upper limits on any deviations of the multipole coefficients from GR using the gravitational wave detections so far, but also for science case studies of next generation gravitational wave detectors.

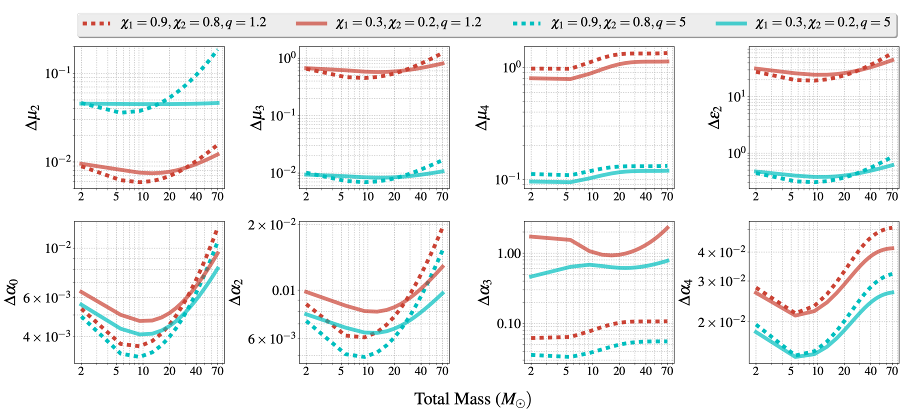

Projected 1-sigma bounds on the multipole and energy coefficients for a network of third generation gravitational wave detector.

We also study the emission of linear momentum flux (LMF) from a compact binary system in a quasi-elliptic orbit within the multipolar post-Minkowskian post-Newtonian framework. We compute the closed form expression for the LMF at the second post-Newtonian order for a compact binary system moving in quasi-elliptic orbits. Moreover, we use the quasi-Keplerian representation to express the same. This can be considered as a first step to estimate the associated recoil of the remnant blackhole.

In the last chapter, we propose a method to track the merger rate distribution of the binary neutron star systems as a function of redshift in the context of third generation gravitational wave detector. This method does not depend on the direct measurement of the distance but the SNRs of the detected gravitational wave events.